SuperNEMO Experiment : Study of Systematic Uncertainties of Track Reconstruction and Energy Calibration. Evaluation of Sensitivity to 0nbb with Emission of Majoron for Se-82.

Miroslav Macko

université de BORDEAUX

THÈSE EN COTUTELLE

présentée à

L'UNIVERSITÉ DE BORDEAUX

ÉCOLE DOCTORALE SCIENCES PHYSIQUES ET DE L'INGÉNIEUR

SPÉCIALITÉ ASTROPHYSIQUE, PLASMAS, NUCLÉAIRE

et à

L'UNIVERSITÉ COMENIUS DE BRATISLAVA

FACULTÉ DE MATHÉMATIQUES, PHYSIQUE ET INFORMATIQUE

SPÉCIALITÉ PHYSIQUE NUCLÉAIRE ET SUBNUCLÉAIRE

par

Miroslav MACKO

pour obtenir le grade de

DOCTEUR

SuperNEMO Experiment: Study of Systematic Uncertainties of Track Reconstruction and Energy Calibration. Evaluation of Sensitivity to $0\nu\beta\beta$ with Emission of Majoron for ^{82}Se.

Sous la direction de

Fabrice PIQUEMAL et de **Ivan ŠTEKL**

Soutenue le **17 décembre 2018** devant la commission d'examen formée de:

M. D. DUMORA	Professeur, Université de Bordeaux	Président du jury
M. D. FRANCO	Chargé de recherche, Université Paris-Diderot	Rapporteur
M. S. JULLIAN	Direct. de recherche emérite, CNRS, Univ. Paris-Saclay	Examinateur
M. J. MASARIK	Doyen de faculté, Université Comenius de Bratislava	Examinateur
M. D. VÉNOS	Chercheur, Acad. des sciences de la Rép. tchèque	Examinateur
M. P. VOGEL	Professeur emérite, California Institute of Technology	Rapporteur

Expérience SuperNEMO: Études des incertitudes systématiques sur la reconstruction de traces et sur l'étalonnage en énergie. Evaluation de la sensibilité de la $0\nu\beta\beta$ avec émission de Majoron pour le ^{82}Se.

Résumé

La thèse présentée est composée de divers projets que j'ai réalisés au cours de la phase de construction du démonstrateur SuperNEMO pendant la période 2015-2018.

L'expérience SuperNEMO, située dans le laboratoire souterrain LSM, est conçue pour rechercher $0\nu\beta\beta$ de ^{82}Se. Sa technologie, qui tire parti du suivi des particules, est unique dans le domaine des expériences de double désintégration bêta. La reconstruction de la topologie des événements est un outil puissant pour la suppression de fond naturel.

Une partie de la thèse est consacrée à un travail expérimental. J'ai participé à la préparation de modules optiques, partie intégrante du calorimètre SuperNEMO. Les résultats de la préparation et des tests de 520 modules optiques sont présentés dans la thèse. En outre, je présente les résultats de la cartographie complète des sources ^{207}Bi effectuée à l'aide de pixel détecteurs. Je présente également des mesures précises de leurs activités pour lesquelles j'ai utilisé des détecteurs HPGe. Ces sources ^{207}Bi seront utilisées pour l'étalonnage du calorimètre. L'étude a joué un rôle clé dans le choix des 42 sources qui participeront à l'étalonnage du démonstrateur.

Une autre partie de la thèse contient des projets axés sur les simulations de Monte Carlo. Dans un premier temps, j'ai étudié la précision de reconstruction de vertex réalisable par un algorithme de reconstruction développé pour l'expérience SuperNEMO. La précision est évaluée à l'aide de différentes méthodes statistiques dans diverses conditions (champ magnétique, énergie des électrons, angles d'émission, etc.). Les facteurs influençant la précision, en fonction des résultats obtenus, sont discutés.

En 2018, j'ai également effectué les simulations du blindage contre les neutrons. Différents matériaux de blindage d'épaisseurs différentes ont été (dans la simulation) exposés à un spectre de neutrons réaliste provenant du LSM et les flux situés derrière le blindage ont été estimés. Il a été démontré que les parties du détecteur en fer devraient capturer la grande majorité des neutrons passant le blindage. Je discute également un problème de simulation des rayonnements gamma de désexcitation après capture de neutrons thermiques, apparaissant dans les logiciels standard. Je propose un nouveau générateur étendu capable de résoudre le problème et de démontrer le concept dans un exemple analytiquement résolu.

Avec le standard $0\nu\beta\beta$, SuperNEMO sera capable de rechercher des modes plus exotiques de la décroissance. Dans cette thèse, je présente les limites de demi-vie possibles que SuperNEMO peut atteindre pour $0\nu\beta\beta$ avec l'émission d'un ou deux Majorons. L'étude est réalisée en fonction de l'activité de contamination interne par les isotopes ^{208}Tl et ^{214}Bi. La période de mesure après laquelle SuperNEMO devrait pouvoir améliorer les limites de demi-vie de NEMO-3 (au cas où la décroissance ne serait pas observée) est estimée.

Mots-clés: décroissance double beta bêta sans émission des neutrino, SuperNEMO, Majoron, simulations, la masse des neutrinos, blindage contre les neutrons, système d'étalonnage, module optique, incertitudes systématiques

SuperNEMO experiment: Štúdia systematických neistôt rekonštrukcie dráh a energetickej kalibrácie. Odhad citlivosti detektora na $0\nu\beta\beta$ s emisiou Majorónu pre ^{82}Se.

Abstrakt

Predkladaná dizertačná práca je zložená z projektov rôzneho charakteru, na ktorých som pracoval vo fáze výstavby SuperNEMO demonštrátora v období rokov 2015-2018.

Experiment SuperNEMO, umiestnený v podzemnom laboratóriu LSM, je zameraný na hľadanie $0\nu\beta\beta$ v ^{82}Se. Experiment je založený na technológii rekonštrukcie dráh elektrónov vznikajúcich v rozpade. Tento prístup je jedinečný v oblasti $0\nu\beta\beta$ experimentov. Rekonštrukcia topológie udalostí je silným nástrojom na potlačenie pozaďovej aktivity vyskytujúcej sa v laboratóriu, ako aj v konštrukčných materiáloch detektora.

Časť práce je venovaná experimentálnym úlohám. Zúčastnil som sa na konštrukcii optických modulov - súčasti hlavného kalorimetra. Práca obsahuje výsledky prípravy a testovania 520 optických modulov, a takisto výsledky kompletného mapovania kalibračných ^{207}Bi zdrojov vykonaného za pomoci pixelových detektorov. V tejto časti sú odprezentované aj výsledky merania ich aktivít za pomoci HPGe detektorov. Štúdia zohrávala kľúčovú úlohu pri výbere 42 zdrojov, ktoré boli nainštalované do prvého SuperNEMO modulu, do demonštrátora, a budú použité na jeho energetickú kalibráciu.

Ďalšiu časť práce tvoria úlohy zamerané na Monte Carlo simulácie. Prvým z nich, je štúdia presnosti rekonštrukcie vertexu dvojitého beta rozpadu. Rozpadové vertexy sú rekonštruované tzv. CAT (Cellular Automaton Tracker) algoritmom vyvinutým pre experiment SuperNEMO. V štúdii sú porovnávané viaceré spôsoby definovania presnosti rekonštrukcie. Presnosť je skúmaná v závislosti na magnetickom poli v detektore, energii elektrónov, uhlov ich emisie atď. Na základe výsledkov sú v štúdii pomenované faktory, ktoré ovplyvňujú presnosť rekonštrukcie vertexov dvojitého beta rozpadu.

V roku 2018 som takisto vypracoval štúdie neutrónového tienenia. Očakávané toky neutrónov za tienením boli odhadnuté pomocou Monte Carlo simulácie. Kvalita odtienenia neutrónov z realistických pozaďového spektra, nameraného v LSM, bola skúmana pre tri rôzne materiály rôznych hrúbok. Výsledky ukázali, že neutrónový tok prechádzajúci tienením bude primárne zachytávaný na komponentoch detektora zhotoveného zo železa. V rámci štúdie neutrónového tienenia je takisto diskutovaný problém simulácie deexcitačných gama kaskád, produkovaných jadrami, po záchyte termálnych neutrónov. Štandardné simulačné softvérové balíčky využívajú generátory gama kaskád nepostačujúce pre potreby štúdie. Navrhol som nový generátor, ktorý je schopný tieto problémy vyriešiť. Funkčnosť generátora bola preukázaná na príklade jednoduchého systému.

Okrem štandardného $0\nu\beta\beta$ je SuperNEMO experiment schopný hľadať aj jeho exotickejšie verzie. V práci sa nachádzajú odhady limitov času polpremeny $0\nu\beta\beta$ s emisiou jedného alebo dvoch Majorónov, dosiahnuteľné SuperNEMO demonštrátorom. Tieto limity sú študované v závislosti na aktivite izotopov ^{208}Tl a ^{214}Bi, ktoré kontaminujú zdrojovú ^{82}Se fóliu. Bola odhadnuá doba merania, za ktorú bude SuperNEMO schopný vylepšiť limity času polpremeny, pre dva spomenuté rozpadové módy, dosiahnutých experimentom NEMO-3.

Kľúčové slová: bezneutrínový dvojitý beta rozpad, SuperNEMO, Majorón, simulácie, hmotnosť neutrína, neutrónové tienenie, kalibračný systém, optický modul, systematické neistoty

SuperNEMO Experiment: Study of Systematic Uncertainties of Track Reconstruction and Energy Calibration. Evaluation of Sensitivity to $0\nu\beta\beta$ with Emission of Majoron for ^{82}Se.

Abstract

Presented thesis is composed of variety of projects which I performed within the construction phase of SuperNEMO demonstrator during the period 2015-2018.

SuperNEMO experiment, located at underground laboratory LSM, is designed to search for $0\nu\beta\beta$ of ^{82}Se. Its technology, which takes advantage of particle tracking, is unique in the field of double beta decay experiments. Event topology reconstruction is powerful tool for suppression of naturally-occurring background radiation.

Part of the thesis is dedicated to experimental work. I took part in assembly and testing of optical modules - the integral part of SuperNEMO calorimeter. Results of tests after assembly of 520 optical modules are presented in the thesis. Furthermore, I present results of complete mapping of ^{207}Bi sources performed using pixel detectors. I also present precise measurements of their activities for which I used HPGe detectors. These ^{207}Bi sources will be used for calibration of the calorimeter. Study played a key role in choice of 42 sources which were installed in the demonstrator and will take part in calibration of the demonstrator.

Another part of the thesis contains projects focused on Monte Carlo simulations. In first of them, I studied a vertex reconstruction precision achievable by reconstruction algorithm developed for SuperNEMO experiment. Precision is evaluated using different statistical methods in variety of different conditions (magnetic field, energy of electrons, angles of emission, etc.). Factors influencing the precision, based on the achieved results are discussed.

In 2018, I also performed simulations of neutron shielding. Variety of shielding materials with different thicknesses were (in the simulation) exposed to realistic neutron spectrum from LSM and the fluxes behind the shielding were estimated. It was shown that the parts of the detector made of Iron should be expected to capture vast majority of neutrons passing the shielding. I also discuss a problem with simulation of deexcitation gamma radiation, emitted after thermal neutron capture, which arises in standard software packages. I proposed new extended generator capable to resolve the problem and demonstrate the concept in analytically solvable example.

Along with standard $0\nu\beta\beta$, SuperNEMO will be capable of searching for more exotic modes of the decay. In the thesis, I present possible half-life limits achievable by SuperNEMO for $0\nu\beta\beta$ with emission of one or two Majorons. The study is performed as a function of activity of internal contamination from ^{208}Tl and ^{214}Bi isotopes. Measurement period after which SuperNEMO should be able to improve half-life limits of NEMO-3 (in case the decay would not be observed) are estimated.

Keywords: Neutrino-less Double Beta Decay, SuperNEMO, Majoron, simulations, neutrino mass, neutron shielding, calibration system, optical module, systematic uncertainties

Acknowledgments

First of all, I would like to thank my both supervisors Ivan Štekl and Fabrice Piquemal for all the discussions, guidance and help during these three years. A collaboration with you was truly beneficial for development of my skills and abilities in physics. At the same time, I would like to express my gratitude to my consultant Rastislav Hodák who is familiar with all the smaller or bigger issues I was facing during my Ph.D. studies and was always there prepared to help with advise or to offer helping hand. I would like to thank also to my (as I informally called him) "shadow supervisor" Fedor Šimkovic. I appreciate all the support he provided to me whenever I needed some help.

Furthermore, I want to express my "remerciements" to the neutrino team in CENBG, namely Cristine Marquet, Frédéric Perrot, Emmanuel Chauveau, Cédric Cerna, Arnaud Huber and Jean Jouve for introducing me into their institute, a cosy château, and for hosting me there during my three half-year stays. It was my pleasure to spend that time in Bordeaux. Special thanks go to Bertram Blank who allowed me to use his detector for measurements of absolute activities of calibration sources. I want to thank as well to my friends on a Czech side, except for already mentioned Rastislav Hodák, also to Lukáš Fajt, Adam Smetana, Jakub Vlášek and Ekaterina Rukhadze for helping me to accomodate myself at my new home institute. I wish to acknowledge staff of LSM, in particular Guillaume Warot for offering me helping hand with the calibration source measurements which I performed in the undeground laboratory.

Moja veľmi špeciálna vďaka ide takisto administratíve na FMFI UK a ÚTEF ČVUT, za oboje spomeniem hlavne Helenu Patríkovú, Martinu Vanišovú či Soňu Štichovú. Bez ich neustáleho trpezlivého naprávania mojich administratívnych prešľapov by som tento administratívne náročný model dvojitého doktorátu asi ani nezvládol.

Nakoniec by som chcel poďakovať tým pre mňa najdôležitejším ľuďom, ktorými sú moja mamina Anna Macková, sestry Betka a Mária Mackové, babka Mária Macková a moja najmilšia Oleksandra Veseľská. Vašu bezhraničnú podporu som neustále cítil počas týchto rokov a hlavne v závere bola jednym z kľúčových faktorov, ktoré mi dodali silu nevzdať sa.

V úplnom závere by som chcel venovať zopár riadkov svojmu otcovi Mariánovi Mackovi. Tým čím som sa stal, je minimálne z polovice tvoja obrovská zásluha. Bol si vždy mojím (nielen) intelektuálnym vzorom a poradcom na všetko. "Niektorí ľudia sa nikdy nič nenaučia, pretože veľmi skoro všetkému rozumejú," túto tvoju zásadu si vždy opakujem a stala sa mi dôležitým oporným bodom v mojej profesionálnej kariére. Ďakujem ti za tvoj humor, intelekt a oporu. Táto práca je venovaná práve tebe.

Venované môjmu ocinovi
Dedicated to my Dad
Dédié à mon papa

Contents

List of Figures 4

List of Tables 8

List of Abbreviations 10

Introduction (français) 12

Introduction (English) 16

1 Neutrino Physics and Its History 20
- 1.1 Neutrino Postulate . . . 20
- 1.2 Discovery of Neutrino . . . 21
- 1.3 Neutrinos in Standard Model . . . 21
  - 1.3.1 Neutrino Flavours . . . 23
- 1.4 Neutrinos Beyond the Standard Model . . . 23
  - 1.4.1 Solar Neutrino Problem . . . 24
  - 1.4.2 Neutrino Mixing and Oscillations . . . 25
  - 1.4.3 Supernova Neutrinos . . . 26
  - 1.4.4 Neutrino Hierarchies . . . 27
  - 1.4.5 Neutrino Masses and Their Nature . . . 28
- 1.5 Double Beta-Decay Processes . . . 29
  - 1.5.1 Two-Neutrino Double Beta-Decay . . . 29
  - 1.5.2 Neutrino-Less Double Beta-Decay . . . 30
  - 1.5.3 Nuclear Matrix Elements . . . 31
  - 1.5.4 Experimental Status of Double Beta-Decay . . . 32

2 SuperNEMO Experiment 40
- 2.1 Laboratoire Souterrain de Modane . . . 40
- 2.2 Description of the Detector . . . 41
  - 2.2.1 ^{82}Se Source Foils . . . 42
  - 2.2.2 Tracking Detector . . . 44
  - 2.2.3 Calorimeters . . . 44
  - 2.2.4 Status of the Demonstrator . . . 45
- 2.3 Construction of Main Calorimeter Walls . . . 46
  - 2.3.1 Optical Module Production Procedure . . . 46

2.3.2 Optical Module Resolution Test and Finalization 47

3 Measurements of ^{207}Bi Calibration Sources 50
3.1 SuperNEMO Calibration System 50
3.1.1 Automatic Calibration Source Deployment System 51
3.1.2 Description of Calibration Sources 52
3.2 Mapping of ^{207}Bi Deposition Distribution in Calibration Sources 53
3.2.1 Timepix Pixel Detectors 53
3.2.2 Detector Energy Calibrations 54
3.2.3 Test Measurements 57
3.2.3.1 Data Analysis 59
3.2.3.2 Study of the Energy Spectra 61
3.2.4 Detector Spatial Calibrations 62
3.2.4.1 Source Placement Convention 67
3.2.5 Results 69
3.2.5.1 Systematic Uncertainty Estimation 72
3.3 Measurements of Source Activities 73
3.3.1 Relative Measurements 73
3.3.1.1 First Phase 75
3.3.1.2 Second Phase 75
3.3.1.3 Distribution of Calibration Sources in SuperNEMO Detector 76
3.3.2 Absolute Measurements 78
3.3.2.1 Measurements of Source Depths 78
3.3.2.2 Activity Measurements and Analysis 80
3.3.2.3 Discrepancy Between Results 83
3.4 Conclusions 85

4 Vertex Reconstruction Precision Studies 86
4.1 Description of Used Software Tools 87
4.1.1 Falaise 87
4.1.2 MiModule 88
4.1.2.1 Class MiFilters 89
4.2 Definition of Vertex Precision Quantities 92
4.2.1 Vertex Reconstruction Efficiency 93
4.2.2 RMS Precision 94
4.2.3 FWHM Precision 96
4.2.4 Sigma Precision 101
4.3 Vertex Precision as a Function of Electron Energy 102
4.3.1 Comparison of RMS and FWHM Precision 103
4.3.2 Comparison of Vertex Precision of Various Processes 105
4.3.3 Comparison of Vertex Precision for Different Magnetic Fields . . . 112
4.3.4 Vertex Efficiencies 113
4.4 Vertex Precision as a Function of Electron Angles 114
4.4.1 Decay Angle vs. Escape Angle 115
4.4.2 FWHM Precision 116
4.4.3 Fit Function Justification 119
4.5 Vertex Precision as a Function of Position on the Foil 120
4.6 Vertex Precision as a Function of Foil Angles 123
4.6.1 Sigma Results 124

4.6.2 Events in Central Cross . . . 128
4.6.3 Events in Diagonals . . . 130
4.7 Conclusions . . . 135

5 Simulations of SuperNEMO Neutron Shielding 138
5.1 Simulations of the Shielding . . . 139
5.1.1 Phase One: Neutrons Passing Through Shielding . . . 140
5.1.2 Phase Two: Mapping of Demonstrator . . . 145
5.2 Problem of Neutron Capture Generators . . . 155
5.2.1 Thermal Neutrons in Geant4 . . . 156
5.2.2 Stair Generator . . . 158
5.2.3 Possible Solution . . . 160
5.2.3.1 Naming Convention . . . 161
5.2.3.2 Description of Generator . . . 162
5.2.3.3 Solution for a System with Two Intermediate States . . . 165
5.2.3.4 Proof of the Concept by Analytical Solution . . . 168
5.3 Conclusions . . . 172

6 Estimation of Sensitivity of SuperNEMO to $0\nu\beta\beta$ with Majoron Emission 173
6.1 Calculation of Half-Life Limits . . . 174
6.1.1 Calculation of Detection Efficiencies ε . . . 174
6.1.2 Calculation of Signal-to-Background Ratios . . . 175
6.1.3 Sensitivity Results . . . 180
6.2 Conclusions . . . 182

Summary 186

Bibliography 188

A Complete Results of Measurements of ^{207}Bi Calibration Sources 194
A.1 Mapping Results . . . 194
A.2 Results of Activity Measurements . . . 197
A.2.1 Results of Relative Activity Measurements . . . 197
A.2.2 Results of Absolute Activity Measurements . . . 199

B Detailed Description of Feldman-Cousins Method 202
B.1 Calculation of Half-Life of Rare Processes . . . 202
B.2 Statistical Nature of Observed Counts . . . 204
B.2.1 Experiments Without Background . . . 204
B.2.2 Experiments with Background - Collapse of Classical Method . . . 206
B.3 Feldman-Cousins Method . . . 206
B.3.1 Ordering Principle . . . 209
B.3.1.1 Likelihood Ratio Ordering Principle . . . 210
B.3.1.2 Numerical Artefacts . . . 211
B.3.2 Experiments with no Discovery . . . 212

C Numerical Values of Half-Life Limits for $0\nu\beta\beta\chi^0$ and $0\nu\beta\beta\chi^0\chi^0$ 215

List of Figures

1.1 Scheme of detection principle in Reines-Cowan experiment. 21
1.2 All particles of Standard Model. 22
1.3 Detection principle of muon neutrino discovery experiment. 23
1.4 Energy spectrum of neutrinos of different origin. 24
1.5 Two possible neutrino mass hierarchies. 27
1.6 Theoretical and experimental Double beta-decay energy spectra. 32
1.7 Values of nuclear matrix elements for $0\nu\beta\beta$ candidate isotopes. 33
1.8 Visualisation of GERDA experiment. 35
1.9 Scheme of KamLAND-Zen experiment. 36
1.10 Scheme of NEMO-3 experiment. 37
1.11 Distribution of isotopes in NEMO-3 experiment. 38

2.1 Scheme of LSM and its place in Fréjus tunnel. 40
2.2 Simplified scheme of tracko-calo detection method. 41
2.3 Scheme of SuperNEMO demonstrator. 42
2.4 Photos of ^{82}Se source foils for SuperNEMO demonstrator. 43
2.5 Photos of robot developed for the preparation of the tracker cells. 44
2.6 Scheme of SuperNEMO calorimeters and coordinate system. 45
2.7 Pictures of SuperNEMO optical module. 46
2.8 Photos of polystyrene block used in SuperNEMO optical module. 47
2.9 Process of preparation of optical modules. 48
2.10 Measured energy resolutions of optical modules in the main wall. 49
2.11 Me, with my first completed optical module. 49

3.1 Simplified decay scheme of ^{207}Bi. 50
3.2 Simplified scheme of SuperNEMO calibration source deployment system. . 51
3.3 Photo of ^{207}Bi calibration sources and their dimensions. 52
3.4 Case with all available ^{207}Bi calibration sources. 53
3.5 Photos of three Timepix pixel detectors. 54
3.6 Scheme of charge sharing effect taking place in pixels of Timepix detectors. 55
3.7 Relation between time over threshiold and energy in Timepix detectors. . . 56
3.8 Photo of energy calibration setup for Timepix detectors. 57
3.9 Energy spectra of Timepix detectors before and after calibration. 58
3.10 Energy spectrum of fluorescence in Iron as seen by detector H11-W0163. . 59
3.11 Example of a frame measured by Timepix detector. 59
3.12 Example of energy deposition distribution measured by Timepix detector. . 60

3.13 Energy spectra of particles coming from ^{207}Bi measured by Timepix detectors. 62
3.14 Comparison of energy deposition distributions obtained by two different cuts. 63
3.15 Calibration source alignment convention used in mapping measurements. . 63
3.16 Metallic grid used for spatial calibration of Timepix detectors. 64
3.17 Four reference points used for spatial calibration of Timepix detectors. . . . 66
3.18 Result of the spatial calibration of Timepix detectors. 67
3.19 Naming convention for positions of calibration sources w/ plastic envelope. 68
3.20 Naming convention for positions of calibration sources w/o plastic envelope. 68
3.21 Quantities extracted from mapping of calibration sources. 70
3.22 Results of mapping of calibration sources. 71
3.23 Results of mapping of calibration sources with plot of droplet radii. 72
3.24 Detector A used for relative measurements of calibration source activities. . 74
3.25 Gamma spectrum measured by detector A. 74
3.26 Plot of relative activities of calibration sources. 76
3.27 Scheme of calibration source placement in the SuperNEMO demonstrator. . 77
3.28 Detector B used for absolute measurements of calibration source activities. 78
3.29 Cross-section of calibration source holder in absolute activity measurements. 79
3.30 Scheme of measurements of calibration source depths. 79
3.31 Gamma spectrum measured by detector B. 81
3.32 Performance of fit performed on chosen ROI in the spectrum from detector B. 82
3.33 Comparison of calibration source (absolute) activities. 83
3.34 Comparison of source activities obtained by two independent analysis methods. 84

4.1 Discrepancy between expected and measured angular distribution in NEMO-3. 86
4.2 Example of event visualization from software package Falaise. 90
4.3 Visualization of two reconstructed vertices and a real vertex. 92
4.4 Definition of vertex residuals. 93
4.5 Examples of distributions of vertex residuals Δy and Δz from simulation. . . 94
4.6 Effect of electron scattering in foil on vertex residuals Δy and Δz. 95
4.7 Correlation plots between vertex coordinates y_1 vs. y_2 and z_1 vs. z_2. 97
4.8 Distribution of vertex coordinates y_1 and z_1. 99
4.9 Fit applied on distribution of residuals Δy and Δz. 100
4.10 Sample distributions as a function of single electron energies. 103
4.11 Comparison of RMS and FWHM method. 104
4.12 Example of fit quality coefficients. 105
4.13 Dependence of $FWHM_y$ on single electron energies for $0\nu\beta\beta$ processes. . . 106
4.14 Dependence of $FWHM_y$ on single electron energies for bkg processes. . . . 107
4.15 Dependence of $FWHM_z$ on single electron energies for $0\nu\beta\beta$ processes. . . 108
4.16 Dependence of $FWHM_z$ on single electron energies for bkg processes. . . . 109
4.17 Dependence of σ_y on single electron energies. 110
4.18 Dependence of σ_z on single electron energies. 111
4.19 Dependence of σ_y and σ_z on magnetic field. 113
4.20 Comparison of vertex efficiencies for $0\nu\beta\beta$ and $2\nu\beta\beta$. 114
4.21 Definition of Φ_{dec} and Φ_{esc}. 115
4.22 Correlation between Φ_{dec} and Φ_{esc} for various processes. 116
4.23 Correlation between Φ_{dec} and Φ_{esc} for various processes after data cuts. . . 117
4.24 Distributions of Φ_{dec} and Φ_{esc} for various processes. 118
4.25 Distributions of Φ_{dec} and Φ_{esc} for various processes in cos scale. 118

4.26 Distributions of Φ_{dec} and Φ_{esc} for various processes in cos scale after data cuts. 118
4.27 $FWHM_y$ and $FWHM_z$ precision as function of Φ_{esc}. 119
4.28 $FWHM_y$ and $FWHM_z$ precision as function of Φ_{esc} after data cuts. 119
4.29 Fit performance demonstration as a function of Φ_{esc}. 120
4.30 Distribution of events passing SDBDRC on the source foil. 121
4.31 $FWHM_y$ precision as a function of source foil position. 122
4.32 $FWHM_z$ precision as a function of source foil position. 122
4.33 Definition of foil angles α and β. 123
4.34 σ_y precision as a function of foil angles α. 124
4.35 σ_z precision as a function of foil angles α. 125
4.36 σ_y precision as a function of foil angles β. 126
4.37 σ_z precision as a function of foil angles β. 127
4.38 Geometrical scheme of events in bin A. 128
4.39 Distribution of vertex residuals Δy in bin A. 129
4.40 Distribution of vertex residuals Δy in subbins A_1-A_4. 130
4.41 Geometrical scheme of events in some diagonal bins (B). 131
4.42 Distribution of vertex coordinates y_1 in chosen bins (B, secondary diagonal). 132
4.43 Effect of X-calo on acceptance of electron events. 133
4.44 Distribution of vertex coordinates y_1 in chosen bins (B, primary diagonal). . 133
4.45 Distribution of vertex coordinates y_1 for different values of magnetic field. . 134
4.46 Foil distribution of events with rejection of X-calo. 135

5.1 Scheme of fake double beta event produced by backgorund neutron. 139
5.2 Plot of realistic neutron background spectrum in LSM. 140
5.3 Scheme of first phase neutron simulation (neutron flux passing the wall). . . 141
5.4 Spectra of low energy neutrons passing the shielding. 143
5.5 Spectra of high energy neutrons passing the shielding. 144
5.6 Scheme of second phase neutron simulation (neutron captures in detector). . 146
5.7 2D projections of 3D distribution of neutron captures in whole detector. . . 149
5.8 2D projections of 3D distribution of neutron captures in Iron 150
5.9 2D projections of 3D distribution of neutron captures in Copper 151
5.10 2D projections of 3D distribution of neutron captures in Plexiglass 152
5.11 2D projections of 3D distribution of neutron captures in Delrin 153
5.12 2D projections of 3D distribution of neutron captures in SN-metal 154
5.13 Photo of Geiger cell endcap. 155
5.14 Tracks from simulation of thermal neutron capture in cube made of Iron. . . 156
5.15 Energy released in event after neutron capture in Iron from Geant4 simulation. 158
5.16 Scheme of gamma cascades and their energy spectrum (one intermediate level). 159
5.17 Scheme of gamma cascades with notation (two intermediate levels). 161
5.18 Plot showing performance of my generator under ideal conditions. 170
5.19 Plot showing performance of my generator under imperfect conditions. . . . 171

6.1 Energy spectra of various double-beta processes. 173
6.2 Detection efficiencies extracted from simulation. 176
6.3 S/B ratios and energy spectra for $0\nu\beta\beta\chi^0$ and backgrounds. 178
6.4 S/B ratios and energy spectra for $0\nu\beta\beta\chi^0\chi^0$ and backgrounds. 179
6.5 Upper limit μ_U as a function of expected background counts. 181
6.6 Half-life limits for $0\nu\beta\beta\chi^0$. 183
6.7 Half-life limits as functions of measurement period. 184

B.1 Demonstration of classical confidence interval calculation (no background). 205
B.2 Demonstration of classical confidence interval calculation (with background). 207
B.3 Example of confidence belt calculation. 208
B.4 Example of central and one-sided confidence belts. 209
B.5 Example of confidence belts obtained by Feldman-Cousins method. 212
B.6 Demonstration of numerical artefacts occurring in Feldman-Cousins method. 213

List of Tables

1.1 Recommended values of $2\nu\beta\beta$ half-lives. 30
1.2 The best limits for $0\nu\beta\beta$ half-life and effective neutrino mass. 34
1.3 $2\nu\beta\beta$ half-life values measured by NEMO-3 experiment. 39

3.1 Table of ^{207}Bi source dimensions A, B, C, D, E and F. 52
3.2 Products of ^{207}Bi decay. 61
3.3 Four spatial calibration reference points in grid's coordinate system. 65
3.4 Four spatial calibration reference points in detector's coordinate system. . . 65
3.5 Statistics of chosen ^{207}Bi mapping measurements. 69
3.6 Results of chosen ^{207}Bi mapping measurements. 70
3.7 Final distribution of calibration sources among 42 slots in demonstrator. . . 77
3.8 Measured depths of ^{207}Bi sources. 80
3.9 Values used in calculations of absolute activities of ^{207}Bi sources. 82

4.1 Detection efficiencies of chosen processes obtained by Falaise simulation. . 91
4.2 List of datasets used in vertex resolution studies. 102

5.1 Neutron fluxes passing the wall in simulation in nine different scenarios. . . 142
5.2 Number of neutron captures caused in detector by thermal neutrons. 148
5.3 Number of neutron captures caused in detector by neutrons with E > 0.3 eV. 148
5.4 Performance of Geant4 generator in neutron capture simulation. 157
5.5 Performance of Stair Generator in neutron capture simulation. 160
5.6 Number of cascades and gammas for given number of intermediate states. . 162

6.1 Simulated samples used in sensitivity estimation. 175

A.1 Statistics of ^{207}Bi calibration source mapping measurements (part 1). 194
A.2 Statistics of ^{207}Bi calibration source mapping measurements (part 2). 195
A.3 Results of ^{207}Bi calibration source mapping measurements (part 1). 196
A.4 Results of ^{207}Bi calibration source mapping measurements (part 2). 197
A.5 Relative activities of calibration sources with plastic envelope (part 1). . . . 197
A.6 Relative activities of calibration sources with plastic envelope (part 2). . . . 198
A.7 Relative activities of calibration sources without plastic envelope (part 1). . 198
A.8 Relative activities of calibration sources without plastic envelope (part 2). . 199
A.9 Absolute activities obtained by my method (part 1). 199
A.10 Absolute activities obtained by my method (part 2). 200
A.11 Absolute activities obtained by Frédéric's method (part 1). 200

A.12 Absolute activities obtained by Frédéric's method (part 2). 201

B.1 Demonstration of likelihood ratio ordering principle. 211

C.1 Calculated half-life limits for $0\nu\beta\beta\chi^0$ (part 1). 215
C.2 Calculated half-life limits for $0\nu\beta\beta\chi^0$ (part 2). 216
C.3 Legend explaining colour coding of ROIs. 216
C.4 Calculated half-life limits for $0\nu\beta\beta\chi^0\chi^0$ (part 1). 216
C.5 Calculated half-life limits for $0\nu\beta\beta\chi^0\chi^0$ (part 2). 216
C.6 Calculated half-life limits for $0\nu\beta\beta\chi^0\chi^0$ (part 3). 217

List of Abbreviations

BSM - (physics) **b**eyond **S**tandard **M**odel
CAT - **c**ellular **a**utomaton **t**racker
CD (bank) - **c**alibrated **d**ata
CENBG - **C**entre **E**tudes **N**ucléaires de **B**ordeaux **G**radignan
CERN - **C**onseil **E**uropéen pour la **R**echerche **N**ucléaire
CKM (matrix) - **C**abibbo–**K**obayashi–**M**askawa
CL - **C**onfidence **L**evel
CTU - **C**zech **T**echnical **U**niversity
DONUT - **D**irect **O**bservation of the **Nu** **T**au
EC - **e**lectron **c**apture
FWHM - **f**ull **w**idth at **h**alf **m**aximum
GERDA - **Ger**manium **D**etection **A**rray
GID - **g**eometry **id**entifier
HdM - **H**ei**d**elberg - **M**oscow (experiment)
HWHM - **h**alf **w**idth at **h**alf **m**aximum
IBM - **I**nteracting **B**oson **M**odel
IEAP - **I**nstitute of **E**xperimental and **A**pplied **P**hysics
IGEX - **I**nternational **G**ermanium **Ex**periment
IMB (detector) - **I**rvine–**M**ichigan–**B**rookhaven
ISM - **I**nteracting Nuclear **S**hell **M**odel
ITEP (Moscow) - **I**nstitute for **T**heoretical and **E**xperimental **P**hysics
KamLAND-Zen (experiment) - **KamLAND**-**Ze**ro **N**eutrino
LAPP - **L**aboratoire d'**A**nnecy-le-Vieux de **P**hysique des **P**articules
LEGEND - **L**arge **E**nriched **G**ermanium **E**xperiment for **N**eutrinoless **D**ecay
LEP - **L**arge **E**lectron–**P**ositron Collider
LNGS **L**aboratori **N**azionali del **G**ran **S**asso
LSM - **L**aboratoire **S**outerrain de **M**odane
LUCIFER - **L**ow-background **U**nderground **C**ryogenic **I**nstallation **F**or **E**lusive **R**ates
MSSL - **M**ullard **S**pace **S**cience **L**aboratory
MSW (effect) - **M**ikheyev–**S**mirnov–**W**olfenstein
m.w.e. - **m**eter **w**ater **e**quivalent
NEMO - **N**eutrino **E**ttore **M**ajorana **O**bservatory
PMNS (matrix) - **P**ontecorvo–**M**aki–**N**akagawa–**S**akata
PMT - **p**hoto**m**ultiplier **t**ube
PTD (bank) - **p**article **t**rack **d**ata

PS - **p**oly**s**tyrene
QED - **Q**uantum **E**lectro**d**ynamics
QRPA - **Q**uasiparticle **R**andom **P**hase **A**pproximation
RMS - **r**oot **m**ean **s**quare
ROI - **r**egion **o**f **i**nterest
SAGE - The **S**oviet–**A**merican **G**allium **E**xperiment
SD (bank) - **s**imulated **d**ata
SDBDC - **S**tandard **D**ouble **B**eta **D**ecay **R**econstruction **C**riteria
SLAC - **S**tandford **L**inear **A**ccelerator **C**enter
SM - **S**tandard **M**odel (of elementary particles)
SNO - **S**udbury **N**eutrino **O**bservatory
SNU - **s**olar **n**eutrino **u**nit
SSM - **S**tandard **S**olar **M**odel
ToT - **T**ime **o**ver **T**reshold
TPC - **t**ime **p**rojection **c**hamber
UCL - **U**niversity **C**ollege **L**ondon

Introduction (français)

Le modèle standard (SM) de la physique des particules est une théorie des particules fondamentales et de leurs interactions. Les théoriciens, en utilisant le formalisme lagrangien, ont réussi à fusionner des interactions électromagnétiques, faibles et fortes en un seul cadre théorique. Il décrit de manière extrêmement précise une vaste gamme de processus entre quarks et leptons. C'est indéniablement la théorie la plus précise des particules fondamentales de la physique contemporaine. Cependant, malgré l'énorme effort des physiciens théoriciens les plus brillants soutenus par les résultats d'expériences très complexes et sophistiquées, la gravité n'était pas encore incluse dans le cadre. De plus, les observations de la cinématique de certaines galaxies ont montré un déséquilibre de leur dynamique et de leurs prédictions basées sur nos connaissances actuelles. La différence est causée par la présence d'un nouveau type inconnu de particules - la matière noire. Le problème de la quantification de la gravité et l'existence de matière noire sont des exemples typiques de ce que l'on appelle la physique au-delà du modèle standard (BSM). Standard Model a réussi à décrire toutes les particules actuellement connues et, dans le passé, il a même réussi à prédire l'existence de nombreuses d'entre elles. Le modèle standard, cependant, n'est "que" une approximation à basse énergie d'une physique plus générale; il n'est donc pas étonnant que son tableau ne soit pas complet.

La physique des particules contemporaine est actuellement à la recherche d'un pont entre le modèle standard et la physique au-delà du modèle standard. La clé du succès pourrait être cachée dans la physique des neutrinos. Le modèle standard décrit les neutrinos comme des particules sans masse qui interagissent faiblement. En observant les oscillations des neutrinos, cependant, nous savons aujourd'hui que cette image n'est pas complète. Bien que petit, la masse du neutrino n'est pas nulle. Malheureusement, les expériences d'oscillation, de par leur nature, ne peuvent fournir les valeurs de trois masses de neutrinos, car leurs observables ne dépendent que de leurs différences absolues.

En 1935, Maria Goeppert-Mayer a proposé l'existence de la double désintégration bêta avec emission de deux neutrinos ($2\nu\beta\beta$). Il s'agit d'une transition nucléaire lorsque deux neutrons liés au noyau se transforment soudainement en deux protons émettant deux électrons et deux anti-neutrinos électronique. Cette désintégration rare est généralement éclipsée par sa version plus simple - une désintégration bêta standard avec une demi-vie nettement plus courte. Néanmoins, il existe des exemples de noyaux où la simple désintégration bêta est soit supprimée par des règles de sélection de spin, soit totalement interdite par la loi de conservation de l'énergie. Avec les valeurs de demi-vie de 10^{18} à 10^{21} années, $2\nu\beta\beta$ est aujourd'hui le processus le plus rare observé. $2\nu\beta\beta$ conserve le nombre leptonique. C'est un processus permis par le modèle standard. En 1939, c'est Wendell H. Furry qui a proposé

l'idée d'une transition nucléaire encore plus rare - la double désintégration bêta sans emission de neutrino ($0\nu\beta\beta$). Comme son nom l'indique, le processus est similaire à $2\nu\beta\beta$ avec une différence importante. Dans $0\nu\beta\beta$, aucun neutrino ne devrait être émis. Un tel processus enfreindrait la conservation du nombre leptonique, qui est interdite par le modèle standard. $0\nu\beta\beta$ représente clairement un candidat pour un processus au-delà du modèle standard. De plus, sa demi-vie dépend de la soi-disant masse effective des neutrinos (ce n'est pas le cas de $2\nu\beta\beta$), qui est une valeur obtenue à partir de la superposition connue des états propres de la masse des neutrinos. L'observation de $0\nu\beta\beta$ fournirait la valeur des masses de neutrinos, qui ne sont pas encore connues. Cependant, la principale importance de $0\nu\beta\beta$ réside dans le potentiel de découverte du pont recherché entre le modèle standard et la physique au-delà du modèle standard. $0\nu\beta\beta$ ne peut exister que si le neutrino serait sa propre antiparticule ou appelée plutôt que soit-disant particule de Majorana. Le concept de particule de Majorana n'existe pas dans le modèle standard et il pourrait fournir l'une de ses extensions possibles. Aucun autre processus que $0\nu\beta\beta$ ne pourrait prouver le caractère Majorana des neutrinos.

Bien que $0\nu\beta\beta$ puisse constituer une première étape importante au-delà du modèle standard, il n'a malheureusement pas encore été observé. Un effort énorme est investi dans la recherche de ce mode de désintégration rare. Typiquement, les expériences $0\nu\beta\beta$ (ainsi que les autres expériences dans le domaine de la physique des neutrinos) sont placées sous terre, où la radioactivité naturelle omniprésente est supprimée de plusieurs grandeurs. Nous pouvons diviser les expériences $0\nu\beta\beta$ en deux catégories de base.

Il y a tout d'abord les expériences dans laquelle l'isotope source sert en même temps de détecteur. Dans ce groupe, nous pouvons trouver des détecteurs au germanium tels que GERDA ou Majorana, qui fusionneront bientôt dans l'expérience LEGEND de l'échelle de tonnes. ^{76}Ge est l'un des isotopes candidats pour $0\nu\beta\beta$ trouvé dans le Ge naturel. Dans le même temps, les cristaux de germanium servent de détecteurs HPGe. Dans le passé, c'était l'expérience Heidelberg-Moscow (qui utilisait également du Germanium) qui avait beaucoup attiré l'attention de la communauté en annonçant l'observation de $0\nu\beta\beta$. Cela a été prouvé faux par GERDA. Un autre type d'expérience source = détecteur utilise d'énormes vaisseaux de xénon liquide qui servent de source (en particulier d'isotopes ^{134}Xe et de ^{136}Xe) et de scintillateur en même temps. EXO avec sa mise à niveau nEXO sont des exemples de telles expériences. Dans la catégorie source = détecteur, nous pouvons également trouver des expériences bolométriques. Par exemple, l'expérience CUORE utilise des cristaux TeO_2 refroidis à quelques mK. ^{130}Te est un autre isotope potentiel capable de $0\nu\beta\beta$. Les électrons émis lors de la désintégration chauffent le cristal et l'excès de chaleur peut être mesuré grâce au changement de la résistance électrique du cristal. Il existe toute une gamme d'autres expériences $0\nu\beta\beta$ appartenant généralement à l'une des sous-catégories mentionnées.

Deuxièmement, il existe des expériences qui tirent parti de l'approche lorsque la source est séparée du système de détection. SuperNEMO et son prédécesseur NEMO-3 sont un exemple. L'énergie des électrons de la désintégration est détectée par des scintillateurs en plastique. Leur caractéristique la plus unique, cependant, est la reconstruction de la topologie des événements. Les grilles de fils en mode Geiger sont utilisées pour le suivi des particules. L'isotope source a la forme d'une feuille mince. La feuille peut être échangée contre un autre isotope d'intérêt. C'est une caractéristique unique des expériences où la source et le détecteur sont séparés. NEMO-3 était capable d'étudier simultanément sept isotopes (c'était: ^{48}Ca, ^{82}Se, ^{96}Zr, ^{100}Mo, ^{116}Cd, ^{130}Te et ^{150}Nd). L'expérience SuperNEMO utilise ^{82}Se. Néanmoins, ^{150}Nd pourrait être utilisé à l'avenir.

La thèse présentée résume tout le travail que j'ai effectué pendant trois ans (2015-2018) de mon doctorat au sein de la collaboration SuperNEMO. Dans les lignes suivantes je vais

résumer brièvement le contenu de chaque chapitre.

- **Chapitre 1** contient un bref aperçu de l'histoire de la physique des neutrinos. L'histoire commence avec le célèbre postulat de Pauli sur les neutrinos et sa découverte 26 ans plus tard. Aperçu historique offre une description de la variété des expériences clés dans l'histoire des neutrinos, telles que la première détection du neutrino muonique ou les expériences résolvant un Problème de neutrinos solaires. De plus, certains des concepts théoriques les plus importants pour la physique des neutrinos sont abordés. Le chapitre se termine par une brève introduction à la physique de la double désintégration bêta et un bref aperçu des expériences sur le terrain.

- **Chapitre 2** offre une brève description de toutes les parties intégrantes du démonstrateur SuperNEMO. SuperNEMO est divisé en trois parties principales: le feuille source, le détecteur de suivi et le calorimètre. En 2016, j'ai participé à l'assemblage et au test de modules optiques utilisés pour la construction des principaux calorimètres SuperNEMO. Le processus de préparation avec les résultats est décrit à la fin du chapitre.

- **Chapitre 3** est dédié aux mesures de sources ^{207}Bi qui seront utilisées pour l'étalonnage énergétique du démonstrateur. Au début du chapitre, une brève description du système de déploiement source automatique est fournie. Les sources d'étalonnage sont présentées. Le chapitre est divisé en deux parties principales. La première partie de ce chapitre contient une description détaillée des mesures que j'ai effectuées afin de cartographier le dépôt de la gouttelette ^{207}Bi dans les sources. Dans les mesures, j'ai utilisé trois détecteurs Timepix. L'ensemble du processus de calibration et de préparation des mesures est présenté. Les détecteurs ont été étalonnés et préparés dans IEAP CTU à Prague en octobre 2017. Les premières mesures d'essai ont été effectuées dans le LSM à la fin d'octobre 2017. Les mesures finales ont été effectuées en décembre 2018 également dans le LSM. La méthode d'analyse et les algorithmes logiciels, que j'ai utilisés pour l'extraction de quantités d'intérêt, sont expliqués en détail. Enfin, à la fin de la première partie, les résultats sont présentés et résumés. La deuxième partie du chapitre traite des mesures d'activité que j'ai effectuées pour les sources d'étalonnage au cours de l'été 2018 dans CENBG. Les mesures ont été effectuées à l'aide de deux détecteurs HPGe différents. L'un a été utilisé pour mesurer les activités relatives de toutes les sources disponibles (40 + 2 mesurées en LSM), tandis que le second a été utilisé pour une mesure précise des activités absolues des 25 sources choisies. Les résultats sont discutés sous forme de résumé des graphiques à la fin du chapitre. Une base de données complète de toutes les valeurs mesurées dans le cartographie de sources et dans les mesures d'activité est incluse dans l'Annexe A.

- **Chapitre 4** est une suite libre des études sur les incertitudes systématiques du démonstrateur SuperNEMO. Alors que le Chapitre 3 était axé sur les études susceptibles d'améliorer ultérieurement les incertitudes systématiques liées à l'étalonnage énergétique, ce chapitre est motivé par les incertitudes liées au suivi des particules. La reconstruction topologique d'événements de double désintégration bêta dans le détecteur SuperNEMO permet d'obtenir des informations sur les distributions angulaires d'électrons émis dans la désintégration. NEMO-3 a observé une légère différence entre la prévision théorique et la mesure. La différence peut provenir d'une nouvelle physique ou d'un effet systématique. Pour tirer une conclusion, il est nécessaire d'étudier en détail la systématique du suivi des particules. Le chapitre se concentre sur l'évaluation des limites de la précision de la reconstruction de vertex. Au début

du chapitre, le logiciel Falaise, utilisé pour l'étude, est présenté. La précision de reconstruction de vertex est définie en utilisant quatre quantités statistiques différentes. Ensuite, l'applicabilité des méthodes est comparée. La précision est étudiée tout au long du chapitre en fonction de l'énergie d'un seul électron, des angles entre les électrons, de l'angle entre l'électron et la feuille source ou de la position du vertex sur la feuille source. L'influence du champ magnétique et de la diffusion d'électrons dans la feuille source sur la précision de reconstruction de vertex est discutée. En conséquence, une liste de directives résumant tous les effets les plus importants influant sur la précision de reconstruction de vertex est fournie.

- **Chapitre 5** aborde le sujet du blindage contre les neutrons du démonstrateur SuperNEMO. En 2018, j'ai mené des études comparatives sur les matériaux capables de protéger contre les neutrons pour contribuer dans une discussion sur la conception du blindage. L'étude présentée dans ce chapitre tire parti d'un spectre de neutrons réaliste mesuré dans le LSM. Le passage des neutrons du spectre à travers le blindage est simulé et les flux attendus sont estimés. Les flux sont comparés pour neuf scénarios de blindage à l'aide du logiciel Geant4. Pour chaque scénario, les flux de neutrons traversant le mur sont simulés à l'aide de Falaise (logiciel SuperNEMO). Les matériaux de détecteur qui tendent à capturer la plupart des neutrons sont identifiés. La deuxième partie du chapitre est dédiée aux générateurs de capture de neutrons thermiques utilisés dans les logiciels standard de simulation. Les problèmes liés à la génération correcte de cascades gamma sont discutés. Un nouveau générateur est proposé et sa fonctionnalité est illustrée à titre d'exemple.

- **Chapitre 6** aborde le sujet des calculs de sensibilité des détecteurs à la décroissance double bêta. Le processus complet de calcul de la sensibilité est effectué. Le but de ce chapitre était d'obtenir une estimation de la sensibilité de $0\nu\beta\beta$ avec l'émission d'un ou deux Majorons pour le démonstrateur SuperNEMO. Le processus de calcul est initié par une simulation des efficacités de détection et une recherche de ROI avec le meilleur rapport signal/bruit de fond. Ce ROI peut fournir la mesure de demi-vie la plus précise possible si la décroissance a été observée. Si la décroissance reste non observée, la limite de demi-vie peut être extraite à l'aide de la méthode de Feldman-Cousins. Les limites de demi-vie aux modes de Majoron de $0\nu\beta\beta$ ont été étudiées en fonction de l'activité de ^{208}Tl et de ^{214}Bi (présent dans feuille source) et l'exposition de l'expérience. La période de mesure, après laquelle SuperNEMO devrait améliorer les limites de NEMO-3 pour les deux modes de désintégration, est estimée. La base de données complète des résultats obtenus dans ce chapitre est présentée à l'Annexe C. La méthode de Feldman-Cousins est décrite en détail en Annexe B. Plusieurs aspects et particularités de la méthode sont commentés et démontrés en annexe.

La thèse comprend des travaux expérimentaux (mesures de source d'étalonnage) et de simulation (précision du vertex, blindage contre les neutrons et études de Majoron) complétées par des tâches purement mathématiques (algorithmes d'analyse pour la calibration spatiale de détecteurs ou proposition de générateur de capture de neutrons, par exemple).

Introduction (English)

The Standard Model of particle physics (SM) is a theory of fundamental particles and their interactions. Theoreticians in its Lagrangian formalism managed to merge Electromagnetic, Weak and Strong interactions into one theoretical framework. It precisely describes a vast range of interaction processes between quarks and leptons. It is undeniably the most precise theory of fundamental particles of contemporary physics. However, despite the enormous effort of brightest theoretical physicists supported by results of very complex and sophisticated experiments, the gravity was not yet included in unified theory of electroweak and strong interactions framework. Furthermore, the observations of kinematics of certain galaxies have shown mismatch of their dynamics and predictions based on our current knowledge. The difference is caused by presence of new, unknown type of particles - dark matter and unknown force - dark energy. The unsolved problem with quantization of gravity and existence of dark matter are typical examples of so-called physics beyond the Standard Model (BSM). The SM managed to describe all the currently known particles and in the past it even succeeded to predict existence of many of them. The SM, however, is "only" a low energy approximation of more general physics, thus, it is not surprising that the picture it offers is not complete.

Contemporary particle physics is currently hunting for a bridge between SM and BSM. Key to the success might be hidden in the physics of neutrinos. The SM describes the neutrinos as Weakly interacting massless particles. However, the observation of neutrino oscillations brings a modification to the SM. Although small, the mass of the neutrino is not zero. Unfortunately, the oscillation experiments, by their nature, cannot provide values of three neutrino masses, because their observables depend only on their squared mass differences.

In 1935, Maria Goeppert-Mayer proposed the existence of two-neutrino double beta decay ($2\nu\beta\beta$). It is a nuclear transition when two neutrons bounded in nucleus are suddenly transformed into two protons emitting two electrons and two electron anti-neutrinos. This rare decay is typically overshadowed by its simpler version - the standard beta decay with significantly shorter half-life ($\sim$900 s). Nevertheless, there are examples of nuclei where single beta decay is either suppressed by spin selection rules or totally forbidden by law of energy conservation. With the half-life values of 10^{18} years up to 10^{21} years, $2\nu\beta\beta$ is nowadays the rarest process observed by physicists. $2\nu\beta\beta$ preserves lepton number. It is a process permitted by Standard Model. In 1939, it was Wendell H. Furry who proposed an idea of even rarer nuclear transition - Neutrino-less double beta decay ($0\nu\beta\beta$). As the name suggests, the process is similar to $2\nu\beta\beta$ with one important difference. In $0\nu\beta\beta$, no neutrinos are expected to be emitted. Such a process would violate lepton number conservation which is forbidden in SM. $0\nu\beta\beta$ clearly represents a candidate for a process beyond

the SM. Furthermore, its half-life depends on so-called effective neutrino mass (this is not true for $2\nu\beta\beta$) which is a value obtained from known superposition of neutrino mass eigenstates. Observation of $0\nu\beta\beta$ would provide value of neutrino masses, which are currently still not known. However, the main importance of $0\nu\beta\beta$ lies in the potential to discover a bridge from SM towards BSM physics. $0\nu\beta\beta$ can exist only if neutrino would be its own antiparticle or, so-called Majorana particle. The concept of Majorana particle does not exist in Standard Model and would provide one of its possible extensions. To our present knowledge, no other process than $0\nu\beta\beta$ could prove the Majorana character of neutrinos.

Despite the fact that $0\nu\beta\beta$ could be an important first step beyond the SM, unfortunately, it was not yet observed. Enormous effort is invested into the search for this rare decay mode. Typically, $0\nu\beta\beta$ experiments (as well as the other neutrino-related experiments) are placed underground, where omnipresent natural radioactivity is suppressed by several magnitudes. We can divide $0\nu\beta\beta$ experiments into two basic categories.

Firstly, there are experiments in which the source isotope serves at the same time as detector. In this group, we can find Germanium detectors such as GERDA or MAJORANA which will soon merge into the biggest - ton scale $0\nu\beta\beta$ experiment - LEGEND. ^{76}Ge is one of the candidate isotopes for $0\nu\beta\beta$ found in natural Ge. At the same time Germanium crystals serve as HPGe detectors. In the past, it was Heidelberg-Moscow experiment (which also used Germanium) which drew lot of attention of community by announcement of observation of $0\nu\beta\beta$. It was proven false by results of GERDA. Another type of source = detector experiment use huge vessels of liquid Xenon which serves as a source (especially isotopes ^{134}Xe and ^{136}Xe) and as a scintillator at the same time. EXO with its upgrade nEXO are examples of such experiments. In source = detector category we can find also bolometric experiments. For instance, experiment CUORE uses TeO_2 crystals cooled down to few mK. ^{130}Te is another potential $0\nu\beta\beta$ isotope. The electrons emitted in the decay heat up the crystal and the heat excess can be measured thanks to the change of the electrical resistance of crystal. There is a whole range of other $0\nu\beta\beta$ experiments which typically belong to one of the mentioned subcategories.

Secondly, there are experiments which take advantage of approach when source is separated from the detection system. SuperNEMO and its predecessor NEMO-3 are such examples. Energy of electrons from the decay are detected by plastic scintillators. Their most unique feature, however, is the reconstruction of topology of the events. Grid of wires in Geiger mode are employed for particle tracking. The source isotope has a form of thin foil. The foil can be exchanged for other isotope of interest. It is an unique feature of the experiments where source and detector are separated. NEMO-3 was capable to study seven isotopes simultaneously (it was: ^{48}Ca, ^{82}Se, ^{96}Zr, ^{100}Mo, ^{116}Cd, ^{130}Te and ^{150}Nd). SuperNEMO experiment is using ^{82}Se, ^{150}Nd might be employed in future.

Presented thesis sums up all the work which I performed during three years (2015-2018) of my Ph.D. studies within the SuperNEMO collaboration. Let me briefly summarize the contents of each chapter.

- **Chapter 1** contains a brief overview of the history of neutrino physics. The story begins with Pauli's famous neutrino postulate and its discovery 26 years later. Historical overview offers description of variety of key experiments in history of neutrinos, such as first detection of muon neutrino or the experiments resolving decades long Solar neutrino problem. On top of them, some of the most important theoretical concepts important for neutrino physics are discussed. Chapter ends with a brief introduction into the physics of Double beta decay and short review of the experiments performed in the field.

- **Chapter 2** offers short description of all the integral parts of SuperNEMO demonstrator module. SuperNEMO is divided into three main parts: source foil, tracking detector and the calorimeter. In 2016, I took part in assembly and testing of optical modules used to build main SuperNEMO calorimeters. The process of preparation with results is described at the end of the chapter.

- **Chapter 3** is dedicated to measurements of ^{207}Bi sources which will be used for the energy calibration of demonstrator. The goal of this work is to reduce systematic uncertainties coming from energy calibration by knowing better the source characteristics. At the beginning of the chapter, a brief description of automatic source deployment system is provided. Calibration sources are presented. This chapter is divided into two parts. First part of the chapter contains extensive description of measurement which I performed in order to map the deposition of ^{207}Bi droplet in the sources. In the measurements, I used three Si Timepix detectors. The whole process of their calibration and preparation of the measurements is presented. I calibrated the detectors in IEAP CTU in Prague in October 2017. First trial measurements, I performed in LSM at the end of October 2017. Final measurements were performed in December 2017 also in LSM. The analysis method and the software algorithms, that I used for extraction of quantities of interest, are explained in detail. Finally, at the end of first part, the results are presented and summarized. The second part of the chapter contains discussion of activity measurements which I performed for the calibration sources during summer 2018 in CENBG. Measurements were performed using two different HPGe detectors. One was employed in order to measure relative activities of all the available sources (40 + 2 measured in LSM) while the second was used for precise measurement of absolute activities of chosen (25) sources. Results are discussed in the form of summarizing plots at the end of the chapter. Full database of all the values measured in both the source mapping and activity measurements are included in Appendix A.

- **Chapter 4** is a continuation of studies of systematic uncertainties of SuperNEMO demonstrator. While Chapter 3 was focused on the studies which could later improve systematic uncertainties emerging from the energy calibration, this chapter is motivated by the uncertainties originating in particle tracking. Topological reconstruction of Double beta decay events in SuperNEMO detector allows one to obtain information about angular distributions of electrons emitted in the decay. NEMO-3 have observed slight discrepancy between the theoretical prediction and the measurement. The difference might originate from a new physics or it might be just a systematic effect. Systematic uncertainties in particle tracking are very important because new physics could have impact on the angular distribution. This chapter is focused on the evaluation of precision of vertex reconstruction achievable by SuperNEMO demonstrator. At the beginning of the chapter, the software package Falaise, used for the study, is presented. The vertex reconstruction precision is defined using four different statistical quantities. Subsequently, the applicability of the methods is compared. The precision is studied throughout the chapter as a function of single electron energy, angles between the electrons, angle between the electron and foil or position of the vertex on the source foil. Influence of the magnetic field and electron scattering in the source foil on the vertex reconstruction precision is discussed. As a result, list of guidelines summarizing all the most important effects influencing the vertex reconstruction precision is provided.

- **Chapter 5** covers the topic of neutron shielding of SuperNEMO demonstrator. In

2018, I performed comparative studies of materials capable to shield neutrons as a contribution to a discussion about shielding design. The study presented in the chapter takes advantage of realistic neutron spectrum measured in LSM. Behaviour of neutrons (fluxes and energy losses) passing through the shielding is simulated in details. Obtained fluxes and energy spectra are compared for nine shielding scenarios using software package Geant4. For each scenario, neutron fluxes passing the wall are simulated using Falaise (SuperNEMO software package). Detector materials which tend to capture most of the neutrons are identified. Second part of the chapter is dedicated to generators of thermal neutron capture used in standard software packages for simulations. Problems with proper generation of gamma cascades are discussed. New generator is proposed and its functionality is demonstrated on an illustrative example.

- **Chapter 6** discusses the topic of detector sensitivity calculations. The goal of the chapter was to obtain sensitivity estimation to $0\nu\beta\beta$ with emission of one or two Majoron(s) for SuperNEMO demonstrator. The process of calculation is initiated by simulation of detection efficiencies and search for region of interest (ROI) with the best signal-to-background ratio. Such ROI can provide the most precise half-life measurement if the decay was observed. If the decay remains unobserved, the half-life limit can be extracted using Feldman-Cousins method. Half-life limits to Majoron modes of $0\nu\beta\beta$ were studied as a function of activity of ^{208}Tl and ^{214}Bi (present in the foil) and experiment's exposure. Measurement period, after which, SuperNEMO should improve limits of NEMO-3 for both decay modes, are estimated. Full database of the results obtained in the chapter is presented in Appendix C. The method of Feldman-Cousins is extensively described in Appendix B. Several aspects and peculiarities of the method are commented and demonstrated in the appendix.

The thesis is a balanced compilation of experimental tasks (calibration source measurements) and simulation tasks (vertex precision, neutron shielding and Majoron studies) completed by purely mathematical tasks (e.g. analysis algorithms for spatial calibration of pixel detectors or neutron capture generator proposal).

Chapter 1

Neutrino Physics and Its History

1.1 Neutrino Postulate

In the beginning of the 20th century, the radioactivity was already known thanks to discovery of Antoine Henri Becquerel in 1896 [1, 2]. It was already Ernest Rutherford, in 1899, who was able to distinguish between α- and β-decay by the ability to penetrate paper or Aluminium. Later, particle emitted in β-decay was identified as an electron. In that time, they understood β-decay as a process where only the electron is emitted (Equation 1.1).

$$(A,Z) \rightarrow (A,Z+1) + e^{-} \tag{1.1}$$

After discovery of gamma radiation, it was known that alpha and gamma radiations have one feature in common - their spectra are composed of narrow peaks. It is caused by the fact that the particle is carrying all the energy from the difference between states of initial and final nucleus. In contrary, in 1914 James Chadwick showed that beta spectrum behaves differently. It has a continuous spectrum [3]. This indicated that the energy of β-decay is lost somewhere. Apparent non-conservation of spin was another important issue which was needed to be accounted for. It was known that β-decay leaves nucleus mass number unchanged which implies that nuclear spin should be integer number for nuclei with even number of nucleons. Spin of electron is 1/2, so it was obvious that spin could not be conserved for nuclei with even number of nucleons. Neils Bohr suggested that the energy might not be conserved for every decay but only in statistical sense. However, Charles Drummond Ellis and Nevill Francis Mott in [4] ruled out that idea by determination of upper bound of beta energy spectrum. The limit should not exist if Bohr's assumption was right.

In 1930, Wolfgang Pauli sent his famous letter to conference participants in Tübingen in which he postulated existence of new light particle [5]. He described it as a neutral particle of maximal mass of 0.01 proton masses, different from light quanta, with spin 1/2, thus obeying exclusion principle. He named the particle neutron. He proposed that it is emitted in the β-decay along with electron. However, he did not fully believe in the scenario assuming that the particle would probably already had been discovered. The name neutron was later given to much heavier particle discovered by James Chadwick in 1932. In 1934, Enrico Fermi developed theory of β-decay giving the particle the name it has today - the neutrino. The name was a pun: ending -one has a augmentative purpose in Italian language giving impression that neutrone (the Italian version of neutron) is denoting "something large and neutral". He replaced ending -one with suffix -ino giving the name diminutive sense. Fermi's theory of β-decay was analogy of the quantum electrodynamics (QED). He assumed that

proton is transformed into neutron by emission of electron along with anti-neutrino (Equation 1.2).

$$(A,Z) \rightarrow (A,Z+1) + e^{-} + \bar{\nu} \tag{1.2}$$

1.2 Discovery of Neutrino

It was already Wolfgang Pauli who expected that the detection of the particle which he postulated would be a very difficult task. He expressed his scepticism in the statement, "I have done a terrible thing, I have postulated a particle that cannot be detected." Finally, the task was not impossible. It took 26 years after the postulate to detect neutrino. In 1956, Clyde Cowan and Frederick Reines published article claiming the neutrino discovery [6]. They achieved this important milestone by taking advantage of beta capture process proposed by Wang Ganchang in 1942 [7]:

$$\bar{\nu}_e + p^{+} \rightarrow n^{0} + e^{+} \tag{1.3}$$

The Reines-Cowan experiment, as it is called, used the nuclear reactor in Savannah river in South Carolina (USA) as a source of the anti-neutrinos. The experimental device was composed of two large tanks of water (200 l each) surrounded by tanks of liquid scintillator. Positron in beta capture (Equation 1.3), created when the anti-neutrino from reactor hits the proton in the water, annihilates fast. As a result, two gammas, with the energy of 511 keV each, are produced. The gammas caused flashes in scintillator tanks and the light was collected in photomultiplier tubes. After they realized that the method is not conclusive enough they added 40 kg of cadmium chloride into each tank with water. Cadmium has a big cross section for the capture of neutron. When neutron is captured, gammas are emitted. The gamma from neutron capture was expected 5 μs after the annihilation pair (Figure 1.1). The measurement in coincidence allowed Reines and Covan to recognize neutrino captures more reliably. The results were compared to data with reactor turned off. During 1371 hours of measurements (including the background data taking) they were able to measure 1-3 anti-neutrinos per hour out of the flux of order 10^{13} anti-neutrinos per cm^2 every second. Only Frederic Reines was awarded the Nobel prize for this discovery in 1995 because Clyde Cowan died in 1974.

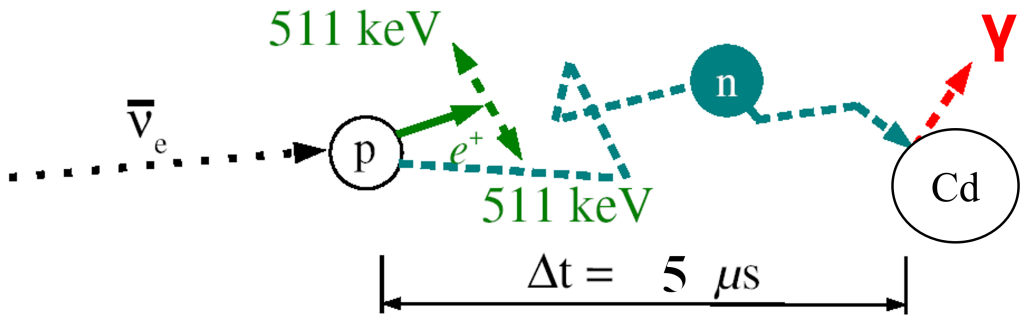

Figure 1.1: Scheme of detection principle in Reines-Cowan experiment.

1.3 Neutrinos in Standard Model

Currently, physics distinguishes four types of fundamental forces in nature: Strong, Electromagnetic, Weak and Gravity. Standard Model of particle physics (SM) is theory unifying

first three: Strong, Electromagnetic and Weak interaction. However, despite an effort of theorists, gravity was not incorporated yet. In 1961, Sheldon Glashow found a way how to combine electromagnetic interaction with weak interaction [8]. In 1967, Higgs mechanism [9, 10, 11] was incorporated into Glashow's electroweak theory by Steven Weinberg [12] and Abdus Salam [13] giving it the modern form we know today. Formulation of SM was finalized in 1970s after experimental proof of existence of quarks. Since 1970s, SM is considered as very reliable model of fundamental particles. SM gained even more credence after experimental discoveries of top quark in 1995 [14, 15], tau neutrino in 2000 [16] and Higgs boson in 2012 [17, 18]. However, SM is only low energy approximation of more general physics and extension is inevitable. Experimental evidence inconsistent with SM was already found - this physics is called physics beyond Standard Model - BSM physics.

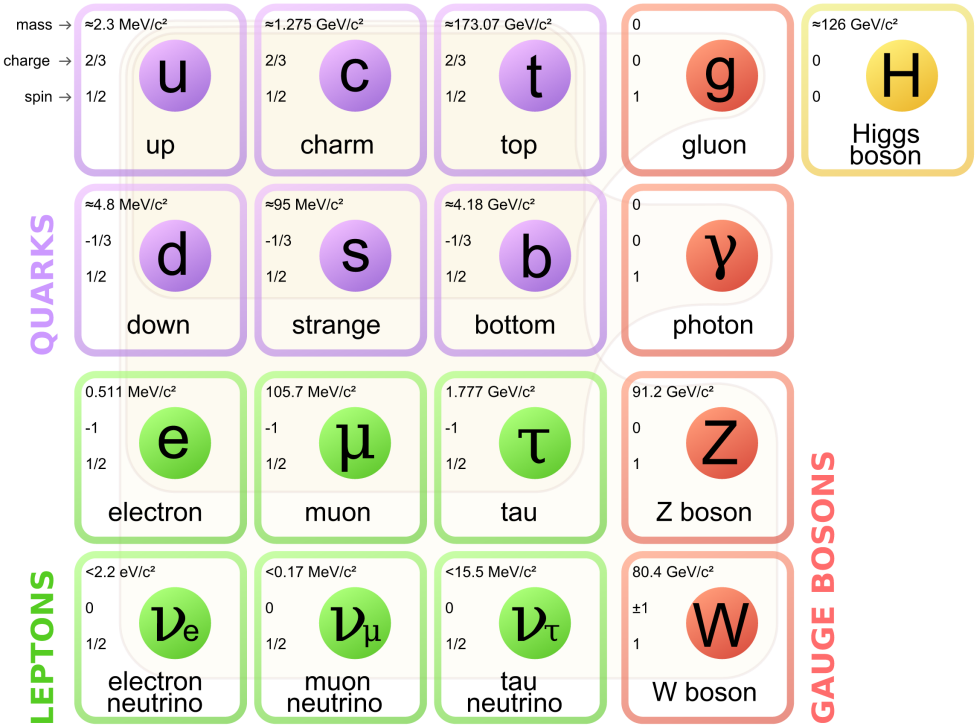

Figure 1.2: All particles of Standard Model.

SM is formulated in form of Lagrangian formalism and describes theoretically interaction of fermions with half integer spin via gauge bosons (integer spin) which act as force carriers. The electromagnetic force is provided by photon, weak interaction by $W^{\pm}$ and Z^0 bosons and strong force is mediated by eight gluons. Gravity as a part of BSM physics is not included. Inclusion of Higgs boson explained why gauge bosons have mass. Fermions in SM are divided into two main groups. Six quarks (up, down, charm, strange, top, bottom) are undergoing all interactions (Strong, Electromagnetic, Weak and also Gravity) while electromagnetically charged leptons (electron, muon and tau lepton) only Electromagnetic, Weak and Gravity. Neutrinos, the last three fermions, have no electromagnetic charge, thus they interact only weakly in the framework of SM. The diagram showing all SM particles within the categories can be seen in Figure 1.2.

Analogically to quarks, leptons are divided into three families (generations). In each family there is charged fermion and its neutrino, i.e. electron and electron neutrino, muon and muon neutrino, tau and tau neutrino. The neutrinos in SM are massless. This was proven wrong experimentally by observation of neutrino oscillations [19] (see Section 1.4.1). It is

one of the aforementioned proofs that SM needs extension and neutrinos might hide the key to BSM physics.

1.3.1 Neutrino Flavours

The discovery of neutrino opened an important chapter in history of experimental particle physics. Knowing that neutrino was a real particle, physicist were interested to know it better. In 1962, new type of neutrino was observed, so-called μ-neutrino, in experiment performed by Leon Lederman, Melvin Schwartz and Jack Steinberger [20]. This type of neutrino was already theoretically predicted in 1940 by several people and named "neutretto" [21]. In the experiment, π-mesons (so-called pions) were accelerated which made it possible to study the nature of weak forces in higher energies. Positive (negative) pion is decaying (in more than 99% of cases) into positive (negative) muon and anti-neutrino (neutrino) (Equation 1.4).

$$\begin{aligned} \pi^+ &\rightarrow \mu^+ + \nu_\mu \\ \pi^- &\rightarrow \mu^- + \bar{\nu}_\mu \end{aligned} \tag{1.4}$$

The pions from accelerator were decaying during the flight. Created muons were absorbed by 13.5 m thick wall and neutrinos continued to detector (Figure 1.3). If there would be only one type of neutrino, electrons and muons caused by impact of neutrinos would be created randomly, in equal rate. However, they observed significant excess of muons. This led them to conclusion, that neutrino from pion decay have identity designated by the nature of interaction by which they were created. New neutrino was named μ-neutrino (and designated

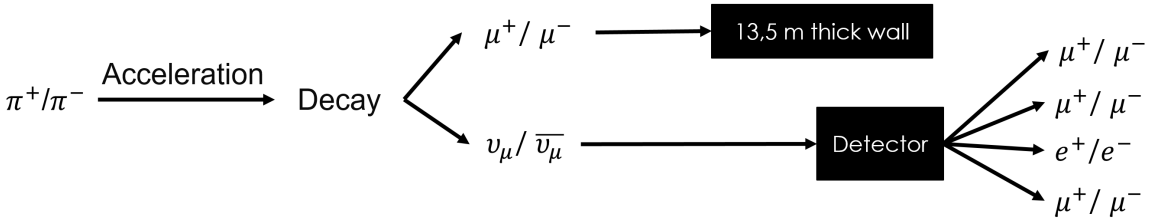

Figure 1.3: Simplified scheme of detection principle in muon neutrino discovery experiment.

ν_μ) because in the lepton vertex it is always created along with μ-lepton. This implies that the neutrino from beta decay is of electron type and designated ν_e. The Nobel prize for discovery of ν_μ was awarded in 1988.

In 1975, when the third type of lepton was discovered - the τ-lepton - in SLAC [22], analogically, the existence of third type of neutrino - τ-neutrino (ν_τ) - was expected. Its discovery was achieved by DONUT collaboration from Fermilab in 2000 [16]. The data were confirmed later by post-analysis from LEP in CERN. Up to date, we distinguish three types (so-called flavours) of neutrinos - ν_e, ν_μ and ν_τ. The existence of other types of neutrinos is being experimentally investigated (for example [23]).

1.4 Neutrinos Beyond the Standard Model

As mentioned before, neutrinos in Standard Model are massless. This is, however, inconsistent with experimental observations. Neutrinos are not, obviously, described fully by SM and they hold information about BSM physics.

1.4.1 Solar Neutrino Problem

The sources of neutrinos are divided into two main groups - natural and artificial. Artificial sources are made by human, for example nuclear reactors (reactor anti-neutrinos) and particle accelerators (accelerator neutrinos). Group of natural sources include neutrinos from neutrino cosmic background one second after Big Bang (cosmological/relic neutrinos), neutrinos produced in nuclear reactions in the Sun (solar neutrinos), neutrinos from the supernovae explosions (supernova neutrinos), neutrinos originating inside of the Earth (geoneutrinos), neutrinos created in atmosphere of the Earth by interaction of cosmic radiation (atmospheric neutrinos), neutrinos from active galactic nuclei (AGN neutrinos) and cosmogenic neutrinos produced by interaction of ultra-high energy cosmic rays with cosmological photon background. Plot depicting fluxes of neutrinos of different origin can be found in Figure 1.4.

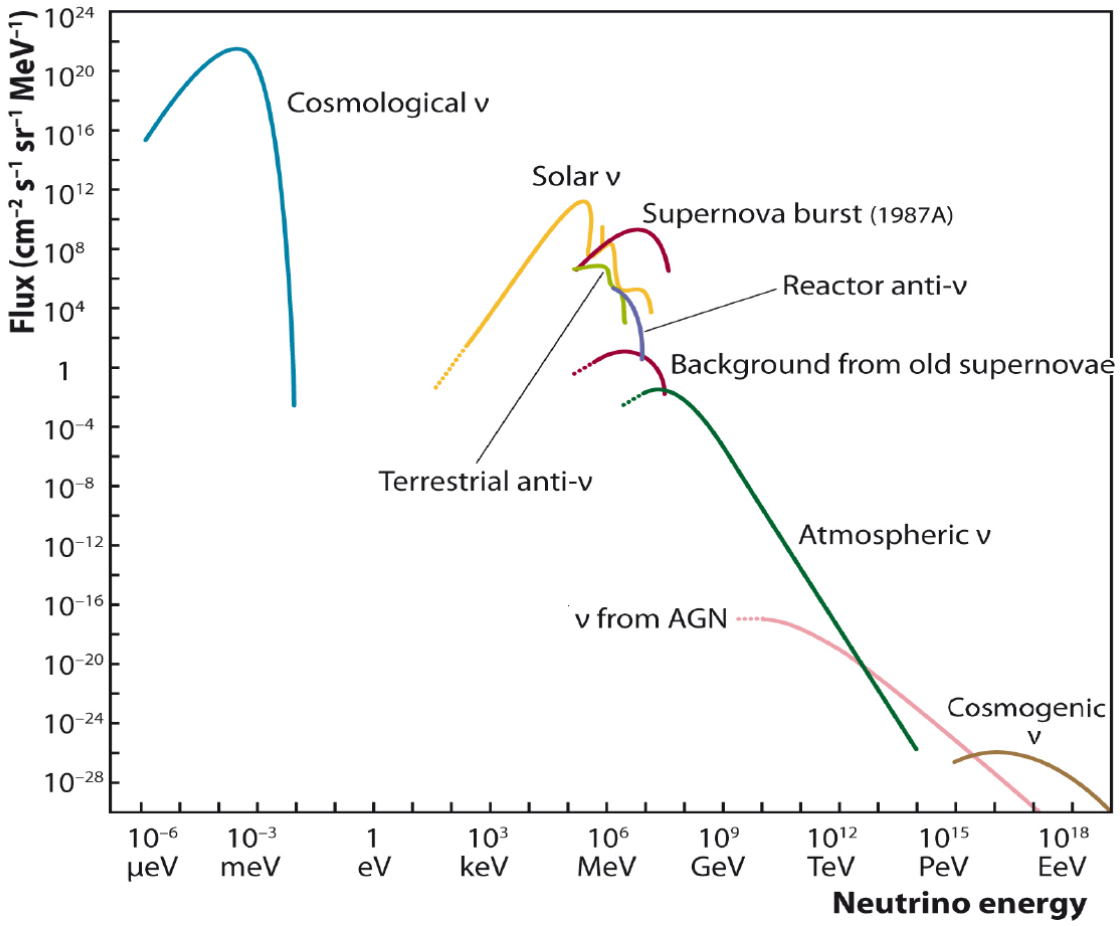

Figure 1.4: Distribution of known neutrino types among the energy range. Plot represents flux of neutrinos of different origin separately. Source: [24].

Solar neutrinos were puzzling neutrino physicists for three decades. Proton-proton chain reaction (so called P-p cycle), which takes place in the core of the Sun [25], is accompanied by emission of ν_e. These neutrinos travel without interaction through the Sun and are emitted uniformly into the space. Some of them reach the Earth. In 1960s, Raymond Davis, Jr. and John N. Bahcall prepared experiment focused on the detection of these neutrinos - the Homestake experiment. It was placed in golden mine in South Dakota in the depth of 1.5 km in order to be shielded from cosmic ray radiation occurring on the surface. Homestake

experiment started the era of underground neutrino experiments. It was continuously in operation from 1970 to 1994. Experimental technique was based on 615 t of tetrachloroethylene (C_2Cl_4) which is total of 2.2×10^{30} nuclei of ^{37}Cl. Electron neutrino, which came from the Sun, underwent capture by ^{37}Cl which was transformed into ^{37}Ar accompanied by emission of electron (Equation 1.5).

$$\nu_e + {}^{37}Cl \rightarrow {}^{37}Ar + e^- \tag{1.5}$$

Every few weeks, Davis and Bahcall bubbled Helium through the tank to extract Argon. Few cm^3 were extracted including the stable Argon isotopes. Then the decay of ^{37}Ar was observed. This helped to determine the rate of neutrino events. Bahcall calculated that according to the Standard Solar Model (SSM), the expected rate should be 9.3 ± 1.3 SNU[1]. However, they measured only 2.56 ± 0.32 SNU [26]. The theoretical predictions were revised several times by theoreticians improving the precision of the model but the difference seemed not to lie in the theoretical refinement. Experiment was also checked for errors, but conclusion was that it works correctly. There was lack of neutrinos in the detector. This problem is called the solar neutrino problem.

It was not clear whether the processes in the Sun were understood properly, thus the main interest of theoreticians was pointed towards SSM. Several experiments were constructed in order to account for this question. Kamiokande [27] in Japan (1985 - 1995), SAGE [28] in Baksan, Russia (1989 - 2007) or Gallex [29] in Gran Sasso, Italy (1991 - 1997). All of them have seen lack of neutrinos. Kamiokande was capable of measuring the momentum of the neutrinos. It confirmed that these neutrinos really originate in the Sun. The lack of solar neutrinos was, finally, explained by occurence of so-called neutrino oscillations. Their existence was proposed in 1958 by Bruno Pontecorvo [30].

1.4.2 Neutrino Mixing and Oscillations

Under the term neutrino oscillations we understand the continuous change of the flavour of neutrino along the trajectory of flight. In contrary to assumption of Standard Model of particle physics, it would be only possible if neutrino had non-zero mass. The reason is as follows: if we assume three neutrino mass eigenstates (denoted ν_1, ν_2, ν_3) to be different from flavour eigenstates (denoted ν_e, ν_μ, ν_τ) there is a unitary transformation between the bases[2]:

$$\begin{aligned} |\,\nu_\alpha\rangle &= \sum_i U_{\alpha i}\,|\,\nu_i\rangle \\ |\,\nu_i\rangle &= \sum_\alpha U^*_{\alpha i}\,|\,\nu_\alpha\rangle \end{aligned} \tag{1.6}$$

Rewritten into matrix form:

$$\begin{pmatrix} |\,\nu_e\rangle \\ |\,\nu_\mu\rangle \\ |\,\nu_\tau\rangle \end{pmatrix} = \begin{pmatrix} U_{e1} & U_{e2} & U_{e3} \\ U_{\mu 1} & U_{\mu 2} & U_{\mu 3} \\ U_{\tau 1} & U_{\tau 2} & U_{\tau 3} \end{pmatrix} \begin{pmatrix} |\,\nu_1\rangle \\ |\,\nu_2\rangle \\ |\,\nu_3\rangle \end{pmatrix} \tag{1.7}$$

The unitary matrix providing transformation between two bases is called PMNS (Pontecorvo – Maki – Nakagawa – Sakata) matrix [31, 32]. It is an analogue to CKM (Cabibbo

[1] SNU - Solar neutrino unit denotes one neutrino capture per 10^{36} nuclei every second.

[2] Greek index α is used to denote flavour states and Latin i to denote mass states.

– Kobayashi – Maskawa) matrix for quark mixing. If we limit our discussion only to case of two neutrino mixing of flavours ν_α and ν_β, it has form:

$$\begin{pmatrix} |\,\nu_\alpha\rangle \\ |\,\nu_\beta\rangle \end{pmatrix} = \begin{pmatrix} cos(\theta) & sin(\theta) \\ -sin(\theta) & cos(\theta) \end{pmatrix} \begin{pmatrix} |\,\nu_1\rangle \\ |\,\nu_2\rangle \end{pmatrix} \tag{1.8}$$

Here θ is called mixing angle. When neutrinos are propagated, their state evolve along the trajectory. We can assume, that the momentum of neutrino is far bigger than its rest mass. In that case probability for neutrino with energy E to change flavour from ν_α to ν_β is:

$$P(\nu_\alpha \to \nu_\beta) = sin^2(2\theta) sin^2\left(\frac{\Delta m^2_{ij} L}{4E}\right), \qquad \alpha \neq \beta \tag{1.9}$$

Here, L is the distance travelled by neutrino, θ is neutrino mixing angle and Δm^2_{ij} mass squared difference of i-th and j-th mass state, i.e. $\Delta m^2_{ij} = m^2_i - m^2_j$. From Equation 1.9 we can easily see that probability of oscillation $P(\nu_\alpha \to \nu_\beta)$ is non-zero only if $\Delta m^2_{ij} \neq 0$ holds (assuming that first sine in the product is non-zero which was observed). In other words, it means that neutrino oscillations are possible only in case when at least one of the mass eigenstates of neutrino would be non-zero. This breaks apart the assumption of mass-less neutrinos in Standard Model.

In the case of Solar neutrinos they are produced uniquely as the electron neutrinos but oscillations make them change their flavour during the flight towards the Earth. All the experiments mentioned above, which have seen lack of neutrinos, were capable to detect only electron neutrinos. In 1996, experiment Super-Kamiokande (upgrade of Kamiokande) started data collection. In 1998, they provided the first evidence of neutrino oscillations by observation of atmospheric ν_μ oscillating into ν_τ [33]. One year later, in 1999, SNO (Sudbury Neutrino Observatory) came into operation. SNO was focused on the measurement of neutrinos coming from decay of ^{8}B (around 10 MeV). These electron-neutrinos are not very affected by vacuum neutrino oscillations rather than by so-called MSW effect [34] which has influence on the neutrino oscillations in matter (in this case solar matter). SNO was able to count the number of detected electron-neutrinos and number of neutrinos of all flavours collectively. In 2001, their results supported the existence of neutrino oscillations [19]. In 2015, Nobel prize was given to Takaaki Kajita (Super-Kamiokande) and Arthur B. McDonald (SNO) "for the discovery of neutrino oscillations, which shows that neutrinos have mass".

1.4.3 Supernova Neutrinos

Neutrino oscillations provided clear evidence that the Standard Model of particle physics is not complete. However, the hint that neutrino has non-zero mass came even sooner. In 1987, unique explosion of Supernova 1987A was observed [35]. This supernova is approximately 168 000 light years away in our galactic neighbourhood (in Large Magellanic Cloud). It was the first supernova explosion observable by naked eye since 1604 [36]. In the explosion, estimated 10^{58} anti-neutrinos were created. Three neutrino observatories were capable to measure anti-neutrinos from this burst. In Kamiokande, they detected 12 anti-neutrinos [37], in IMB (Irvine – Michigan – Brookhaven) detector eight [38] and Baksan measured five anti-neutrinos [39]. The most interesting result was obtained by Kamiokande. Their 12 measured anti-neutrinos arrived in two pulses by 9 and 3 while anti-neutrinos from second

pulse were delayed by 9.219 to 12.439 seconds after the first pulse [37]. This was hint, although not an evidence, that neutrinos might have mass. In other case, they would arrive all together propagating at the speed of light in vacuum. Although, 25 detected anti-neutrinos is not a huge number, it was significant increase to background values. It was the first observation of supernova anti-neutrinos and the beginning of neutrino astronomy. The observations were consistent with theoretical supernova models and also allowed physicists to set upper limits on neutrino mass and number of neutrino flavours [40].

1.4.4 Neutrino Hierarchies

The existence of neutrino oscillations serves as a clear signature of neutrinos with non-zero mass. As it was already shown in Equation 1.9, by oscillation experiments, it is possible to extract only the square mass differences $\Delta m^2_{ij} = m^2_i - m^2_j$. These values are measured. However, the three neutrino mass states ν_1, ν_2 and ν_3 remain unknown.

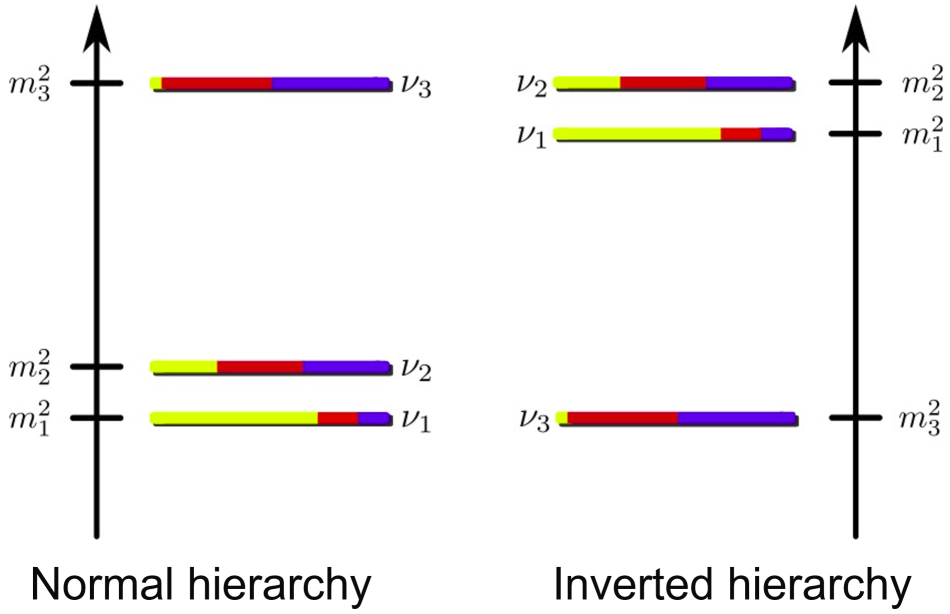

Figure 1.5: Two possible neutrino mass hierarchies. The case of $\nu_1 < \nu_2 < \nu_3$ (with one heavier neutrino state) depicted on the left - is called "Normal" hierarchy while the case on the right, fulfilling $\nu_3 < \nu_1 < \nu_2$ (with two heavier neutrino states), is called "Inverted" hierarchy.

Furthermore, the ordering of the states - so-called neutrino hierarchy - can not be provided by oscillation experiments. From solar neutrino observations and measurements of atmospheric neutrinos we know the values of Δm^2_{21} and $|\Delta m^2_{32}|$ [41]:

$$\begin{aligned} \Delta m^2_{Sun} = \Delta m^2_{21} &= (7.53 \pm 0.18) \times 10^{-5} eV^2 \\ |\Delta m^2_{atm}| = |\Delta m^2_{32}| &= (2.44 \pm 0.06) \times 10^{-3} eV^2 \end{aligned} \tag{1.10}$$

The convention $m_1 < m_2$ is adopted which allows us to narrow possible neutrino hierarchies to two cases depicted in Figure 1.5. They differ only by number of heavier states. The case with one heavier neutrino state is called "Normal" hierarchy while the case with two heavier neutrino states is so-called "Inverted" hierarchy.

1.4.5 Neutrino Masses and Their Nature

Based on previous discussion, new terms generating neutrino masses are needed as a extension of Lagrangian of SM. Depending on chirality of particles we recognize left-handed (spin and momentum of particle are parallel) and right-handed (spin and momentum of particle are anti-parallel) particles. In Standard Model, only the left-handed neutrinos and right-handed anti-neutrinos enter into interactions.

Let us have a look on three possible extensions of SM Lagrangian generating neutrino masses:

Dirac mass term

Assuming the existence of both, left-handed (ν_α^{L}) and right-handed (ν_α^{R}) neutrino fields, we are able to compose so-called Dirac mass term of Lagrangian given in Equation 1.11.

$$\mathscr{L}^D = -\sum_{\alpha,\alpha'} \overline{\nu}_{\alpha'}^R M_{\alpha,\alpha'}^D \nu_\alpha^L + \mathrm{h.c.} \tag{1.11}$$

Indices α and α' stand for neutrino flavours (e, μ and τ) and $\mathrm{M^D}$ is complex 3×3 matrix coupling left-handed and right-handed neutrino. In respect to equation of neutrino mixing (Equation 1.6), the ν_α^{L} are mixed in the following way:

$$\nu_\alpha^L = \sum_{i=1}^{3} U_{\alpha i}\nu_i^L, \tag{1.12}$$

Here, i (i = 1, 2 or 3) denotes the Dirac mass state with mass $\mathrm{m_i}$ and $\mathrm{U_{\alpha i}}$ is unitary neutrino mixing matrix. If matrix $\mathrm{M^D}$ is non-diagonal, the individual lepton numbers $\mathrm{L_e}, \mathrm{L}_\mu, \mathrm{L}_\tau$ are not conserved. However, this mass term does not mix particles with anti-particles, thus the total lepton number $\mathrm{L} = \mathrm{L_e} + \mathrm{L}_\mu + \mathrm{L}_\tau$ is conserved.

Majorana mass term

Another possibility to construct neutrino mass term was proposed by Ettore Majorana. His mass term is coupling neutrinos with anti-neutrinos as follows:

$$\mathscr{L}^M = -\sum_{\alpha,\alpha'} (\overline{\nu}_{\alpha'}^L)^c M_{\alpha\alpha'}^M \nu_\alpha^L + \mathrm{h.c.} \tag{1.13}$$

Index c denotes charge conjugated neutrino spinor $\nu^{\mathrm{c}} = \mathrm{C}\overline{\nu}^{\mathrm{T}}$, where C is charge conjugation operator. $\mathrm{M^M}$ is complex symmetric 3×3 matrix. Majorana mass fields $\chi_{\mathrm{i}}^{\mathrm{L}}$ are mixed into flavour fields in following way:

$$\nu_\alpha^L = \sum_{i=1}^{3} U_{\alpha i}\chi_i^L, \tag{1.14}$$

where again $\mathrm{U_{\alpha i}}$ is unitary neutrino mixing matrix. Charge conjugated mass fields $\chi_{\mathrm{i}}^{\mathrm{c}}$ differ to $\chi_{\mathrm{i}}^{\mathrm{L}}$ only by a phase factor ξ_{i}: $\chi_{\mathrm{i}}^{\mathrm{c}}\xi_{\mathrm{i}} = \chi_{\mathrm{i}}$. Neutrinos are indistinguishable to anti-neutrinos and processes violating total lepton number are allowed[3]. Majorana mass term, as already mentioned, is coupling neutrinos with anti-neutrinos. As a result, Majorana mass term violates even total lepton number $\mathrm{L} = \mathrm{L_e} + \mathrm{L}_\mu + \mathrm{L}_\tau$. The existence of such mass term in quark

[3]For example neutrino-less double beta-decay, see Section 1.5.2

sector or for charged leptons is impossible because the charge conservation would be violated, which is not the case for neutrinos.

Dirac - Majorana mass term

The last possibility is relatively simple combination of previous two. It is the most general and, thanks to presence of Majorana part, it does not conserve total lepton number.

$$\mathscr{L}^{D+M} = -\sum_{\alpha\alpha'}\left[\frac{1}{2}(\overline{\nu}^L_{\alpha'})^c M^{M,L}_{\alpha\alpha'}\nu^L_\alpha + \frac{1}{2}\overline{\nu}^R_{\alpha'}M^{M,R}_{\alpha\alpha'}(\nu^R_\alpha)^c + \overline{\nu}^R_{\alpha'}M^D_{\alpha\alpha'}\nu^L_\alpha\right] + \text{h.c.} \tag{1.15}$$

$M^{M,L}$ and $M^{M,R}$ are complex non-diagonal symmetric 3×3 matrices. In this general case, the flavour fields ν^L_α and ν^R_α are composed of six Majorana mass fields:

$$\nu^L_\alpha = \sum_{i=1}^{6} U^L_{\alpha i}\chi^L_i, \quad \nu^R_\alpha = \sum_{i=1}^{6} U^R_{\alpha i}\chi^R_i. \tag{1.16}$$

For mixing matrices $U^L_{\alpha i}$, $U^R_{\alpha i}$ we have these orthonormalization conditions:

$$\sum_{i=1}^{6} U^L_{\alpha i}U^R_{\alpha' i}\xi_i = 0, \quad \sum_{i=1}^{6} U^L_{\alpha i}(U^L_{\alpha' i})^* = \delta_{\alpha\alpha'}, \quad \sum_{i=1}^{6} U^L_{\alpha i}(U^R_{\alpha' i})^* = \delta_{\alpha\alpha'}. \tag{1.17}$$

According to the mass generation process, neutrino can be either of Dirac ($\nu \neq \overline{\nu}$) or of Majorana nature ($\nu = \overline{\nu}$).

1.5 Double Beta-Decay Processes

Unknown neutrino masses as well as the problem of neutrino hierarchies are important problems of contemporary neutrino physics. The possible solutions might be hidden in a processes called by generalized name of double beta-decay.

1.5.1 Two-Neutrino Double Beta-Decay

Two-neutrino double beta-decay is nuclear decay proposed in 1935 by Maria Goeppert-Mayer [42]. It is a nuclear transition where two neutrons are instantaneously transformed into two protons by emission of two electrons and two electron anti-neutrinos (Equation 1.18).

$$(A,Z) \to (A,Z+2) + 2e^- + 2\bar{\nu}_e \tag{1.18}$$

It is the double analogy of ordinary β^--decay (Equation 1.2), usually denoted by $2\nu\beta\beta$. However, the term double beta-decay with two neutrinos (anti-neutrinos) might be used to name also one of the following combinations of β^+-decay or electron capture (EC):

$$\begin{aligned}
(A,Z) &\to (A,Z-2) + 2e^+ + 2\nu_e, && (2\nu\beta^+\beta^+)\\
e^- + (A,Z) &\to (A,Z-2) + e^+ + 2\nu_e, && (2\nu\beta^+/EC)\\
2e^- + (A,Z) &\to (A,Z-2) + 2\nu_e + 2\gamma, && (2\nu EC/EC)
\end{aligned} \tag{1.19}$$

In next, if not stated otherwise, $2\nu\beta\beta$ would stand for the process described by Equation 1.18. This process is rare compared to ordinary β-decay, so its half-life $T^{2\nu}_{1/2}$ reaches

Decay	Q-value [keV]	$T^{2\nu}_{1/2}$ [yr]
^{48}Ca $\rightarrow^{48}$ Ti	4267	$4.4^{+0.6}_{-0.5} \times 10^{19}$
^{76}Ge $\rightarrow^{76}$ Se	2039	$1.65^{+0.14}_{-0.12} \times 10^{21}$
^{82}Se $\rightarrow^{82}$ Kr	2996	$(0.92 \pm 0.07) \times 10^{20}$
^{96}Zr $\rightarrow^{96}$ Mo	3349	$(2.3 \pm 0.2) \times 10^{19}$
^{100}Mo $\rightarrow^{100}$ Ru	3034	$(7.1 \pm 0.4) \times 10^{18}$
^{100}Mo $\rightarrow^{100}$ Ru(0^+_1)	1905	$6.7^{+0.5}_{-0.4} \times 10^{20}$
^{116}Cd $\rightarrow^{116}$ Sn	2813	$(2.87 \pm 0.13) \times 10^{19}$
^{128}Te $\rightarrow^{128}$ Xe	867	$(2.0 \pm 0.3) \times 10^{24}$
^{130}Te $\rightarrow^{130}$ Xe	2528	$(6.9 \pm 1.3) \times 10^{20}$
^{136}Xe $\rightarrow^{136}$ Ba	2458	$(2.19 \pm 0.06) \times 10^{21}$
^{150}Nd $\rightarrow^{150}$ Sm	3371	$(8.2 \pm 0.9) \times 10^{18}$
^{150}Nd $\rightarrow^{150}$ Sm(0^+_1)	2626	$1.2^{+0.3}_{-0.2} \times 10^{20}$
^{238}U $\rightarrow^{238}$ Pu	1144	$(2.0 \pm 0.6) \times 10^{21}$

Table 1.1: Recommended averaged values of half-lives for several $2\nu\beta\beta$ nuclei [43]. Q values are taken from National Nuclear Data Center website [44].

$10^{19} - 10^{25}$ years and can be calculated as follows:

$$\frac{1}{T^{2\nu}_{1/2}} = \frac{\Gamma_{2\nu}}{ln(2)} = G^{2\nu}(Q,Z) \mid M^{2\nu} \mid^2 \tag{1.20}$$

$\Gamma_{2\nu}$ is a decay rate, Q is total energy released in $2\nu\beta\beta$, $G^{2\nu}(Q,Z)$ is kinematical phase space factor and $M^{2\nu}$ is nuclear matrix element. This decay mode was already observed in case of several candidate nuclei. Their list along with their Q-values and measured half-lives can be found in the Table 1.1.

1.5.2 Neutrino-Less Double Beta-Decay

In 1939, Wendell H. Furry proposed possibility of neutrino-less mode of double beta-decay [45]. This would be only possible if neutrino is its own antiparticle, so-called Majorana particle. The process would look similar to $2\nu\beta\beta$ but without anti-neutrinos in final

state (Equation 1.21).

$$(A,Z) \rightarrow (A,Z+2) + 2e^{-} \tag{1.21}$$

Interest in this decay mode lies in the possibility to prove that neutrino is of Majorana nature. For now, it is the only known possible way to prove it. Moreover, the half-life ($T^{0\nu}_{1/2}$) of $0\nu\beta\beta$ is in the direct relation with neutrino mass values (Equation 1.22).

$$\frac{1}{T^{0\nu}_{1/2}} = \frac{\Gamma_{0\nu}}{ln(2)} = \mid m_{\beta\beta} \mid^2 G^{0\nu}(Q,Z) \mid M^{0\nu} \mid^2 \tag{1.22}$$

$\Gamma_{0\nu}$ is decay width of $0\nu\beta\beta$, Q is kinetic energy emitted in the process, $G^{0\nu}(Q,Z)$ is a phase space factor and $M^{0\nu}$ is nuclear matrix element of $0\nu\beta\beta$. Here, $m_{\beta\beta}$ is so-called effective neutrino mass given by linear combination of all three neutrino masses (Equation 1.23).

$$m_{\beta\beta} = \sum_{i=1}^{3} U_{ei}^2 m_i \tag{1.23}$$

In $0\nu\beta\beta$ experiments, two electrons coming from one vertex are expected to be observed. However, the same signal is expected from $2\nu\beta\beta$ decay because the two neutrinos are not detected This fact puts $2\nu\beta\beta$ decay into position of background event when searching for $0\nu\beta\beta$. Luckily, this problem is possible to solve just by looking at the spectrum. If we look at the sum of kinetic energies of both electrons, in case of $2\nu\beta\beta$ decay, some energy from $Q_{\beta\beta}$ value is taken away by neutrinos. Accordingly to the simple beta-decay, energy spectrum of $2\nu\beta\beta$ is thus continuous. In contrary, in case of $0\nu\beta\beta$ there are no neutrinos, and all energy from $Q_{\beta\beta}$ is transformed into kinetic energy of both electrons. So the theoretical $0\nu\beta\beta$ signal is expected to be a peak at the end of $2\nu\beta\beta$ spectrum as depicted in Figure 1.6a. In real experimental situation, this peak has a shape of Gaussian distribution because of the non-zero energy resolution (Figure 1.6b). In case of poor energy resolution this peak might overlap with the $2\nu\beta\beta$ continuum. The detection techniques with sufficiently high energy resolution in the region of $Q_{\beta\beta}$ are thus required for $0\nu\beta\beta$ experiments.

1.5.3 Nuclear Matrix Elements

The knowledge of nuclear matrix elements of $0\nu\beta\beta$ is unavoidable in order to extract effective neutrino mass from half-life of $0\nu\beta\beta$. Unfortunately, these matrix elements can be measured independently only partially, thus they have to be calculated. This fact underlines the importance of having precise theoretical nuclear models. The matrix elements are crucial for planning of future experiments. Increase of factor 2 in uncertainty is projected into four-fold raise in amount of isotope needed to reach some certain neutrino mass limit.

In order to calculate the nuclear matrix elements, the many-body wave-functions of nuclei in question should be known precisely. Many different approaches are currently used in order to address this question. Let me briefly present three of them.

First one is the ISM (Interacting Nuclear Shell Model). This model treats only limited number of orbits which are not far from Fermi level. All the possible correlations are included and treated exactly. The disadvantage of this approach is that it could result into quite robust calculation where basis as big as 10^{11} Slater determinants is needed to be treated. This is the reason why this method is suitable mainly for smaller nuclei such as ^{48}Ca [46].

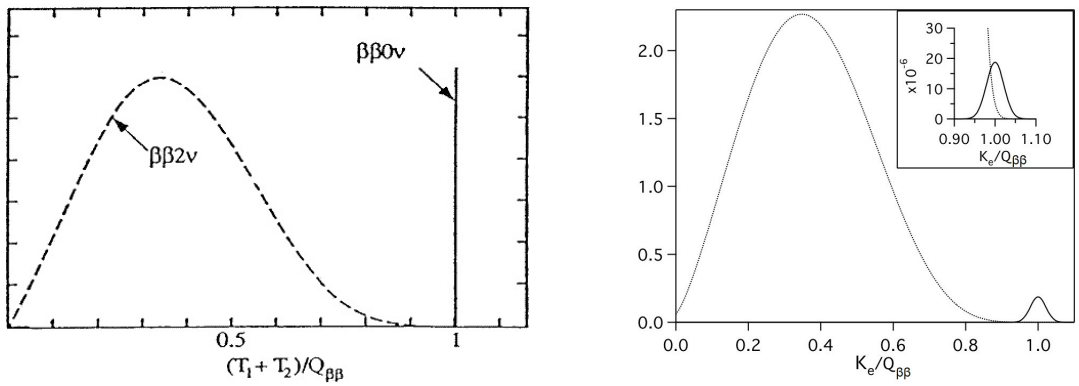

(a) (b)

Figure 1.6: Double beta-decay spectra. X-axis in both figures represents sum of kinetic energies of both electrons in units of $Q_{\beta\beta}$ value. Y-axis is the amplitude in arbitrary units in both cases. (a): Theoretical spectrum of double beta-decay. $2\nu\beta\beta$ continuous spectrum is in dashed line while $0\nu\beta\beta$ is represented as a delta function at the end of the spectrum. Its height is exaggerated. (b): Theoretical double beta-decay spectrum. The effect of non-zero energy resolution of detector is taken into account. Peak which belongs to $0\nu\beta\beta$ is of Gaussian shape and its height is exaggerated. In top right corner the zoom of the region around $Q_{\beta\beta}$ value is displayed. In this case, $0\nu\beta\beta$ peak is shown in its real relative size compared to $2\nu\beta\beta$ continuum. Clear overlap is visible. This effect can be inhibited by improvement in the energy resolution of detection.

Another model is the Quasiparticle Random Phase Approximation (QRPA). Compared to ISM, QRPA is using much large valence space but it is not able to take into account all possible configurations. The single particle states are obtained from solution of Schrödinger equation in mean-field approximation using Woods-Saxon potential. BCS (Bardeen – Cooper – Schrieffer) approximation is employed, so proton and neutron numbers are not exactly conserved. This method generally works the best for bigger nuclei but further development is needed in order to achieve sufficient precision for calculation of nuclear matrix elements for $0\nu\beta\beta$. One of such attempts was a topic of my master thesis where the approach of possible non-linear extension of phonon operator was studied [47].

Third commonly used model is so-called Interacting Boson Model (IBM). This model is building the nuclear wave-function in terms of nucleon pairs with L = 0 and L = 2. The double beta-decay is modelled in terms of 0^+ and 2^+ neutron pairs transferring into proton pair. This model was used for both small and large nuclei.

A full discussion of different contemporary nuclear models is far beyond the scope of this thesis. Let me, at least, present the current status of nuclear matrix elements for $0\nu\beta\beta$ in form of the Figure 1.7.

1.5.4 Experimental Status of Double Beta-Decay

In past decades, several experiments (e.g. Heidelberg-Moscow, NEMO-3, CUORICINO, ...) adopted various techniques to search for $0\nu\beta\beta$. Many others were developed for the new generation of experiments. Even though, the variety of approaches is relatively wide, there are still few principles which are followed by all $0\nu\beta\beta$ experiments. First of all, good resolution of electron energies is needed to be able to distinguish the $0\nu\beta\beta$ in the energy spectrum from $2\nu\beta\beta$ and other types of background. The mass of studied isotope is the key

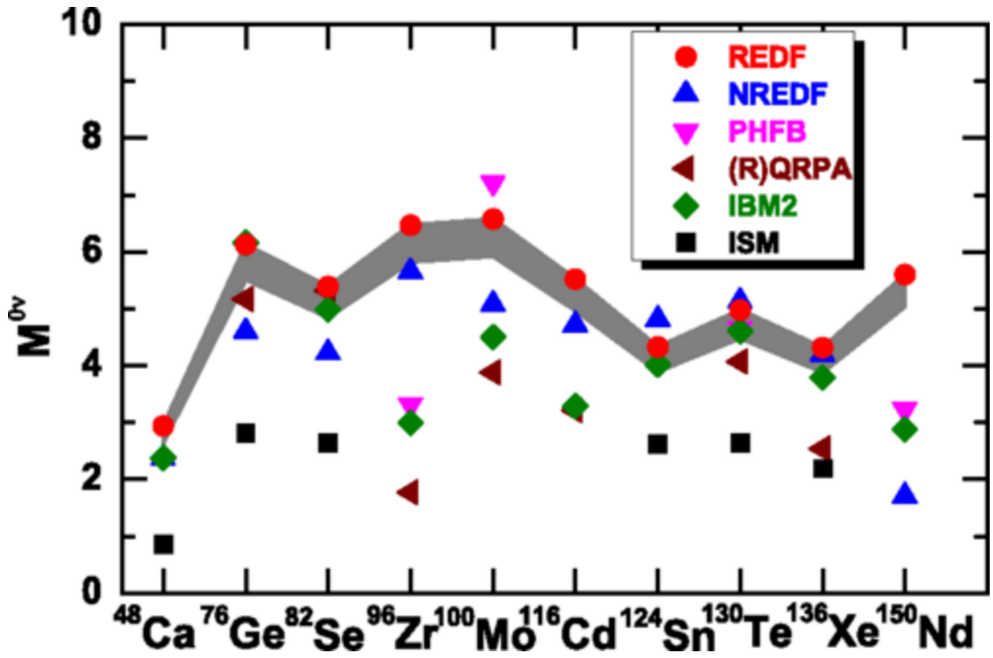

Figure 1.7: Current status of theoretical calculations of nuclear matrix elements for $0\nu\beta\beta$ [48]. Except for IBM, ISM and QRPA methods, results of PHFB (Projected Hartree - Fock - Bogoliubov) and EDF (Energy Density Functional) methods are presented. The differences are still relatively big despite of the theoretical effort invested into this topic.

parameter which increases expected experimental sensitivity of neutrino-less double beta-decay half-life. Sensitivity can be calculated by Equation 1.24.

$$T_{1/2}^{0\nu\beta\beta} > ln(2)\frac{N_A}{W}\varepsilon\frac{am_s t}{\alpha\sqrt{b}} \tag{1.24}$$

The parameters in the equation are as following: $T_{1/2}^{0\nu\beta\beta}$ - neutrino-less double beta-decay half-life, α - number of standard deviations for given confidence level, ε - efficiency of detection and identification of true events, a - isotopic abundance of studied $0\nu\beta\beta$ isotope in investigated sample, W - is molecular weight of source isotope, m_s - total mass of studied sample, t - duration of data taking period and b - number of expected background events. Detailed discussion about origin of this equation and calculation of half-life limits takes place in Chapter 6 and Appendix B. The current best limits for variety of isotopes are presented in Table 1.2. Given a value of nuclear matrix elements, they also yield the upper limit for effective neutrino mass. Some examples of techniques used to search for $0\nu\beta\beta$ are presented in next sections.

Germanium experiments

This type of experiments aim to study the $0\nu\beta\beta$ of ^{76}Ge. They belong to the type of experiments where source serves as the detector at the same time. They use Ge semiconductor diodes enriched at about 86% in ^{76}Ge, having high detection efficiency. At the level of 2 039 keV ($Q_{\beta\beta}$ value of ^{76}Ge) the energy resolution can be as small as few keV when using cooling system, for example liquid Argon. The detection principle is relatively simple. A particle, interacting with detector, produces charge carriers which are collected, amplified

Decay	Q-value [keV]	$T^{0\nu}_{1/2}$ [yr]	$\mid m_{\beta\beta} \mid$ [eV]	Experiment
^{48}Ca $\rightarrow^{48}$ Ti	4268	$> 5.8\times10^{22}$	< 3.1-15.4	CANDLES [49]
^{76}Ge $\rightarrow^{76}$ Se	2039	$> 3.5\times10^{25}$	< 0.18-0.48	GERDA [50]
^{82}Se $\rightarrow^{82}$ Kr	2998	$> 3.6\times10^{23}$	< 1-2.4	NEMO-3 [51]
^{96}Zr $\rightarrow^{96}$ Mo	3356	$> 9.2\times10^{21}$	< 3.6-10.4	NEMO-3 [52]
^{100}Mo $\rightarrow^{100}$ Ru	3034	$> 1.1\times10^{24}$	< 0.33-0.62	NEMO-3 [53]
^{116}Cd $\rightarrow^{116}$ Sn	2814	$> 1.9\times10^{23}$	< 1-1.8	AURORA [54]
^{128}Te $\rightarrow^{128}$ Xe	867	$> 1.5\times10^{24}$	< 2.3-4.6	Geochem. exp. [55]
^{130}Te $\rightarrow^{130}$ Xe	2528	$> 4\times10^{24}$	< 0.26-0.97	CUORE [56]
^{136}Xe $\rightarrow^{136}$ Ba	2458	$> 1.07\times10^{26}$	< 0.06-0.16	KamLAND-Zen [57]
^{150}Nd $\rightarrow^{150}$ Nd	3371	$> 2\times10^{22}$	< 1.6-5.3	NEMO-3 [58]

Table 1.2: List of the best current lower limits set for the half-life of $0\nu\beta\beta$ and upper limits on effective neutrino mass [59]. Limits are at 90% C.L. Uncertainty of the mass upper limit is caused by limited knowledge of $0\nu\beta\beta$ matrix elements $M^{0\nu}$.

and turned into a voltage signal. The signal is proportional to energy deposited in detector. The most known experiments of first generation based on Germanium are Heidelberg-Moscow (HdM) and International Germanium Experiment (IGEX). The low limit on $0\nu\beta\beta$ half-life was set to level of 1.9×10^{25} yr (90% C.L.) by HdM [60] and 1.57×10^{25} yr (90% C.L.) by IGEX [61]. Part of HdM collaboration announced the observation of $0\nu\beta\beta$ signal in 2004 [62] but the proof is not convincing enough and the result is considered controversial. GERDA (Germanium Detection Array, Figure 1.8) the following generation of Ge detector, was designed to verify results of HdM. Low limit on $0\nu\beta\beta$ half-life was set to level of 3.5×10^{25} yr (90% C.L.) by GERDA during Phases I and II of its run [63]. GERDA have excluded with 99% probability that HdM discovered $0\nu\beta\beta$, already after the analysis of data from Phase I [64]. MAJORANA is example of another similar experiment in preparation which aims to employ 40 kg of Selenium. Collaboration with GERDA in its Phase III is being prepared under the name LEGEND (Large Enriched Germanium Experiment for Neutrino-less Decay).

Bolometer experiments

Bolometers are calorimeters at very low temperatures. As in the previous case, this type of detection technique also takes advantage of source being the detector. Particle passing through the detector leaves the heat proportional to its energy in bolometer. Heat is then

Figure 1.8: Visualisation of GERDA experiment.

measured by very sensitive semiconductor thermistors. The bolometers should be cooled down to 10 mK. In general, the deposition efficiency of energy in bolometrs is high, but the data collection is slow. There are several $0\nu\beta\beta$ experiments using bolometric method. CUORICINO was located in the LNGS (Laboratori Nazionali del Gran Sasso, Italy) and ran from March 2003 to July 2008. It used 40.7 kg of enriched and also natural TeO_2 crystals at the temperature of 8 mK. The limit on $0\nu\beta\beta$ half-life was set by CUORICINO at the level of 2.8×10^{24} yr (90% C.L.) for ^{130}Te [65]. CUORE is next generation bolometer $0\nu\beta\beta$ experiment and successor of CUORICINO. Its prephase CUORE-0 is now in operation. The aim is to increase the mass from 40.7 kg (CUORICINO) to 741 kg which corresponds to 206 kg of ^{130}Te. First results from CUORE-0 in combination with CUORICINO data show $0\nu\beta\beta$ half-life exclusion up to 4×10^{24} yr (90% C.L.) [56]. The expected sensitivity of CUORE, assuming low background of 0.01 cts/(keV$\cdot$ kg $\cdot$ y), during five years of operation is on the level of 9.5×10^{25} yr (90% C.L.) [66]. LUCIFER (Low-background Underground Cryogenic Installation For Elusive Rates) is $0\nu\beta\beta$ bolometer experiment aimed to study ^{82}Se in the form of crystals of ZnSe. LUCIFER will be composed of 15 kg of enriched ^{82}Se. The expected sensitivity of $0\nu\beta\beta$ half-life after 5 years of running and the background level of 10^{-3} cts/(keV$\cdot$ kg $\cdot$ y) is on the level of 6.0×10^{25} yr (90% C.L.) [67].

TPC and liquid scintillator experiments

Time projection chambers are particle detectors observing ionisation electrons, induced when charged particle interacts with the detector target. Anode wires attract the ionisation

electrons and collect them. These electrons carry information about the track of initial ionising particle which can be reconstructed in three dimensions if the anode wires are organized in specific pattern inside of the chamber. These experiments also belong to the category of experiments where the target coincides with the source.

EXO-200 is a cylindrical liquid xenon time projection chamber (TPC) aimed to study 200 kg of 80.6% enriched ^{136}Xe. The data taking started in 2011. After two years of data taking, the limit on $0\nu\beta\beta$ half-life (for ^{136}Xe) was reached at the level of 1.1×10^{25} yr (90% C.L.) [68].

KamLAND-Zen (KamLAND-Zero neutrino) is another liquid scintillator experiment and successor of KamLAND detector (Figure 1.9). KamLAND detector was originally used as an oscillation experiment. It was composed of spherical balloon of 6.5 m radius filled with liquid scintillator sensitive to antineutrinos coming from Japanese nuclear reactors. The KamLAND-Zen is an upgrade of the detector dedicated to measurement of $0\nu\beta\beta$. Another spherical balloon of 3 m radius was inserted inside of the original one. This inner balloon is filled with liquid scintillator doped by enriched Xenon (^{136}Xe). Liquid scintillator in outer balloon serves as detection medium and shielding at the same time. Such a design ensures fully contained energy depositions which makes up for the biggest problem of liquid scintil-

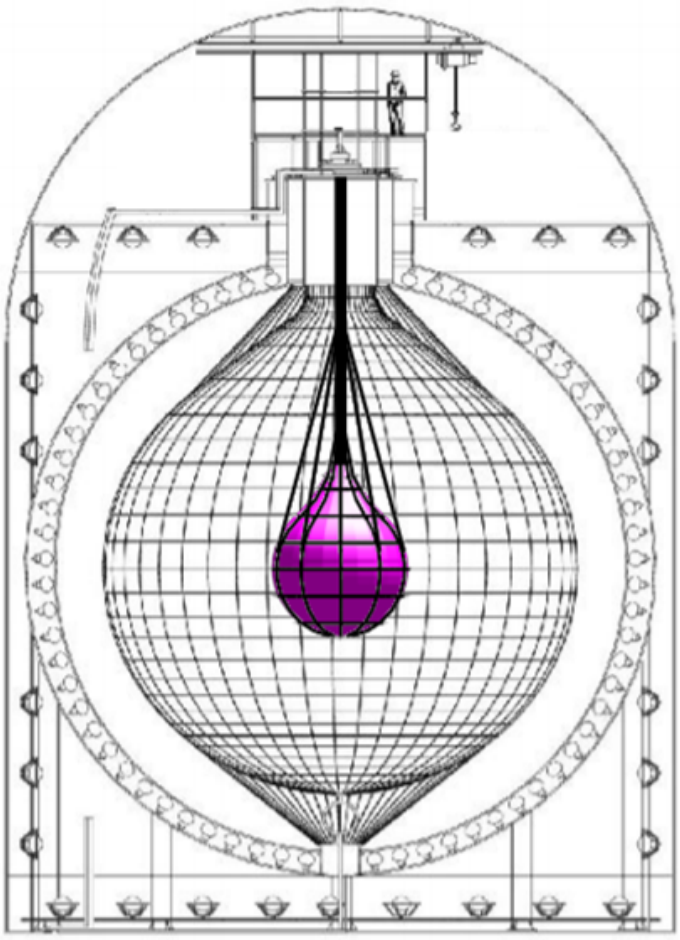

Figure 1.9: Scheme of KamLAND-Zen experiment. Inner balloon (highlighted in violet colour) containing Xe-doped liquid scintillator is inserted inside of the bigger balloon filled with liquid scintillator.

lator experiments - poor energy resolution. KamLAND-Zen went into operation in 2011 in Kamioka mine (Japan). The whole setup comprises 330 kg of ^{136}Xe. Neither this experiment have seen an excess in the energy region of $0\nu\beta\beta$ setting the low limit on $0\nu\beta\beta$ half-life (for ^{136}Xe) at the level of 1.9×10^{25} yr (90% C.L.) [69]. The aim of another experiment in the category - SNO+ - is to become the largest scintillator detector in the world. It will be placed in the Sudbury Neutrino Observatory - 2 km deep underground laboratory inside Vale's Creighton Nickel mine near Sudbury, Ontario, Canada. 780 tonnes of LAB (Linear AlkylBenzene) scintillator will be installed and loaded with ^{130}Te. The signal will be read out by 9500 8" PMTs. The experiment will aim to reach sensitivity of neutrino mass below 0.1 eV.

Tracker-Calorimeter experiments

This type of $0\nu\beta\beta$ take advantage from the information about particle energy from calorimeters with position and momentum information obtained from trackers. Contrary to three already presented methods, in this method source is separated from the detection system. The main advantage of this approach lies in increased background rejection based simply on the event topology.

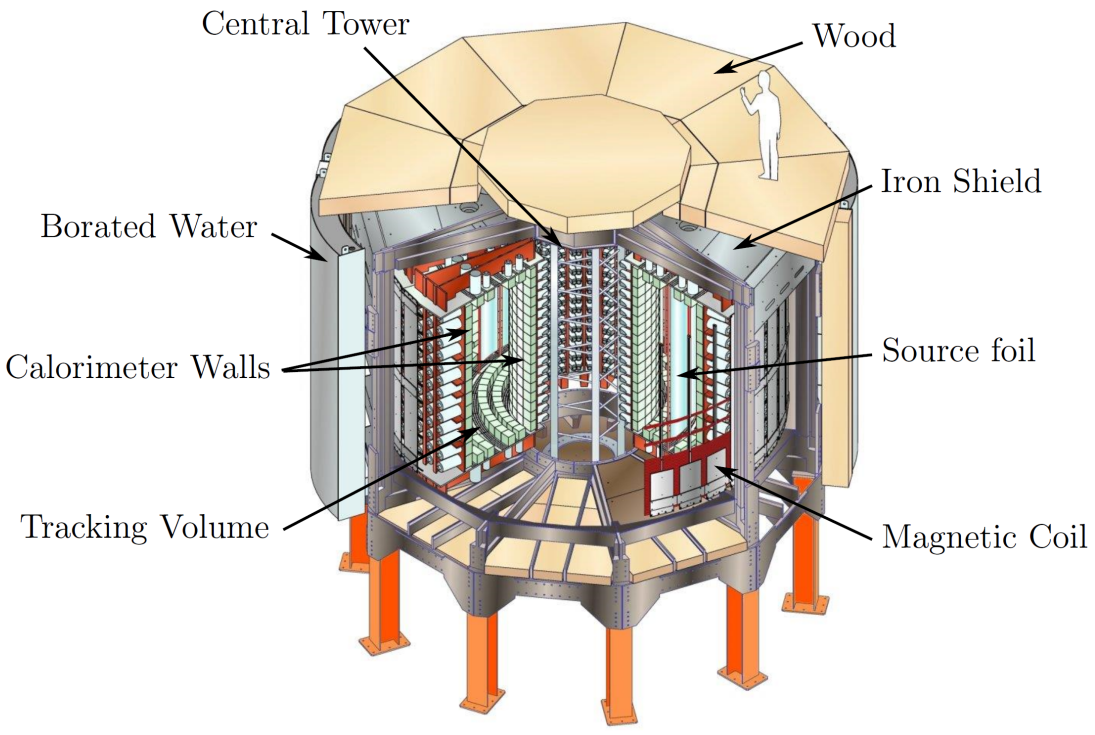

Figure 1.10: Schematic section of NEMO-3 experiment [70].

Main aim of NEMO-3 (The Neutrino Ettore Majorana Observatory) experiment was precise measurement of $2\nu\beta\beta$ half-lives of several isotopes as well as search for $0\nu\beta\beta$. From all 11 different isotopes known to be $2\nu\beta\beta$ radioactive it was NEMO-3 which managed to measure 7 of them including one measurement of $2\nu\beta\beta$ transition to exicted state. Whole project started in 1990s with two prototypes NEMO-1 [71] and NEMO-2 [72].

In NEMO-3 [73, 74] electrons coming from $0\nu\beta\beta$ were detected by scintillating calorimeters and tracked by tracking wires in Geiger mode (Figure 1.10).

The geometry of detector was of cylindrical shape divided into 20 sectors. These sectors were dedicated to different $0\nu\beta\beta$ isotopes, namely: ^{100}Mo (12 sectors), ^{82}Se (2 sectors), ^{130}Te (2 sectors), ^{116}Cd (1 sector). Small volumes of ^{150}Nd, ^{96}Zr and ^{48}Ca were also measured. Finally, sectors composed of Copper and very pure oxide of natural Tellurium were used for measurements of external background in the experiment. The distribution of the sources in the experiment and their amounts are shown in the Figure 1.11.

Energy and time-of-flight of electrons was acquired from 1 940 plastic scintillator blocks. Data from blocks were read out by 3" and 5" photomultiplier tubes (PMT). The information about electron tracks were obtained by 270 cm long vertical Geiger wires enclosing the source foils positioned in the center of each sector (see Figure 1.10). The tracking method is very effective way to reduce background based on rejection by the event topology. Solenoid surrounding the detector produced 25 G magnetic field (parallel to the Geiger wires) inside of the experiment. The whole detector was enclosed in 20 cm thick external shield made of low radioactivity iron in order to reduce γ-rays and thermal neutrons. Another layer of shielding, made of borated water, was applied on top of the iron. It served for thermalisation of fast neutrons and capture of thermal neutrons.

NEMO-3 was placed in LSM (Laboratoire Souterrain de Modane) in Fréjus tunnel on the French - Italian border. The laboratory is in the depth of 1 700 m protected by rock which corresponds to 4 800 m.w.e. During the run period of 8 years (January 2003 - January 2011) which corresponds to 5 years of data taking, $0\nu\beta\beta$ was not observed. NEMO-3 managed to set the lower limit for $0\nu\beta\beta$ on the level of 10^{24} yr for ^{100}Mo [53]. Moreover, $2\nu\beta\beta$ half-lives of many isotopes were measured for the first time in history. Their full list can be found in Table 1.3.

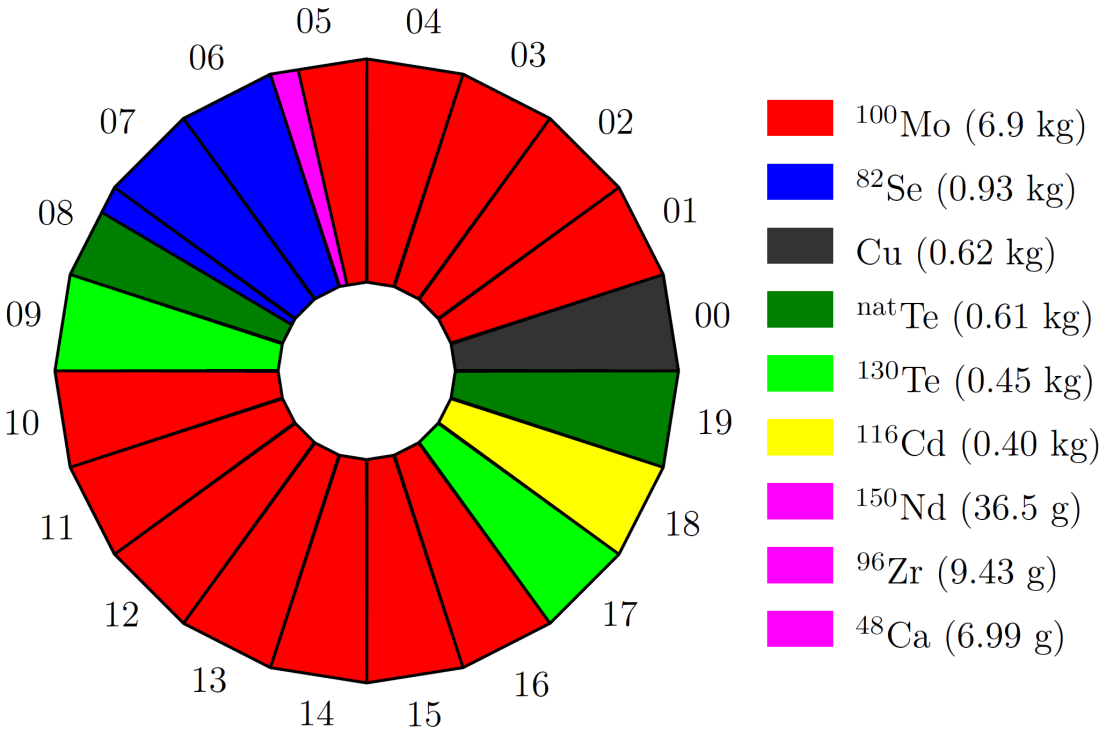

Figure 1.11: Composition of sectors containing measured isotopes in NEMO-3 experiment [70].

Decay	Q-value [keV]	$T^{2\nu}_{1/2}$ [yr]	Ref.
^{48}Ca $\rightarrow^{48}$ Ti	4267	$\left[6.4^{+0.7}_{-0.6}(stat)^{+1.2}_{-0.9}(syst)\right] \times 10^{19}$	[75]
^{82}Se $\rightarrow^{82}$ Kr	2996	$[(9.93 \pm 0.14(stat) \pm 0.72(syst)] \times 10^{19}$	[70]
^{96}Zr $\rightarrow^{96}$ Mo	3349	$[2.35 \pm 0.14(stat) \pm 0.16(syst)] \times 10^{19}$	[76]
^{100}Mo $\rightarrow^{100}$ Ru	3034	$[0.716 \pm 0.001(stat) \pm 0.054(syst)] \times 10^{19}$	[77]
^{100}Mo $\rightarrow^{100}$ Ru(0^+_1)	1905	$\left[5.7^{+1.3}_{-0.9}(stat) \pm 0.8(syst)\right] \times 10^{20}$	[78]
^{116}Cd $\rightarrow^{116}$ Sn	2813	$[2.74 \pm 0.04(stat) \pm 0.18(syst)] \times 10^{19}$	[79]
^{130}Te $\rightarrow^{130}$ Xe	2528	$[7.0 \pm 0.9(stat) \pm 1.1(syst)] \times 10^{20}$	[80]
^{150}Nd $\rightarrow^{150}$ Sm	3371	$\left[9.11^{+0.25}_{-0.22}(stat) \pm 0.63(syst)\right] \times 10^{18}$	[81]

Table 1.3: Values of half-lives of $2\nu\beta\beta$ nuclei measured by NEMO-3. Q-values are taken from National Nuclear Data Center website [44].

Chapter 2

SuperNEMO Experiment

SuperNEMO represents a new generation of $0\nu\beta\beta$ experiments. Taking advantage from experience with its predecessor, NEMO-3, its detection principle is based on the full reconstruction of two electron tracks coming from double beta-decay along with the measurement of their individual energies. The aim is to study $0\nu\beta\beta$ of ^{82}Se. Technology which allows to reconstruct the topology of double beta decay events is unique in the field. It improves the background rejection and measurement of otherwise unobservable quantities, for instance the angular distribution of the electrons. It might be a crucial step towards a new physics.

2.1 Laboratoire Souterrain de Modane

$0\nu\beta\beta$ experiments look for very rare events and it is important to protect them against cosmogenic radioactivity occuring on the Earth's surface. SuperNEMO experiment is, therefore, placed in Laboratoire Souterrain de Modane (LSM). LSM is underground laboratory and it is the deepest of its kind in Europe. It is placed in South-East of France on the border between France and Italy near Modane. LSM is located in Fréjus highway tunnel 1.7 km underground under the peak of mount Fréjus which represents 4800 m.w.e. The scheme of the tunnel and the mount Fréjus can be seen in Figure 2.1. As it is visible in the scheme, the laboratory is placed near the border, on the French side. Throughout the thesis, I follow

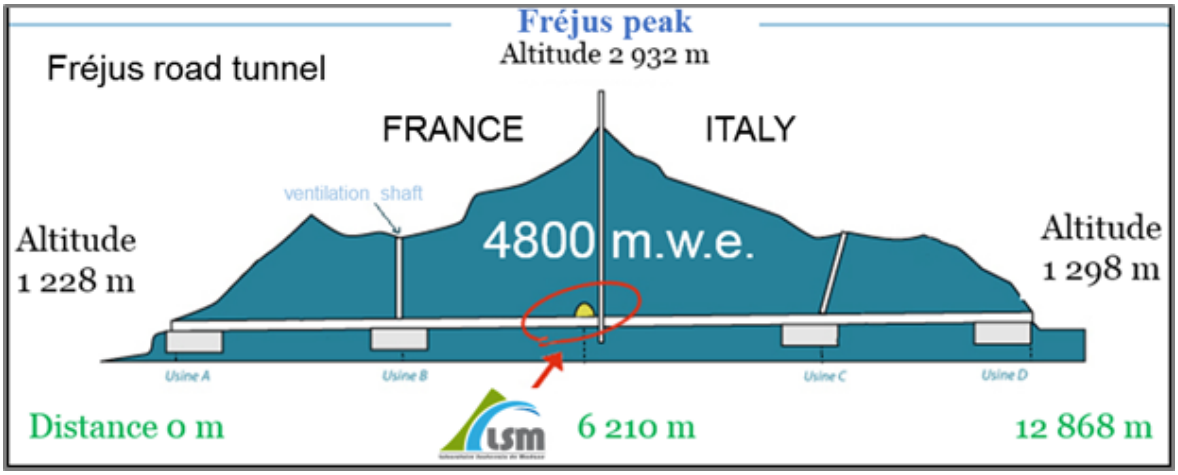

Figure 2.1: Scheme of mount Fréjus and the Fréjus highway tunnel. Laboratory LSM is placed roughly in the middle of the tunnel, right under the peak of the mountain.

naming convention normally used by collaboration. Parts of the detector are given adjectives based on the country they are closer to. Therefore, the terms like "Italian calorimeter" or "French calorimeter" designate the calorimeter wall on Italian side or French side, respectively. Same convention applies for tracker, as well as for other parts of the detector. The atmospheric muons are in the laboratory attenuated by a factor of million. Only 4-5 muons pass to the laboratory per day.

2.2 Description of the Detector

SuperNEMO takes advantage of so-called tracko-calo method of $0\nu\beta\beta$ detection. Standard methods of $0\nu\beta\beta$ detection use only the electron energy spectrum as a criterion of distinction between $0\nu\beta\beta$ and $2\nu\beta\beta$ or backgrounds. Experiment based on tracko-calo method has access to extra information via full topological reconstruction of events. Tracko-calo method combines three basic detection components (shown in Figure 2.2). Electrons from $\beta\beta$ source pass through tracking detector with high granularity, giving an information about the electron tracks. The electrons are subsequently detected in segmented calorimeters which are capable to provide single electron energy. The main advantage of this approach lies in the improved background rejection. Events from natural background have typically different topology and tracking allows to better reject such events. Information about electron tracks give possibility to study for example an angular distribution of $2\nu\beta\beta$. The detection system is separated from the source which allows to study various different isotopes without being fixed to one specific.

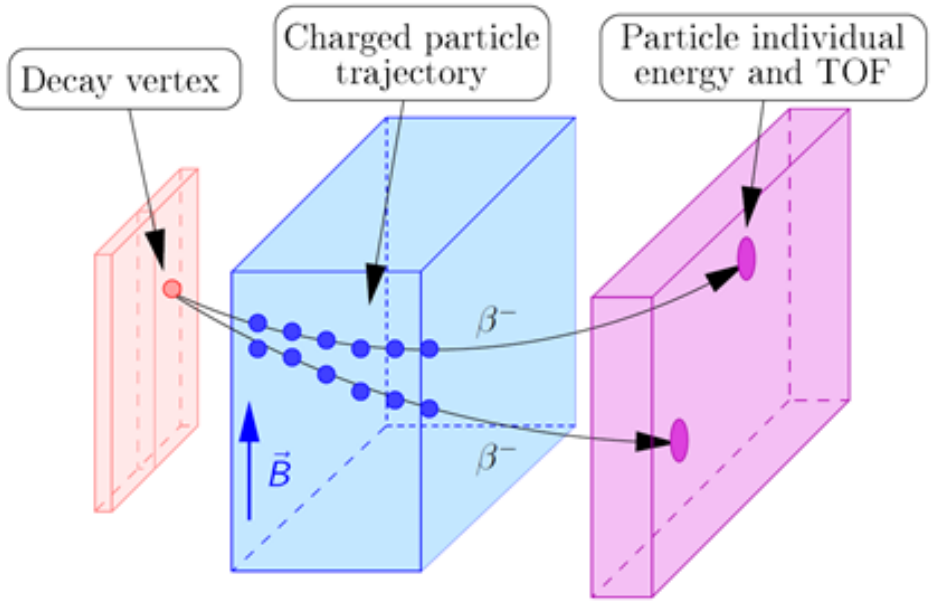

Figure 2.2: Simplified scheme of tracko-calo detection method. Pink block represents $\beta\beta$ source (emission of electrons), blue block stands for tracking detector (information about tracks) and the violet block on the right represents calorimeter (values of single electron energies).

Since 2005, large effort was invested into the research and development of SuperNEMO experiment. The main improvements in comparison to its predecessor NEMO-3, were achieved in the enrichment and radiopurity of ^{82}Se source foils, the energy resolution of calorimeters and the reduction of problematic Radon background.

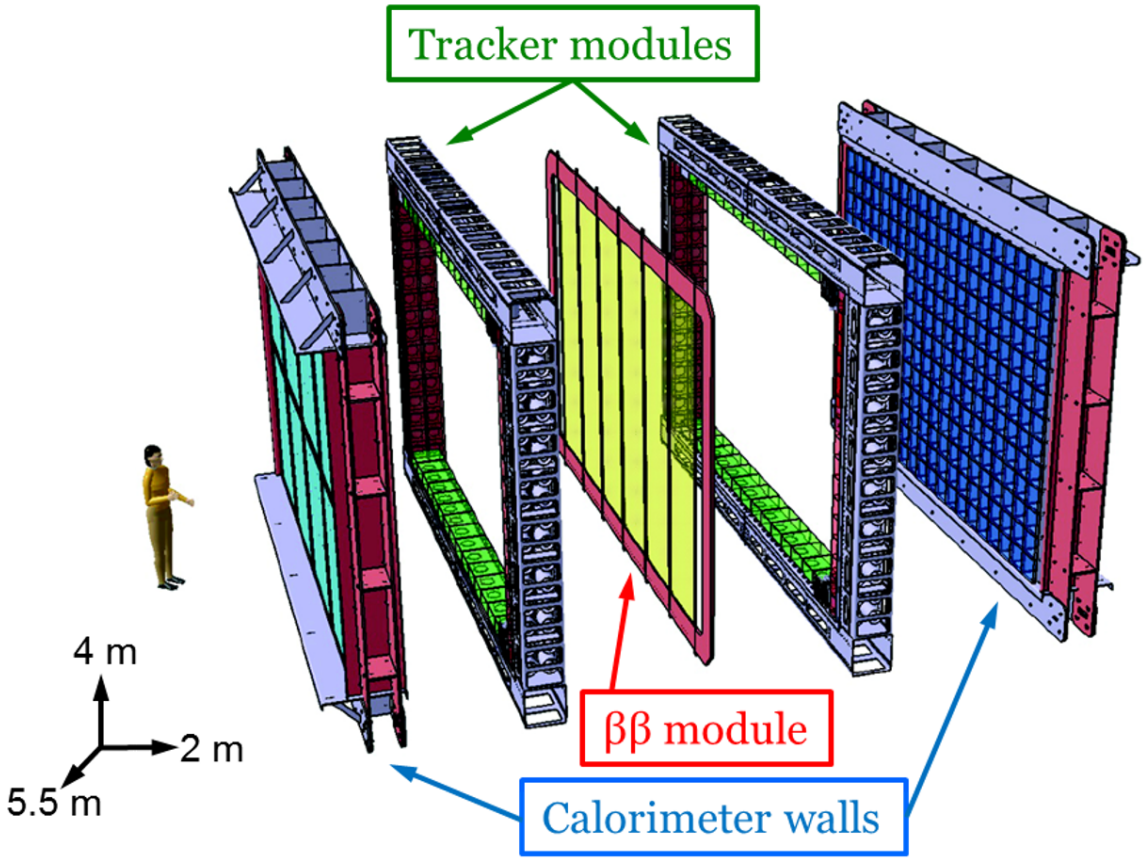

Figure 2.3: Schematic picture of one SuperNEMO module designed to study 7 kg of ^{82}Se in form of foils ($\beta\beta$ module).

SuperNEMO experiment aspires to reach sensitivity of 10^{26} years to half-life of $0\nu\beta\beta$ in ^{82}Se. The SuperNEMO is designed to measure 100 kg of ^{82}Se distributed among 20 modules [82, 83].

The first module, the demonstrator, will start phase of data taking in early 2019. The aim of demonstrator is to prove the detector concept and to fine tune all the systems. Demonstrator with roughly 6 kg of ^{82}Se should be able to reach sensitivity of 4.9×10^{24} years to half-life of $0\nu\beta\beta$ in ^{82}Se. A SuperNEMO module is composed of three main parts organized in a planar geometry. The source foil ($\beta\beta$ module) composed of enriched Selenium is in its center sandwiched by tracking detector. This is all encapsulated between scintillator blocks (Figure 2.3).

2.2.1 ^{82}Se Source Foils

$0\nu\beta\beta$ experiments observing isotopes such as ^{76}Ge, ^{130}Te, ^{134}Xe or ^{136}Xe typically take advantage of approach when the source isotope serves as the detector at the same time. SuperNEMO plays unique role in the field because its source is independent of detection system. Experiment of this type can measure various different isotopes. In NEMO-3, seven different isotopes (^{48}Ca, ^{82}Ca, ^{96}Zr, ^{100}Mo, ^{116}Cd, ^{130}Te and ^{150}Nd) were measured in parallel, although, the one with the most observed mass was ^{100}Mo. There are several important requirements to meet, in order to choose a $0\nu\beta\beta$ decay candidate. First of all, it is important to consider $Q_{\beta\beta}$ value of the decay of the isotope. Gamma radiation from natural background

can reach up to 2.615 MeV (^{208}Tl from ^{232}Th chain). The higher, the $Q_{\beta\beta}$ value is above this value, the better chance is to eliminate the background in the region of interest. Natural elements are usually composed of several different isotopes. High abundance of isotope of interest in the natural (or already enriched) sample increases the exposure and gives higher chances to observe $0\nu\beta\beta$. If the abundance is not sufficient in the composition of naturally occurring element of choice, the enrichment should take place. The efficiency and difficulty of enrichment technology differs from isotope to isotope. It is another factor to be considered. Large phase-space of $0\nu\beta\beta$ results into lower half-lives. When choosing the isotope, one should also take into account the phase-space factor of the isotope. Finally, it is also important to choose isotope with long half-lives of $2\nu\beta\beta$. $2\nu\beta\beta$ is the main, and what is the most important, irreducible, background for $0\nu\beta\beta$. Long half-lives of the process for the isotope of choice can increase the chances to observe $0\nu\beta\beta$.

Isotope ^{82}Se was chosen for SuperNEMO demonstrator thanks to its natural abundance and high value of $Q_{\beta\beta}$ (2996 keV). Approximately 7 kg of enriched isotope will be placed in demonstrator in form of the foil strips whose thickness will reach 40-55 mg/cm^2. The isotope is enriched by centrifugation method which can enrich natural Selenium up to 90% to 99% content of ^{82}Se. The method might be applied to ^{150}Nd with $Q_{\beta\beta}$ value of 3371 keV which would make ^{150}Nd an isotope of choice for future SuperNEMO modules.

^{82}Se has a form of powder after the enrichement. The powder is deposited on a very thin Mylar foil. The foils were prepared in ITEP (Institute for Theoretical and Experimental Physics) in Moscow and LAPP (Laboratoire d'Annecy-le-Vieux de Physique des Particules) in Annecy (Figure 2.4). The source foils are already installed in the LSM.

Figure 2.4: Left: Source foil prepared in ITEP in Russia. Right: Source foil prepared in LAPP in France.

2.2.2 Tracking Detector

Source foil is, from both sides, surrounded by tracking detector (tracker). The tracker is composed of 14 970 wires operating in Geiger mode. Research and development of the tracker took place at University of Manchester in Great Britain. The (Geiger) wires are made of steel with diameter of 40 μm to 50 μm. The wires were assembled at the Manchester University and sent to Mullard Space Science Laboratory (MSSL) of the University College London (UCL). There, they were assembled into form of 2034 cells with a help of robot (Figure 2.5). The tracker module is divided into four parts named C0, C1, C2 and C3. Each quarter was assembled in MSSL in a large clean tent. The tracker will be encapsulated in a radon-tight chamber filled with a gas. The gas will be composed of 94.85% of Helium, 4% of Ethanol 1% of Argon and 0.15% of water. The tracker is already installed in LSM.

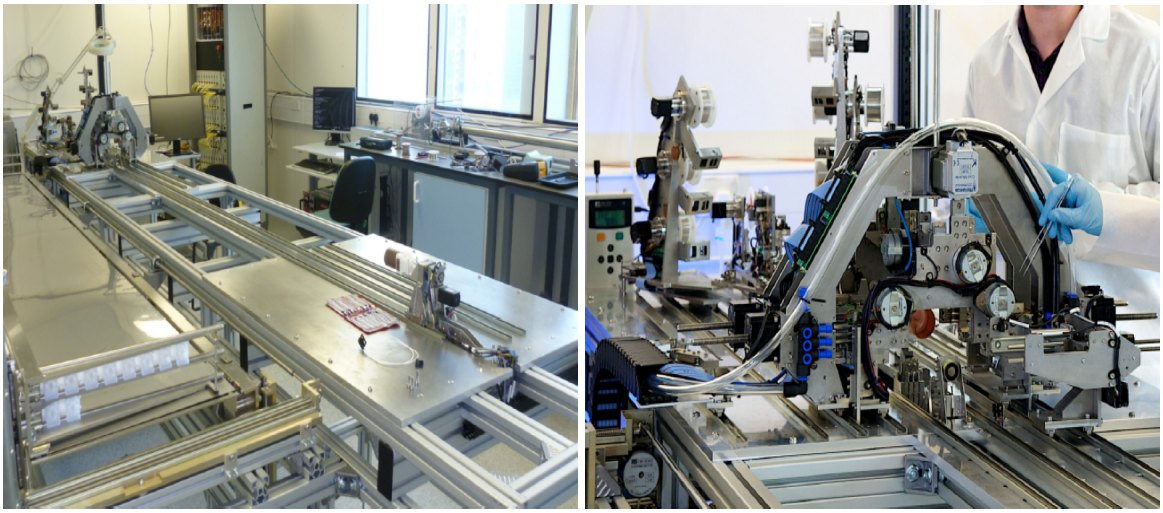

Figure 2.5: Photos of robot developed for the preparation of the tracker cells.

2.2.3 Calorimeters

The energy of the electrons emitted in double beta decay events is measured by calorimeter made of plastic scintillators. The calorimeter is composed of three main parts, the "main calorimeter (walls)", the "X-calo" (xcalo) and "gveto". The three parts surround the detector in all five sides except for the bottom as it can be seen in scheme in Figure 2.6. The scheme is for simplicity missing one main calorimeter wall and one xcalo wall. In the figure also the definition of coordinate system is shown. The definition is strictly followed throughout the whole thesis. Basic calorimeter unit is so-called optical module. The main parts of the optical module are plastic scintillator (in our case polystyrene) and PMT which is glued to the plastic scintillator for tight connection. Xcalo walls are placed at the smaller, vertical, sides of the tracker. The calorimeters were directly connected to the tracker, its production was, therefore, done at UCL in Great Britain. Xcalo consists of 128 optical modules, each with resolution of roughly 12% at 1 MeV. Gveto, on top of the module, is composed of 64 optical modules with resolution of 15% at 1 MeV. Both xcalo and gveto are using 5" PMTs reused from NEMO-3. Finally, the main calorimeter, covers the detector from both sides parallel to source foil. It consists of two main walls composed of 520 optical modules. One wall is on the Italian side while the opposite one on French side. Their assembly took place in CENBG (Centre Etudes Nucléaires de Bordeaux Gradignan). Plastic scintillator in

optical module is based on the polystyrene. 0.6% of para-terphenyl (pTP) and 0.05% of 1,4-bis(5-phenyloxazol-2-yl) benzene (POPOP) fluorescent additives are serving as wavelenght shifters for better detection efficiency. The optimization of content of pTP and POPOP with respect to the energy resolution was achieved in IEAP CTU (Institute of Experimental and Applied Physics Czech Technical University) in Prague. In [84] it was shown that PS blocks with 1.5% of pTP and 0.05% of POPOP can reach better energy resolution. The production process was switched to these enhanced PS blocks after the study was done. The production process of main calorimeter walls is presented in Section 2.3. PMTs used to build main calorimetric walls are 8" in diameter with resolution of 8% at 1 MeV.

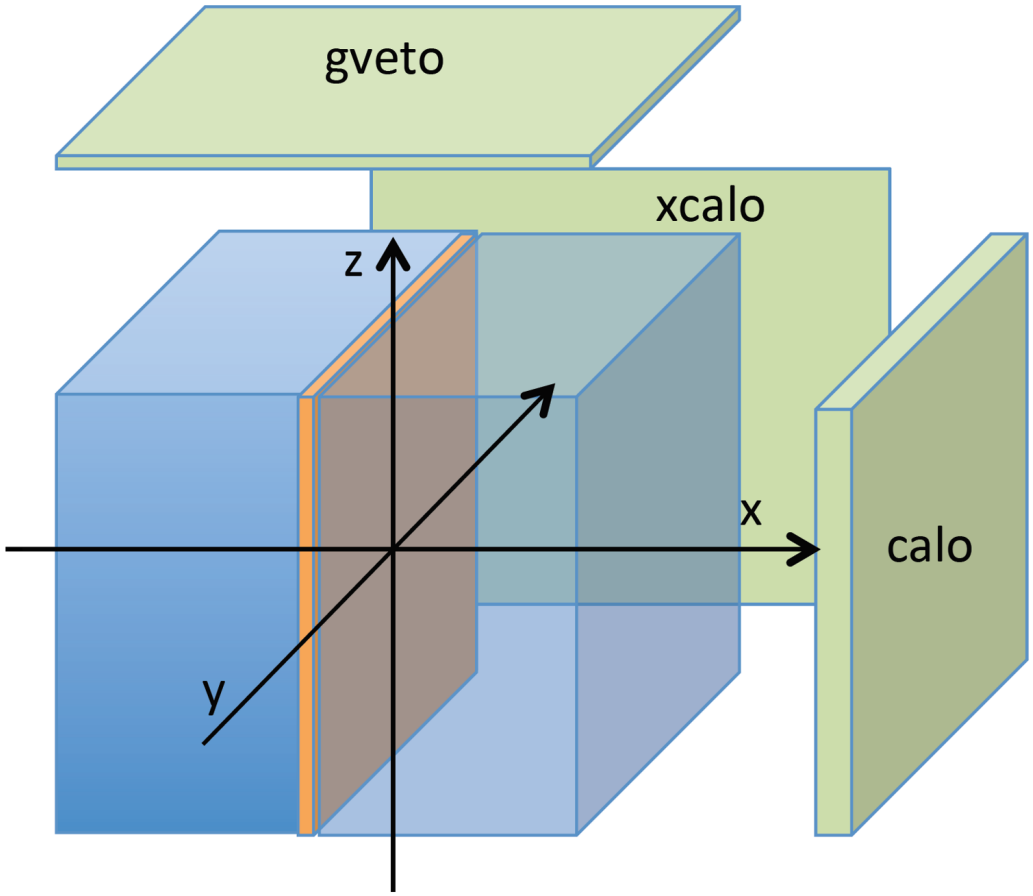

Figure 2.6: The scheme of SuperNEMO calorimetric walls. Except for main walls ("calo") SuperNEMO module will be composed of x-calo walls ("xcalo") on the short side and g-veto on top ("gveto"). The picture also shows standard definition of coordinates, used for example for simulation purposes, where y and z direction are defining the plane of source foil and x is perpendicular.

2.2.4 Status of the Demonstrator

The goal of the demonstrator is to achieve sensitivity of $0\nu\beta\beta$ half-life at the level of 6×10^{24} yr, which is equal to upper neutrino mass limit of 0.2 - 0.4 eV. Furthermore, in full design (20 modules) with more than 100 kg of ^{82}Se, the limit on $0\nu\beta\beta$ half-life is expected at the level of 10^{26} yr, yielding the upper limit on neutrino mass on the level of 0.04 - 0.11 eV.

Currently, the works on construction of demonstrator parts (source foil, tracker and calorimeters) are finished and they are all already present in LSM. The cabling works are in progress and should be finished at the beginning of 2019. Automatic calibration source deployment system (see also Chapter 3) was already installed. The SuperNEMO should obtain first data in 2019. In parallel, the works on shielding design are taking place.

2.3 Construction of Main Calorimeter Walls

Assembly of the optical modules for main calorimeter walls was performed in CENBG and finished in summer 2016. In autumn 2016, the main calorimeter walls were already built at the LSM. During my first stay in CENBG in first half of 2016, I took part in the assembly of optical modules. Let me briefly present the procedure in following sections.

2.3.1 Optical Module Production Procedure

The basic constituent of each optical module is a polystyrene block of 10 kg produced in company NUVIA (former ENVINET) in Kralupy nad Vltavou near Prague, Czech Republic. As waveshifters, para-terphenyl (pTP) and 1,4-bis(5-phenyloxazol-2-yl) benzene (POPOP) fluorescent additives were mixed into polystyrene (PS) in the process of production. These blocks were shipped to CENBG (near Bordeaux, France) and their production of optical modules was finalized there along with tests of the performance.

One finalized optical module consists of two main parts: aforementioned PS block and 8" (or 5", for xcalo and gveto) PMT glued to the block (Figure 2.7).

In order to avoid impurities in the preparation process, whole production was placed in a clean room. At the beginning, the polystyrene modules were cleaned with acetone, isopropanol and distilled water. After drying, the dimensions of the PS block were measured

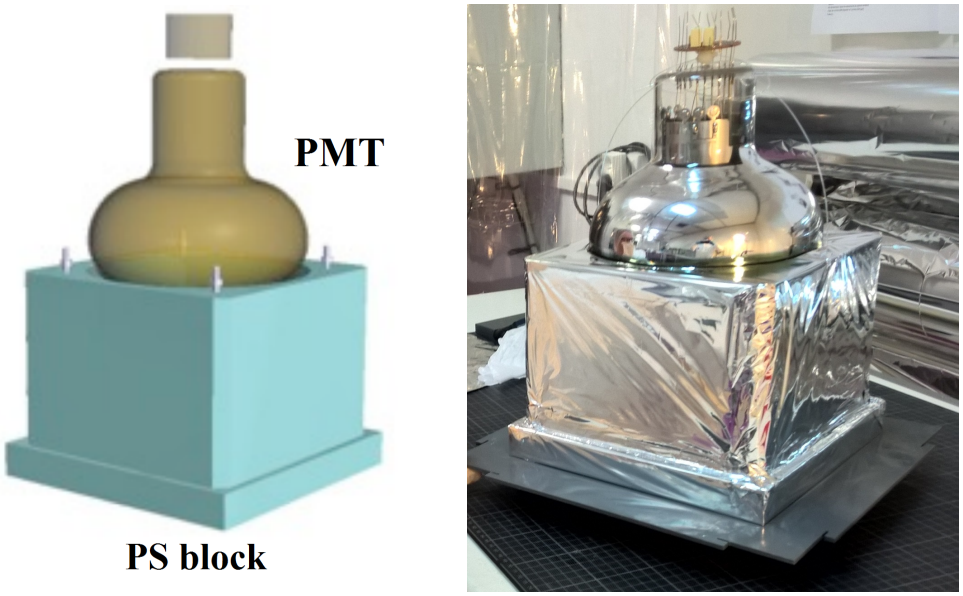

(a) (b)

Figure 2.7: (a): Simplified layout of optical module consisting of polystyrene block and photomultiplier tube. (b): Real optical module after wrapping into Teflon and Mylar is finished.

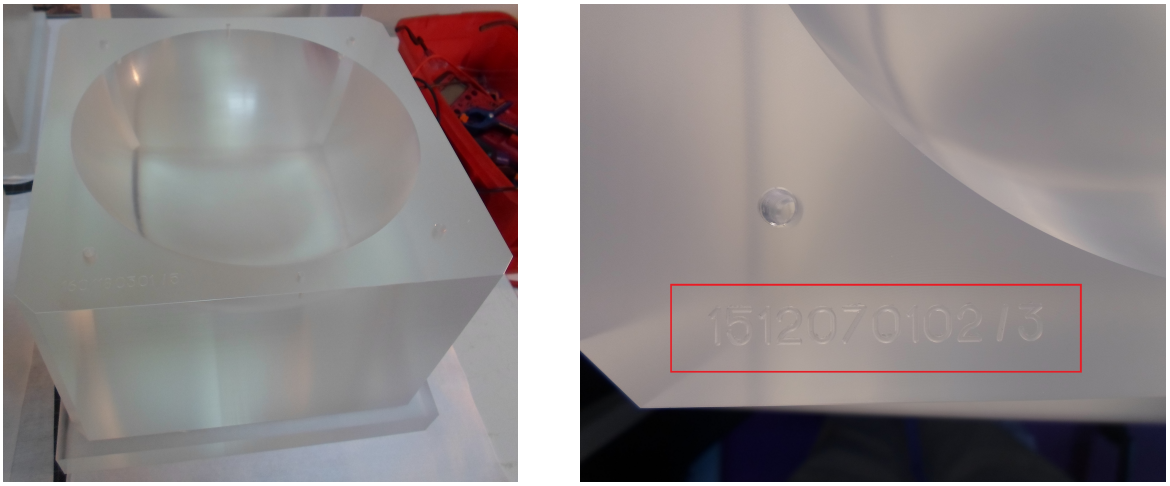

(a) (b)

Figure 2.8: (a): Picture of real PS block produced by NUVIA. (b): Production number placed on top of each block.

and visually checked for impurities in polystyrene. Each block was labelled on top by production number (Figure 2.8b). In next step, optical fibres were glued on top (Figure 2.9a). The fibres serve for LED calibration of optical modules.

Subsequently, Hamamatsu PMT was glued on top into the spherical cut-out in the block (Figure 2.9b). The drying process took 24 hours. The glue used for this step was chosen with regard to its radiopurity (same applies to all materials used in construction of SuperNEMO demonstrator) and its refractive index close to the refractive indices of PS block and PMT. Two different types of PMTs are used in the SuperNEMO demonstrator. For main walls 8" Hamamatsu PMTs were employed while for xcalo and gveto it was 5" PMTs previously used in NEMO-3 experiment. After the PMT was in the place, the optical module was wrapped into three layers of teflon tape (0.6 mm of total thickness) from sides (Figure 2.9c) and two layers of mylar foil (total thickness 12 μm) from botom and from sides (Figure 2.9d). This procedure was done in order to improve the light yield of the optical module. Thanks to wrapping, the photons were confined inside the module and guided to PMT more effectively. Moreover, it prevented outside photons to enter the optical module. In the process, electronics responsible for data collection from PMT was soldered on top.

2.3.2 Optical Module Resolution Test and Finalization

The modules which went through all previous procedure steps were subsequently tested for their resolution with ^{90}Sr source [85]. Electrons from ^{90}Sr were bent towards the collimator by electromagnet and 1 MeV electrons were chosen. These electrons impacted into the optical module from the bottom and spectrum was obtained. Whole testing process took place in light-tight box to prevent unwanted light to be registered. The value of resolution of each module was obtained. Histogram showing the resolution of all optical modules with 8" PMTs can be seen in Figure 2.10. After the resolution measurement, eight optical modules were grouped on the preparation table in two rows of four modules. Very high radiopurity glue was applied on top of each. A metallic shielding protecting optical modules from magnetic field was placed on top in a way that only bottom faces of each optical module was sticking out (Figures 2.9e and 2.9f). The connection between modules was strengthened by 32 plastic screws. Such optical brick was then packed in the box and shipped to LSM.

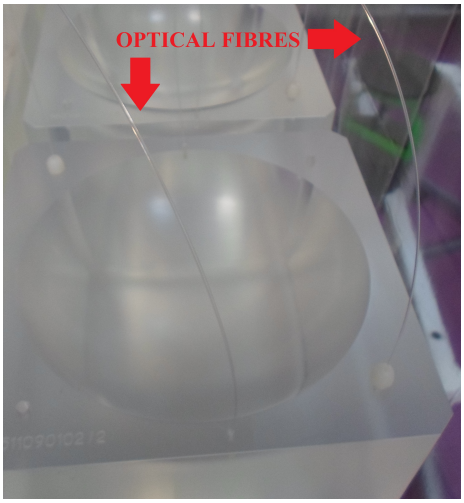

(a) Gluing of optical fibres.

(b) PMT gluing.

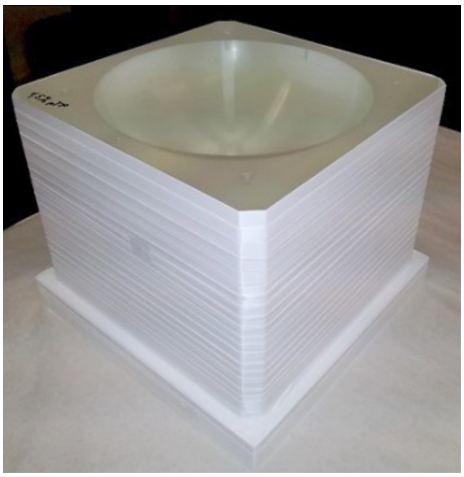

(c) Teflon wrapping.

(d) Mylar wrapping.

(e) Encapsulation of eight optical modules into the shielding.

(f) Final brick prepared to be packed, shipped and assembled.

Figure 2.9: Different steps of optical module preparation process. Note that in steps c) and d) PMT is missing on top. These optical modules were used for testing and PMT was glued to them after they were wrapped in Teflon and Mylar.

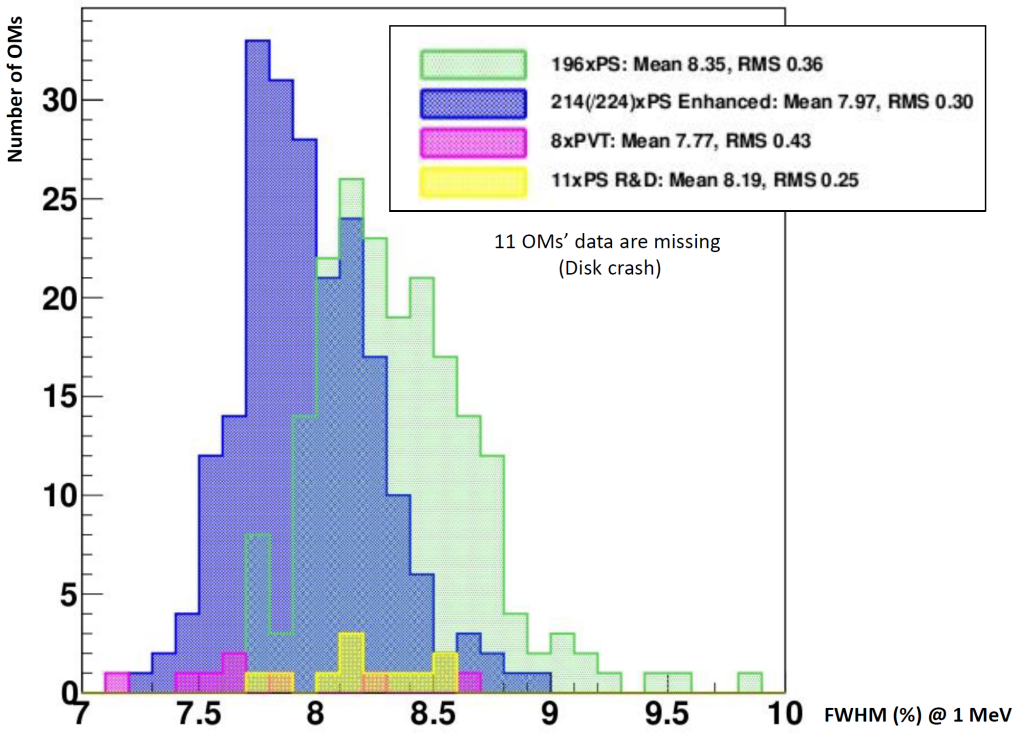

Figure 2.10: Histogram of resolution of optical modules with 8" PMTs used in the main wall of SuperNEMO demonstrator (data about eleven of them are missing due to disc crash). Modules of standard quality (PS - green) were produced before the composition of pTP and POPOP was optimized [84]. Enhanced optical modules (PS Enhanced - blue) are produced after the mentioned optimization. Eight modules (PVT - pink) were participating in process of research on composition of pTP and POPOP and their composition differs slightly. Eleven optical modules (PS R&D - yellow) were used to develop the optical module preparation procedure.

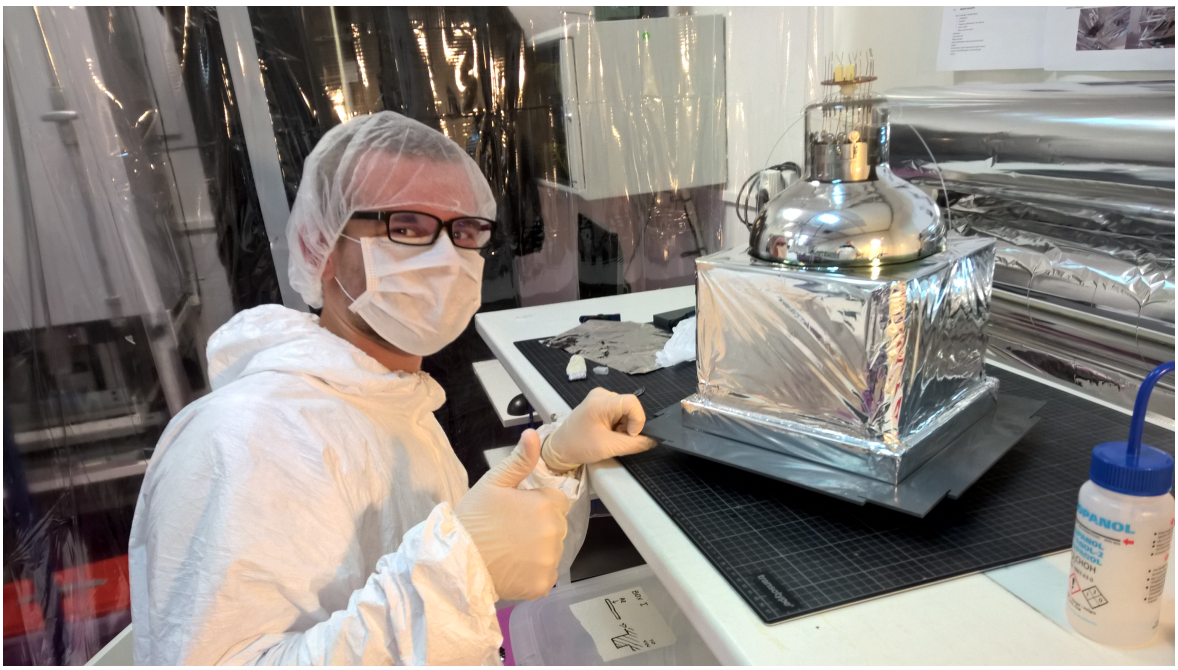

Figure 2.11: Me, in clean room in CENBG, with my first completed optical module.

Chapter 3

Measurements of ^{207}Bi Calibration Sources

In order to calibrate NEMO-3 calorimeters, ^{207}Bi sources were employed. The same strategy was chosen for SuperNEMO experiment. However, experience with NEMO-3 have shown that insufficient knowledge of calibration source properties can give rise to large experimental uncertainties on the half-life of $2\nu\beta\beta$ as well as lower the sensitivity for half-life of $0\nu\beta\beta$. These effects can be removed by precise investigation of calibration sources. In this chapter I will describe in detail all the necessary measurements which I performed in order to better quantify calibration sources.

3.1 SuperNEMO Calibration System

^{207}Bi is a complex emitter. It undergoes electron capture with subsequent emission of gamma quanta. Electron from internal conversion, accompanied by X-ray can be emitted instead of the gamma. Simplified scheme of the most common decay cascades of ^{207}Bi is depicted in Figure 3.1.

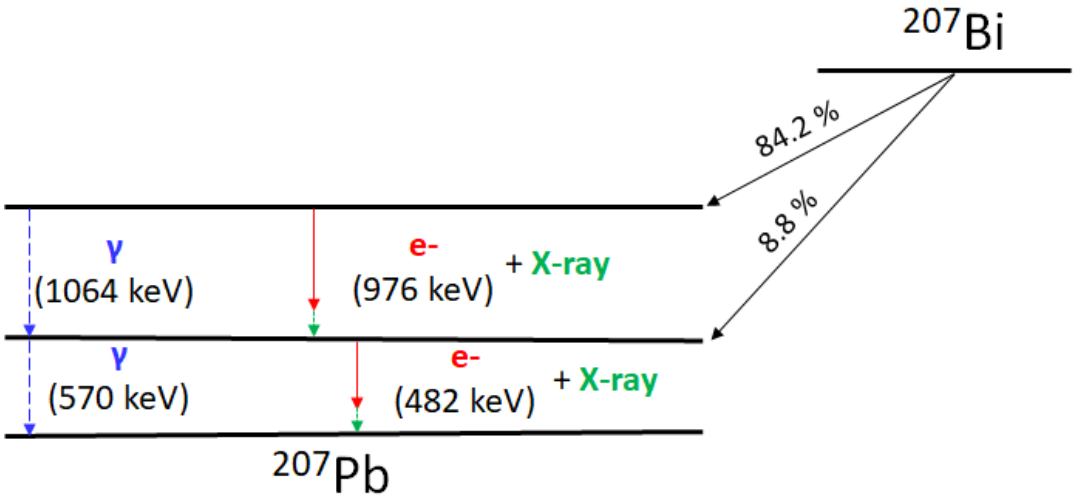

Figure 3.1: Simplified decay scheme of ^{207}Bi. The isotope decays by electron capture and can produce gamma rays as well as electrons or X-rays. The scheme contains only the most common decay cascades.

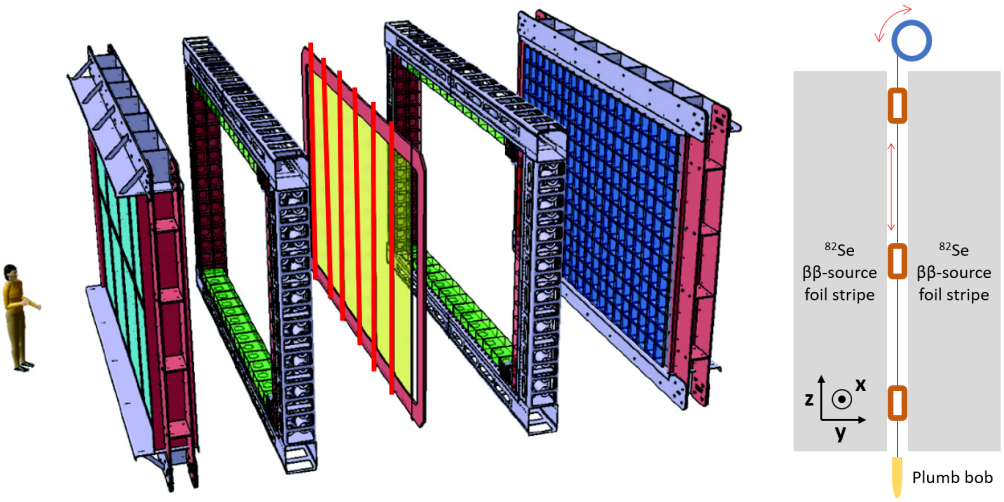

Figure 3.2: Left: Red vertical lines symbolize six gaps between $\beta\beta$ source foil strips where automatic deployment system deploys the calibration sources. Right: Simplified scheme of ^{207}Bi deployment system. In the gap between ^{82}Se $\beta\beta$ source foil the sources (brown rectangles) can be vertically (red arrows) deployed by automatic system. Deployment will be controlled by stepping motor connected to wheel on top (blue colour) which is able to wrap the steel wire. Plumb bob has a role of load keeping the wire straight. It is marked by light orange colour at the bottom. Note that the scheme is only symbolic, the number of sources is incorrect and the dimensions in the figure are not to scale.

Electrons from the ^{207}Bi are useful for energy calibration of the calorimeter optical modules. These electrons can be also useful in order to experimentally test the precision of reconstruction of the electron tracks. I profited from the X-rays and gammas coming from this emitter in the measurements.

Before opening the discussion about the measurements of sources, let me briefly describe SuperNEMO calibration system. Calibration of a SuperNEMO module is a process which will take place several times per month. For this purpose, the calibration sources have to be placed and removed regularly from well defined positions inside the module. However, during the operation a SuperNEMO module should be sealed, preventing any leak of the atmosphere which is inside of the tracker. This limits the access inside, which makes manual operation of calibration system impossible. Therefore, SuperNEMO calibration will be performed by automatic deployment developed by group from University of Texas at Austin [86].

3.1.1 Automatic Calibration Source Deployment System

Between some of the adjacent pairs of ^{82}Se $\beta\beta$ source foil stripes there is a narrow gap (Figure 3.2 - Left) designed for the insertion of ^{207}Bi calibration sources. The automatic calibration source deployment system consists of six Copper plumb bobs suspended by steel wires from SuperNEMO source frame. Each wire will be wrapped on a wheel on top of the SuperNEMO module. Wheel can be rotated by a stepper motor. Between the plumb bob on the bottom and wheel on top, seven calibration sources will be attached to steel wire. Stepping motor is able to vertically adjust the position of the sources or to remove them completely from the SuperNEMO module. Symbolic scheme of the deployment system can be found in Figure 3.2 - Right.

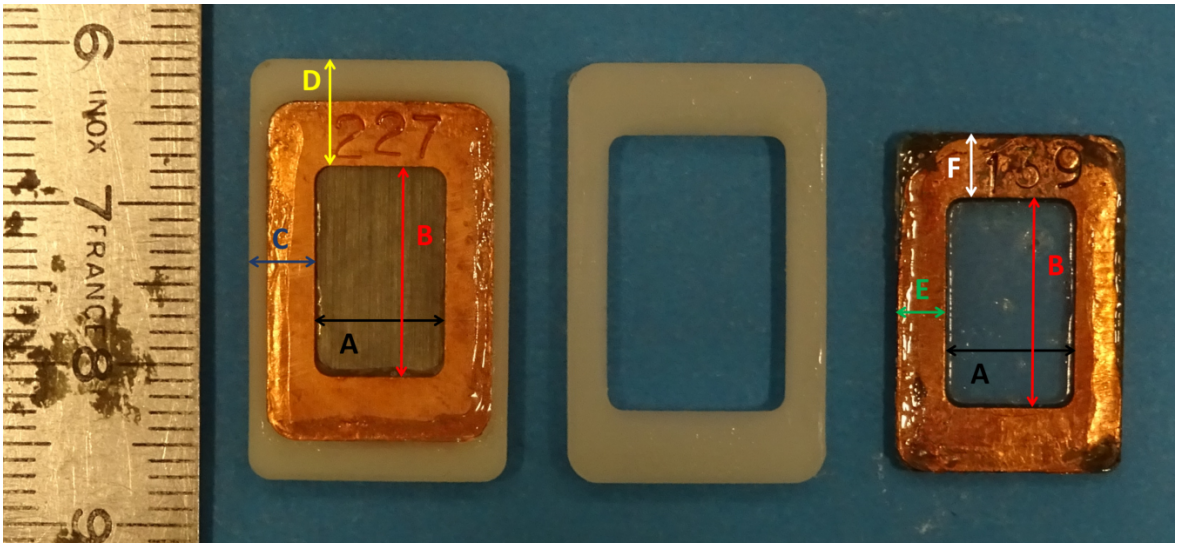

Figure 3.3: Photo of the SuperNEMO calibration sources. The source on the right is what I call "without plastic envelope" and the one on the left, next to the ruler is source which I will call "with plastic envelope" because the white plastic frame (in the middle of the photo) was glued to them. Dimensions defined in the photo are listed in Table 3.1.

	A [mm]	B [mm]	C [mm]
Pixel counting	8.2	13.11	4.14
Direct measurement (calliper)	7.91	12.99	4.15
	D [mm]	E [mm]	F [mm]
Pixel counting	6.61	3.12	3.98
Direct measurement (calliper)	6.66	3.2	4.01

Table 3.1: Source dimensions A, B, C, D, E and F defined in Figure 3.3 measured by pixel counting and direct measurement with calliper.

3.1.2 Description of Calibration Sources

SuperNEMO calibration sources have a rectangular shape (Figure 3.3). A source has a form of ^{207}Bi dropled deposited between two transparent mylar foils and sealed by radiopure Copper frame. Example of such source is on the right side of Figure 3.3. Sources in these form will be used in SuperNEMO calibration for the automatic deployment system.

SuperNEMO will exploit the same ^{207}Bi calibration sources used in NEMO-3, but without the plastic envelope (see Figure 3.3). At the time of this study, not all the sources have been modified. The distinction between two types of sources is crucial in my analyses and, therefore, I always explicitly refer to them as to sources "with" or "without" plastic envelope.

Dimensions of the sources were measured by two different methods to constrain the systematics. First method which I performed myself was indirect. I took photos of source of choice with a ruler. The ruler gave a scale. Number of pixels per centimeter counted thanks to the ruler in the photo served as scaling coefficient. Then I counted number of pixels representing individual dimensions introduced in Figure 3.3. Using the scale coefficient I represented these dimensions in cm. As one can imagine, such a methodology is dependent on the perspective distortion introduced when taking the photo. Even though, I took the picture perpendicularly to the plane of the source and assumed the distortions to be negligible, it is still non-trivial to satisfactorily quantify them. Therefore, I asked my colleague Ramon

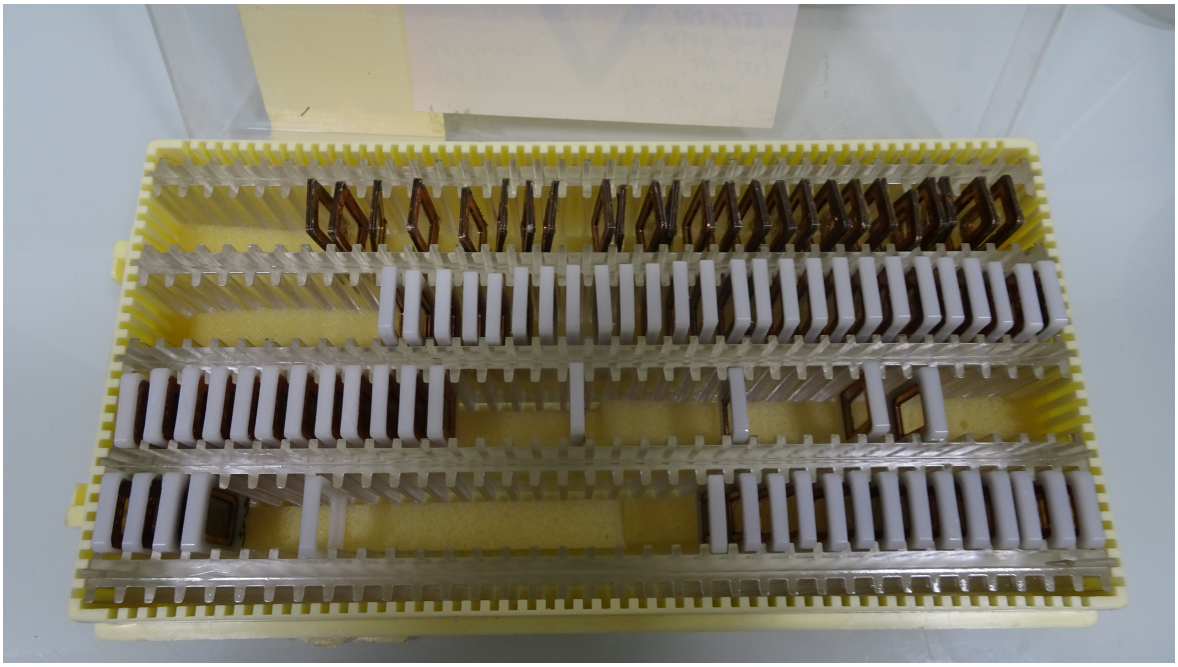

Figure 3.4: Case with all available ^{207}Bi calibration sources.

Salazar to perform direct measurement using calliper. Both methods are within reasonable difference consistent with each other. Measured values can be found in Tables 3.1.

3.2 Mapping of ^{207}Bi Deposition Distribution in Calibration Sources

SuperNEMO calibration sources consist of droplet of ^{207}Bi deposited between two layers of transparent mylar foil. In Figure 3.3 (on the right) one can see an example of such source. The mylar in the center is sealed from both sides by radiopure Copper frame. In the ideal case, the droplet is well centered within the Copper frame and electrons emitted from ^{207}Bi loose almost no energy when exiting the source via mylar foil. However, if the droplet was smeared in the proces of encapsulation of mylar by two Copper frames, it is possible to find source liquid between two Copper layers on the edge of the source. Electrons which decayed in the region of such leak would have to pass Copper frame to exit from source, loosing non-negligible amount of energy in the process. These electrons would not have the expected energy and might contribute to imprecisions in energy calibration. In order to quantify the quality of the source, it is, thus, important to measure its deposition distribution.

Moreover, the deposition distribution maps for each sample of calibration source can be used as an input for Monte Carlo simulation to improve quality of calibration. Between September 2017 and January 2018, I performed complete deposition distribution study of 49 ^{207}Bi calibration sources. The section is dedicated to the description of methodology, data analysis and results of this study.

3.2.1 Timepix Pixel Detectors

Pixel semiconductor detectors are employed in a broad range of imaging applications. One of its biggest advantages lies in the design. Each pixel contains separate electronics

Figure 3.5: Photos of the Timpepix pixel detectors used in the study. From left: H04-W0163 (300 μm Silicon sensor), H11-W0163 (300 μm Silicon sensor) and L05-W0163 (1 mm Silicon sensor). The chip is located in the top part of the detector, lower, blue part is USB interface developed in IEAP CTU in Prague [88].

with digital counter which allows each particle to be processed separately. One pixel is composed of semiconductor diode with reverse bias voltage applied to both ends. The voltage causes the depletion zone between two semiconductors in the diode to become wider. When particle passes through the depletion zone, charge is created by electric field, collected at the contacts and afterwards processed by the read-out electronics. More information about semiconductor pixel detectors and their applications can be found in [87].

Timepix pixel detectors which I used in the study belong to category of so called hybrid pixel device. Hybrid pixel detector consist of two chips. Fist chip is the sensor which is composed of semiconductor diode with one common and one pixelated contact. Second chip contains read-out electronics for all pixels. Their advantage to the monolithic pixel detectors (with one chip) is that their sensor can be made of range of materials (e.g. Si, GaAs, CdTe, etc.) while monolithic are limited uniquely to Silicon. However, in the study, I used three Timepix detectors with Silicon chip. Their photos can be seen in the Figure 3.5. The chip thickness of first two detectors (H04-W0163 and H11-W0163) was 300 μm while the last one (L05-W0163) had chip of 1 mm thickness. All three consisted of 65536 pixels aligned in 256$\times$256 square matrix. Size of one pixel is 55$\times$ 55 μm^2. Full chip covers the area of 1.4$\times$1.4 cm^2.

3.2.2 Detector Energy Calibrations

Timepix detector family is a successor of Medipix detector family developed by Medipix collaboration [89, 90]. Medipix detectors were used as a counting detectors capable of counting particles in individual pixels. The essential upgrade which Timepix detector family received was a clock counting in each pixel. Each pixel in Timepix detector can be configured to operate in one of three following modes: Medipix mode, Timepix mode and Time over threshold (ToT) mode. In Medipix mode, as the name suggest, the particle numbers are counted in each pixel without any extra information about particle. Timepix mode allows to study the coincidences of the impacting particles, as it is capable of measuring time of arrival of the particle. In ToT mode, Timepix detector is able to provide information about the

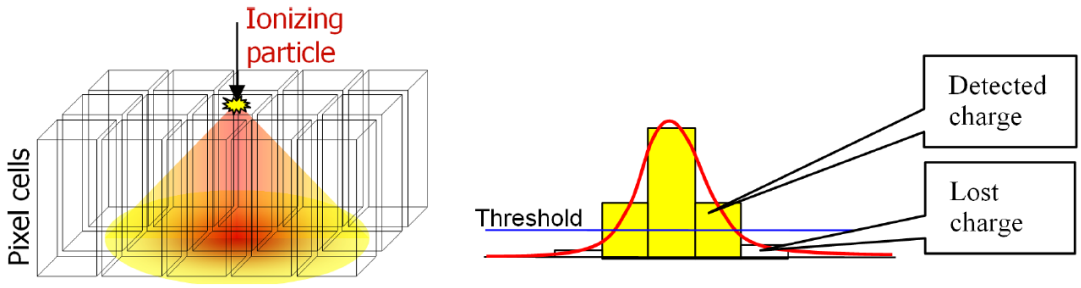

Figure 3.6: Scheme of charge sharing effect in pixel detector. Picture taken from [87]. Left: Charge cloud created by ionizing particle is expanding into adjacent pixels due to electromagnetic repulsion and diffusion. Right: Plot of charge distribution detected by central pixel (peak in the middle) and adjacent pixels (tails) due to charge sharing effect. If charge in adjacent pixels is lower than threshold in the pixel the charge is lost and energy of the particle is underestimated.

energy left by the particle in individual pixels. A limitation for this type of detector is caused by effect called charge-sharing. In the case when pixels are small and/or sensor is thick, the collected charge cloud created in one pixel expands due to charge repulsion and diffusion and can be collected by adjacent pixels (Figure 3.6 - Left). In the adjacent pixels the tail of the charge might not exceed the threshold value and therefore it becomes lost (Figure 3.6 - Right). In consequence, collected charge is often lower than its original value which affects the energy resolution. In ToT mode, energy is not obtained by direct measurement and calibration is needed. The principle of measurement in the ToT mode is as following: clock in the pixel measures the period during which charge signal caused by impacting particle exceeded pre-set threshold in the pixel. This quantity is called Time over Threshold (ToT). There is a relation between energy deposited in the pixel and ToT which was measured and modelled by a function given by Equation 3.1.

$$ToT(E) = aE + b - \frac{c}{E - t}. \tag{3.1}$$

The equation represents Time over Threshold as a function of the energy deposited in the pixel by incident particle. a, b, c and t are the parameters of the function. While t represents an energy threshold in the pixel, a and b define the linear part of the curve valid as a good approximation for majority of the energy range. The function is depicted in the Figure 3.7.

Due to a complexity of the sensor, it is natural to expect different response in different pixels. Therefore, energy calibration has to be performed separately for each pixel. In the process of energy calibration, detector is exposed to X-ray fluorescent radiation taking only clusters[1] of one pixel size into the account. Current leaked into the adjacent pixels due to the charge sharing effects can be estimated based on the simulations and corrected. More information about the calibration and charge sharing effect can be found in [91, 92, 93].

Before I could perform the measurements I needed to calibrate each one of the three detectors. As it was already mentioned, energy calibration has to be done for each pixel individually. In practice, this means to find set of parameters a, b, c and t in Equation 3.1, for each pixel separately. This can be really time consuming process taking into account a fact that we need to provide enough statistics for calibration to each one of the 65536 pixels

[1]Cluster is a group of adjacent pixels representing one particle which deposited energy in each pixel. Size of a cluster is given by number of pixels included in the cluster.

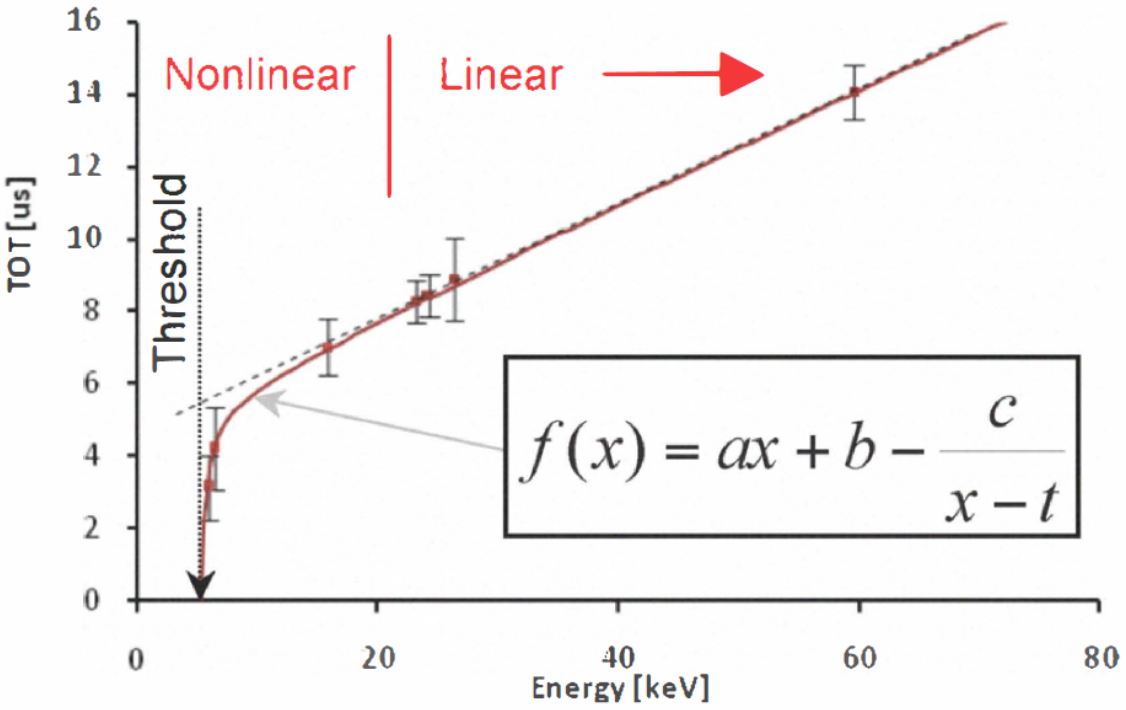

Figure 3.7: Relation between time over threshold and energy used for energy calibration of pixel detectors. Source of image: [91].

in order to make fitting possible.

As a first step before the calibration itself, I had to find appropriate value of biasing voltage for each detector. Biasing voltage (bias) is increasing the size of a depletion zone in the pixel (diode) improving the detection sensitivity of the pixel. After it reaches maximum, it saturates. I irradiated the chip with X-ray fluorescent radiation and measured rates while I was changing the bias of the detector supplied by voltage source. At the saturation point, I obtained value of the bias which I used for all the process of calibration and measurements. For 300 μm thick Timepix detectors H04-W0163 and H11-W0163 I obtained bias value of 90 V and 100 V, respectively. It is provided by the USB interface in the Figure 3.5 [88]. However, for 1 mm detector, one needs extra voltage supply capable to deliver bias of 460 V (L05-W0163).

After setting the biases one needs to do so-called "threshold equalization". In Timepix detector, the pixels are designed to be identical to one another. However, in reality the differences occur. In threshold equalization, the global threshold value is fine tuned for each pixel in a way that the dispersion is as small as possible. Pixelman [94], a software interface for Timepix detectors, provides simple plugin which performs threshold equalization. It also gives possibility to mask noisy (faulty) pixels. After the equalization is finished, it is important to save and use always the same configuration in calibration and measurements.

Detectors are in this point prepared for calibration. As I mentioned above, X-ray fluorescent radiation was employed. I used three different fluorescent foils irradiated by Amptek Mini-X X-ray lamp. During the calibration, X-ray lamp was irradiating fluorescent foil (Fe, Cu or Cd) initiating X-ray fluorescence in the target foil. The energy of the X-rays coming from the foils have sharp values (Fe: 6.398 keV, Cu: 8.04 keV, Cd: 23.106 keV), therefore, such foils are suitable for calibration of the detector. The photo of calibration setup can be found in Figure 3.8. The output from the calibration measurements is a set of files contain-

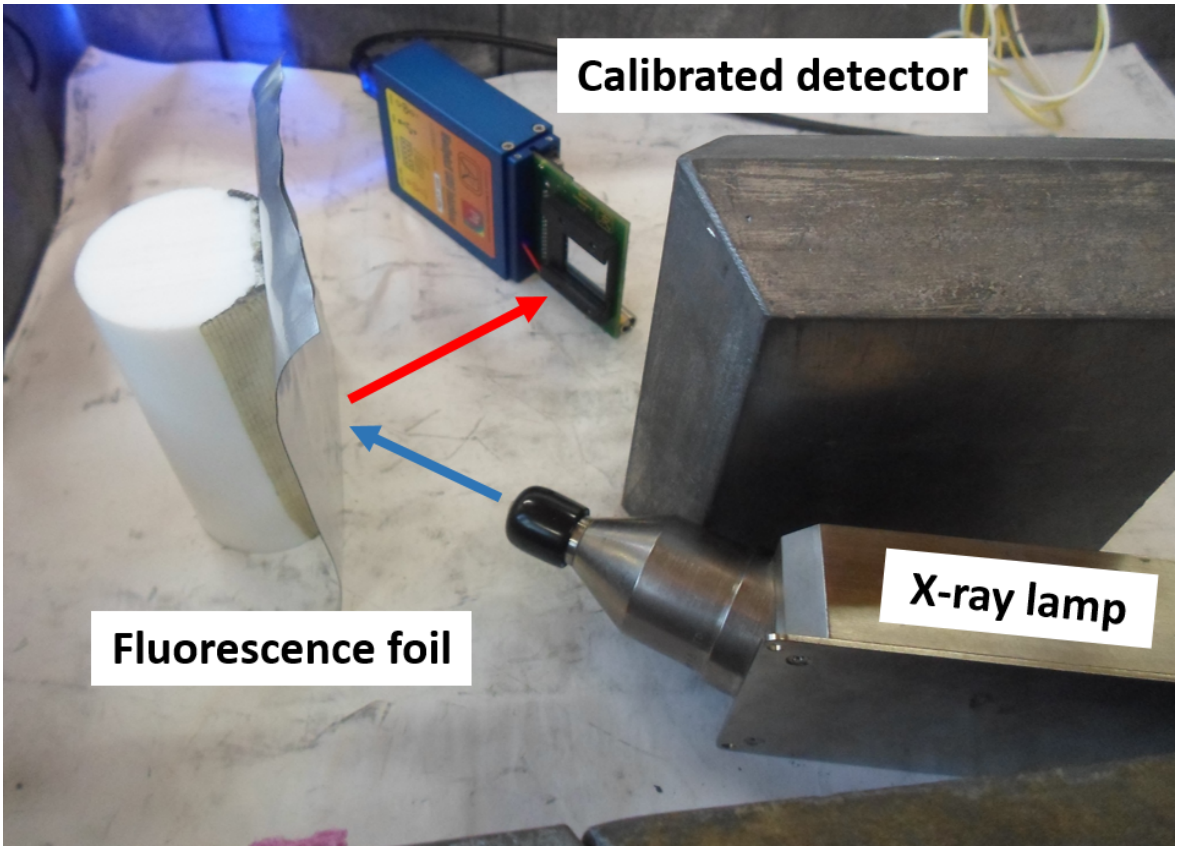

Figure 3.8: Photo of Timepix detector calibration setup. The X-ray lamp irradiates Fluorescent foil with spectrum of X-ray radiation (blue arrow). Atoms in the foil are excited and subsequently deexcited by X-rays of unique energy (red arrow). These rays impact the detector and provide the calibration.

ing spectra in terms of ADC channels (time over threshold) for each individual pixel. Each spectrum is fitted and the peak value is assigned to be the ToT value representing energy of fluorescence X-rays. Such a couple of values represent a point on the calibration curve from Figure 3.7. Each fluorescence foil dataset yields one such point for each pixel. As a last step, the points are fitted by function given by Equation 3.1, giving parameters a, b, c and t. Each quadruplet of the parameters is unique for individual pixel. Therefore, resulting calibration files are four 256×256 matrices containing calibration parameters a, b, c and t.

In the Figures 3.9 and 3.10 one can find global spectra (i.e. all pixels combined) from all three used detectors before and after calibration. The calibration tests were performed using the same fluorescence foils as during the calibration (i.e. Fe, Cu and Cd) and one extra foil made of Zr (15.744 keV). From the figures one can also extract the values of energy resolution, typically on the order of few keV. The calibration was performed with success and detectors prepared for measurements.

3.2.3 Test Measurements

After the completion of calibration it was necessary to investigate the possibilities of the measurement and develop the most suitable and effective method. The best possibility was to perform short measurements with various setups. In October 2017 I spent one week in LSM in order to perform test measurements with the calibration sources.

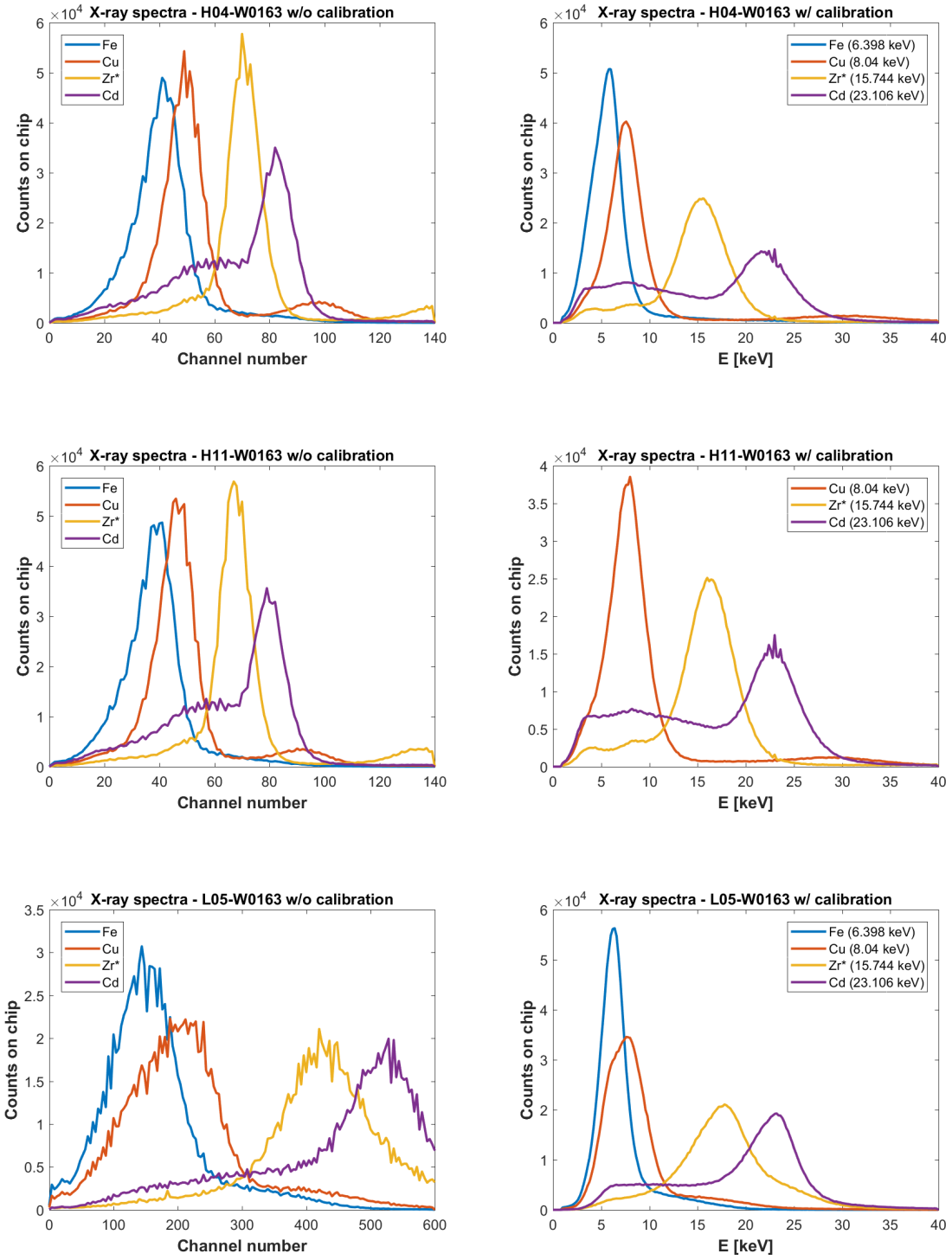

Figure 3.9: Calibration test spectra. All three detectors were tested with fluorescence foils before (left column) and after (right column) calibration. Similarly to calibration, only one pixel clusters were accepted regardless of the position on the chip. Each row represents detectors H04-W0163, H11-W0163 and L05-W0163 respectively. The spectra before calibration are represented in channel number (ToT). All three fluorescent foils from calibration were employed in the test. Asterisk represents Zirconium foil measurement which was not used for the calibration. In case of H11-W0163, data after calibration for Fe foil were lost due to disk failure. The spectrum can be found in the screenshot after the measurement in Figure 3.10.

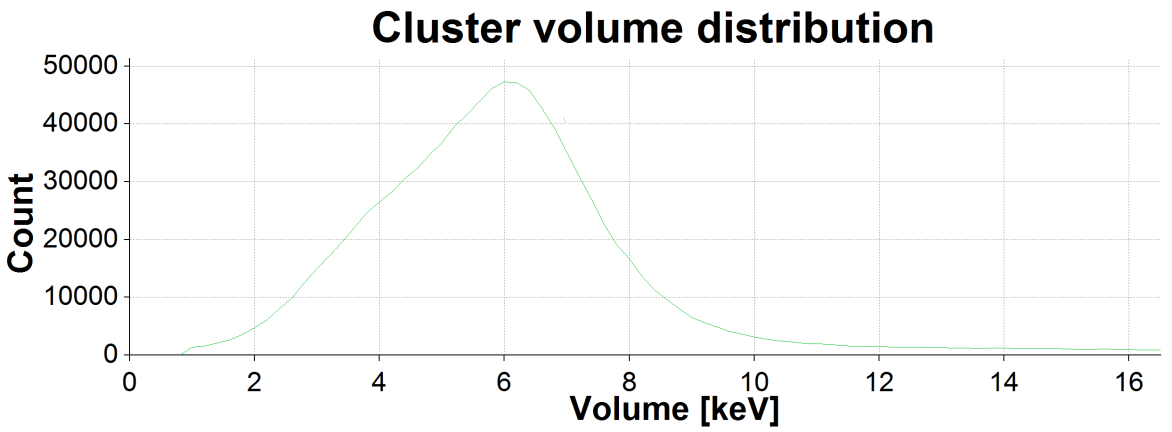

Figure 3.10: Energy from Fe foil as seen by detector H11-W0163 after the calibration. The picture represent Pixelman screenshot after the test as the data from the measurement were lost, therefore not included in Figure 3.9.

3.2.3.1 Data Analysis

Before a discussion about the measurements, let me talk about the data extracted from the detector and the software I developed for the analysis. Timepix detectors produce data in form of cyclic snapshots of a given acquisition time (frames) followed typically by 200 ms of dead time reserved for data storage. As it was already discussed, each pixel is capable to detect particle independently. With proper calibration provided, data in each pixel are saved in a simple form of three columns storing x and y coordinates of pixel and energy deposited in the pixel, respectively. Only the pixels with detected signal are written in the file in order to eliminate redundant data. This type of output I call "raw output" and it can be represented in a form of frame image in Figure 3.11. It is possible to recognize different particle tracks in the figure. In case when the particle deposited all its energy in the detector, the sum of all energies detected in the pixels belonging to its track should be equal to initial energy of the particle. Except for the raw data output, which I already described, Pixelman

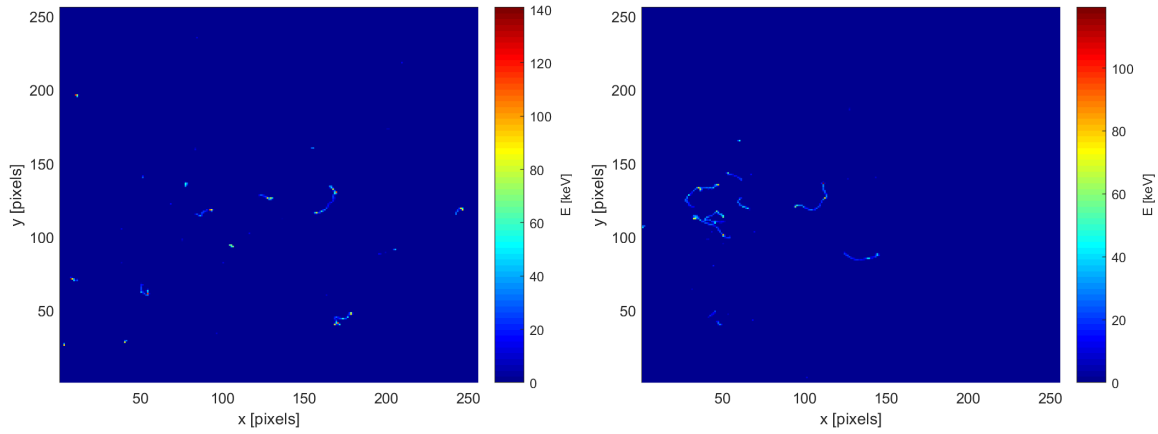

Figure 3.11: Figures representing two randomly chosen dataframes obtained during the test measurements with ^{207}Bi calibration sources. The length of presented frame was set to 1 s. One can see example of different spots representing different types of particles. Typically one pixel spots are photons while long curved tracks are electrons.

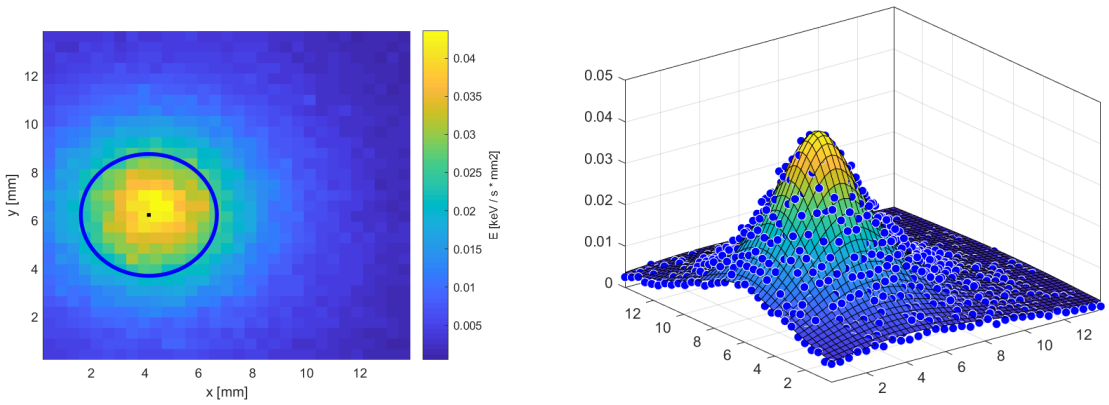

Figure 3.12: Two representations of the energy deposition for source number 133. Note that, each bin represents area of 8×8 pixels. Left: Two-dimensional representation of the energy deposition on the chip. Right: Discrete datapoints represent values of the energy deposited in each spatial bin during the full duration of measurement. The image depicts a fit of the distribution given by Equation 3.2.

provides also "clustered output" [95]. All the triggered pixels in one dataframe are grouped in clusters based on the criterion of adjacency. Cluster represents one particle. The energy of the cluster as well as its position is saved into a file. The cluster position is represented by unique number, defined as an average position of each pixel belonging to the cluster. Data contains also so-called cluster size which is number of pixels in the cluster. In my analysis software, I always took advantage of clustered output.

In order to obtain reliable data in the clustered output, we need to set length of one frame carefully. It takes 200 ms to read out the data from detector independently of the length of the frame. On one side, the longer the frame lengths is, the lower the relative dead time of the detector is. On the other side, longer frames allow the detector to collect more statistics and rise a chance to find overlapping clusters. This is something what needs to be avoided because overlapping clusters are represented as single particle in the final output causing distortions in data. Standard frame length can go down to fractions of a second. However, after few short testing measurements I came to a conclusion that the calibration sources are weak enough to open the frame for 1 s without affecting the data quality.

For the purpose of data analysis, I developed Matlab script capable of reading the clustered data output format. All the frames in the measurement are superimposed by the script giving the energy distribution of all the clusters as shown in the Figure 3.12 - Left. Extra blue circle represents size of the source while black dot represents its center. Both were added to the dataset after distribution was fitted by function given by Equation 3.2.

$$f(x,y) = \frac{A}{(x-x_0)^2 + (y-y_0)^2 + \gamma}. \tag{3.2}$$

The center of the source is here represented by fitting parameters (x_0, y_0) and the radius of the blue circle is calculated as HWHM value of the 2D distribution, i.e. $\sqrt{\gamma}$. Fitting function was chosen empirically, according to the best fit criterion. As it can be seen in the Figure 3.12 - Right, fitting function describes the distribution sufficiently well.

Gammas		X-rays		Electrons	
E [keV]	I_{abs} [%]	E [keV]	I_{abs} [%]	E [keV]	I_{abs} [%]
569.7	97.8	9.2 - 15.9	33.2	5.3 - 15.8	54.4
897.8	0.1	72.8	21.7	0.0 - 87.9	2.9
1064	74.5	75.0	36.5	56.3 - 61.9	1.8
1442	0.1	84.5 - 85.5	12.5	481.7	1.5
1460	1.6	84.5 - 87.6	16.2	975.6	7.1
1770	6.9	87.2 - 87.4	3.7	1047.8 - 1050.6	1.8

Table 3.2: Products from decay of ^{207}Bi. Gamma line of 328.1 keV was omitted due to its negligible absolute intensity. The most significant X-rays and electrons were chosen. Source [96].

3.2.3.2 Study of the Energy Spectra

In search for proper ROI for data analysis, I performed several comparative measurements. First of all, I studied the shape of the energy spectrum. ^{207}Bi is a complex emitter decaying by electron capture with half-life of 31.55 yr. It produces gammas, X-rays as well as Auger electrons (Table 3.2). In Figure 3.13 one can find comparison of the energy spectra as measured by 300 μm thick detector (H11-W0163) and 1 mm thick detector (L05-W0163).

Let us first have a look at the low energy part of the spectrum (5 keV - 30 keV) represented by Figures 3.13a and 3.13b. By looking at the Table 3.2 one can conclude that the lower part of the spectrum represents the X-rays (9.184 keV - 15.860 keV) and Auger electrons (5.327 keV - 15.817 keV) from the electron capture of ^{207}Bi. In both cases X-rays and the electrons are detected very efficiently, as their energy is not sufficient to traverse the detector. However, in the high energy part of the spectrum one can expect gammas, but for them both thicknesses of Silicon layer are practically transparent. Electrons of high energy, depose energy depending on the thickness of detector. While 300 μm detector is too thin to fully stop the electrons (Figure 3.13c), in the case of 1 mm detector, one can observe peak of electrons of 481.7 keV and 975.6 keV appearing (Figure 3.13d). As the detector was calibrated with low energy X-ray fluorescent sources, we can notice imprecision of the calibration in high energy region which is demonstrated by second peak (975.6 keV) being displaced towards the high energy.

Based on the presented analysis of the energy spectra, I decided to choose ROI for all the measurements to be between 3 keV and 30 keV. Detectors of both thicknesses give similar spectrum in the region, therefore, we can expect comparable results regardless of the detector used in the study. Lower boundary of 3 keV instead of 5 keV as presented in Figures 3.13 was chosen in order to ensure that the peak in the low energy part of the spectrum is fully contained.

Chosen ROI appears to be the right choice from the point of view of final localisation of the source droplet. Figure 3.14 shows the influence of the energy cut on the localisation of the ^{207}Bi droplet. It is possible to recognize that in Figure 3.14 - Right (low energy, low pixel size cut), the Bismuth droplet is better localised than in the Figure 3.14 - Left, representing high energy part of the spectrum with effectively no cut on the pixel size. The HWHM of the droplet from low energy dataset is 1.24 times smaller. The reason for the difference lies in the interaction between electrons from high energy part of the spectrum. These electrons leave curvy tracks several pixels long in the chip. However, in the clustered output only one unique position is assigned to each cluster regardless of its size. In case of clusters composed

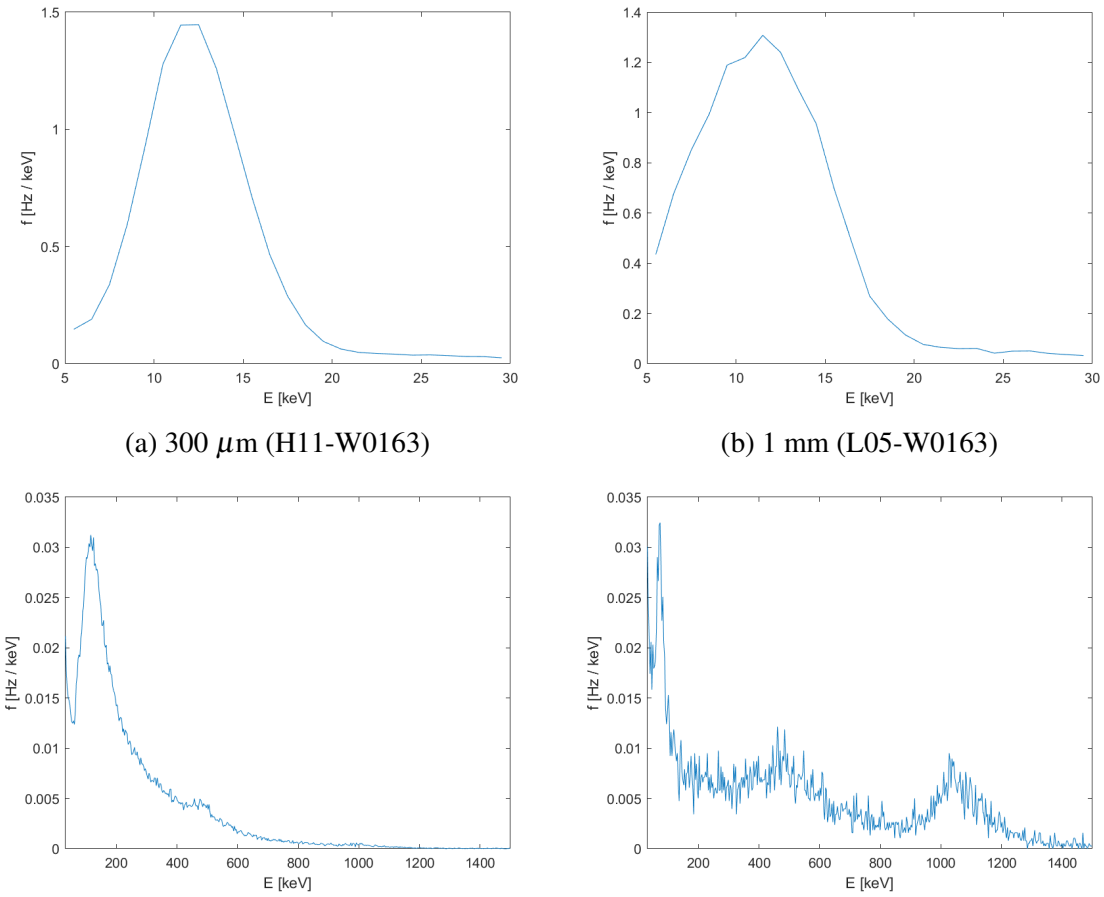

(a) 300 μm (H11-W0163)

(b) 1 mm (L05-W0163)

(c) 300 μm (H11-W0163)

(d) 1 mm (L05-W0163)

Figure 3.13: Comparison of different regions of energy spectra obtained by measurement of source number 71 with the detectors of the different thickness. While in the low part of the spectrum (5 keV - 30 keV) - figures on top - no significant difference is observed, in the high energy part of the spectrum (30 keV - 1500 keV) - figures at the bottom - we can notice peaks appearing in measurement with detector of 1 mm thickness. Reasons for the difference are discussed in the text.

of at least two pixels, this brings an uncertainty in the cluster localisation. The lower energy region is dominated by X-rays which typically leave only one pixel clusters. Therefore, their position is measured with precision of one pixel. In order to ensure maximal precision of the cluster position I decided to work only with clusters of the size of one pixel from the aforementioned low energy part of the spectrum. On one side, combination of both cuts decreased the measurement statistics to 43-50%, on the other side, it increased the precision of the main result of the study - the localisation of the ^{207}Bi droplet.

3.2.4 Detector Spatial Calibrations

If we look at the Figure 3.12 - Left we can notice another important question which has to be solved. The fit presented in the figure provides the radius (HWHM of the distribution) of the characteristic size of the source droplet as well as the position of the source. Nonetheless, the position (x_0, y_0) is given in the frame of reference of the detector chip. In other words,

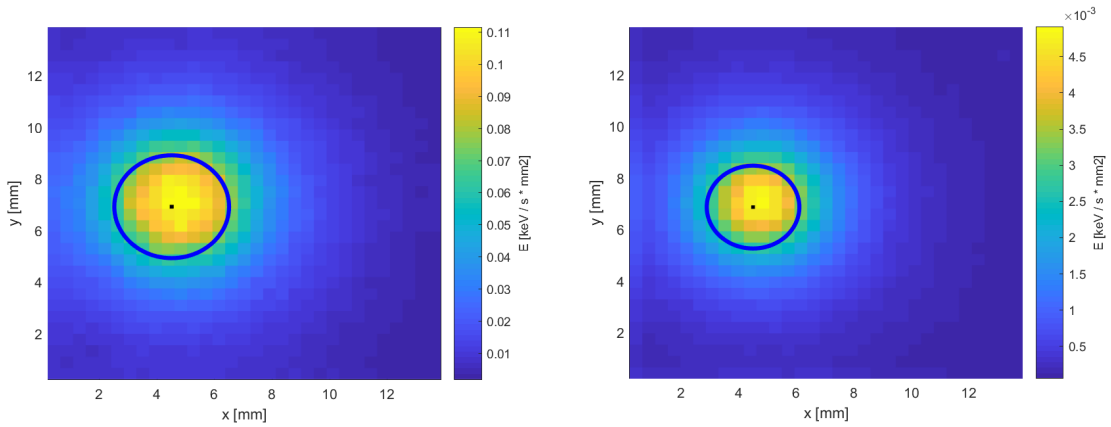

Figure 3.14: Result from measurement of source number 139. Images represent comparison of the same data with two different cuts. Left: Dataset including all the clusters with energy between 30 keV and 1300 keV and pixel size less than 100. Right: Dataset including clusters of low energy between 3 keV and 30 keV. Only clusters of pixel size 1 were included.

position of the source is known relatively to the detector chip. However, the main aim of the study is to measure relative position of the source droplet and the Copper source frame. It was necessary to reproduce its position and represent it in the data. In order to achieve this goal, I performed spatial calibration of each detector. During all the measurements, the source was carefully positioned in the same reference position, as it is depicted in the Figure 3.15.

This convention provided stable reference point for the spatial calibration. As a next step, I took laser-perforated metallic grid and placed it on the detector in the way, that top left corner of the grid (yellow point in Figure 3.16 - Left) was aligned with the measurement reference point. Subsequently, I irradiated the grid with X-rays and obtained pattern shown in the Figure 3.16 - Right. Missing hole in the measured calibration dataset helped to identify exact row and the column of each hole in otherwise symmetrical and repetitive pattern. Note

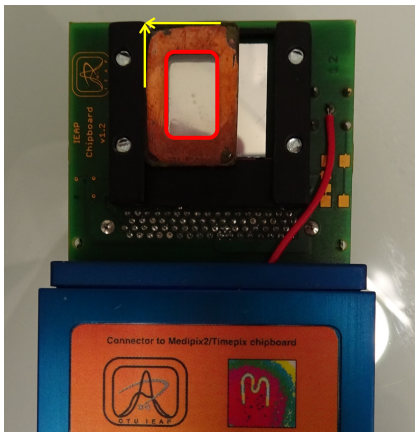

Figure 3.15: Alignment of the measured source on the detector. Sources in all the measurements were aligned with the top left corner of black plastic holder as depicted by yellow arrows. The relative position of the red Copper frame window and the top left point were known thanks to the previous measurements of the source dimensions listed in the Table 3.1.

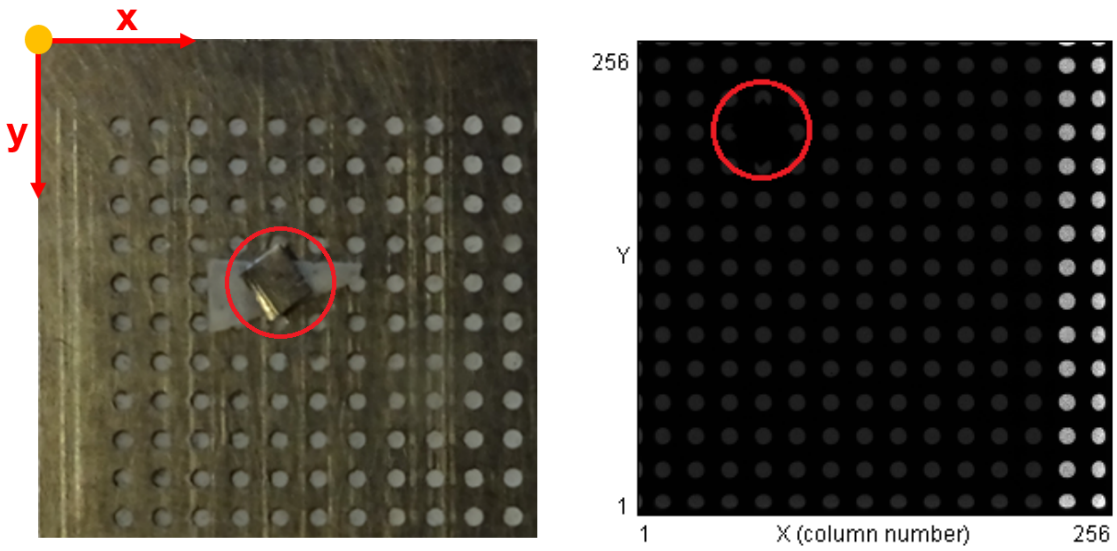

Figure 3.16: Left: Photo of the spatial calibration metallic grid. Yellow point was in the process of spatial calibration aligned with standard reference point defined in the Figure 3.15. Right: Image of the calibration grid as seen by detector L05-W0163 after exposure to X-rays. Note that, the covered hole (highlighted by red circle) appears in fourth column and third row instead of fifth row and firth column (left figure) because first two rows and first column are out of the sensitive area of the detector as well as the grid's yellow reference point.

that, the y axis of grid's coordinate system is oriented the opposite direction relatively to the pixel detector y axis (Figure 3.16). Moreover, the origin of both coordinate systems are shifted relatively to each other. It implies, that the transformation between the coordinate systems won't be simply shifted or rescaled but one needs to employ linear algebra in order to tackle the problem mathematically.

Let me explain the mathematical background of the spatial calibration. In the following, all the vectors will be implicitly columns unless transposed. The goal of the calibration is to find a transformation matrix A and shift vector $\mathrm{b} = (\mathrm{b}_1, \mathrm{b}_2)$ providing a transformation between any vector $\mathrm{v} = (\mathrm{v}_1, \mathrm{v}_2)$ (in mm) in the calibration grid's coordinates and vector $\mathrm{p} = (\mathrm{p}_1, \mathrm{p}_2)$ in pixel detector's coordinates (in pixels) such as:

$$p = Av + b. \tag{3.3}$$

Let us now have four different vectors (points in space) in calibration grid coordinates v_1, v_2, v_3 and v_4 represented in pixel detector coordinates: p_1, p_2, p_3 and p_4, respectively. The transformation relation from Equation 3.3, therefore holds for each vector:

$$p_i = Av_i + b, \quad i = 1,2,3,4. \tag{3.4}$$

Now, if we define matrices V_1, V_2, P_1, P_2 and B:

$$V_1 = (v_1, v_2);\ V_2 = (v_3, v_4);\ P_1 = (p_1, p_2);\ P_2 = (p_3, p_4);\ B = (b, b), \tag{3.5}$$

following matrix equations also hold as a consequence of the Equation 3.4:

$$P_1 = AV_1 + B; \quad P_2 = AV_2 + B. \tag{3.6}$$

	v_1 (mm)	v_2 (mm)	v_3 (mm)	v_4 (mm)
x	6.16	11.58	11.58	6.16
y	6.08	6.08	11.06	11.06

Table 3.3: Coordinates of four chosen grid points in grid's coordinate system obtained by measurement by caliper presented in Figure 3.17 - Left.

	p_1 (pix.)	p_2 (pix.)	p_3 (pix.)	p_4 (pix.)
x	67.96	159.48	159.52	68.01
y	207.62	207.68	116.06	116.05

Table 3.4: Coordinates (rounded to two decimal places) of four chosen grid points in detector's coordinate system obtained by fit presented in Figure 3.17 - Right.

If we substract second equation from the first we eliminate the unknown matrix B:

$$P_1 - P_2 = A\left[V_1 - V_2\right]. \tag{3.7}$$

Finally, we multiply equation from the right side with matrix inverse $[\mathrm{V}_1 - \mathrm{V}_2]^{-1}$ and swap sides:

$$A = \left[P_1 - P_2\right]\left[V_1 - V_2\right]^{-1}. \tag{3.8}$$

Equation 3.8 provides recipe for calculation of the transformation matrix A given values of four points in both coordinate systems. With A already known, the shift vector b is obtained from Equation 3.4:

$$b = p_i - Av_i. \tag{3.9}$$

The calculation should work for any chosen $\mathrm{i} = 1,2,3,4$. Having matrix A and vector b, it is possible to transform any vector v in calibration grid coordinates into vector p in pixel detector coordinates. The opposite transformation can be achieved by inverted relation:

$$v = A^{-1}\left(p - b\right). \tag{3.10}$$

Here, A^{-1} represents inverse of matrix A.

Let me now demonstrate how the presented method works. As an example, I will use spatial calibration of detector L05-W0163. As it was already discussed, the first step to perform the spatial calibration is to choose four points and express them in both coordinate systems.

Figure 3.17 - Left shows choice of my four points represented on the photo of the grid. These four points were (thanks to the covered hole) identified in the dataset measured by the detector (3.17 - Right). Green lines represent two horizontal and two vertical linear fits and their intersections represent the coordinates of my four chosen points in detector's coordinate system. All the measured (fitted) coordinates in both coordinate systems are summarized in the Table 3.3 (Table 3.4).

Having all the important ingredients for my mathematical recipe it is possible to construct matrices V_1, V_2, P_1 and P_2 from Equation 3.5:

$$V_1 = \begin{pmatrix} 6.16 & 11.58 \\ 6.08 & 6.08 \end{pmatrix}, \qquad V_2 = \begin{pmatrix} 11.58 & 6.16 \\ 11.06 & 11.06 \end{pmatrix}, \tag{3.11}$$

$$P_1 = \begin{pmatrix} 67.96 & 159.48 \\ 207.62 & 207.68 \end{pmatrix}, \quad P_2 = \begin{pmatrix} 159.52 & 68.01 \\ 116.06 & 116.05 \end{pmatrix}. \tag{3.12}$$

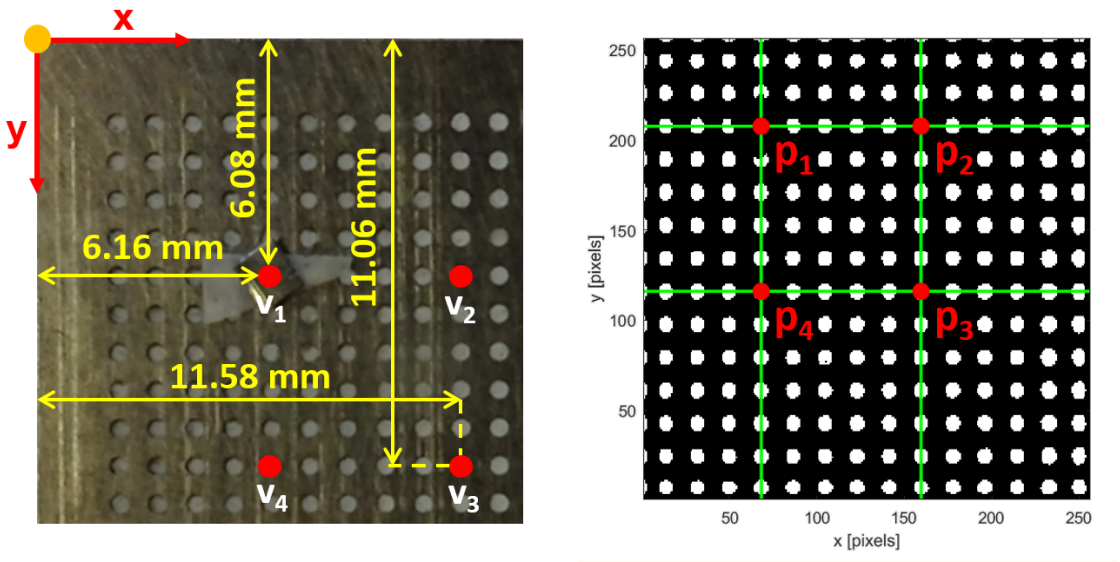

Figure 3.17: Left: Dimensions of the grid measured by calliper. They represent the coordinates of four chosen calibration vectors v_1, v_2, v_3 and v_4. Right: Same four points identified in the dataset from exposure by X-rays in Figure 3.16 - Right. The contrast of the image was enhanced before the fitting (green lines) was performed.

Subsequently, I calculated $V_1 - V_2$, $P_1 - P_2$:

$$V_1 - V_2 = \begin{pmatrix} -5.42 & 5.42 \\ -4.98 & -4.98 \end{pmatrix}, \quad P_1 - P_2 = \begin{pmatrix} -91.56 & 91.47 \\ 91.57 & 91.63 \end{pmatrix}, \tag{3.13}$$

as well as $[V_1 - V_2]^{-1}$:

$$[V_1 - V_2]^{-1} = \begin{pmatrix} -0.0923 & -0.1004 \\ 0.0923 & -0.1004 \end{pmatrix}. \tag{3.14}$$

It was important to choose my four points in such way, that the matrix $V_1 - V_2$ was not singular. Finally, by application of Equation 3.8 and, subsequently, Equation 3.9, we obtain matrix A and shift vector b for transformation from grid's coordinate system to coordinate system of detector:

$$A = \begin{pmatrix} 16.885 & 0.0087 \\ 0.0062 & -18.3936 \end{pmatrix}, \quad b = \begin{pmatrix} -36.1 \\ 319.4 \end{pmatrix}. \tag{3.15}$$

For the inverse transformation defined by Equation 3.10, we can use matrix:

$$A^{-1} = \begin{pmatrix} 0.0592 & 0 \\ 0 & -0.0544 \end{pmatrix}. \tag{3.16}$$

Let me briefly discuss obtained results. Looking at matrices A and A^{-1} we can conclude that we obtained correct and expected results. Within precision of one decimal place the off-diagonal elements are zero which suggest no rotation between the two coordinate system which is indeed true. Moreover, minus sign next to the bottom right elements of the two matrices describe mathematically the fact, that the directions of y axes are mutually opposite

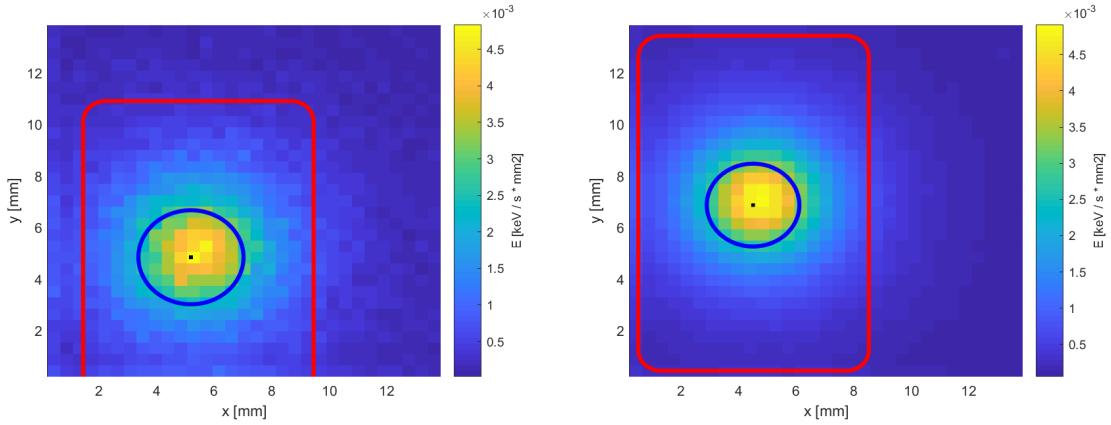

Figure 3.18: Example of two measurement results after the addition of Copper source frame window (red rectangle). Left figure represents measurement of source number 75 while figure on the right represents measurement of the source number 139. It is clearly visible that the position of the red Copper frames are in the different positions. This is expected, because source number 75 (Left) is source with plastic envelope while source number 139 (Right) has no plastic envelope. Note that both datasets are expressed in mm instead of the pixels which was achieved by using size of one pixel (0.055 mm) as a scaling factor.

between the two coordinate systems. In contrary, the directions of the x axes are mutually the same which is represented by positive sign of the elements in first row and first column in both matrices (Figure 3.16). Looking at the b vector we can state expected fact, that the origins of the two coordinate systems are mutually displaced.

If we look at the dimensional analysis of the values, b vector is represented in pixels. It represents the relative displacement of grid's coordinate system relatively to origin of the detector's coordinate system. Negative x value suggests displacement to the left from the chip and y which is higher than 256 (number of pixel rows) suggests that the reference measurement point is above the chip. This is exactly the situation implied by Figure 3.16. Finally, we conclude that the values of matrix A^{-1} are in mm per pixel, based on the fact that this matrix has to transform pixels in which vector p is expressed into mm, the units of vector v. The diagonal elements of the matrix A^{-1} provide rescaling. The values 0.0592 and 0.0544 represent the size of one pixel in mm. The two values were obtained indirectly, but still within a good precision they represent correct size of standard Timepix detector pixel (0.055 mm). The presented process was performed with each one of the detectors using my own Matlab script. With the transformation relations at disposal, it is easy to express any point in the detector (or outside) in both coordinate systems. Based on the source frame measurements (Table 3.1), it was simple task to represent the red source frame window from Figure 3.15 into the measured dataset. Example is shown in Figure 3.18.

3.2.4.1 Source Placement Convention

Before I will start to discuss the final results obtained in the study, one last topic remains still to be covered. As it was already mentioned, both types of calibration sources (with and without plastic envelope) are of rectangular shape and they are emitting decay products to both sides perpendicular the area of the rectangle. Therefore, in order to make unambiguous conclusion about source droplet position, it is important to clarify on which side the mea-

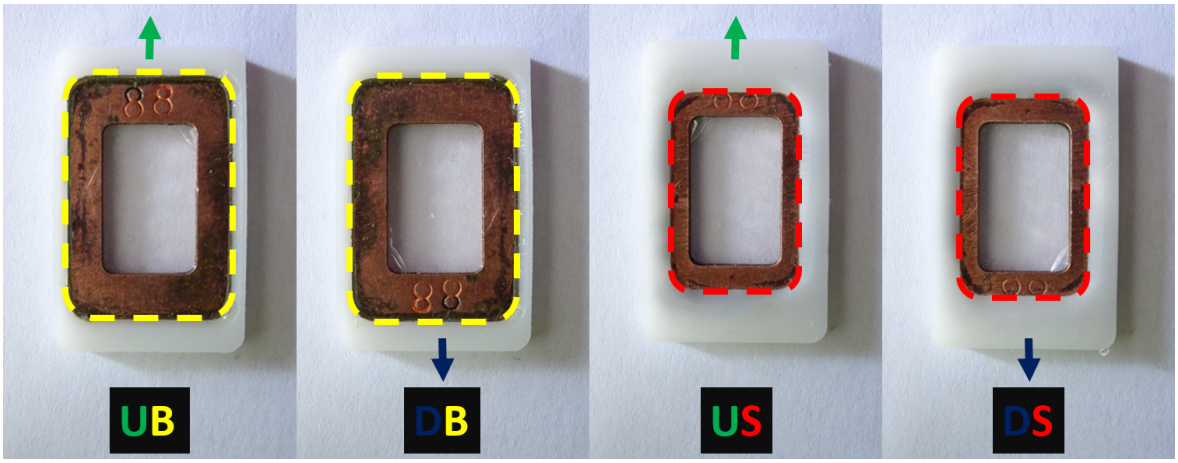

Figure 3.19: Four different positions of source number 88. U stands for upward position, D for downward position, B for the side with big opening and S for side with small opening. Further details are explained in the text.

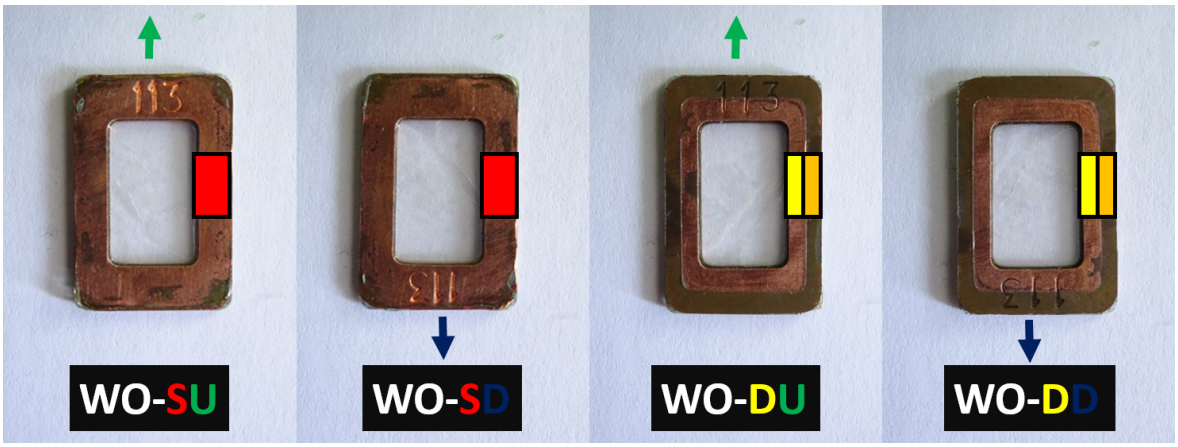

Figure 3.20: Four different positions of source number 113. U stands for upward position, (second) D for downward position, S for the side with single colour opening and (first) D for side with double colour. Prefix "WO-" is added to distinguish positions of source without plastic frame easier. Further details are explained in the text.

surement was performed. Furthermore, once we have chosen the side of the source facing the detector, the source can still be rotated by 180 degrees in its plane. These two symmetries together define four different positions which have to be named and distinguished in order to provide replicable results.

Figure 3.19 contains photos of a source number 88 with plastic envelope. Source can be placed (with respect to predefined upward position) in four different measurement positions. In case of source with plastic envelope it is possible to distinguish a side with a big opening (positions UB and DB, B stands for big) and opposite side with a small opening (positions US and DS, S stands for small). Moreover, on each side, source number is engraved. It helps to distinguish upward placement (positions UB and US) from downward placement (positions DB and DS). Analogical positions can be defined for source without plastic envelope. However, if we look at the Figure 3.20 we can spot slight difference. Without plastic envelope there is no possibility to define each side based on the size of the plastic opening.

Nevertheless, two sides of any source without plastic envelope can be distinguished thanks to the difference in colour, single colour (positions WO-SU and WO-SD) and double colour (positions WO-DU and WO-DD). The upward positions (WO-SU and WO-DU) and downward positions (WO-SD and WO-DD) are defined exactly in the same fashion as in the case of source with plastic envelope, based on the engraved source number. Note that, for easier orientation in the convention, all the positions concerning sources without plastic frame have prefix "WO-". The convention defined in the Figures 3.19 and 3.20 has to be (and will be) strictly followed in the thesis. At this point, last important remark should be made. If we take Figure 3.15 as an example, we can state that the measured source is in position WO-SU. However, it is the double coloured side which is facing the detector. For the sake of practicality the name of the position is based on what observer sees. It is not important which side is seen by detector (unless stated otherwise).

3.2.5 Results

During my second stay in LSM in December 2017, I performed final measurements. During 12 days, I managed to measure 49 different sources in 52 measurements (three sources were measured two times). The duration of one measurement was variable, ranging from few hours to few days. Statistics of chosen measurements can be found in the Table 3.5.

The table includes the name of the detector involved in the measurement as well as number of counts in ROI (N_{ROI}) and total dataset (N_{TOT}), their fraction and the flux of energy detected per unit time (E_{ROI} / t_{live}). Full information about all performed measurements can be found in Table A.2 in Appendix A. Based on the presented number, it is possible to distinguish two types of detector. If we look at the particle rates, we can notice that 300 μm thick detectors (H04-W0163 and H11-W0163) detected particle rates approximately on the level of 7-9 Hz. However, 1 mm thick detector (L05-W0163) have seen higher rates of 11 or more Hz. It is another demonstration of higher detection efficiency due to the thickness of the detector. Note that, the particle rates allow us to calculate activities relatively to one chosen source. However, according to the difference in the detection efficiency which I have just discussed, it is impossible to compare activities between sources measured by thicker detector and the sources measured by thinner detectors.

M.	Detector	t_{live} [s]	N_{ROI} [1]	N_{TOT} [1]	$\frac{N_{ROI}}{N_{TOT}}$ [%]	$\frac{N_{ROI}}{t_{live}}$ [Hz]	$\frac{E_{ROI}}{t_{live}}$ [keV / s]
73	H04-W0163	5 994	49 656	114 585	43.34	8.28	92.88
74	H11-W0163	6 384	53 527	123 395	43.38	8.38	101.28
111	H11-W0163	13 813	125 124	288 873	43.31	9.06	110.18
120	L05-W0163	45 669	552 206	1 095 402	50.41	12.09	134.99
126	H04-W0163	199 776	1 474 716	3 428 264	43.02	7.38	82.38
126*	H04-W0163	166 317	1 290 921	3 038 524	42.49	7.76	86.55
132	H11-W0163	197 260	1 719 104	3 955 332	43.46	8.71	104.58
132*	H11-W0163	165 699	1 440 205	3 324 424	43.32	8.69	104.86
139	L05-W0163	197 151	2 342 662	4 723 626	49.59	11.88	133.00
139*	L05-W0163	165 604	1 965 319	3 973 773	49.46	11.87	133.82

Table 3.5: Statistics of chosen measurements. M. in the first column stands for number of measured source. Rows with asterisk denote repeated measurement under same experimental conditions.

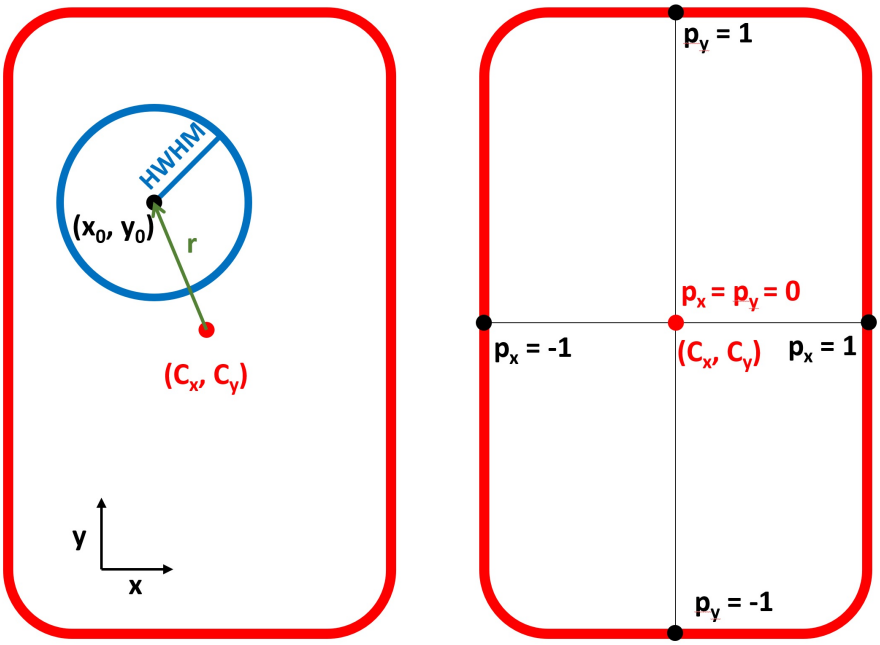

Figure 3.21: Graphical representation of the quantities extracted from the measurement. They are explained in further detail in the text.

The quantities of interest extracted from the measurement are depicted in Figure 3.21. Black point is center of ^{207}Bi droplet (x_0, y_0) obtained by fit described in Section 3.2.3.1. The fit provides also HWHM value of the distribution (characteristic dimension of the source). The droplet is symbolized in the picture by blue circle with the radius of distribution's HWHM. Red point is a center of the source frame. Its coordinates are (C_x, C_y). Finally, green arrow represents the most important quantity, "the dislocation vector", r. It is a vector whose origin is in the center of source frame and the end in the center of ^{207}Bi droplet: $r = (x_0 - C_x, y_0 - C_y)$. It represents the dislocation of the source droplet from the center of the source frame. Therefore, its length is a measure of this dislocation. In the right side of the same figure one can find definition of complementary dislocation parameters p_x and p_y. They represent the same information given by coordinates of dislocation vector but in relative terms with respect to source frame dimensions. Both have value from interval $\langle -1, 1 \rangle$. p_x

M.	Position	x_0 [mm]	y_0 [mm]	HWHM [mm]	$x_0 - C_X$ [mm]	$y_0 - C_Y$ [mm]	p_x [1]	p_y [1]	r [mm]
126	WO-DU	3.02	6.79	2.44	-1.22	0.11	-0.31	0.02	1.23
126*	WO-DU	3.00	7.01	2.14	-1.24	0.33	-0.31	0.05	1.28
132	WO-DU	3.99	7.29	1.96	-0.25	0.57	-0.06	0.09	0.62
132*	WO-DU	3.94	7.46	1.95	-0.29	0.74	-0.07	0.11	0.79
139	WO-DU	4.50	6.88	1.61	-0.02	-0.07	0.00	-0.01	0.07
139*	WO-DU	4.47	7.03	1.62	-0.05	0.08	-0.01	0.01	0.10

Table 3.6: Table summarising all obtained quantities for chosen measurements. M. in the first column stands for number of measured source. Measurements with asterisk denote repeated measurement under same experimental conditions. Colour coding of dislocation vector length denotes source category described in the text.

$(p_y) = 0$ represents situation when source is perfectly horizontally (vertically) aligned while p_x $(p_y) = -1$ represents source deposition on the left (bottom) edge of the source frame and p_x $(p_y) = 1$ represents source deposition on the right (top) edge of the source frame. The parameters are dimensionless.

Finally, let me discuss the results. Table 3.6 includes data from six measurements of three repeatedly measured sources. All the previously mentioned quantities can be found in the table. The coordinates of the droplet and source frame center is expressed in the mm. Note that, their values are the coordinates in the detector coordinate system rescaled from pixels into mm by size of one pixel (0.055 mm). Last column shows a length of the dislocation vector. Majority of the sources were centred well within 1.5 mm or less. In order to simplify the description of the sources, I decided to divide them into three basic categories. Category A includes all the sources with r < 0.5 mm (green category), category B all the sources with 0.5 mm < r < 1 mm (yellow category). In category C (red category) the rest of the sources were placed, i.e. 1 mm < r. Full results from all the measurements can be found in Table A.4 in Appendix A.

The results have shown that 21 sources belong to the category A, 23 to category B and 5 into category C. None of the sources showed contamination on the source frame. In other

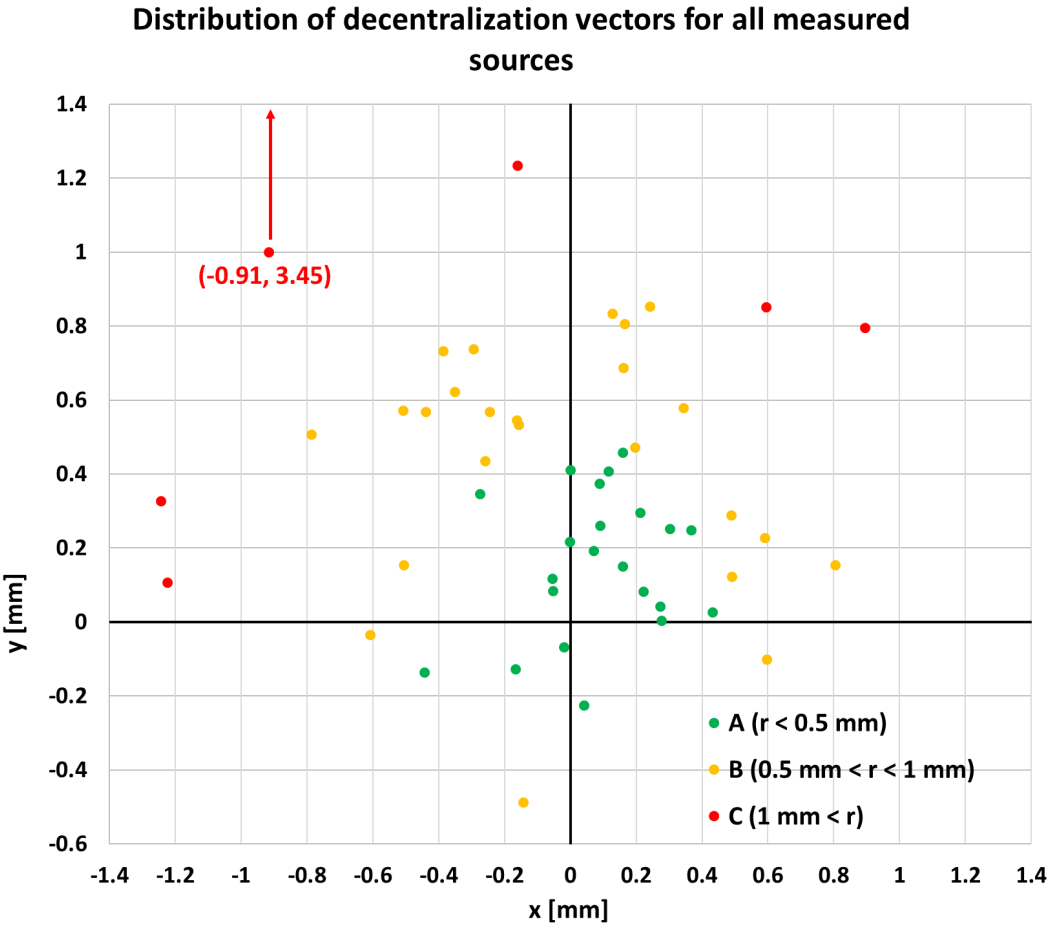

Figure 3.22: Each dot symbolizes one performed measurement. Position represents the dislocation vector coordinates. Origin represents the center of the source frame. Dot colour stands for the source category (A, B or C).

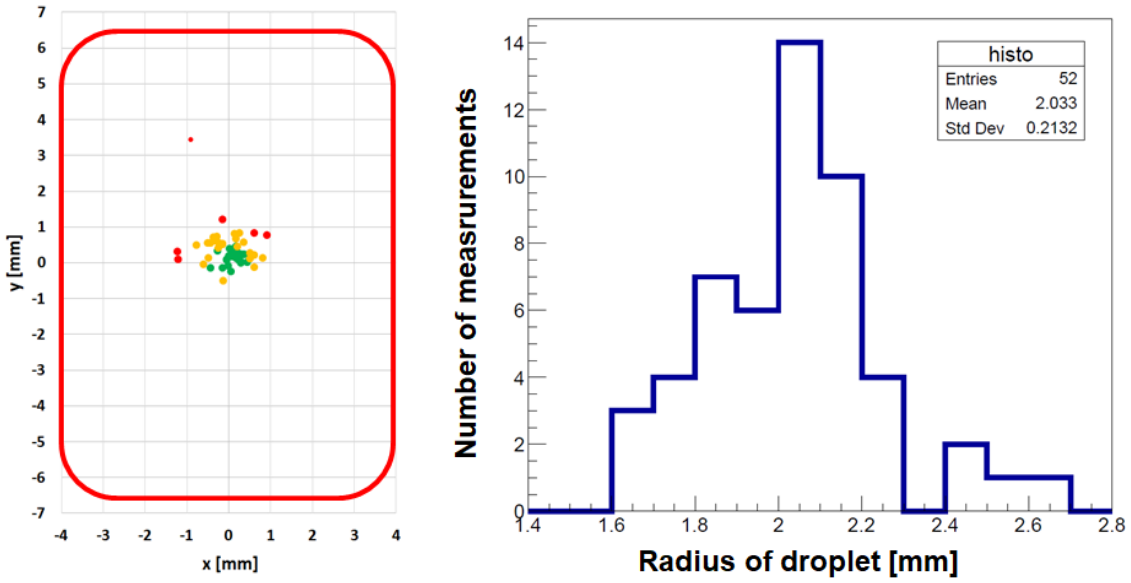

Figure 3.23: Left: Representation of Figure 3.22 relatively to the red source frame. Right: Distribution of the droplet radii in all 52 measurements.

words, all the tested sources are eligible to be used in the calibration. However, thanks to the study it will be possible to choose the best ones. For easier orientation in the results, I represented all the dislocation vectors in Figure 3.22. Figure 3.23 - Left represents the same distribution depicted relatively to the red source frame. On the right side of the same figure one can find distribution of source droplet radii which is in average around 2 mm. The results of the measurements I summarized into an article which is currently under internal review of SuperNEMO collaboration [97].

3.2.5.1 Systematic Uncertainty Estimation

In order to perform uncertainty estimation I took advantage of three repeated measurements. The uncertainty was estimated by comparing the differences between dislocation vectors obtained for the same source in two different measurements. Let us have a look at the uncertainty of the x coordinate first. By comparison of the measurement 132 and 132* the difference in x coordinate is 0.04 mm (difference between -0.25 mm and -0.29 mm). This difference is the biggest among all the repeated measurements In Table 3.6. Measurements 126 and 126* yield only 0.02 mm of difference while measurement 139 and 139* yield difference of 0.03 mm. As a conservative estimate I consider final uncertainty in the x direction the one with the highest value, i.e. $\Delta x = 0.04$ mm. I repeated exactly same process for the y direction. Here, is the biggest difference (0.22 mm) between measurement number 126 and 126*. Again, this value is considered as uncertainty of the measurement in the y direction, i.e. $\Delta y = 0.22$ mm.

It is obvious, that the uncertainty in y direction is significantly larger than the on in x direction. This has simple explanation. If we look at the Figure 3.15 we can notice important detail. The figure shows alignment of the measured source to the reference measurement point (top left corner). While in the left side the source is touching black plastic chip holder and it can be aligned easily, in the horizontal (y) direction, source can move freely and has to be aligned by hand. Naturally, it brings extra uncertainty into the measurement.

3.3 Measurements of Source Activities

Another crucial property of calibration sources which needs to be known, is the activity. SuperNEMO demonstrator is using 42 ^{207}Bi sources for calibration of optical modules in main walls. It is important to ensure that all the optical modules obtain roughly the same number of calibration electrons in order to obtain homogeneous calibration quality all over the calorimeter walls. It can be achieved by avoiding placement of the most active sources on one side of the detector. If at least relative source activities are known, the distribution of the calibration sources can be optimized. Furthermore, the knowledge of absolute activities can help to define the length and frequency of the calibration sessions. Activities serve as an input to the simulations of calibration system. In NEMO-3, ^{207}Bi sources have been measured with an uncertainty on activity at the level of 5%, leading to an uncertainty of 5% on the electron reconstruction efficiency. This uncertainty was, thus dominating the uncertainty on half-life of $2\nu\beta\beta$. Precise measurements of calibration source activities, therefore, have potential to reduce significantly the uncertainty of the half-life.

Such measurements are the main goal of the following section. The activity was measured in two parallel sets of measurement - relative and absolute.

3.3.1 Relative Measurements

Forty-one calibration ^{207}Bi sources were shipped from LSM to CENBG in summer 2018 in order to perform the activity measurements. ^{207}Bi is a complex emitter, emitting not only electrons (key particles for calibration), but also X-rays and gammas. The activity measurements were performed with two different Germanium detectors detecting gammas coming from the sources. ^{207}Bi produces two main gamma lines: 569.7 keV (branching ratio 97.8%) and 1063.7 keV (branching ratio 74.5%). The analysis in the activity measurements was based on the analysis of these two peaks.

Let me firstly talk about relative activity measurements. They were performed by Germanium detector (I will call it detector A) depicted in Figure 3.24.

Detector itself (not visible in the photo) is in the bottom part of the shielding shaft. It is a high-purity coaxial-type Germanium detector with a 100 cm^3 volume hosted at the PRISNA platform at CENBG (Plateforme Régionale Interdisciplinaire de Spectrométrie Nucléaire en Aquitaine). This detector was initially developped by the NEMO collaboration in the early 90's in close collaboration with the Canberra company. The calibration source was placed on top of the detector (i.e. at the bottom of the shaft, shown in photo) with UB side facing the detector (Figure 3.19) in case of source with plastic and WO-SU side facing the detector (Figure 3.20) in case of source without plastic. While the side of the source facing the detector was strictly followed in each measurement, the horizontal alignment (UB vs. DB, US vs. DS, etc.) was kept only approximately.

Detector was shielded, which allowed to measure very clean spectrum shown in Figure 3.25. Figure depicts two mentioned gamma lines which were of interest in both the relative and absolute activity measurements. In the relative measurement I took advantage of only 570 keV which was fitted by Gaussian bell shape function deposited on constant background:

$$f_1(E) = \frac{N}{\sqrt{2\pi}\sigma} e^{-\frac{(E-E_0)^2}{2\sigma^2}} + c. \tag{3.17}$$

Fitting parameters were E_0 (peak position), σ (peak width), c (background) and N (integral of the Gaussian). Integral (N) represents the fitted value of number of events detected

in 570 keV peak. Such value can be used for relative comparison of source activities. Majority of the radiation is undetected and one needs to perform simulation or measurement to extract the detection efficiency in order to calibrate the detector. The calibration of the detector to absolute activities would be, in principle, possible by measrement of detector efficiency, however, such measurement would not provide value with uncertainty better than 5%. Detection efficiency depends on the distance between the source and detector. In my study, there are two types of sources - with and without plastic envelope. Envelope changes slightly the geometry of the source. This slight, few milimeter difference (as it will be shown

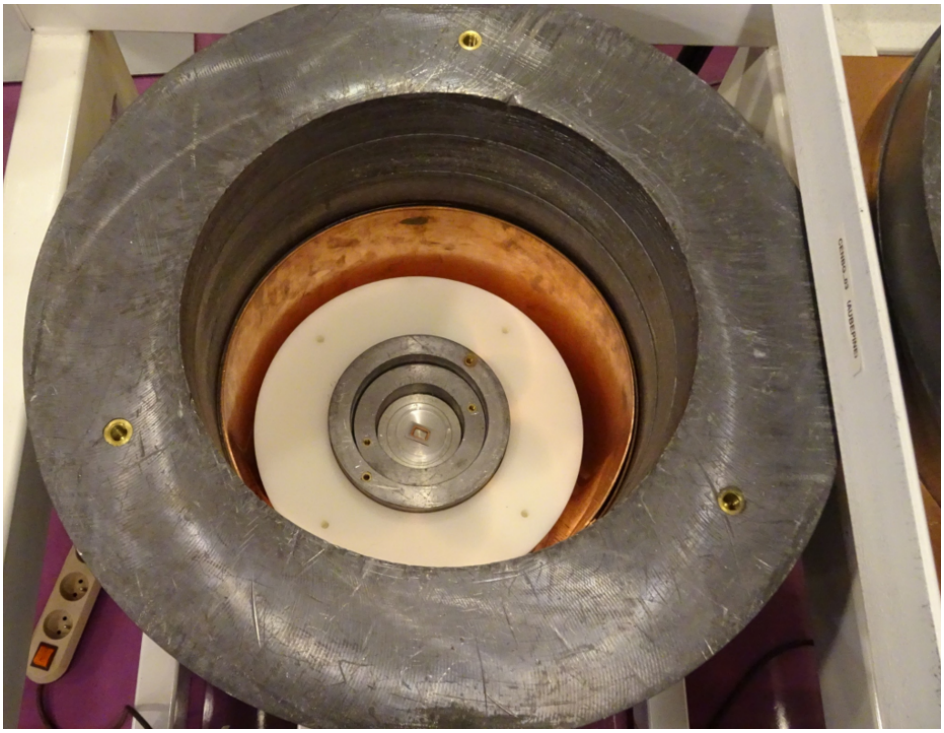

Figure 3.24: Image of the Germanium detector in CENBG employed for relative activity measurements. Inner white cylinder is polyethylene shielding while the outer grey cylinder is lead shielding.

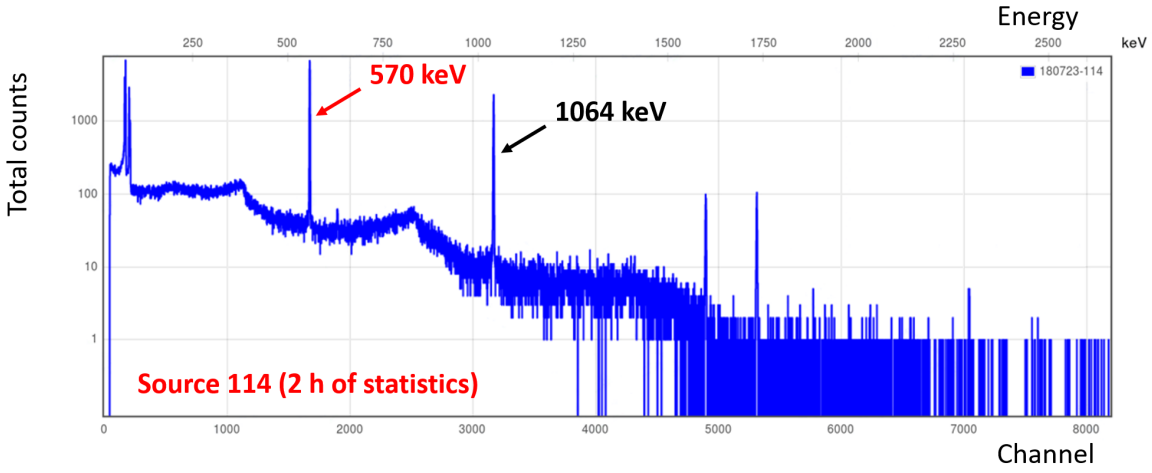

Figure 3.25: Gamma spectrum of source number 114 as measured by detector A. Figure depicts positions of 570 keV and 1064 keV peaks produced by ^{207}Bi.

in following sections) causes difference in the source-detector distance between two types of sources. The difference can be in principle compensated, however, this was not the aim of the relative measurement. Without performing the correction, one should not compare results for sources with plastic envelope and for sources without the envelope.

3.3.1.1 First Phase

Relative measurements were performed for 40 sources. It consisted of two phases. In first phase, all the sources were measured in previously discussed fashion collecting ~6 min of statistics. The aim of the first phase was to briefly obtain list of the most active sources. Only the most active could have been used for absolute activity measurements due to the limited time allocated for the absolute measurements.

After the spectrum measured by detector A was fitted by function in Equation 3.17 in the vicinity of peak 570 keV, integral (parameter N in fit) was considered as a measure of activity. Typically, 1400 - 1600 counts were extracted in the peak. Live time of the measurements were ranging from 330 s to 360 s. In each case, number of counts was divided by measurement's live time and compared. Uncertainty of fit of such short measurement was rather high (1 - 2%), however, sufficiently low to choose the best candidates for absolute measurements, with satisfactory precision and in minimal amount of measurement time.

In following, twenty-four the most active sources (75, 80, 81, 82, 84, 87, 88, 89, 91, 92, 93, 94, 95, 96, 111, 113, 114, 115, 116, 120, 131, 133, 135 and 138) were labelled as "golden" sources. These sources were all measured in absolute measurement. Following ten sources (76, 77, 78, 79, 83, 85, 86, 90, 119 and 139) were labelled as "silver" sources. At the time of the first phase of relative measurement these sources were candidates for absolute measurement. Finally, only one of them (76) was finally measured in precise absolute measurements. Note that, this division was only first rough comparison in order to choose sources which were later advanced for absolute measurement. Finally, there might be examples of silver sources which are more active than some of the golden sources. This is not a problem, as the final results would be based on the relative and absolute measurements with more precise approach presented in following sections.

3.3.1.2 Second Phase

Second phase relative measurements were simple repetition of the first phase. Nevertheless, in second phase, all the sources were measured during at least 2 h. Spectrum was measured again by detector A and fitted by the same function in Equation 3.17 in the vicinity of peak 570 keV, integral (N) was extracted. Naturally, much more statistics was collected. Typically, around 30000 counts were collected in 570 keV peak and obtained fit uncertainty around the level of 0.1%.

Results are summarized in Figure 3.26. X-axis represents count rate extracted by fit in 570 keV peak while y-axis represents integral count rate in full spectrum. Each datapoint is labelled by the number of source. Colour of the label represents type of an source (with or without plastic envelope). It is visible that both types of the sources are distributed rather evenly all along the chart. This might be a hint that the difference in the source geometry (the plastic envelope) does not play very big role in comparison at this level of precision. Nevertheless, without proper absolute reference measurements, sources should not be compared between the categories. Finally, the colour of data point represents distinction between "golden", "silver" and the rest of the sources. All the measurement data points in the plot are aligned close to the red linear function obtained by fit. The correlation between the count

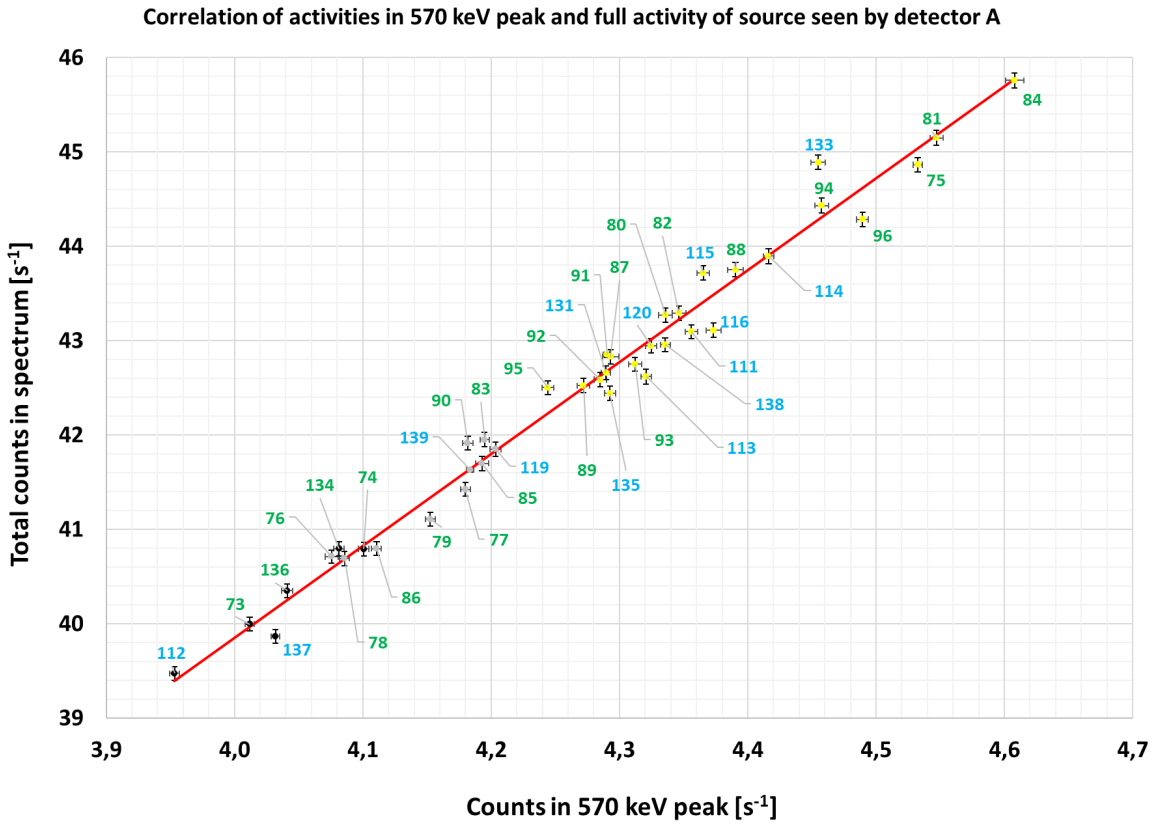

Figure 3.26: Plot representing correlation between count rate from full spectrum and count rate observed in 570 keV peak in each of the measurements of second phase. Datapoints are labelled by number of the measured source. Green label colour represents the source with plastic envelope while blue label represents source without plastic envelope. Colour of the datapoint represents distinction of the source based on the activity introduced in phase one of relative measurements. Yellow colour represents "golden" source, grey colour "silver" source and black colour all the other sources.

rate in full spectrum and in the 570 keV is strong which is due to stable ratio between two measured values. This is a sign of good source quality, that the sources are not contaminated by other gamma emitting isotopes.

Figure 3.26 represents measurements of 40 sources in CENBG. Another three extra source measurements (numbers 123, 132 and 138) were performed in LSM. Sources 84 and 138 were measured as reference sources. All the results from measurements can be found in Tables A.5, A.6, A.7 and A.8 in Appendix A. Based on the relative activity measurement results, we can conclude that the difference of activities of the least and most active sources should not be larger than 15%.

3.3.1.3 Distribution of Calibration Sources in SuperNEMO Detector

With help of the source mapping studies and relative activity measurements presented in the chapter, it was finally possible to decide which 42 the best calibration sources are eligible for calibration of SuperNEMO calorimeter. The sources will be distributed in six columns in gaps between Selenium foils. Each column contains seven sources.

Their approximate positions are shown in Figure 3.27 obtained from simulations of tracker hit rate caused by calibration sources. Each position is denoted by its column and

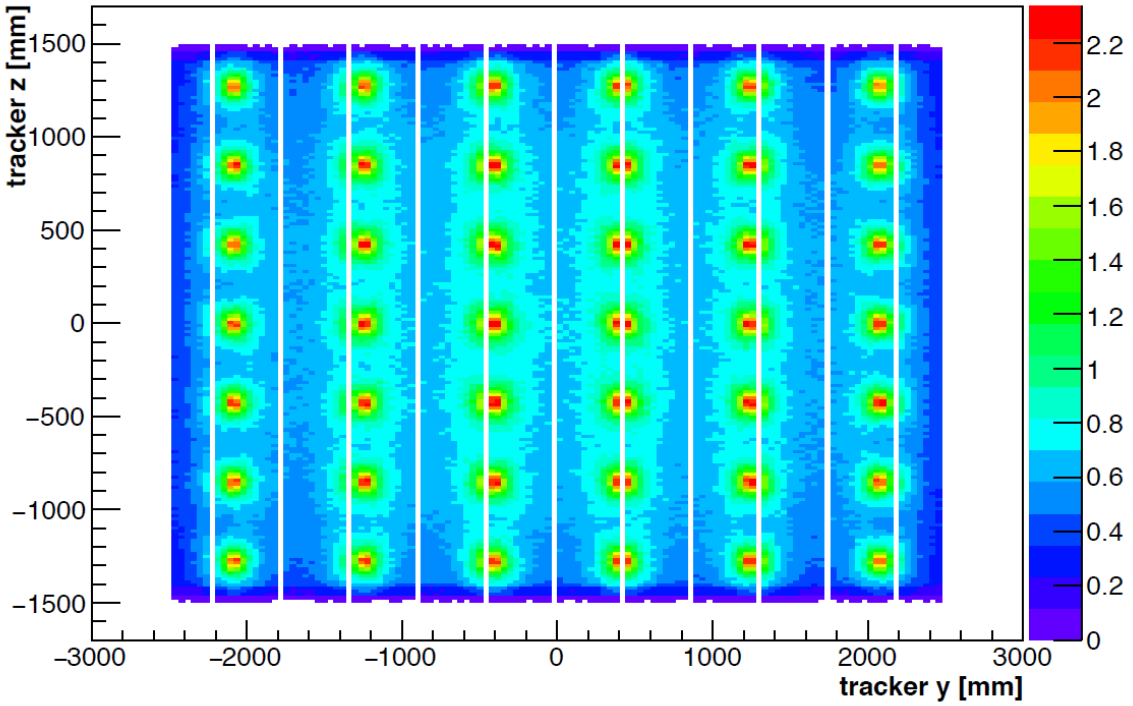

Figure 3.27: Approximate scheme of positions of calibration sources. Vertical spacing between two sources is 42.5 cm. Note that, the sources are in reality lying exactly in the gaps between selenium foils. The slight mismatch in figure is caused by the fact, that the scheme was generated in simulation of the decays of ^{207}Bi and reconstructed by tracker. Therefore, the positions are influenced by precision of the tracking and also binning of the plot. Figure prepared by Carla Macolino.

	Column 1	Column 2	Column 3	Column 4	Column 5	Column 6
Row 7	83	88	86	75	77	120
Row 6	111	76	95	78	91	132
Row 5	73	82	135	87	139	114
Row 4	133	112	84	113	81	137
Row 3	123	80	131	93	119	116
Row 2	115	134	89	74	92	136
Row 1	79	94	85	96	90	138

Table 3.7: Final distribution of calibration sources into 42 positions. The position of viewer in scheme is on the Italian side with respect to the calibration sources. Figure takes advantage of similar colour coding to the one in Figure 3.26. Green font colour represents sources which were measured with plastic envelope while blue represents sources measured without plastic envelope. Yellow cell colour represents all the "golden" sources. Cell with no background colour are the "silver" sources and the rest.

row. Columns are numbered from 1 to 6. If we look from the Italian side of the lab perpendicularly at the Selenium foils (having Italian-side tracker between us and sources), the Column 1 is on the left and Column 6 on the right. Rows are numbered from 1 to 7 with Row 1 at the bottom and Row 7 on the top.

Sources were distributed in 42 positions based on the results of relative activity measure-

ments. The final distribution of the sources is showed in Table 3.7. Both the "golden" sources which were measured with plastic envelope (green font, yellow cell colour, Tables A.5 and A.6) and "golden" sources which were measured without plastic envelope (blue font, yellow cell colour, Table A.7) are independently distributed evenly in order to achieve electron exposure as homogeneous as possible. Note that, before installation of sources, all the plastic envelopes were removed from the sources which had them. After plastic envelopes were removed, positions in Figure 3.19 were no longer relevant for those sources. These positions corresponds to the ones in Figure 3.20 according to following key: UB $\rightarrow$ WO-SU, DB $\rightarrow$ WO-SD, US $\rightarrow$ WO-DU and DS $\rightarrow$ WO-DD. All 42 sources were, after plastic envelope removal installed in WO-DU position facing the Italian side of the lab. Downwards direction was defined with the direction of gravity. Sources were installed into new envelopes developed specifically for SuperNEMO.

3.3.2 Absolute Measurements

All "golden" sources and "silver" source number 76 (together 25 sources) were measured with detector depicted in Figure 3.28. I call it detector B. It is a coaxial Germanium detector. It was chosen for absolute activity measurements because its detection efficiency (at 15 cm) is known within 0.2% systematic uncertainty [98].

It was impossible to measure all of them due to limited time before the sources had to be shipped from CENBG to LSM for installation.

Detector B was used for all the measurements of absolute activities. Source was placed in front of the detector in a movable holder as seen in the figure.

3.3.2.1 Measurements of Source Depths

It was possible to set the distance between the holder and the detector with precision of 0.01 mm. In order to compute detection efficiencies (in our case it was done by simulation) one needs to know the distance (source-detector) with high precision.

Figure 3.29 represents detailed scheme of cross-sections of two types of the sources (with and without plastic envelope. Red dashed line is a reference line to which sampler holder

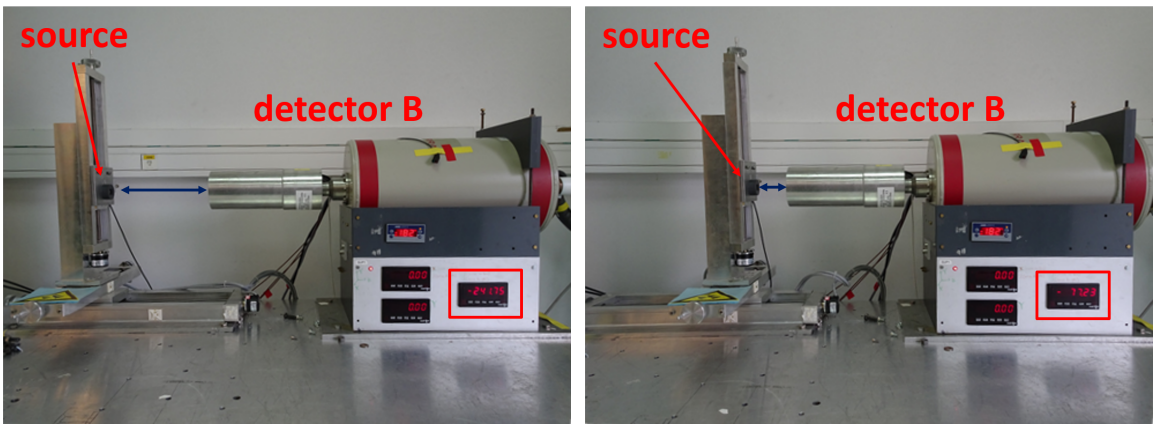

Figure 3.28: Photos of measurement of absolute source activities with detector B. The source was attached to a vertical holder. It was possible to move the holder closer and further from the detector and adapt the source-detector distance (blue arrows) with a precision of 0.01 mm.

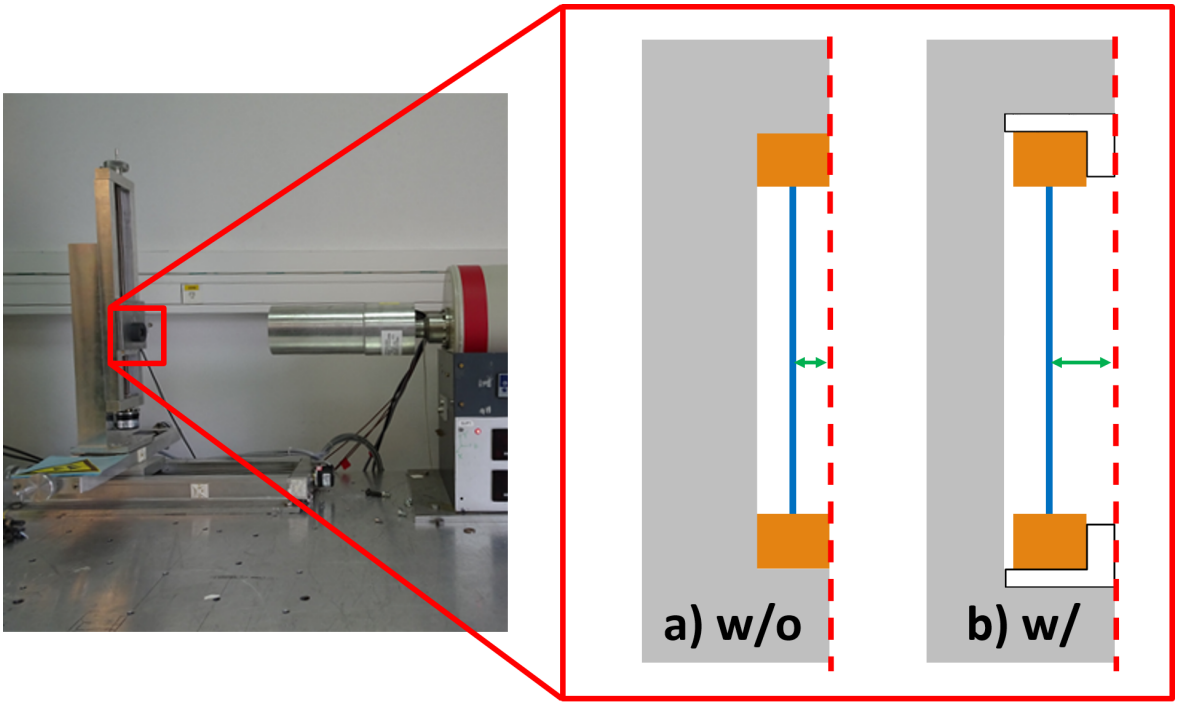

Figure 3.29: Schematic close-up cross section of source holder (grey) with source. There were two different sample holders for both types of calibration sources. Orange rectangles represent cross-section of source frame while blue line the mylar foil. Red dashed line represents an alignment level which was marking the position of source in horizontal direction. The sample holder for source w/ plastic envelope had deeper nest for source placement resulting in difference in offset (green arrows) with respect to red alignment level.

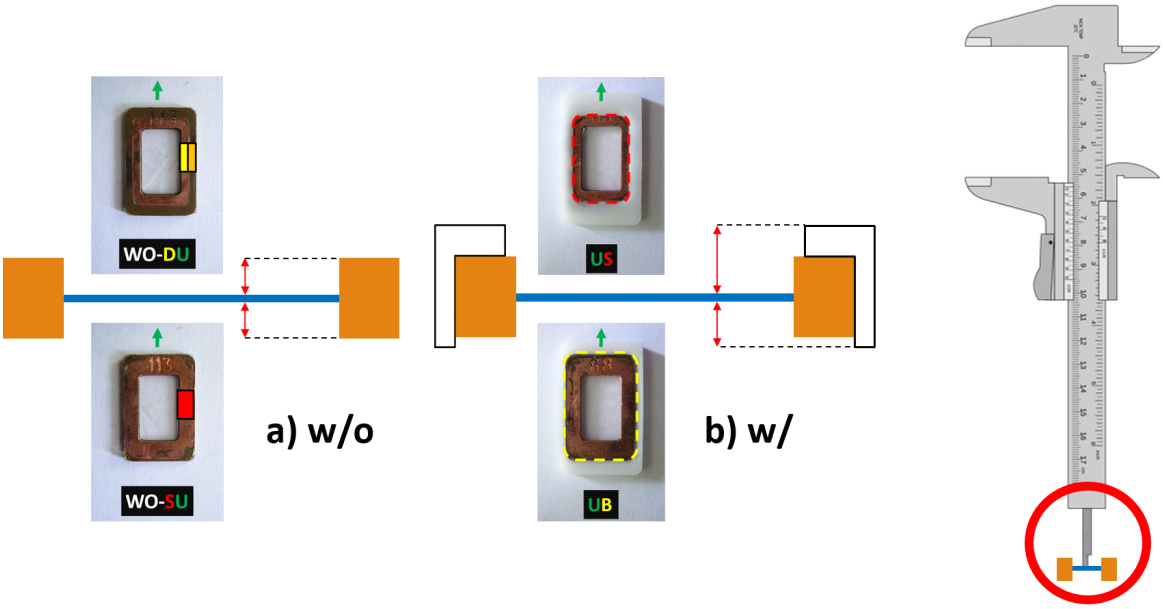

Figure 3.30: Rotated schematic cross section of calibration sources (Left) from Figure 3.29. In the scheme, the sample holders are now omitted. Red arrows depict four source depths which were measured in multiple measurements. Each photo marks the name of the side (WO-DU, WO-SU, US and UB). Right side of the figure shows scheme of the measurement setup of the depths (not to scale) performed by Vernier calliper.

(grey U-shaped object in scheme) was aligned. The presence of plastic envelope in case b) causes the offset of mylar (blue line) to reference line (red dashed line) marked by green arrows to be different to case a) without plastic envelope. The difference in these offsets causes difference in distances source-detector. It was necessary to measure the difference with sufficient precision in order to correct the position of the sample holder for two different cases.

Figure 3.30 shows schemes similar to the right side of Figure 3.29. For both types of sources (w/o and w/) the cross section of the calibration source through its thickness is shown in schematic way. The photos on top and bottom represents the name of the side of the calibration source. Red arrows are measured source "depths" whose difference result in the offset in distance source-detector explained in the Figure 3.29. Specifically, it is a difference between the depth of WO-DU and US causing the difference, as these were the sides of the calibration sources facing the detector in all absolute measurements. Even though, only WO-DU and US are relevant for the activity measurements, depths of sides WO-SU and UB were also measured in order to obtain full specification of the source dimensions. The depths were measured by depth probe of Vernier calliper as it is symbolised in the right side of the Figure 3.30. Each side was measured in ten repeated measurements in order to decrease measurement uncertainties. This gives 20 measurements per source and with 40 available sources it makes 800 measurements all together. Results can be found in Table 3.8.

Side	d [mm]	Δd [mm]
WO-DU	0.633	0.068
WO-SU	0.603	0.054
US	1.796	0.078
UB	1.275	0.063

Table 3.8: Results of measured source depths with their estimated uncertainties.

Results for depths of sides WO-DU and WO-SU are based on 140 measurements each (14 sources without plastic envelope) while depths of sides US and UB are each based on 260 measurements (26 sources with plastic envelope). The difference between the depth of US and WO-DU is 1.769 mm - 0.633 mm = 1.163 mm. Looking back to Figure 3.29 we can state, that in case of the activity measurement of source without plastic envelope holder should be measured 1.163 mm further away from detector in order to compensate for the offset.

3.3.2.2 Activity Measurements and Analysis

Measurements of the sources with detector B were always performed at source-detector distance of 75 mm. This distance, finally, after the offset correction was applied, always represented the distance of mylar surface (where the droplet of ^{207}Bi source is deposited) and the detector. Example of spectrum from measurement of source No. 114 can be seen in Figure 3.31.

Spectrum consists of many peaks originating in the natural background because in this case, the detector was not shielded. Figure also shows (in red) two ROIs containing 570 keV and 1064 keV peaks originating in the measured source. Second ROI contains only 1064 keV peak, therefore it was possible to fit it with a function in Equation 3.17. In case of 570 keV peak, ROI contains another two close peaks. It was, therefore fitted with sum of three

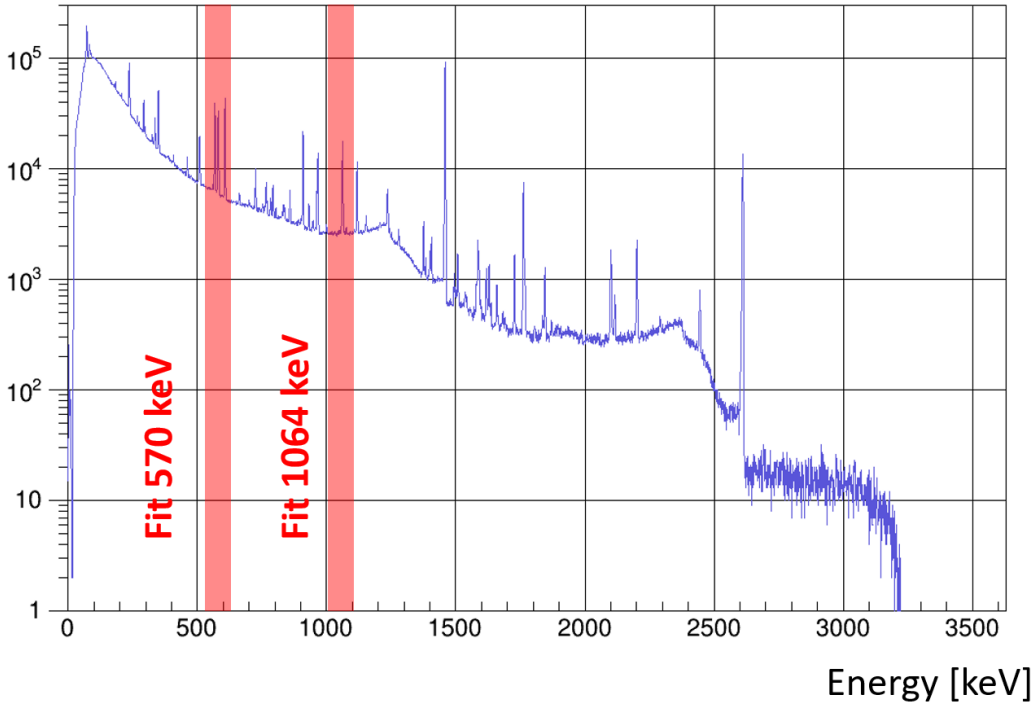

Figure 3.31: Spectrum of source number 114 as measured by detector B. Two red stripes mark the ROI used in the analyses of absolute source activities. Except for the peaks of interest (570 keV and 1064 keV) the spectrum contains many other peaks originating in natural background radiation because the detector was not shielded.

Gaussians on top of linear background:

$$f_3(E) = \sum_{i=1}^{3} \frac{N_i}{\sqrt{2\pi}\sigma_i} e^{-\frac{(E-E_0^i)^2}{2\sigma_i^2}} + aE + b. \tag{3.18}$$

E_0^i stand for the peak positions, σ_i for their widths and parameters N_i represent each peak's integral. Parameters a and b describe background. Parameter N_1 was of my interest as it was representing the integral of counts in 570 keV peak. Performance of the fit can be seen in Figure 3.32. Blue histogram (width of 1 keV) represents measured data in the zoomed region while red curve represents triple Gaussian fit.

After the integral in both the 570 keV (denoted N_{570}) and 1064 keV (denoted N_{1064}) was extracted, the activity can be computed using following equation:

$$A = \frac{N}{t_{live}\varepsilon r} \tag{3.19}$$

N stands for the integral in peak of interest (for 570 keV, N = N_{570} and for 1064 keV, N = N_{1064}). This number should be divided by live time of measurement t_{live} and corrected for detection efficiency ε and branching ratio r. Both detection efficiency and branching ratio are individual for each peak. Their values which were used in the computation of activities can be found in Table 3.9.

Table displays also the absolute uncertainties of branching ratios and detection efficiencies. The live time and number of counts in integral was, naturally, source specific. The uncertainty of live time is negligible and statistical uncertainty of integral (ΔN) was obtained after fit was performed. Uncertainties, as well as the peak counts, are included in Tables A.9

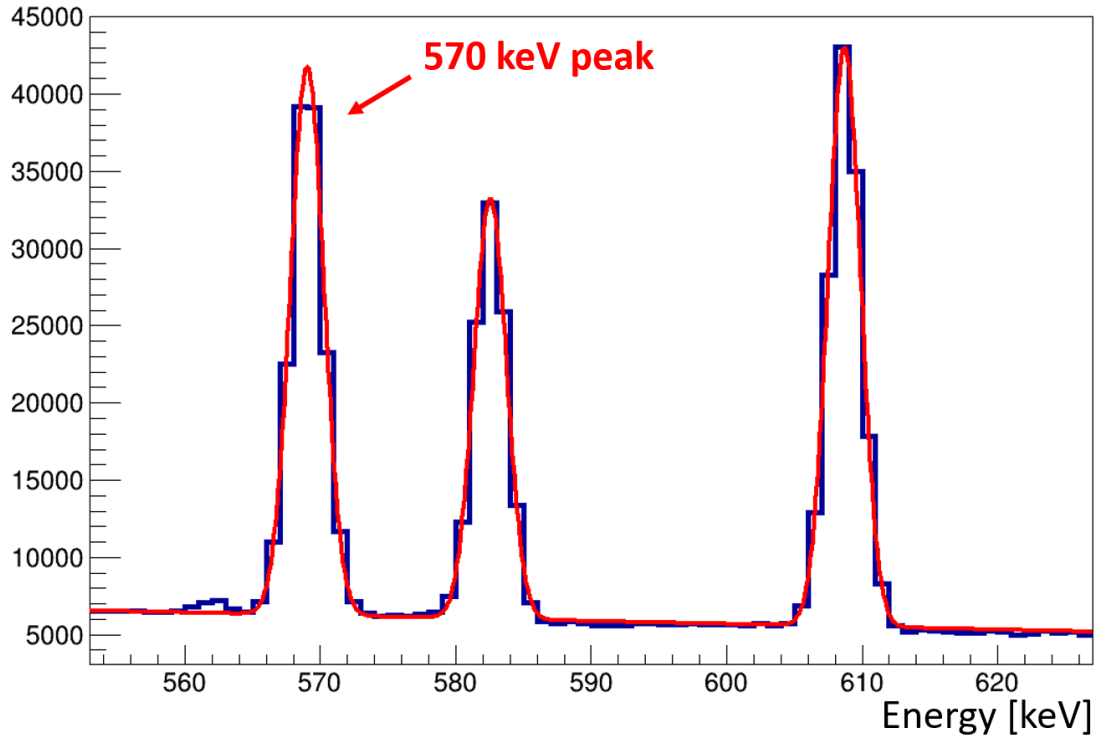

Figure 3.32: Zoom of the ROI in the vicinity of 570 keV from spectrum in Figure 3.31. Blue curve represents measured data and red curve the peak with triple Gaussian given by Equation 3.18.

and A.10 for my analysis and in Tables A.11 and A.12 for my colleague's analysis (discussed in following text). All the mentioned tables can be found in Appendix A.

The relative uncertainty of activity ΔA/A was obtained by formula:

$$\frac{\Delta A}{A} = \sqrt{\left(\frac{\Delta N}{N}\right)^2 + \left(\frac{\Delta r}{r}\right)^2 + \left(\frac{\Delta \varepsilon}{\varepsilon}\right)^2} \tag{3.20}$$

For each source, two values of activity was obtained. Naturally, these two values should give the same results as they describe the same source.

Figure 3.33 includes comparison of results for all 25 sources measured for absolute activities. Results of values obtained by analysis of 1064 keV have roughly two times larger relative uncertainty. It is caused by difference in relative uncertainty of detection efficiency. While in case of 570 keV $\Delta\varepsilon/\varepsilon \approx 0.1$ % for 1064 keV it reaches almost seven times higher value of 0.67%! In the figure one can also notice a discrepancy on a level of three sigma between the activities obtained by two different peaks.

E_γ [keV]	r [1]	Δr [1]	ε [1]	$\Delta\varepsilon$ [1]
570	0.9776	0.0003	0.0102	0.000011
1064	0.7458	0.0049	0.006739	0.000045

Table 3.9: Values of branching ratios (from [99]) and detection efficiencies (from simulations) with their uncertainties used in the analysis of absolute activities.

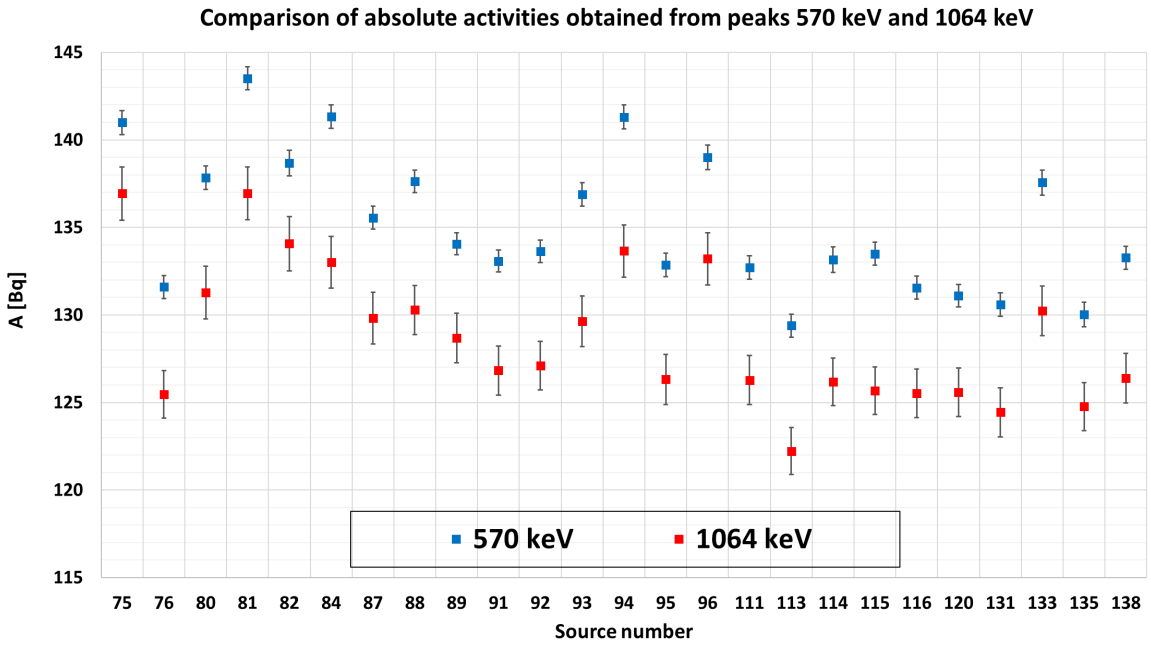

Figure 3.33: Comparison of absolute activities obtained in my analysis from two different peaks.

3.3.2.3 Discrepancy Between Results

Previous analysis of source activities offered two different value extracted from two different peaks. There are two possibilities how to approach such a situation. First of all it is possible to state that within 5% precision the values do agree if this kind of precision is sufficient for our needs. Nevertheless, the aim of the study is to obtain relative uncertainties approaching 1%.

Therefore, it is important to search for the refinement of the values used in analysis. If we look at the Equation 3.19, we can find three experiment-dependent quantities in the formula. Live time of the measurement, is known effectively with perfect precision. Other two - number of counts in the peak (N) and detection efficiency (ε) can contribute to the discrepancy. Let me discuss them in more detail.

Number of counts (integral) extracted from the peak depend on the analysis method. In order to investigate possible mistakes arising from fitting and extraction of number of counts, my colleague Frédéric Perrot set up an independent analysis method for extraction of peak counts in both the peaks 570 keV and 1064 keV. After he obtained number of counts (N) the activity was calculated using the same equation, i.e. Equation 3.19. He also used same value of detection efficiencies and branching ratios from Table 3.9. To put it into nutshell, our analyses analysed independently both peaks, differing only in the method of extraction of peak's integral. Figures 3.34 display the ratio (M/F) of my absolute activity values (M) divided by the ones obtained by Frédéric (F). In top part of the figure, comparative ratio is plotted for 570 keV peak while bottom shows the ratio for 1064 keV. Both analyses are producing consistent results well within the error. In other words, the analysis of Frédéric confirmed the discrepancy between two peaks observed in Figure 3.33. The agreement between our two methods have also shown that the explanation for discrepancy does not lie in the method of extraction of peak integrals but rather in the detection efficiency.

In the time scale of this thesis the investigations of detection efficiency values have

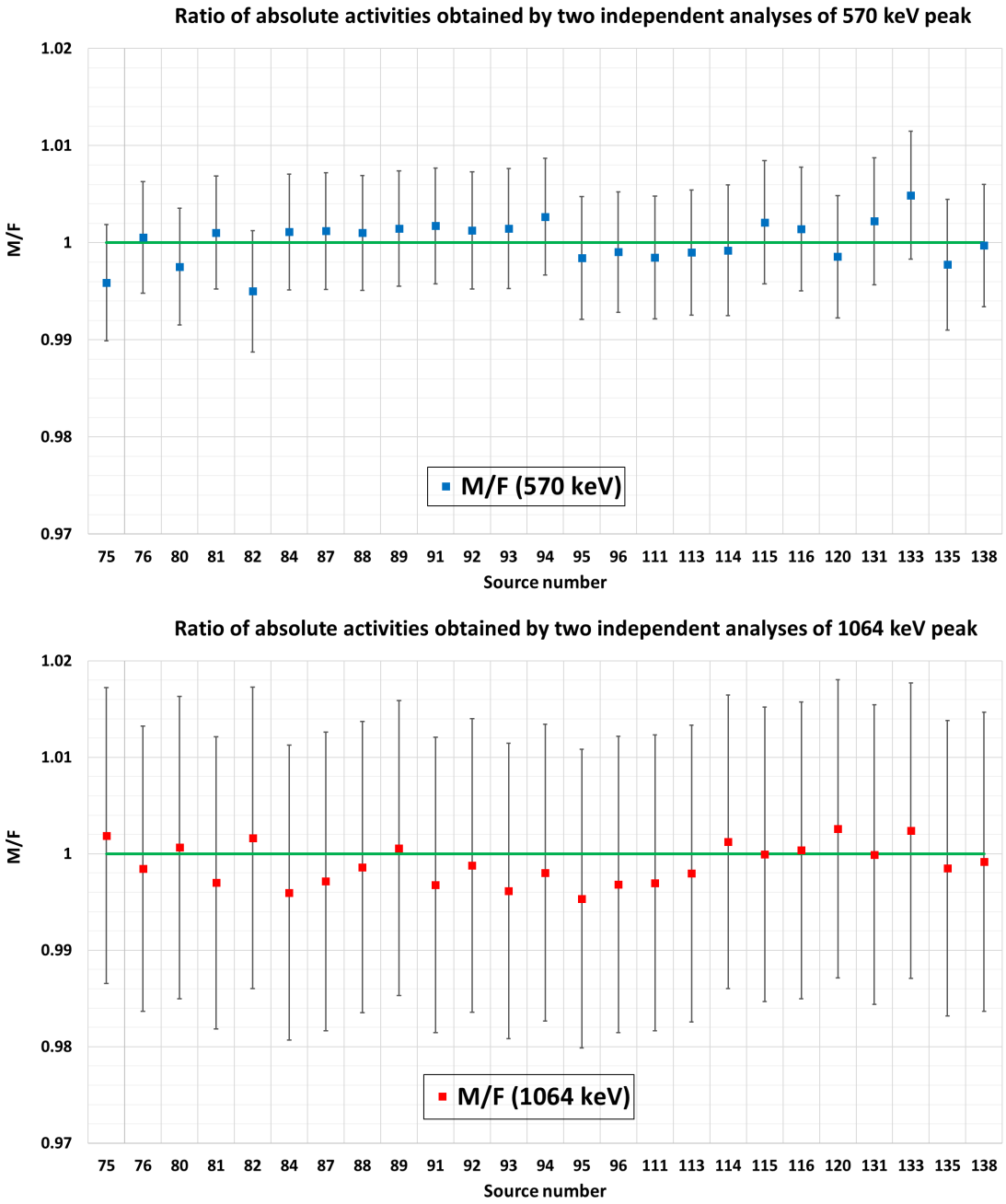

Figure 3.34: Comparisons of results of two independent analyses performed by me and Frédéric. BOth plots show ratio between absolute activity obtained by my method divided by same number obtained by Frédéric's method. Top plot (blue points) shows comparison for peak 570 keV, bottom plot shows comparison of 1064 keV peak. Within the uncertainties, the methods are fully consistent.

started, however, the results are expected to be obtained after its finalisation. The issue is investigated by our colleague in CENBG, Bertram Blank, who kindly provided the Detector B which was already well calibrated for 15 cm. However, the distance source-detector we used in our measurements was 7.5 cm in order to obtain larger statistics in shorter time. For this distance, the detector is not so well calibrated and, therefore, the discrepancy occurred. The detection efficiency for 7.5 cm will be obtained by measurement of source ^{60}Co with known activity. This isotope has two lines which are very close to the energies of gammas

we used in our analyses.

Absolute activities were calculated and within 5% uncertainty the results obtained from two peaks are consistent. However, the study is under investigation. Relative uncertainty of activities expected to be reached after it will be finished is 1%.

3.4 Conclusions

In the chapter, two studies of ^{207}Bi calibration sources were performed. In the first one, the source deposition quality within a source frame was studied. Study was performed by three Silicon Timepix detectors provided by IEAP CTU in Prague. Calibration, test measurements, and the final measurements were performed at the end of 2017. Analysis software was written and results were obtained at the beginning of 2018. Results have shown that no source sample had the ^{207}Bi deposited outside of the mylar foil, on the Copper frame. Five measured sources had the droplet deposited more than one milimeter away from center. When it comes to deposition quality, I conclude, that all the sources were proved to be eligible for calibration, however, the differences in quality were observed within one millimeter. Database of al the results and statistics can be found in Appendix A. Currently an article about the measurements is finished and will be submitted soon for a publication, after it would be approved by collaboration [97].

In the second study, source activities were measured. The uncertainty of activity value is the main contributor to the final uncertainty of $2\nu\beta\beta$ half-life. Study was separated in two measurements with two different Germanium gamma detectors, which I called A and B. With detector A in CENBG, 40 sources were measured during 2 hours each, and relative activities were obtained. Another two sources were measured in LSM with similar method. The measurements played a key role for the source installation in the detector. Based on the study, the sources were distributed in order to reach the best homogeneity of exposure from sources all around the calorimeters from main wall. With detector B, provided by my colleague Bertram Blank, measurements of absolute activities were performed in CENBG. Only 25 sources could be measured in these precise measurement, due to limited time the sources could stay in CENBG. The statistics during at least one day was collected for each source. Calculated activities of the sources were ranging from 125 Bq and 145 Bq. The analysis was based on the counts obtained by fit from 570 keV and 1064 keV peaks. For each source, calculated activity extracted from 1064 keV was typically smaller than the one obtained from 570 keV peak. This is a discrepancy which has to be accounted for, in order to reach 1% total uncertainty in the measurement. Independent method of study of my colleague Frédéric Perrot has shown the same behaviour, therefore, we can conclude, that the difference is not introduced in the analysis. The discrepancy arises from the detector calibration. The detection efficiency of the detector is known within uncertainty, on the level of 0.2% at the source-detector distance of 15 cm. However, the measurements were performed in a distance of 7.5 cm. After the detector efficiency for 7.5 cm will be extracted from measurements with ^{60}Co, the uncertainties of the absolute activities could be reported within the 1% uncertainty. This is a work beyond the scope of the thesis.

Chapter 4

Vertex Reconstruction Precision Studies

SuperNEMO has a very unique position in the field of double beta decay experiments. Information about particle tracks open a vast range of possibilities to test new physics. The real angular distribution at the moment of decay ("decay angle") is not measurable directly. Angle reconstructed by tracking algorithms is the one between the electrons at the moment when they leave the source foil ("escape angle"). Electrons in the source foil are scattered causing the differences between the decay and the escape angles. In order to probe their relationship, simulations are needed. The differences between the angles are studied and explained in Section 4.4.

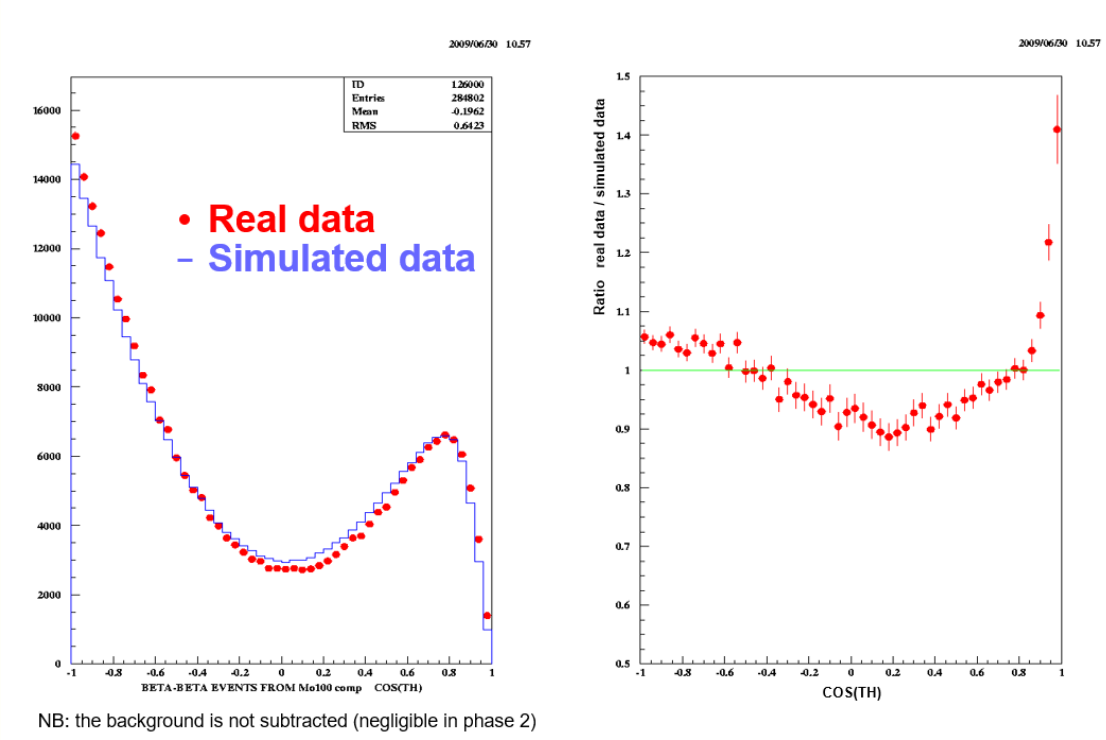

Figure 4.1: Left: Distribution of escape angles θ from $2\nu\beta\beta$ of ^{100}Mo. Figure compares data measured by NEMO-3 experiment (phase 2) with expected distribution obtained from simulation. Right: Ratio of real data to simulation obtained from the figure on the left. Green horizontal line marks value of 1, i.e. agreement of simulation with measurement. Both figures are plotted as a function of cos(θ).

Experience with NEMO-3 experiment have shown the discrepancy between expected distributions of escape angle obtained from simulation and the real data. It is depicted in Figure 4.1. The difference reaches as high as $\pm 10\%$. Moreover, in the case of antiparallel electrons the discrepancy can grow up to 40%. The difference might come from many possible sources. One of the possible explanations might lie in the performance of simulation. Code for calculation of electron scattering might need some improvements to reach sufficient precision. It is also possible, that the discrepancy is caused by poor performance of tracking algorithm in some particular event cases. These events can be identified and removed from dataset in order to improve the precision. Last, and the most exciting option is, that the discrepancy comes from unknown physical phenomenon. Nevertheless, before one could consider the last option, it is necessary to eliminate the other two (or any other possible explanation).

Studies of the discrepancies in NEMO-3 have shown no convincing signature of new physics. SuperNEMO will have opportunity to study the discrepancy in deeper detail. It will take advantage from much larger exposure as well as some other improved experimental parameters. On top of that, SuperNEMO's geometry is planar and, therefore, simpler. New geometry requires a new evaluation of the tracking precision.

The goal of presented chapter is to gain a first insight into the sources of imprecisions in the double beta decay vertex reconstruction. Vertex reconstruction precision (or just vertex precision) is used as a measure of performance of the tracking algorithm. Aim is to study the factors influencing the vertex precision, in order to provide guidelines which could help later in data analysis to improve precision of the angular distributions.

4.1 Description of Used Software Tools

4.1.1 Falaise

For the purpose of simulations, SuperNEMO software group, based in Caen, developed software package called Falaise. It is based on Geant4 software tool [100, 101, 102]. Falaise contains information about all parts of the demonstrator. Except for detailed geometrical models of source foils, tracking detector and calorimeter walls, all the important information about composition, physical properties are included. Based on ongoing performance measurements, these models are permanently improved and developed.

However, Falaise is more than only a tool for simulations. It also includes subpackages which will be later applied for data processing after the data taking will start. This is the reason why simulation with Falaise works in several steps:

1. **Application flsimulate** - This application provides the link to Geant4. It serves for the simulation of raw physical data. In Falaise, data are stored in so-called "data banks". Flsimulate fills data into SD (Simulated Data) bank containing information about particles (charge, mass, kinetic energy, etc.) and vertices. The data in SD bank is the real physical data as if it was measured by ideal devices. Flsimulate has many different useful parameters which can be adjusted. It offers broad range of processes which can be simulated. Except for $2\nu\beta\beta$ and $0\nu\beta\beta$ of ^{82}Se or ^{150}Nd it provides a choice of broad palette of background processes which can mimic double beta-decay, such as decay of ^{214}Bi or ^{208}Tl and many more. Moreover, number of simulated events can be chosen, as well as the position of the initial vertex, in form of geometrical address called GID (Geometry Identifier). GID is number storing information about

different parts of demonstrator geometry. For example GID = 1102 stands for source strip or GID = 1302 stands for main calorimeter wall, etc. Output of flsimulate is stored in file with extension .brio.

2. **Application flreconstruct** - As mentioned above, data from SD bank produced by flsimulate are raw data without inclusion of device imperfections. The data reconstruction as seen by real demonstrator is task for another application - flreconstruct. Brio file produced by flsimulate is taken as an input for flreconstruct. Flreconstruct contains information about the detector, e.g. resolution of optical modules. It also provides data analysis tools. One of them is CAT (cellular automaton tracker) which will be the central object of my studies in following sections. CAT is responsible for reconstruction of particle trajectories. The data from flreconstruct are gathered in CD (calibrated data) and PTD (particle track data) banks. CD bank contains data from SD bank after mock calibration with experimental uncertainties. PTD bank collects particle tracking points grouped into particle tracks as reconstructed by CAT. It also contains information about reconstructed position of foil or calorimetric vertices and connects them with individual reconstructed particle tracks. Similarly to flsimulate, flreconstruct offers output file with .brio extension. Except for aforementioned CD and PTD banks, this file also contains SD bank produced by flsimulate, which means, that it can be also used as an input for another run of flreconstruct. Flreconstruct requires so-called pipeline as an input. Further information about pipelines is given in text below.

3. **Pipeline** - Pipeline is a piece of special code which is calling reconstruction module required by flreconstruct. Some of these modules are already pre-coded in Falaise but they can be also written by user. They can be used for all types of data processing, but also only for a trivial application, such as a data printing on the screen. Name pipelines was given to this concept thanks to the way how they process the data. More pipelines can be chained into bigger pipelines to reach modularity of data processing. Each event is then processed by such chains of pipelines one by one.

4. **Application flvisualize** - It is capable to visualize .brio files into 2D and 3D images. Whole statistics can be browsed event by event and all event data from available data banks are displayed. Flvisualize is application which does not have to be necessarily used in the process of data analysis. Nevertheless, it is very useful for development of applications, e.g. to study special event cases which might not be taken into account otherwise. Example of output from flvisualize can be seen in Figure 4.2.

4.1.2 MiModule

Modules in Falaise can have a wide range of applications. In majority of the cases, they are used for the direct data analysis of the simulated samples in .brio files. However, .brio files produced by flsimulate or flreconstruct might be relatively bulky. They store all the generated information about the events in the sample including all the data banks and visualisation properties. For a specialized application, only a small fraction of the information might be necessary. The purpose of a module for Falaise, which I developed, is to store only the most necessary data into a form of .root files[1]. Depending on the simulated sample, this

[1]File extension .root is a data format provided by software package ROOT developed in CERN [103]. It is a powerful tool for data analysis.

approach produced up to more than 100 times smaller .root files. It allowed me to simulate 100 times bigger samples using the same storage capacity. Naturally, it came at the expense of versatility of such data. Nevertheless, I designed several versions of the module tailored specifically for the needs of performed study. Another disadvantage of the approach is a loss of possibility to visualize the events. However, the studies I have performed, had a character of statistical evaluation of simulated events. For this application, it was sufficient to test the performance of developed code on a small simulated and reconstructed sample with .brio files kept. The visualisation was used to tune the performance of the code. Afterwards, when the code was well tested, large samples of events were simulated and transferred using MiModule into .root files. Brio files keeping the visualisation data were not needed anymore and therefore deleted.

Let me now describe the module. It is composed of several classes labelled with prefix "Mi" which are able to store and handle the data. The main class "MiModule" is called by pipeline. It stores each event as an object of class MiEvent which stores SD, CD and PTD bank in form of pointers to instances of classes "MiSD", "MiCD" and "MiPTD" written by me. These classes are containing different data about event and have methods to operate with them. Even though, there was broad range of simulated and reconstructed data available, I stored only the most necessary data in each bank. For example, in the case of the vertex precision study, only the reconstructed vertex position, energy, particle angles, etc., are relevant. The purpose of MiModule is not only to transfer data files from one type to another. It has several classes and methods which were capable to decide whether the event is relevant for the study or not. For example, MiFilters is a class containing basic requirements on double beta like event (the requirements will be discussed later in the chapter). As an input, the class obtains object of class MiEvent and the output is a boolean logical variable which is true if the event passed all the inner filters incorporated in MiFilters class.

The .root files generated by MiModule I use as a source of data for all standalone applications performing the data analysis.

4.1.2.1 Class MiFilters

It is impossible to describe here all the classes of MiModule, however, class MiFilters plays a very important role in all of my studies, therefore, it is worth dedicating a section to the class.

MiFilters, as the name suggests, is responsible for event filtration. A .root file generated by MiModule contains a sample of raw events of any process. Falaise is able to generate (e.g. $2\nu\beta\beta$, $2\nu\beta\beta$ or background processes such as decay of ^{208}Tl or ^{214}Bi and many more). They are written in the file in form of objects of class MiEvent which keeps all the relevant information about the event. The amount of information stored in the object depends on the version of MiModule in use. Object of class MiFilters is given a pointer to an object of class MiEvent and it returns boolean value true if the event passes all the criteria incorporated in the MiFilter's class and false otherwise.

What is the criteria event has to pass? In a large spectrum of studies performed with Falaise one is uniquely interested in the events which can be considered as candidates for $2\nu\beta\beta$ or $0\nu\beta\beta$. Unwanted events are those, which do not resemble the topology and characteristics of $2\nu\beta\beta$ ($0\nu\beta\beta$). In this process, two electrons are emitted, which implies that two tracks and two calorimeter hits are expected to be seen by detector. In case, when, for example, only one track is seen, there is no guarantee that it comes from $2\nu\beta\beta$ (or $0\nu\beta\beta$). Regardless of whether it is caused by imperfection in detection technique or other influence, these events have to be filtered out. In each of my analyses in the thesis, I used following

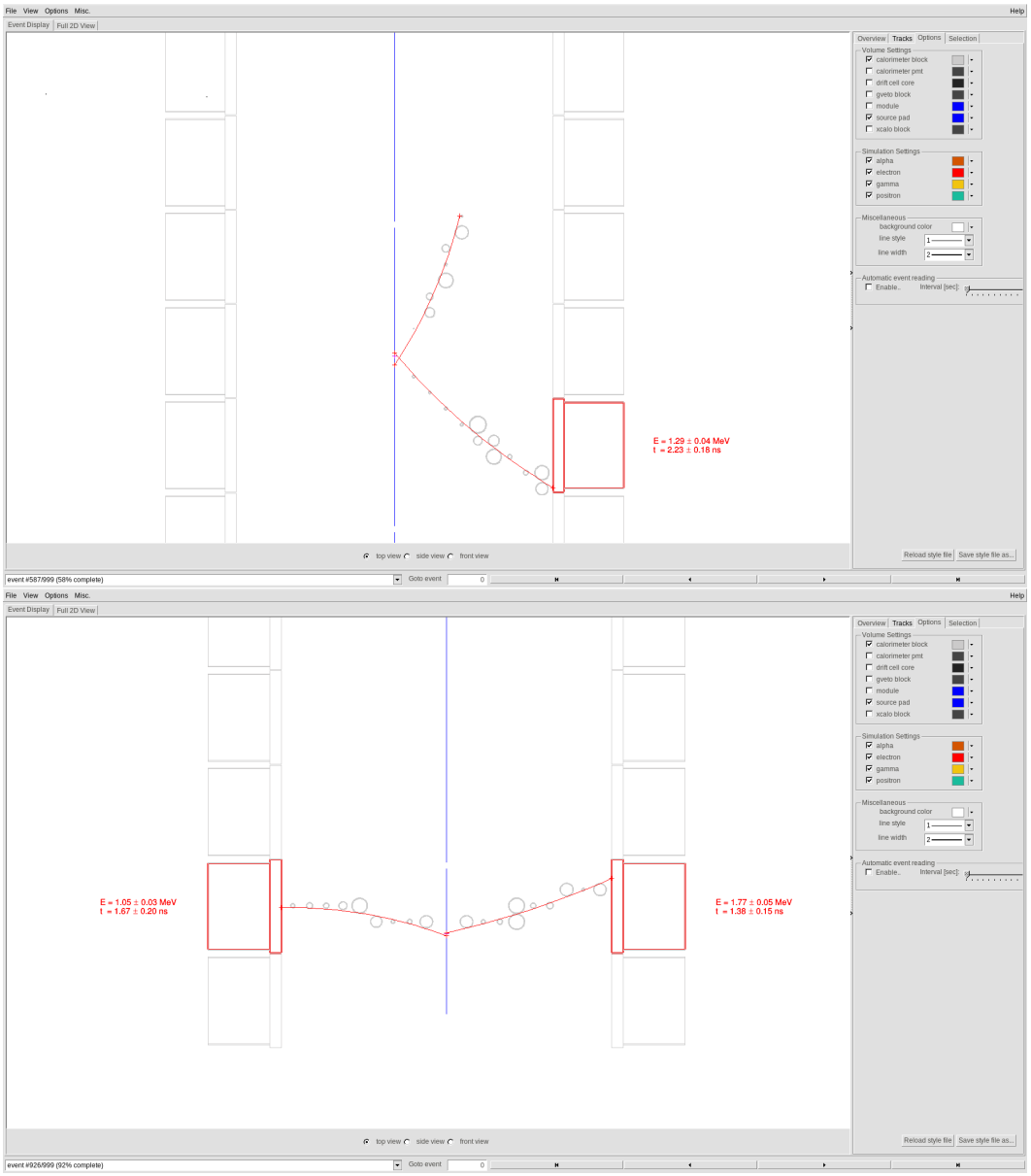

Figure 4.2: Example of output from application flvisualize. Both figures represent top view of SuperNEMO demonstrator. Figure on top represents example of rejected event which did not pass SDBDRC. Event though, it contains two reconstructed tracks, one of them is not associated to a calorimeter. Moreover, there is only one calorimeter hit. The event violates conditions A) and B). In contrary, lower figure represents example of event passing all of the conditions, thus it is accepted.

conditions to filter the events:

A) **Exactly two calorimeter hits** - Event has exactly two vertices (two signals) in two different optical modules.

B) **Exactly two associated calorimeter hits**[2] - Event has exactly two vertices in two

[2]Note that, the condition A) seems to be redundant because it imposes a looser condition on a event. In fact, both are important because if we had only condition B), for example even the events with three calorimeter hits, two of which are associated with particle track and one unassociated, would be accepted. Analogous situation arises in case of condition D) in relation to condition E).

different optical modules which are associated to two different particle tracks. Note that, gamma particles are able to trigger calorimeter blocks, but they do not leave out track in the tracker. That is the reason why only simple condition A) is not sufficient.

C) **Exactly two foil vertices** - In a real situation, naturally, double beta-decay has unique vertex in the source foil. After reconstruction of electron tracks, foil vertices do not overlap due to imprecisions of tracking and experimental uncertainties. This is the reason why exactly two foil vertices, instead of one, are required.

D) **Exactly two reconstructed particles** - In double beta-decay, we expect to see two electrons. In case when more or less particles would be reconstructed, it cannot be guaranteed that the observed process is double beta-decay.

E) **Exactly two negatively charged particles** - Electrons are negatively charged. The event is considered only in case if two reconstructed particles are negatively charged.

The list of the requirements could be extended based on various other (more or less) complicated criteria. The presented ones are basic standard and for the sake of simplicity I will call them Standard Double Beta Decay Reconstruction Criteria (SDBDRC). MiFilters adds one more condition to be passed - the energy range. Event passes this condition if sum of both measured electron energies are within the user defined range. The maximum and the minimum of the energy range is passed in form of two variables of type double to object of class MiFilters when the constructor of the object is called. The energy cut is not necessarily a strict criterion distinguishing between double beta event and backgrounds, nevertheless, it can be helpful to distinguish $2\nu\beta\beta$ from $0\nu\beta\beta$. Moreover, by inclusion of this condition, MiFilters acquires a tool for testing different energy cuts. Only in the case when event meets all these requirements, object MiFilters returns true value. In Figure 4.2 one can see examples of events rejected and accepted by MiFilters.

As I already mentioned, presented conditions are not only a natural requirements imposed on double beta event, it also serves as a source of background elimination. This can be seen from the results of simulations for four different processes in demonstrator: $0\nu\beta\beta$, $2\nu\beta\beta$, decay of ^{208}Tl and decay of ^{214}Bi. The last three are background processes able to mimic $0\nu\beta\beta$. Table 4.1 shows ratios of events passing the above conditions for different types of processes.

Process	Event acceptance [%]	Event acceptance (E > 2 MeV) [%]
$0\nu\beta\beta$	~ 27.8	~ 27.0
$2\nu\beta\beta$	~ 10.4	~ 0.3
^{208}Tl	~ 0.12	~ 0.04
^{214}Bi	~ 0.16	~ 0.012

Table 4.1: Event acceptances (or also detection efficiencies) for chosen processes simulated using Falaise. Acceptance is simple ratio (expressed in %) of accepted events after filtration using conditions explained in this section. Third column shows results for same filtration technique with extra condition (sum of the electron energies is more than 2 MeV).

Background events are more likely to be eliminated by aforementioned conditions than $0\nu\beta\beta$. Moreover, by imposing a condition on the sum of the energy of electrons, we can eliminate also $2\nu\beta\beta$ by factor of more than 30. This, of course, arises from the shape of double beta-decay spectrum (see Fig. 1.6).

Class MiFilters was employed in majority of the studies presented in the thesis. Whenever I discuss filtration of the events based on double beta event criteria listed in the section or energy cuts, it was performed by class MiFilters.

4.2 Definition of Vertex Precision Quantities

Imagine, that we have a simulated event of any process (double beta decay or background) which passed SDBDRC. The event has two electron tracks reconstructed by CAT. However, these two tracks have also two distinct vertices V_1 and V_2 on the source foil.

The situation can be understood from Figure 4.3 - Right. Here, two reconstructed vertices $V_1 = (x_1, y_1, z_1)$ and $V_2 = (x_2, y_2, z_2)$ are displaced from the real physical vertex V_r. The existence of two vertices (instead of one) is a result of experimental uncertainties in the measurement. However, the displacement of these two vertices relatively to the real one is caused also by an electron scattering inside of the source foil. Figure 4.21 represents simulated tracks of two electrons inside of the source foil as seen in simulation. The scattering influences not only the position of the electron when exiting the foil, it can dramatically change the side of the foil, where the electron exits. These effects can be studied only by simulations.

Figure 4.4 depicts the situation from Figure 4.3 seen from the side view. The rectangular area delimited by the vertices can be understood as a measure of imprecision in the vertex reconstruction. Therefore, its sides ($|\Delta y|$ and $|\Delta z|$) can be considered as individual measures

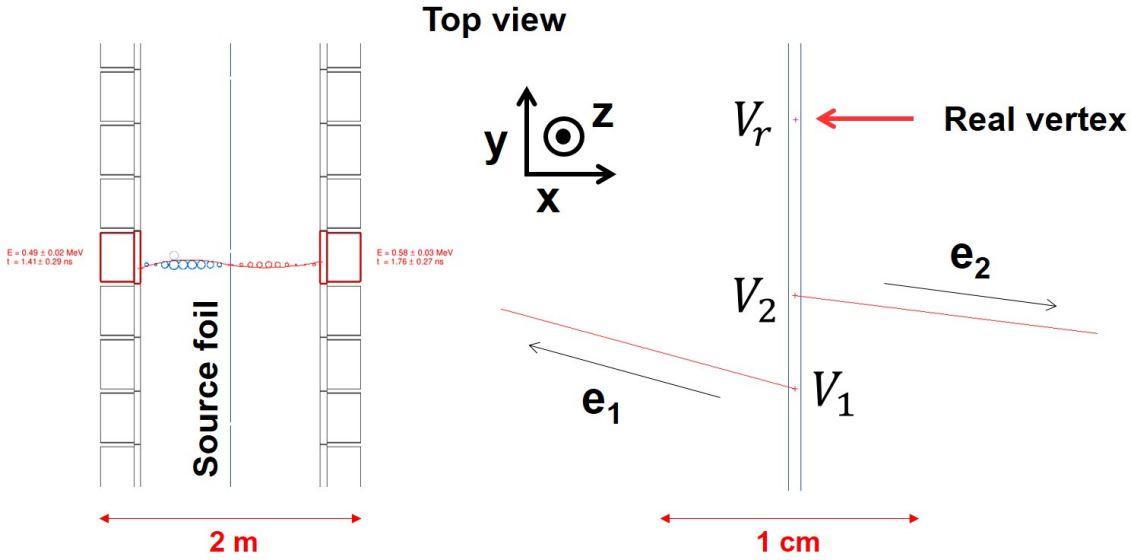

Figure 4.3: Left: Example of simulated $2\nu\beta\beta$ of ^{82}Se event which fulfils SDBDRC. Figure represents top view with source foil in the center and main calorimeter walls on the left and right. Right: Same event with zoom to the vertex. Figure depicts both reconstructed electron tracks (e_1 and e_2) in red, resulting in two different foil vertices V_1 and V_2. Third point, V_r represents real physical vertex not accessible in measurement.

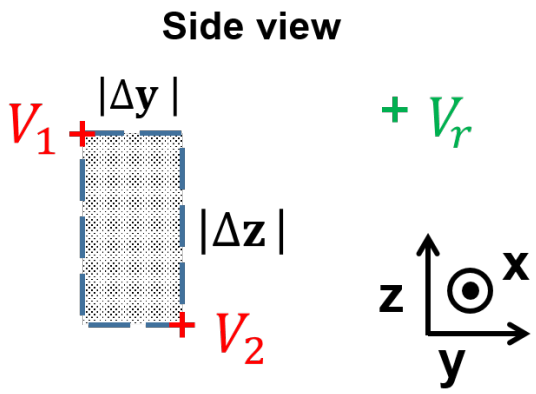

Figure 4.4: Side view on the situation from Figure 4.3. Two electron tracks are exiting the foil perpendicularly to the plane of view. Two red crosses are representing two reconstructed vertices V_1 and V_2. Together they delimit a rectangular area with sides $|\Delta y|$ and $|\Delta z|$ which will be the key quantities in the studies in this chapter. V_r represents position of real simulated vertex.

of the imprecision of vertex reconstruction in both directions parallel to the source foil. I will call them vertex residuals and they are defined in following way:

$$\Delta y = y_1 - y_2, \quad \Delta z = z_1 - z_2. \tag{4.1}$$

Note that, there is no absolute value in the definition of residuals, so they might hold positive as well as negative values. However, this peculiarity causes the distribution of the residuals in given event sample to be symmetric around the zero, rather than being defined only for positive values. The labelling, whether vertex has number one or two is decided based on the arrival time of the electron to the calorimeter. It explains why electrons with higher energies tend to be labelled by number one more often than the ones with lower energies. This effect can be observed in Figure 4.10. Residual in x-direction could be defined in the similar way as Δy and Δz ($\Delta x = x_1 - x_2$) but this quantity is not of the interest in the study as both vertices are always lying inside of the source foil. Source foil is only few hundreds of μm thick and the residual in the x direction is, therefore, always negligible.

4.2.1 Vertex Reconstruction Efficiency

In Figure 4.4 one can observe that, even though, the vertex uncertainty rectangle gives an idea of vertex reconstruction imprecision, it still does not guarantee that the physical vertex V_r would be lying inside of the rectangle. Therefore, it is important to conclude that the vertex residuals are representing mainly the reconstruction mismatch rather than how well it describes the real physical vertex.

In order to describe the rate, at which the real vertex is reconstructed properly within the uncertainty, I defined quantity which I named "Vertex reconstruction efficiency" or just "Vertex efficiency". The quantity is defined as a fraction of events in studied sample for which the projection of real vertex into yz plane is contained within the uncertainty rectangle given by absolute value of vertex residuals $|\Delta y|$ and $|\Delta z|$. The quantity is, however, not measurable.

In following, let us have a look at all the quantities of the interest which can be used to study vertex reconstruction precision.

4.2.2 RMS Precision

Analysis of vertex precision can be performed only when two foil vertices belonging to two tracks are reconstructed. This underlines the importance of already very useful SDBDRC. Possesion of a large sample of events which passed SDBDRC opens a possibility to study vertex residuals statistically. For each event, one can calculate pair of residuals Δy and Δz and represent them in the histograms as it can be seen in the Figure 4.5.

While the distribution of Δz residual resembles Gaussian shape, the distribution of Δy seems to be more pointy, with sharply falling tails. The discussion about a proper description of the shape is presented in following section.

Distributions for both vertex residuals are distributed symmetrically around the zero value. These values represent events when vertices were perfectly matched in the given direction (not necessarily in the other direction). As we are moving further from the center of the horizontal axis, the histogram represents events with continuously higher mismatch

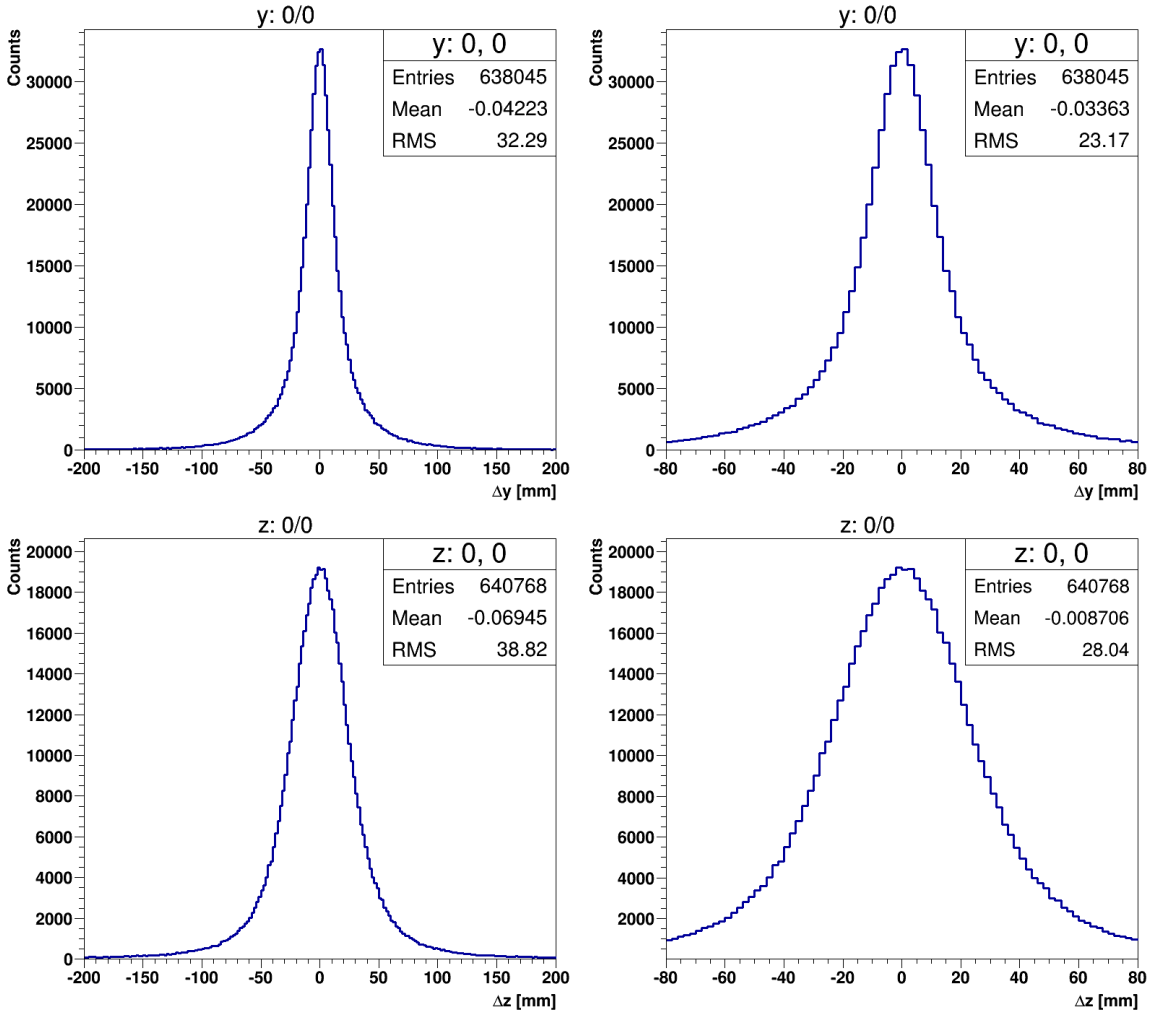

Figure 4.5: Vertex residuals extracted from 4×10^7 simulated events of $2\nu\beta\beta$ of ^{82}Se. The sample represents all the events which passed SDBDRC and energy of each individual electron was in the range from 0 keV to 500 keV. While upper row represents histogram of Δy residuals in the sample in two regions (-200 mm $< \Delta y <$ 200 mm and -80 mm $< \Delta y <$ 80 mm), lower figures represent a histogram of the Δz residuals for the same sample in the same limits.

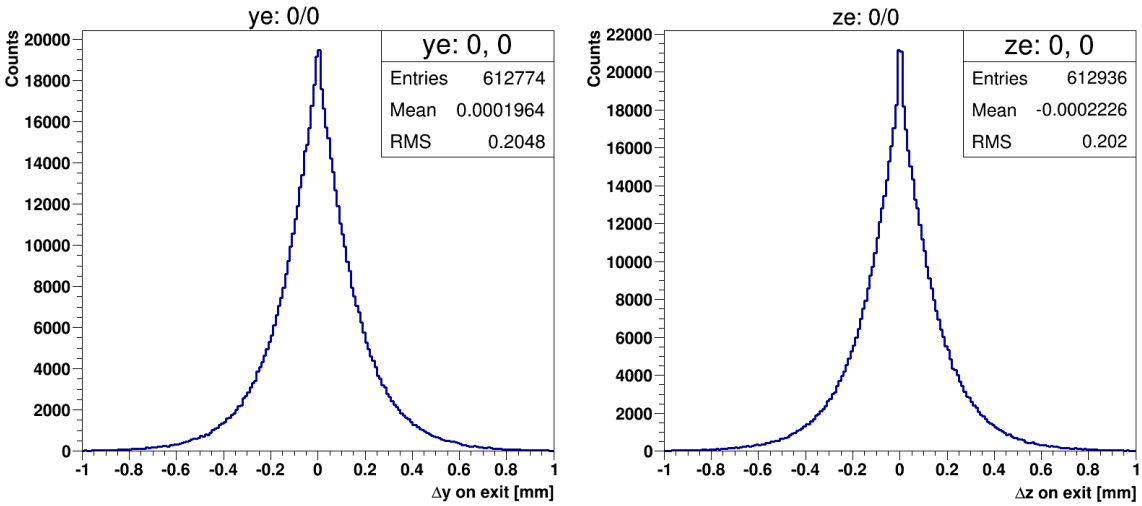

Figure 4.6: Δy and Δz differences extracted from electron positions exactly in the moment when they exited source foil. Plots are extracted from the same data as residuals in Figure 4.5. Note that, these Δy and Δz differences should not be mistaken for the vertex residuals which are defined inside of the foil, not on the surface. Left: Distribution of Δy differences. Right: Distribution of Δz differences.

between the vertices in given direction. Therefore, wide distribution represents statistically higher rate of mismatched vertices than in the case when the distribution is narrower (given the same height). In ideal experiment, with no uncertainties in the particle tracking, one would expect delta function shape placed exactly in zero. This is, however, not completely true. It was already mentioned, that the vertex precision is spoiled by experimental uncertainties as well as the effect of electron scattering inside of the Selenium source foil (depicted in the Figure 4.21). In Figure 4.6 one can observe the effect on vertex mismatch caused by the electron scattering inside of the source foil. Plot represents distribution of Δy and Δz differences between electron positions exactly in the moment when they reach the surface of the source foil, i.e. in the moment when they exit from the foil. Obtained values of positions are not influenced at all by the experimental uncertainties, as they were extracted from the database of simulated tracks (SD bank in Falaise) before reconstruction. Therefore, the figure represents uniquely the influence of the scattering. While basically all the samples of Δy and Δz differences on the exit from the foil are contained well within the 2 mm range (-1 mm, 1 mm), the width of distribution of reconstructed vertex residuals goes well beyond reaching widths of tens of mm. We can state, that the scattering effect has some, but negligible effect on the vertex reconstruction precision. Note that, the distributions of Δy and Δz on exit from the foil have the same distributions in both directions. This should not be surprising, because the distribution is driven by a physical effect isotropic in both directions parallel to the source foil. Nevertheless, this is not true for the final reconstructed vertex residuals. The reconstruction generally works more precisely in y direction. Hints of this difference can be already observed in Figure 4.5 but will be clearly visible in the presented data in following sections.

We can conclude, that the width of the distribution of vertex residuals can serve as a measure of the vertex reconstruction precision. There are several possibilities how to express the width numerically. First one, which I used to analyse simulated samples is a standard deviation. It was already discussed that the center of the distribution of vertex residuals is expected to be in zero, i.e. $\overline{\Delta y} = 0$ and $\overline{\Delta z} = 0$. Taking this fact into account, the standard

deviation formula is simplified into form:

$$RMS_y = \sqrt{\sum_{i=1}^{N_y} \frac{(\Delta y)^2}{N_y}}, \quad RMS_z = \sqrt{\sum_{i=1}^{N_z} \frac{(\Delta z)^2}{N_z}}. \tag{4.2}$$

Standard deviation became simple RMS. While vertex residuals Δy and Δz represent vertex precision of an event, the RMS_y and RMS_z represent the precision of the whole chosen sample. Therefore, it represents the overall performance of the reconstruction algorithm and the tracker itself under given conditions (for example: different decays, electron energies, emission angles and many more). These quantities, I will refer to as RMS precision in y or z direction.

In two histograms on the left side of Figure 4.5, we can observe that RMS_y = 32.29 mm and RMS_z = 38.82 mm. However, the histograms on the right side of the figure show different values: RMS_y = 23.17 mm and RMS_y = 28.04 mm. These two plots represent exactly the same datasets, only in the narrower range. RMS value is very sensitive to values in the tail. It changed significantly, even though, I omitted only negligible amount of the entries in the histogram. This is a subjective element of the method which should be avoided. Therefore, the RMS precision in this thesis is understood as a value obtained when the distribution of the vertex residuals is limited to following interval: -200 mm < Δy, Δz < 200 mm. This convention opens a possibility to discuss the precisions of different samples in relative sense. As a demonstration, we can conclude that the precision in z-direction is less precise than in y-direction as it was already mentioned above. Nevertheless, it would be somehow irresponsible to try to interpret these values as the absolute measures of precision. In order to obtain such quantity I introduced another, complementary method presented in next section.

4.2.3 FWHM Precision

Second method used in the thesis, used for evaluation of precision of vertex reconstruction, is based on the FWHM of the distribution of vertex residuals.

In order to extract FWHM from a distribution, one needs to know proper fitting function which precisely describes the distribution. Let me, firstly, focus on vertex residual Δy. As a starting point in search for the distribution function of vertex residual Δy, we have to keep in mind its definition. Δy is a difference between two random variables y_1 and y_2, i.e. $\Delta y = y_1 - y_2$. Let me define $f_1(y_1)$ and $f_2(y_2)$ as their respective distribution functions. In that case, $f_1(y_1)f_2(y_2)$ represent probability to find simultaneously first vertex in point with coordinate y_1 and second vertex in point with coordinate y_2. However, we are interested only in the couples of given residual Δy. Therefore, we cannot choose both variables simultaneously. Choice of y_2 fixes y_1 at $y_1 = \Delta y + y_2$, for given Δy. Probability to simultaneously find these two values is then equal to $f_1(\Delta y + y_2)f_2(y_2)$. If we now integrate over all scenarios, i.e. all possible values of y_2, we obtain distribution function of a vertex residual $F(\Delta y)$:

$$F(\Delta y) = \int_{-\infty}^{\infty} f_1(\Delta y + y_2) f_2(y_2) dy_2. \tag{4.3}$$

This is well known convolution formula. Presented equation would hold in case if y_1 and y_2 would represent two completely independent variables. Nevertheless, y_1 and y_2 are reconstructed coordinates of two vertices which are expected to be approaching each other. It implies that both y_1 and y_2 should be correlated.

Moreover, as it is demonstrated in Figure 4.7, the correlation between the respective vertex coordinates is very strong and, therefore, Equation 4.3 has to be generalized. Two

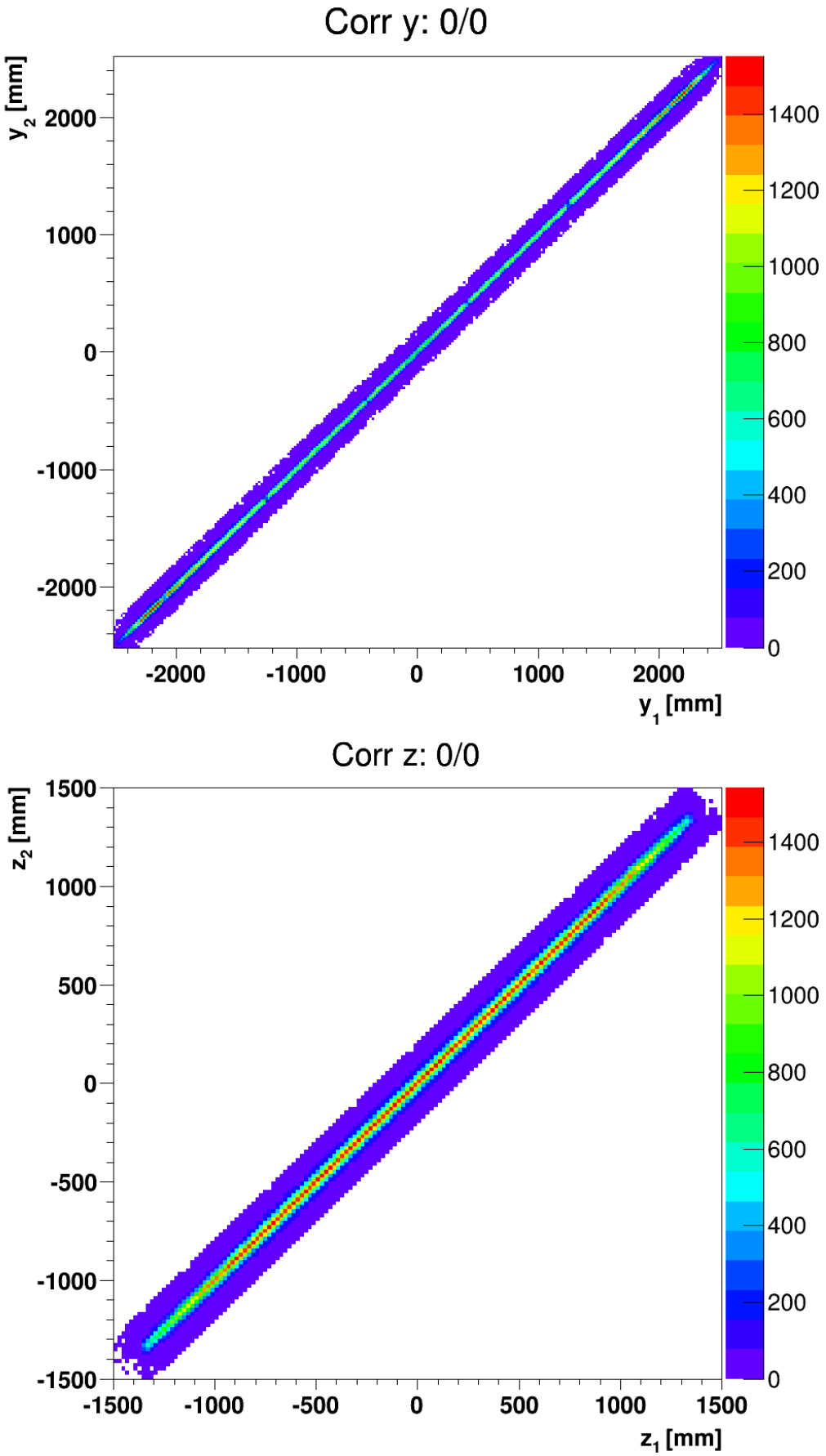

Figure 4.7: Correlation plots of reconstructed vertex coordinates y_1 vs. y_2 (top) and z_1 vs. z_2 (bottom). Presented sample is the same as the one used in Figure 4.5.

dimensional distribution function $f_1(y_1)f_2(y_2)$ was split into two functions of single variable. This was due to the independence of the variables. In case with the correlation, it is impossible to perform this simplification and one has to assume general two dimensional distribution function $p_y(y_1, y_2)$ of y coordinates of reconstructed vertices in given sample. If we now repeat the same procedure as in the previous case, we arrive to generalization of Equation 4.3:

$$F(\Delta y) = \int_{-\infty}^{\infty} p_y(\Delta y + y_2, y_2) dy_2. \tag{4.4}$$

This formula represents recipe for calculation of distribution function of vertex residual Δy in case when y_1 and y_2 are correlated. Naturally, analogous relation holds for the distribution of vertex residual Δz.

Equation 4.4 provides theoretical basis for our search for fitting functions of distributions $F(\Delta y)$ and $G(\Delta z)$. In order to obtain their analytical formula, one would need to guess acceptable analytical formula for two dimensional distributions $p_y(y_1, y_2)$ and $p_z(z_1, z_2)$. Moreover, if we look at the plots in Figure 4.8, showing projections of distributions in Figure 4.7 into y_1 and z_1, we can probe the structure of both two dimensional distributions p_y and p_z in more detail. One could expect that both projections would be uniformly distributed as the vertices are simulated evenly all over the volume of source foil. However, this is far from truth for two reasons. Firstly, it is possible to observe a narrow local minimums in form of bins with significantly lower counts than the neighbouring ones. It is due to the gaps between the Selenium source foil stripes. This phenomenon occurs only in case of projection p_y because the foil is segmented only along horizontal (y) direction (see Figure 4.8 - Top). The bins are not strictly empty, as they should be, because of their width and also vertex can be reconstructed in principle in the gap due to imprecisions in reconstruction. Secondly, even if we ignore the gaps, neither of the distributions is flat. The reason is, that all the samples had to pass SDBDRC before the vertex could be even evaluated. The deviation of both distributions, therefore, represent not the distribution of simulated vertices but the reconstruction success rate in y and z direction. The shape in y-direction is also influenced by presence of the magnetic field. This phenomenon is discussed in detail in Section 4.6.

Let me now briefly sum up all the most relevant findings obtained during the hunt for proper analytical form of fitting functions $F(\Delta y)$ and $G(\Delta z)$. As a theoretical recipe, Equation 4.4 should be preferentially used to obtain distribution $F(\Delta y)$ ($G(\Delta z)$) because of the strong correlation between y_1 (z_1) and y_2 (z_2) demonstrated in Figure 4.7. In order to do that, one would need to know analytical form of two dimensional distribution $p_y(y_1, y_2)$ ($p_z(z_1, z_2)$). It might be difficult to find it, due to its rather complicated form demonstrated at the projections in Figure 4.8.

It is reasonable to expect that functions $F(\Delta y)$ and $G(\Delta z)$, even though, they are represented by a single peak, might not be properly described by some basic Gaussian or Lorentz function, as one may intuitively expect just by looking at the plots in Figure 4.5. Therefore, I decided to propose an ansatz which would have proper degrees of freedom to describe the distributions $F(\Delta y)$ and $G(\Delta z)$ well enough. The choice was following:

$$f(x) = \frac{N}{\left[x^2 + \Gamma\right]^p} \tag{4.5}$$

Squared argument ensures the symmetry of the function, Γ is related to characteristic width of the peak and exponent p gives possibility to tune the rate at which the tails of the function drop. Finally, N is scaling constant, so it was not necessary to normalize the

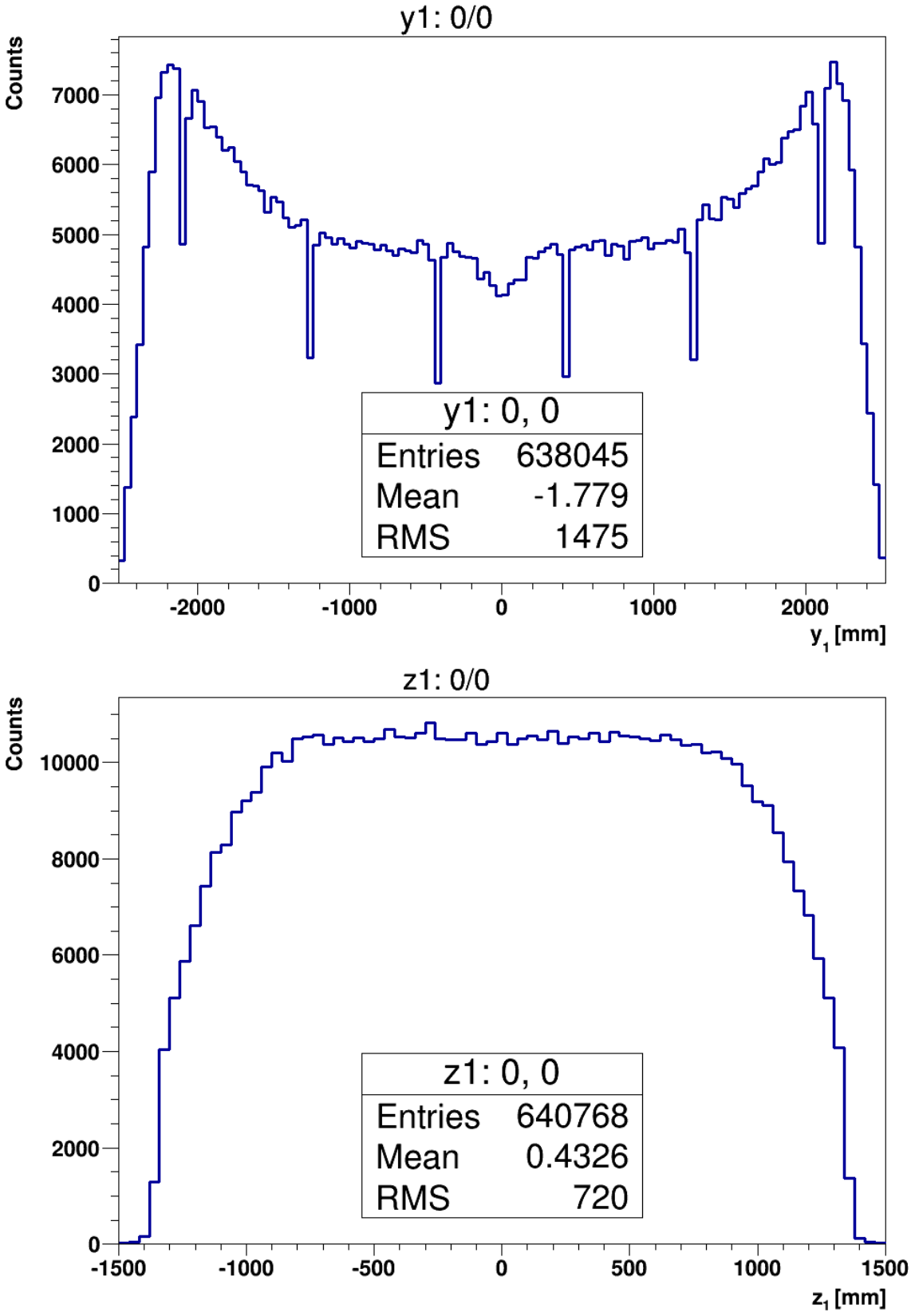

Figure 4.8: Distributions of vertex coordinates of first electron - y_1 on top, z_1 bottom. Distributions were extracted from the same dataset as presented in Figure 4.5. Distributions of y_2 and z_2 look the same, therefore they are not presented in the figure.

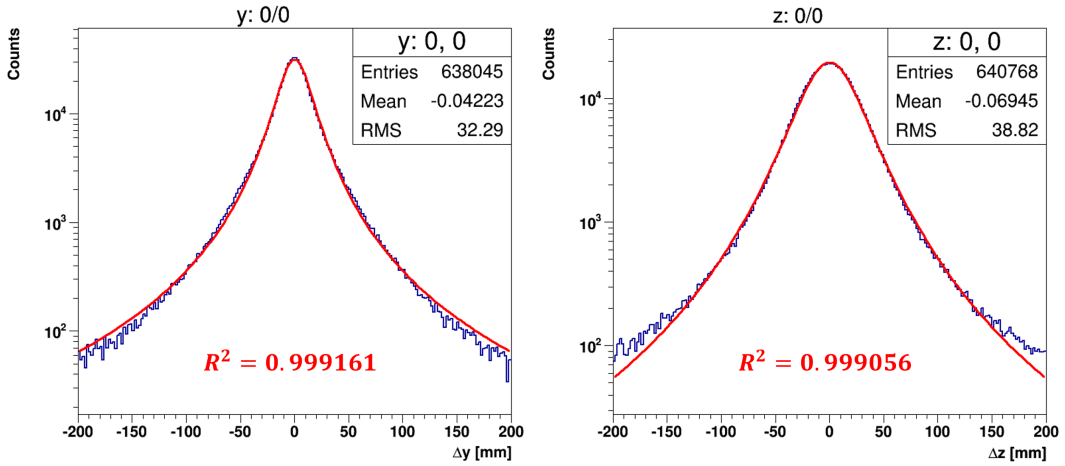

Figure 4.9: Histograms of vertex residuals from Figure 4.5 after they were fitted by function from Equation 4.5. Δy is on the left and Δz on the right side. Plots are shown in logarithmic scale. Function covers satisfactorily majority of the histogram with slight deviation in tails.

fitted distributions. Proposed fitting functions were tested and they proved themselves to be generic enough to describe the distribution of vertex residuals in both directions y and z. Figure 4.9 shows examples of functional shapes from Equation 4.5 fitted to histograms from Figure 4.5. As it will be clarified in following sections, these functions describe the distribution of vertex residuals very precisely in very broad range of different sets of samples if sample size was sufficient. In order to control validity of fit, R^2 was evaluated for every single fit. More about the validity check can be find in Sections 4.3 and 4.4. In Section 4.4 I also present performance comparison of fitting functions from Equation 4.5 with Lorentzian (Δy distribution) and Gaussian fit (Δz distribution).

Having an analytical formula for distributions of vertex residuals, it is possible to extract FWHM value of the fitting function. It is trivial to find a global maximum of the function which lies in the center in point $x = 0$ and has value of

$$f_{max} = f(0) = \frac{N}{\Gamma^p}. \tag{4.6}$$

The points $x_h^{\pm}$ where the peak drop to half of its value can be obtained from equation:

$$f\left(x_h\right) = \frac{N}{\left[x_h^2 + \Gamma\right]^p} = \frac{N}{2\Gamma^p}. \tag{4.7}$$

Solution to this equation is following:

$$x_h^{\pm} = \pm\sqrt{\Gamma\left(\sqrt[p]{2} - 1\right)}. \tag{4.8}$$

Finally, FWHM is the distance between x_h^- and x_h^+:

$$FWHM = 2\sqrt{\Gamma\left(\sqrt[p]{2} - 1\right)}. \tag{4.9}$$

After distribution of vertex residuals Δy and Δz for given sample was fitted by function in Equation 4.5, two sets of fitting parameters (N_y, Γ_y, p_y and N_z, Γ_z, p_z) were obtained. Based on these parameters $FWHM_y$ and $FWHM_z$ were calculated using Equation 4.9. $FWHM_y$ ($FWHM_z$) I call "FWHM precision" of vertex reconstruction in y(z). FWHM represents

full width of the peak of distribution of vertex residual including the negative half. This half arises due to vertex residuals to be defined not as a distance (absolute value: $|y_1 - y_2|$) but as an oriented one dimensional vector: $\Delta y = y_1 - y_2$. Therefore, the real reconstruction imprecision is half of the FWHM value. However, all the plots in the studies will use FWHM precision as a convention.

4.2.4 Sigma Precision

RMS and FWHM represent measures of peak width. RMS is easy to calculate and it is possible to evaluate it even for smaller studied samples. RMS also depends strongly on the chosen range of vertex residuals even in case when only negligible portion of the range is excluded from the sample. RMS is useful as a easy-to-calculate, fast comparison of two samples under condition that we compare the samples for the same range of vertex residuals. On the other side, FWHM serves well as an absolute measure of the vertex precision. However, it is very dependent on the quality of fit, which is poor for small samples. Nevertheless, whenever it is possible, we take FWHM as a representative quantity for evaluation of vertex reconstruction precision.

The aim of following study was to perform comparison of performance of CAT reconstruction in different conditions. FWHM serves well for the purpose. However, another goal is to study possibilities for data cuts to improve signal to background ratio. In order to do that, one needs to compare ranges of vertex residual covering a constant portion of events in different samples. FWHM region ensures stable proportion between peak's height and width in half maximum value but, it is not sensitive to the shape of the function inside of the region. Therefore, FWHM region can cover, in principle, different portions of area under the curve in dependence on the shape of the function. In order to account for this slight variability of shapes, I defined third quantity which I call "sigma (σ) precision".

σ precision is defined as a half of the symmetric interval covering central 68.27% area under curve. It is a σ value for which

$$0.6827 = \frac{\int_{-\sigma}^{\sigma} f(x)dx}{\int_{-\infty}^{\infty} f(x)dx} = \frac{\int_{0}^{\sigma} f(x)dx}{\int_{0}^{\infty} f(x)dx}. \tag{4.10}$$

Here, f(x) represents fitting curve from Equation 4.5. Integration in Equation 4.10 was performed numerically. Ratio of integrals was approximated in following way:

$$R_L = \frac{\sum_{n=0}^{n\Delta x<L} f(n\Delta x)\Delta x}{\sum_{n=0}^{f(n\Delta x)\Delta x<\varepsilon} f(n\Delta x)\Delta x}. \tag{4.11}$$

Note that, in this formula Δx represents numerical integration step and not the vertex residual in x direction. Its value was chosen to be $\Delta x = 10^{-3}$ mm. Cut-off value for infinite integral in denominator was chosen to be $\varepsilon = 10^{-9}$ mm. σ precision is then value of L when R_L = 0.6827. σ precision is naturally defined for both directions y and z. It is a useful quantity for discussion of possible data cuts on vertex because, by definition, interval

$-\sigma < \Delta y, \Delta z < \sigma$ always contain 68.27% of events in given sample. The difference in σ between two samples might be a sign for a establishment of new data cut potential.

4.3 Vertex Precision as a Function of Electron Energy

Study presented in this section is first out of several different vertex precision studies which I performed during my PhD. studies. Aim of the studies is to investigate how precisely is a double beta decay vertex reconstructed in variety of situations. The goal is to quantify the precision and give insight into uncertainties of the angular distributions reconstructed by demonstrator. Such a study might as well contribute to search for new potential data cuts which would favour expected signal over the background.

Reconstruction of the tracks in SuperNEMO demonstrator is performed by CAT (cellular automaton tracker). The tracks are stored in the form of points - signal from individual Geiger wires. Each triggered Geiger wire, provides information about horizontal distance "r" between wire and passing particle and the vertical particle position "z" along the wire. CAT reconstructs and connects each point in order to determine particle tracks, taking into account associated uncertainties.

Precision of the reconstructed tracks can be evaluated by quantification of foil vertex mismatch, as it was extensively discussed in previous sections. Main aim of this study is to determine vertex reconstruction precision as a function of energy of each individual electron. Table 4.2 summarizes all the data samples which were studied in this and following sections.

Following the standard procedure in Section 4.1.1, each dataset was simulated using application flsimulate and reconstructed by flreconstruct using standard SuperNEMO mock calibration pipeline 1.0.0. As a next step, I applied MiModule to reconstructed datasets and obtained .root files ready to be studied.

Analysis program read each event in given data sample. Firstly, object of class MiFilters filters events according to SDBDRC criteria. Obtained reduced sample is subsequently separated into subsamples based on the energy of individual electrons. Each subsample represents one bin in two-dimensional histogram. Figure 4.10 depicts distribution of events among subsamples for chosen data samples. Horizontal axis represents energy of first electron (E_1) and vertical axis represents energy of second electron (E_2).

These two-dimensional distributions are symmetric with respect to axis $E_1 = E_2$. It is

Samp.	Process	Nucleus	Magnetic field [G]	Number of simulated events
S1	β^-	^{208}Tl	25	9.62×10^7
S2	β^-	^{214}Bi	25	2.076×10^8
S3	$0\nu\beta^-\beta^-$	^{82}Se	25	1.04×10^8
S4	$0\nu\beta\beta\chi^0$	^{82}Se	25	1.04×10^8
S5	$0\nu\beta\beta\chi^0\chi^0$	^{82}Se	25	1.038×10^8
S6	$2\nu\beta^-\beta^-$	^{82}Se	0	4.8×10^7
S7	$2\nu\beta^-\beta^-$	^{82}Se	25	1.04×10^8
S8	$2\nu\beta^-\beta^-$	^{82}Se	60	4.79×10^7

Table 4.2: List of datasets used in analyses of vertex precision. They were simulated and reconstructed by Falaise version 2.0.0. More information about Majoron modes $0\nu\beta\beta\chi^0(\chi^0)$ can be found in Chapter 6.

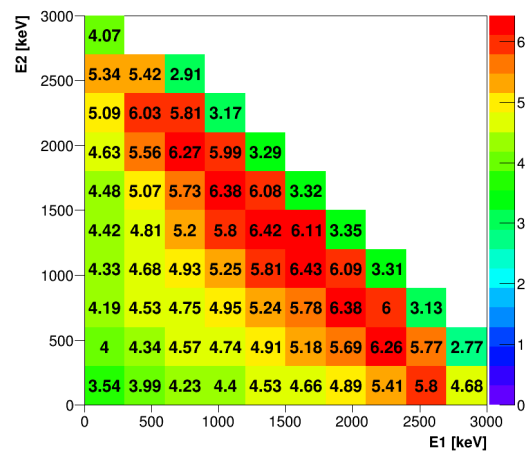

(a) $0\nu\beta\beta$ (S3).

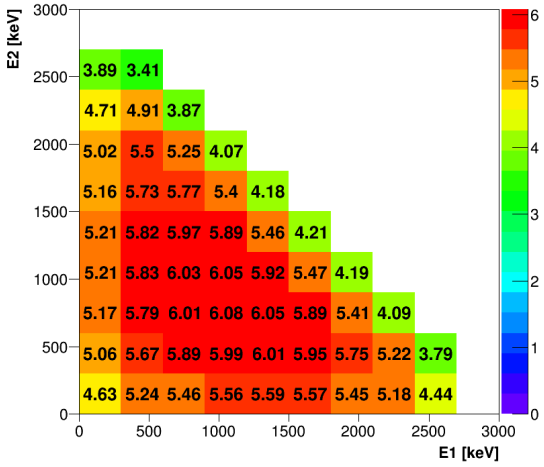

(b) $0\nu\beta\beta\chi^0$ (S4).

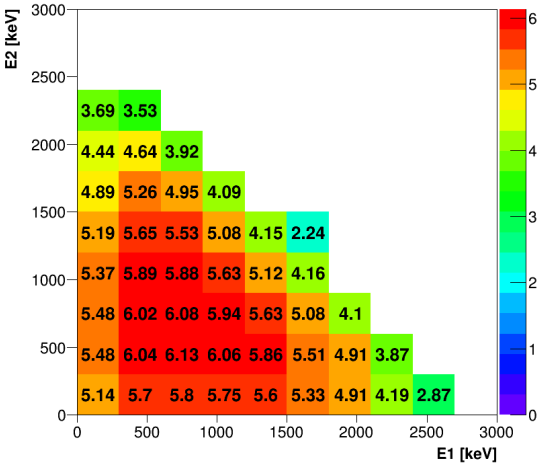

(c) $0\nu\beta\beta\chi^0\chi^0$ (S5).

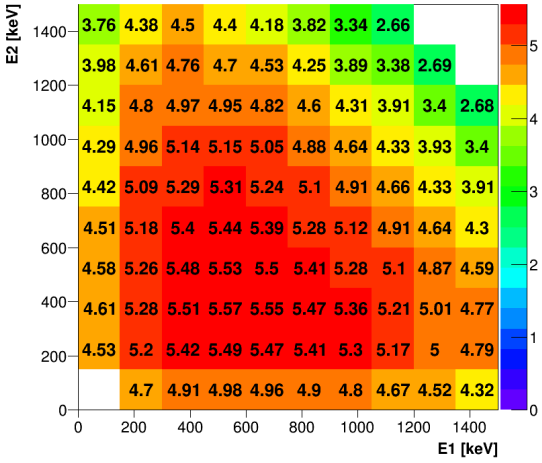

(d) $2\nu\beta\beta$ (S7).

Figure 4.10: Distribution of samples among two-dimensional subsamples representing different single electron energy regions. E1 and E2 represent energies of first and second emitted electron, respectively. Four plots represent four different processes in caption. Sample number is in the bracket. Number in the bin represents decadic logarithm of number of events in the bin. Note that, plot d) represents different scale and binning in comparison to other three.

expected effect, as the electrons are indistinguishable. However, by having a closer look, it is possible to notice that the symmetrical shape is slightly displaced below the line $E_1 = E_2$. First electron is always the one which is detected first, therefore, it is faster, with higher energy. First electron (e_1^-) is expected to have higher energy than the second electron (e_2^-), which explains the aforementioned shift under the line $E_1 = E_2$.

4.3.1 Comparison of RMS and FWHM Precision

Each subsample represents statistical set of vertex residuals Δy and Δz. As it was already described in introduction to the chapter, it is possible to extract several different measures of vertex precision. Let me compare RMS and FWHM precision.

Figure 4.11 shows comparison of the calculated RMS and FWHM precisions for sample

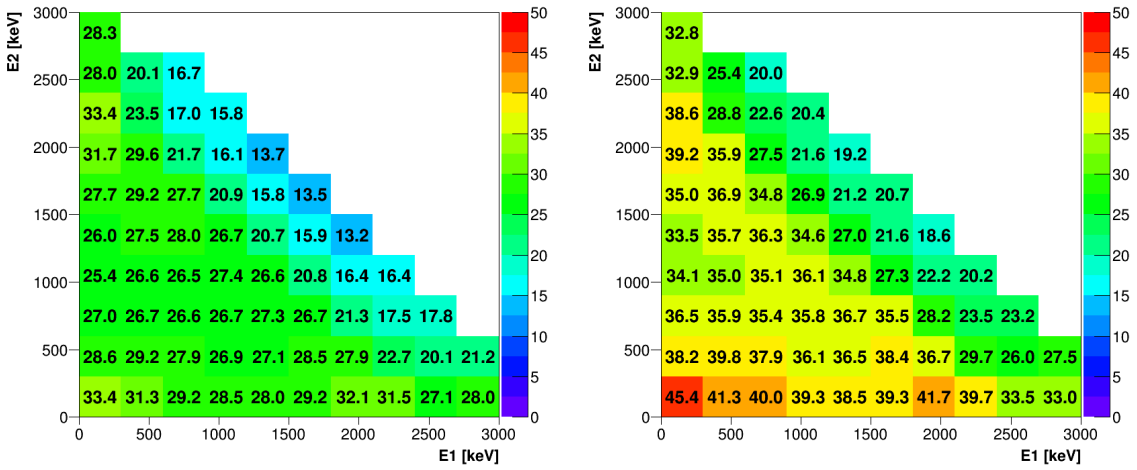

(a) RMS_y. (b) RMS_z.

(c) $FWHM_y$. (d) $FWHM_z$.

Figure 4.11: Comparison of RMS precision (first row) with FWHM precision (second row) as a function of individual electron energy. Results are obtained from $0\nu\beta^-\beta^-$ (sample S3).

S3 ($0\nu\beta\beta$). Note that, based on the definition of precision, higher values represent worse reconstruction than lower values. All the plots show similar feature. Precision is improved towards the higher energies. Electrons with higher energies are less affected by scattering effects inside of the source foil (see Section 4.4). Both the RMS precision results, as well as FWHM results, follow this trend. Nevertheless, both methods give slightly different results. This is due to the sensitivity of RMS to tail values as it was discussed in Section 4.2.2. On the other side, FWHM only depends on the quality of fit.

In order to validate the results of FWHM precision study we should investigate the quality of fit of each subsample. In Figures 4.12a and 4.12b, one can find information about quality of fit in form of $-\log_{10}(1-R^2)$. Here, R^2 is a well known coefficient calculated in following way:

$$R^2 = 1 - \frac{\sum_{i=0}^{N}(y_i - f(x_i))^2}{\sum_{i=0}^{N}(y_i - \bar{y})^2}. \tag{4.12}$$

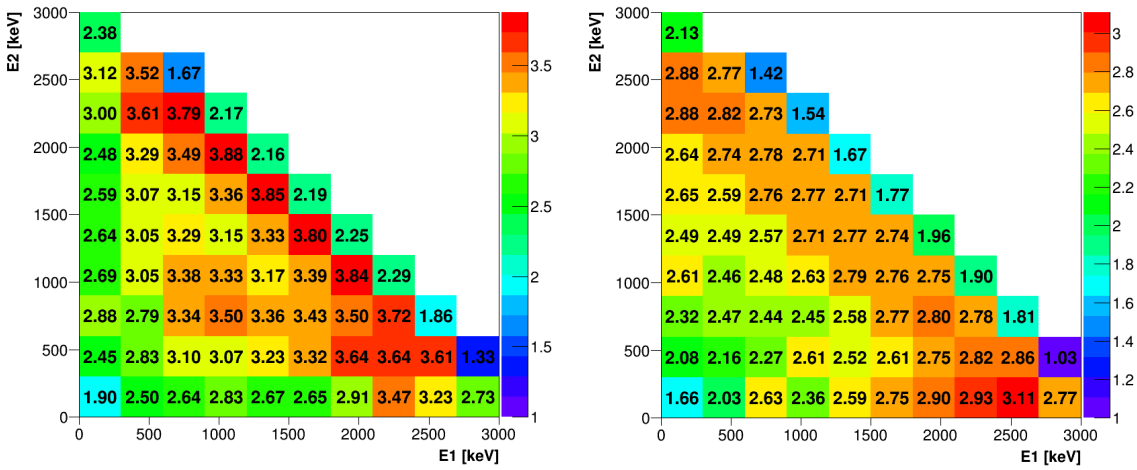

(a) $-\log_{10}(1-R_y^2)$. (b) $-\log_{10}(1-R_z^2)$.

Figure 4.12: Fit quality coefficients $-\log_{10}(1-R^2)$ belonging to subsamples whose FWHM precisions are presented in Figures 4.11c and 4.11d, respectively. The calculation method of the coefficient is explained in the text.

In the equation, x_i and y_i are datapoints, $f(x)$ represents fitting function from Equation 4.5 and $\bar{y}$ represents mean of all y_i values. The closer the R^2 is to 1, the more precisely the fit f(x) describes given data. Therefore, value $-\log_{10}(1-R^2)$ (rounded down) represents number of first decimal places with nine. For example, if $R^2 = 0.99$, then $-\log_{10}(1-R^2) = 2$. Figures 4.12a and 4.12b show very precise fits typically from range 0.99 to 0.9999. Such a justification is powerful argument towards the use of both types of precision obtained from fit (i.e. FWHM and sigma). In order to keep data reliable, I always calculated $-\log_{10}(1-R^2)$ value. Results with $-\log_{10}(1-R^2) > 1$, I considered as acceptable values and those I plotted into graphs. However, cases when $2 \geq -\log_{10}(1-R^2) > 1$ should be interpreted with precaution as their quality might be on the edge of acceptable. Nevertheless, these edge values occur rarely in the datasets, typically in the situations when studied subsample contained extremely low number of events. Unless their occurrence is mentioned for given plot in following studies, the fit performed at least as good as $-\log_{10}(1-R^2) > 2$.

Even though, RMS method gives qualitatively same results as FWHM method, in absolute terms these two methods differ. As it was presented, $-\log_{10}(1-R^2)$ is a good quality check for the second of the two methods. Therefore, from now on, FWHM will be a method of choice for evaluation of vertex precision.

4.3.2 Comparison of Vertex Precision of Various Processes

In the following, I will investigate possibilities for discrimination between different modes of $0\nu\beta\beta$, $2\nu\beta\beta$ and background processes (decays of ^{208}Tl and ^{214}Bi) based on the vertex precision for different single electron energy regions.

In previous examples, it is clear that the precision is improved with higher energies of each electron. The question still remains, whether this rate of improvement is same for each aforementioned process. The differences might yield possibility to distinguish processes.

Figures 4.13 and 4.14 depict comparison of FWHM precision between six different processes. In all cases, it is clearly visible, that precision is improved for electrons of higher energies. For example, in regions where one electron has energy between 1 MeV and 1.5

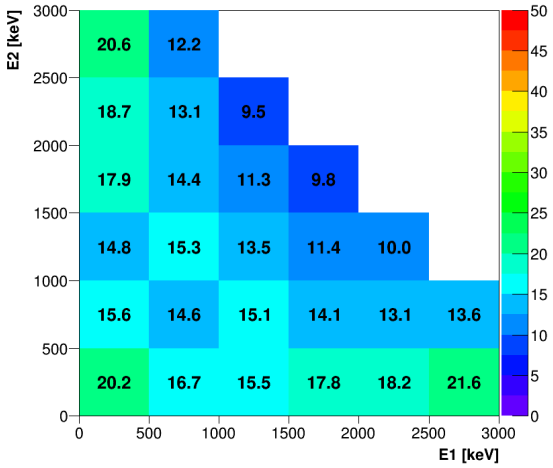

(a) $\mathrm{FWHM_y}$: $0\nu\beta\beta$ (S3).

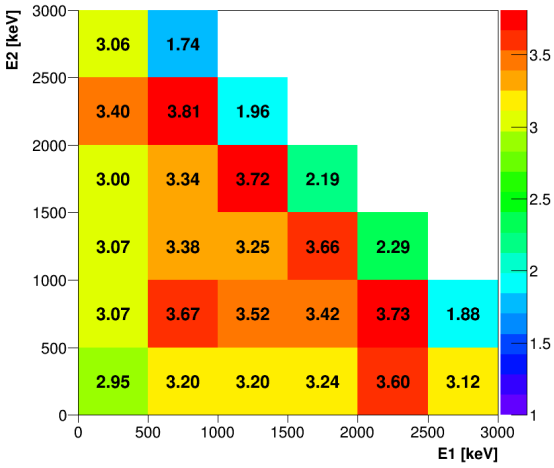

(b) $-\log_{10}(1-\mathrm{R_y^2})$: $0\nu\beta\beta$ (S3).

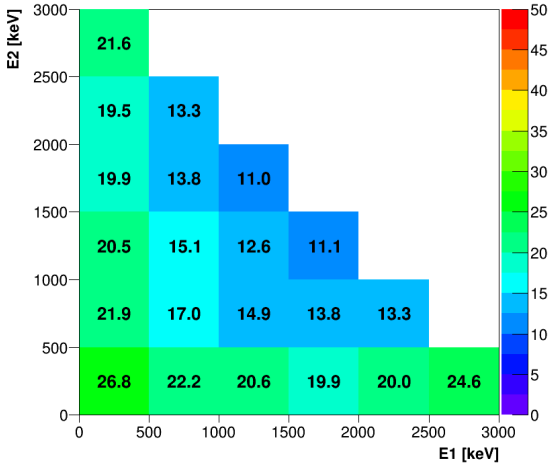

(c) $\mathrm{FWHM_y}$: $0\nu\beta\beta\chi^0$ (S4).

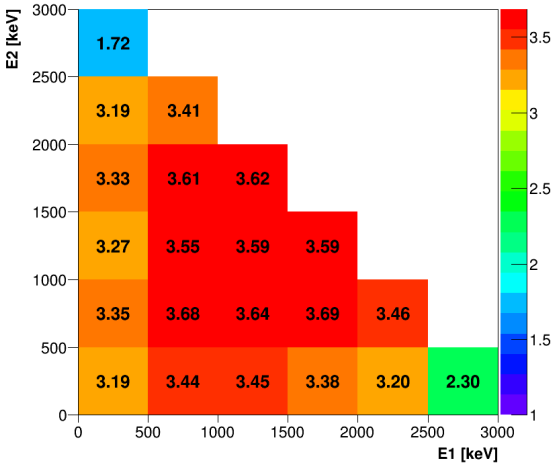

(d) $-\log_{10}(1-\mathrm{R_y^2})$: $0\nu\beta\beta\chi^0$ (S4).

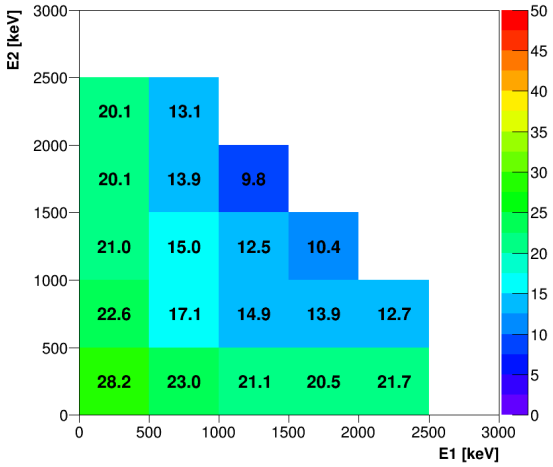

(e) $\mathrm{FWHM_y}$: $0\nu\beta\beta\chi^0\chi^0$ (S5).

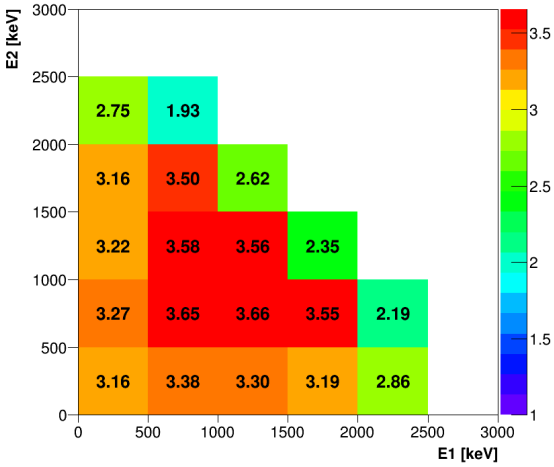

(f) $-\log_{10}(1-\mathrm{R_y^2})$: $0\nu\beta\beta\chi^0\chi^0$ (S5).

Figure 4.13: FWHM precision (in mm) as a function of energies of individual electrons. Each row represents one out of three chosen modes of $0\nu\beta\beta$. In left column FWHM precisions in y-direction are plotted, right column plots show the fit quality expressed by $-\log_{10}(1-\mathrm{R^2})$ coefficient.

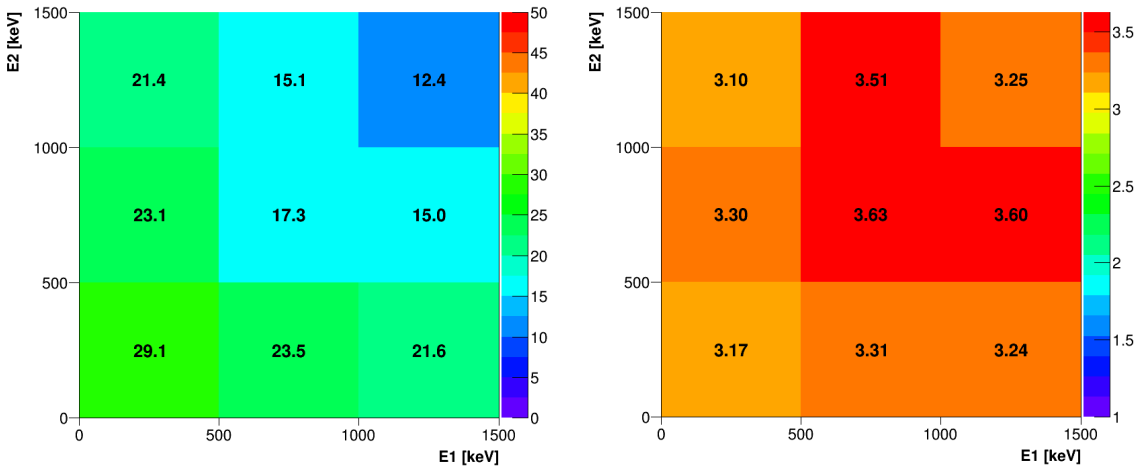

(a) $\mathrm{FWHM_y}$: $2\nu\beta\beta$ (S7).

(b) $-\log_{10}(1-\mathrm{R_y^2})$: $2\nu\beta\beta$ (S7).

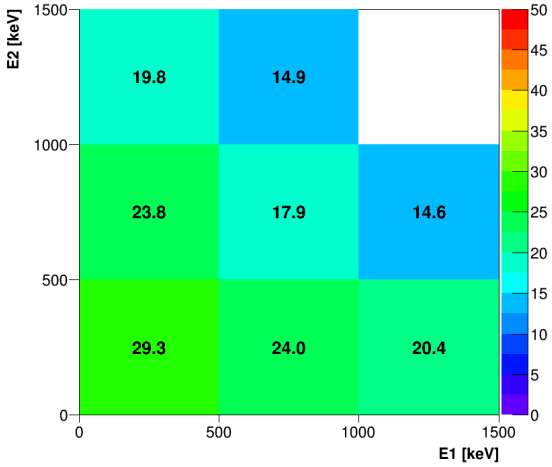

(c) $\mathrm{FWHM_y}$: β^-, ^{208}Tl (S1).

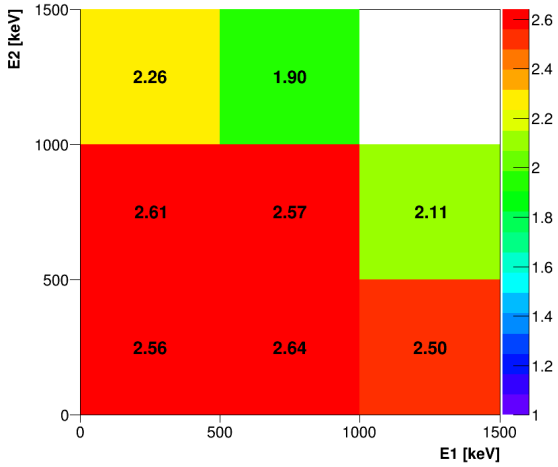

(d) $-\log_{10}(1-\mathrm{R_y^2})$: β^-, ^{208}Tl (S1).

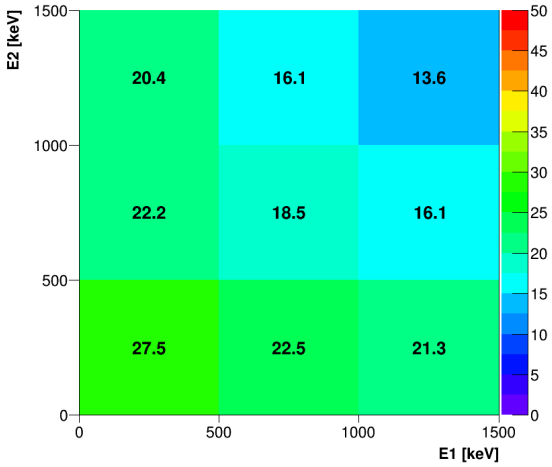

(e) $\mathrm{FWHM_y}$: β^-, ^{214}Bi (S2).

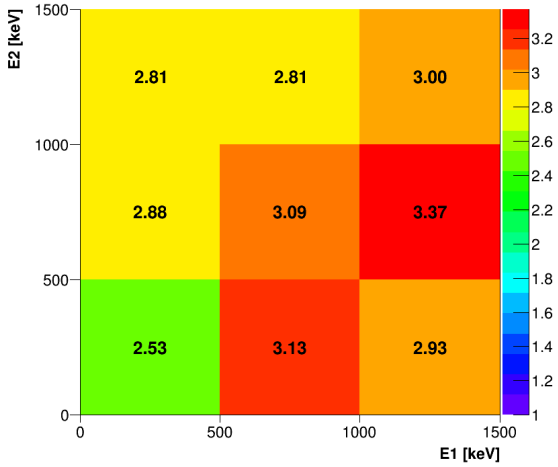

(f) $-\log_{10}(1-\mathrm{R_y^2})$: β^-, ^{214}Bi (S2).

Figure 4.14: FWHM precision (in mm) as a function of energies of individual electrons. Different rows represent results obtained from samples of $2\nu\beta\beta$, decay of ^{208}Tl and decay of ^{214}Bi, respectively. In left column FWHM precisions in y-direction are plotted, right column plots show the fit quality expressed by $-\log_{10}(1-\mathrm{R^2})$ coefficient.

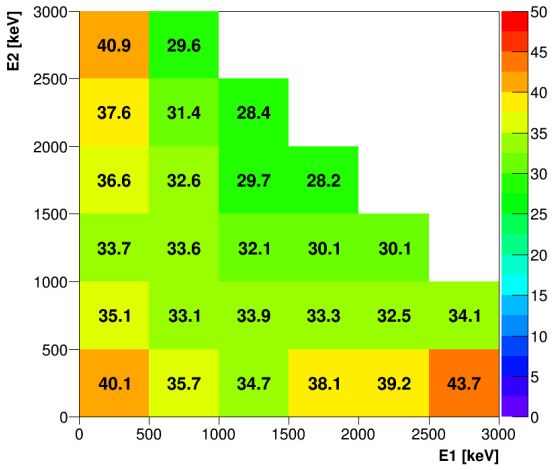

(a) $\mathrm{FWHM_z}$: $0\nu\beta\beta$ (S3).

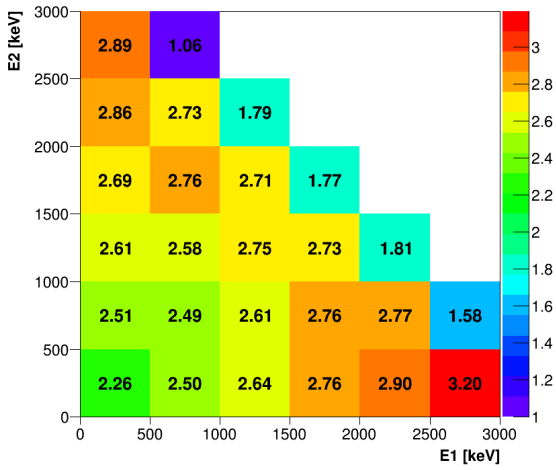

(b) $-\log_{10}(1-\mathrm{R_z^2})$: $0\nu\beta\beta$ (S3).

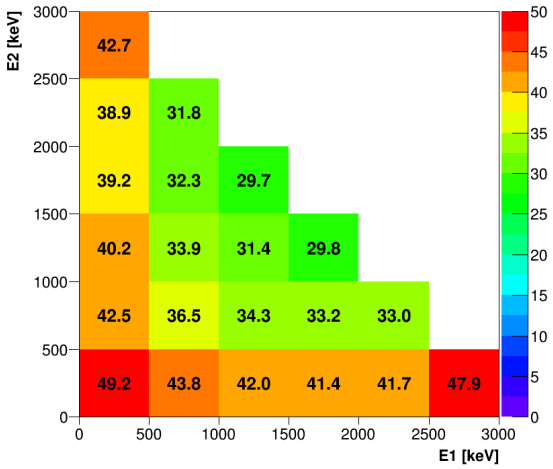

(c) $\mathrm{FWHM_z}$: $0\nu\beta\beta\chi^0$ (S4).

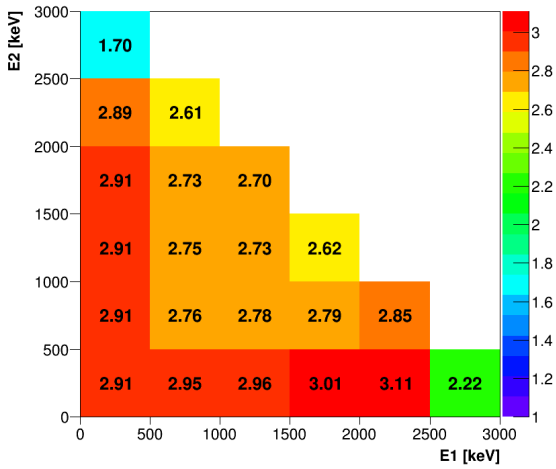

(d) $-\log_{10}(1-\mathrm{R_z^2})$: $0\nu\beta\beta\chi^0$ (S4).

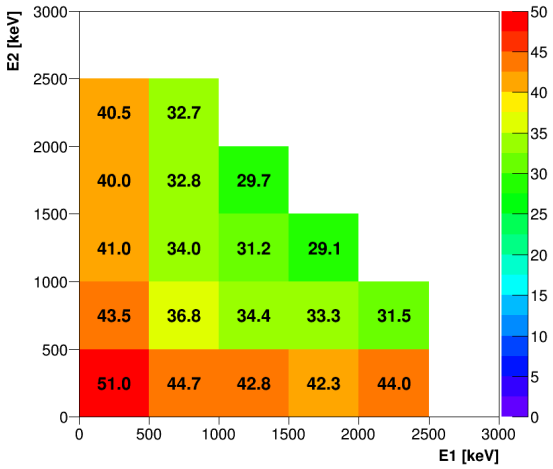

(e) $\mathrm{FWHM_z}$: $0\nu\beta\beta\chi^0\chi^0$ (S5).

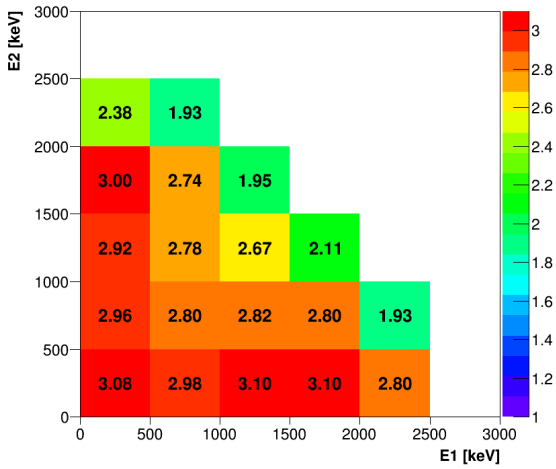

(f) $-\log_{10}(1-\mathrm{R_z^2})$: $0\nu\beta\beta\chi^0\chi^0$ (S5).

Figure 4.15: FWHM precision (in mm) as a function of energies of individual electrons. Each row represents one out of three chosen modes of $0\nu\beta\beta$. In left column FWHM precisions in z-direction are plotted, right column plots show the fit quality expressed by $-\log_{10}(1-\mathrm{R^2})$ coefficient.

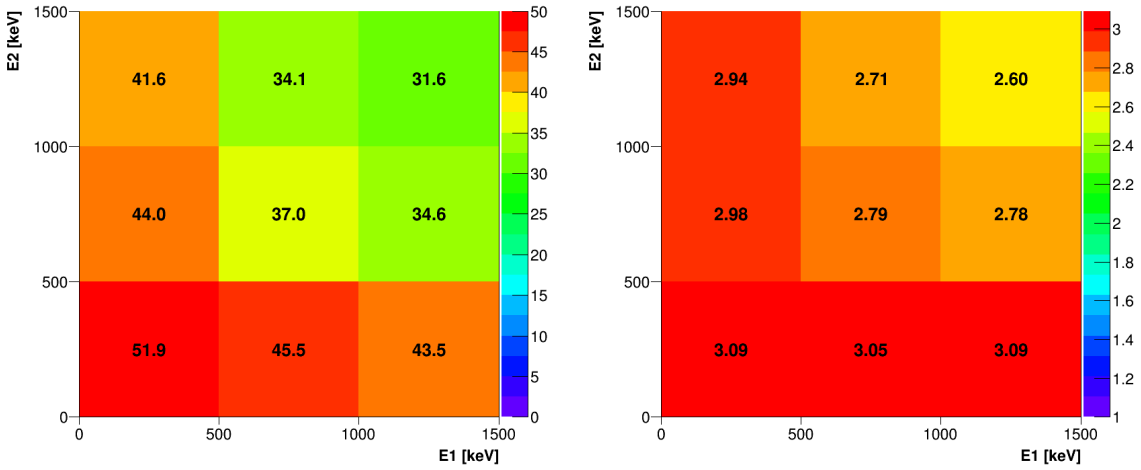

(a) $\mathrm{FWHM_z}$: $2\nu\beta\beta$ (S7). (b) $-\log_{10}(1-\mathrm{R_z^2})$: $2\nu\beta\beta$ (S7).

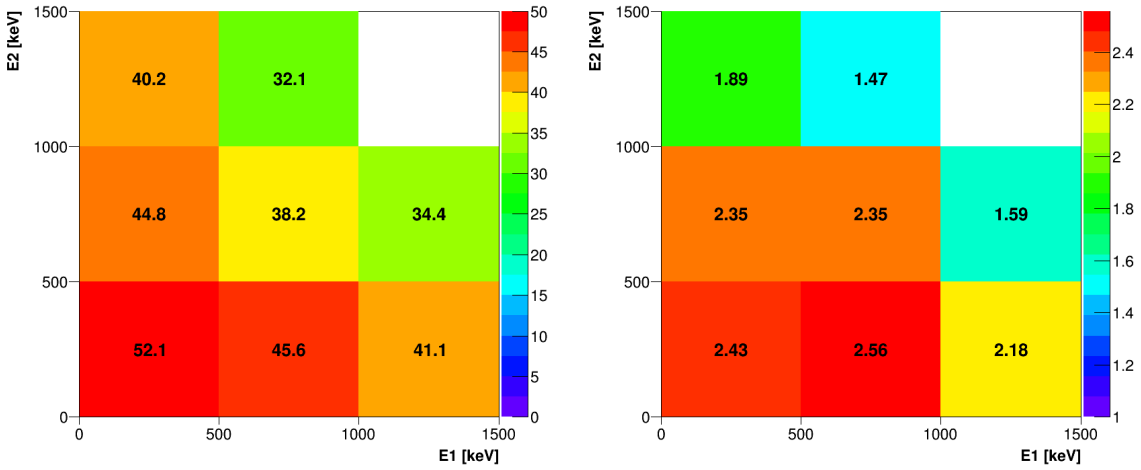

(c) $\mathrm{FWHM_z}$: β^-, ^{208}Tl (S1). (d) $-\log_{10}(1-\mathrm{R_z^2})$: β^-, ^{208}Tl (S1).

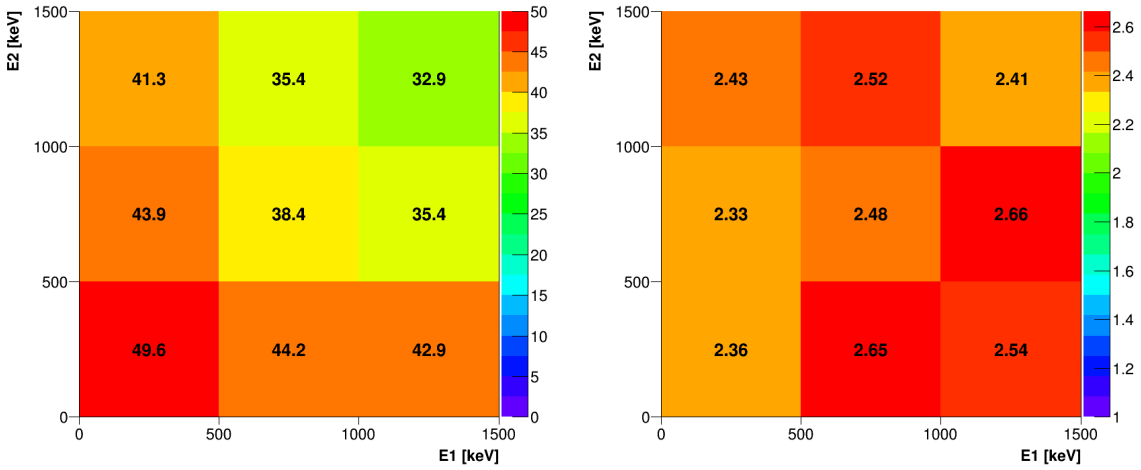

(e) $\mathrm{FWHM_z}$: β^-, ^{214}Bi (S2). (f) $-\log_{10}(1-\mathrm{R_z^2})$: β^-, ^{214}Bi (S2).

Figure 4.16: FWHM precision (in mm) as a function of energies of individual electrons. Different rows represent results obtained from samples of $2\nu\beta\beta$, decay of ^{208}Tl and decay of ^{214}Bi, respectively. In left column FWHM precisions in z-direction are plotted, right column plots show the fit quality expressed by $-\log_{10}(1-\mathrm{R^2})$ coefficient.

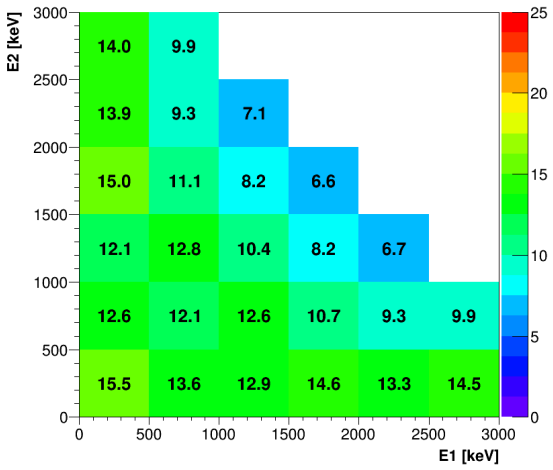

(a) σ_y: $0\nu\beta\beta$ (S3).

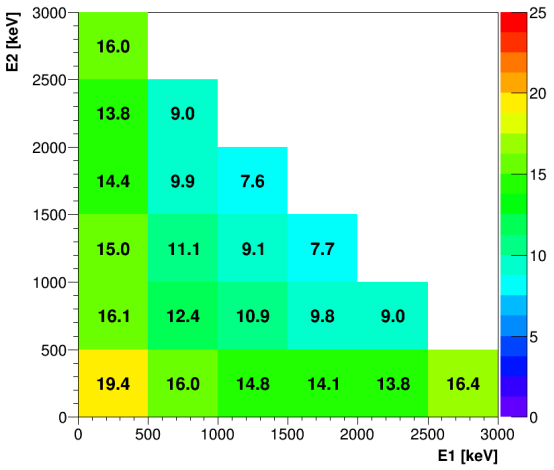

(b) σ_y: $0\nu\beta\beta\chi^0$ (S4).

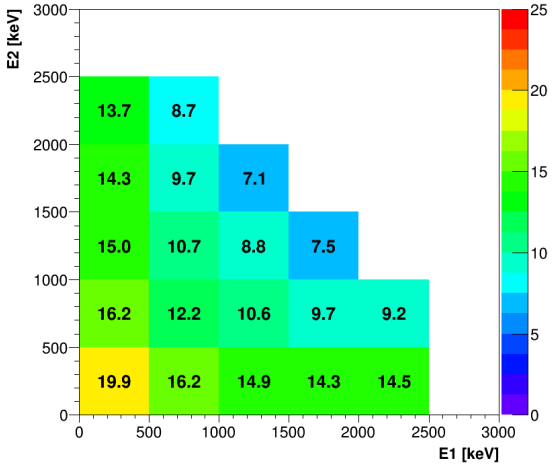

(c) σ_y: $0\nu\beta\beta\chi^0\chi^0$ (S5).

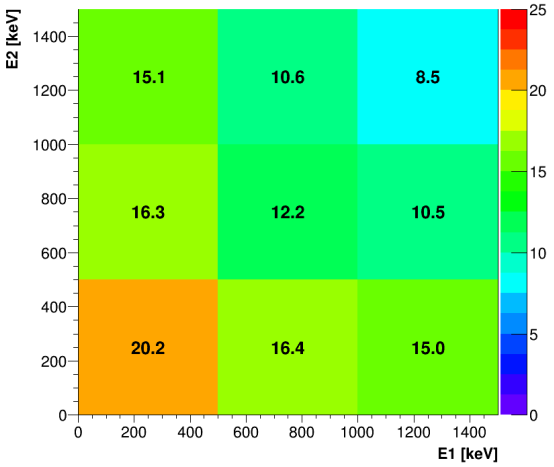

(d) σ_y: $2\nu\beta\beta$ (S7).

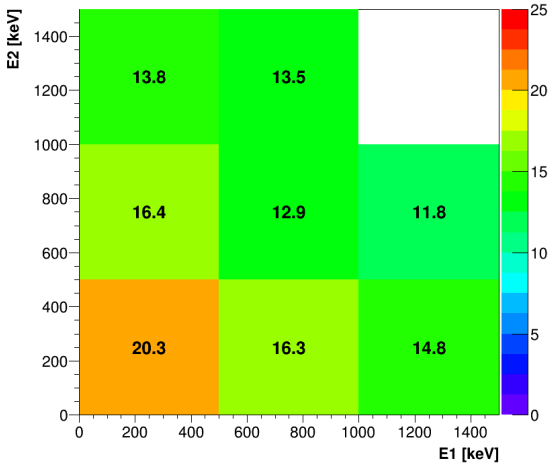

(e) σ_y: β^-, ^{208}Tl (S1).

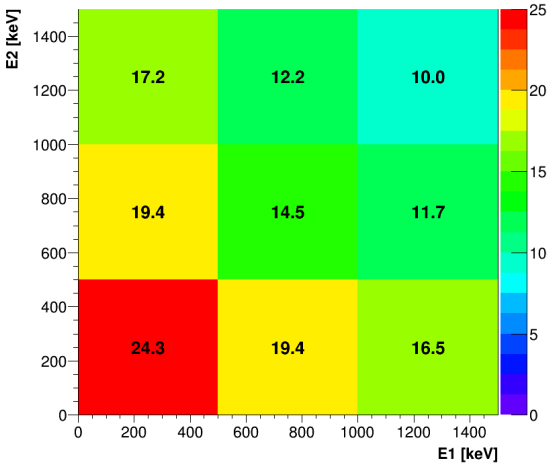

(f) σ_y: β^-, ^{214}Bi (S2).

Figure 4.17: Sigma precision (in mm) in y-direction as a function of energies of individual electrons. Plots are comparing six different decay processes.

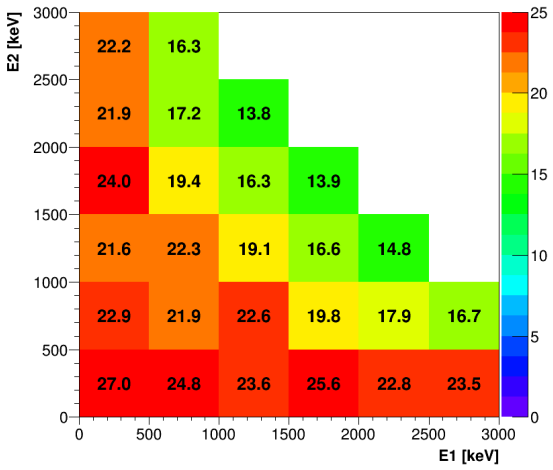

(a) σ_z: $0\nu\beta\beta$ (S3).

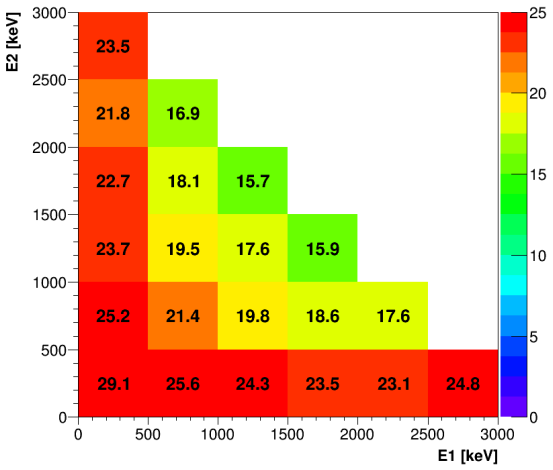

(b) σ_z: $0\nu\beta\beta\chi^0$ (S4).

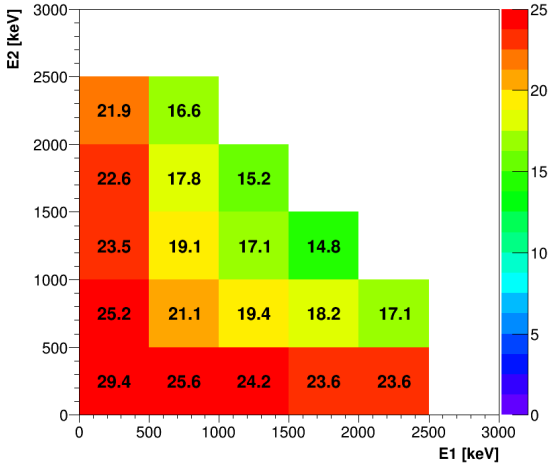

(c) σ_z: $0\nu\beta\beta\chi^0\chi^0$ (S5).

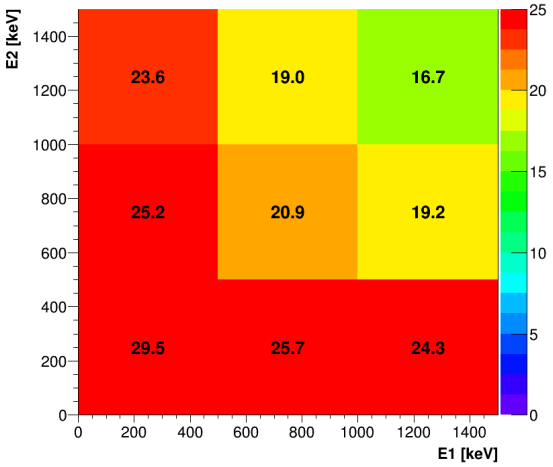

(d) σ_z: $2\nu\beta\beta$ (S7).

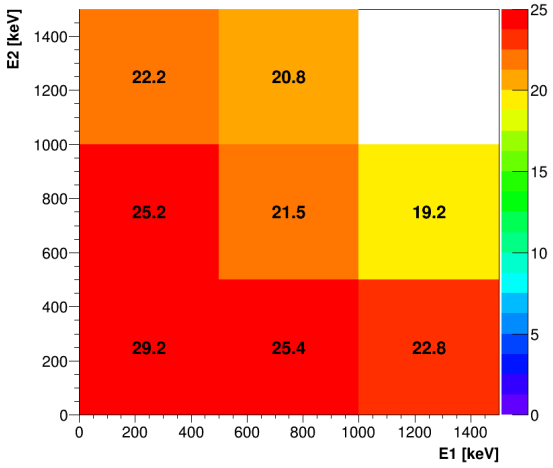

(e) σ_z: β^-, ^{208}Tl (S1).

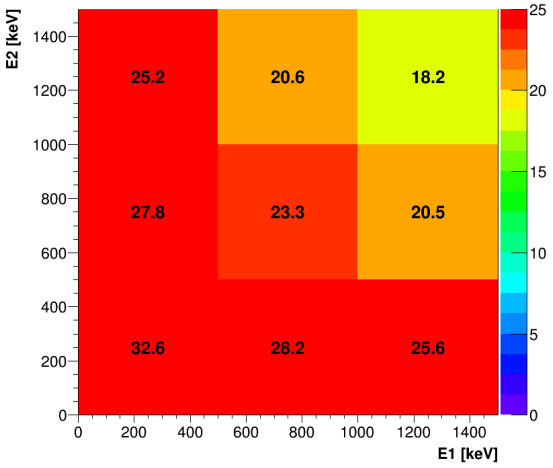

(f) σ_z: β^-, ^{214}Bi (S2).

Figure 4.18: Sigma precision (in mm) in z-direction as a function of energies of individual electrons. Plots are comparing six different decay processes.

MeV while other electron has energy from interval 1.5 MeV to 2 MeV precision can get as good as roughly 10 mm, which represents distance of 5 mm between vertices in y-direction! On the other side, if both electrons have kinetic energy inferior to 0.5 MeV the FWHM precision can drop down to almost 30 mm (15 mm distance). In z-direction FWHM precision shows larger mismatch of reconstructed vertices as it is shown in Figures 4.15 and 4.16. FWHM precisions in this direction range from 30 mm (15 mm absolute distance) up to 50 mm (25 mm absolute distance). Worse reconstruction in z-direction compared to y-direction is expected effect. Each single Geiger wire in the SuperNEMO tracking detector is parallel to z-direction. Information about the position of the particle in z-direction is obtained by measuring the difference of arrival of collected charge to the ends of the wire. In plane perpendicular to Geiger wire (i.e in x- and y-direction) the position is measured by amount of collected charge produced by avalanche caused by passing particle. In principle, latter measurement is more precise, i.e. it yields smaller uncertainties. Therefore, CAT has more precise information about the track of the particle in y- (and also x-) direction than z-direction which results in observed differences in vertex reconstruction precision.

If we compare all FWHM precisions for different processes we can conclude that the results do not seem to be dependent on the type of process, as the plots (in energy regions where information exist) differ only within few percent.

However, plots for $0\nu\beta\beta$ (Figures 4.13a and 4.15a) seem to differ in the region of lowest electron energies ($E_1, E_2 < 1$MeV). In order to get better idea whether this might serve as a potential for a discrimination between $0\nu\beta\beta$ and the other listed processes, let us have a look at the σ precisions. The values are plotted in Figures 4.17 and 4.18. σ precision gives limits of a central interval containing 68.27 % of all events (-σ,σ) in a subsample. Therefore, differences in σ can signalize possibilities to distinguish between different processes. Nevertheless, σ values in the region of lowest electron energies for $0\nu\beta\beta$ are approaching the values for the other processes which implies basically no potential for the discrimination.

Finally, we can conclude, that the vertex reconstruction precision varies with energies of individual electrons. Data show that the reconstruction precision tend to depend only on the energy of the electrons regardless of the process which created them. Achievable precision for different energy regions are summarized in Figures 4.13 - 4.18.

4.3.3 Comparison of Vertex Precision for Different Magnetic Fields

Magnetic field influences shape of the charged particle trajectory. Dependence of vertex reconstruction precision on the energy might also lie in difference in the track shapes. In such case, one should observe differences in vertex precision when magnetic field is varied.

Figure 4.19 compare sigma vertex precisions for different magnetic field applied in the demonstrator, namely 0 G (without field) and 60 G. The behaviour is compared for events of $2\nu\beta\beta$. The differences are not very significant, but it is possible to recognize slightly worse vertex reconstruction in scenario without magnetic field. With no magnetic field, the electrons follow straight trajectories which is the shortest connection between two points in the standard Euclidian geometry. On the other side, with magnetic field present in the demonstrator, electrons follow circular paths and therefore not the shortest distance between two points of the trajectory. This makes the electrons stay longer in the area of the tracker, potentially triggering extra Geiger wires, therefore, collecting more data points. It results in slightly lower experiment uncertainty in the electron trajectory. The trend seems to be confirmed by comparison of results for extreme magnetic field (60 G - right side of Figure 4.19) with magnetic field of 25 G (Figures 4.17d and 4.18d). The precision is slightly better

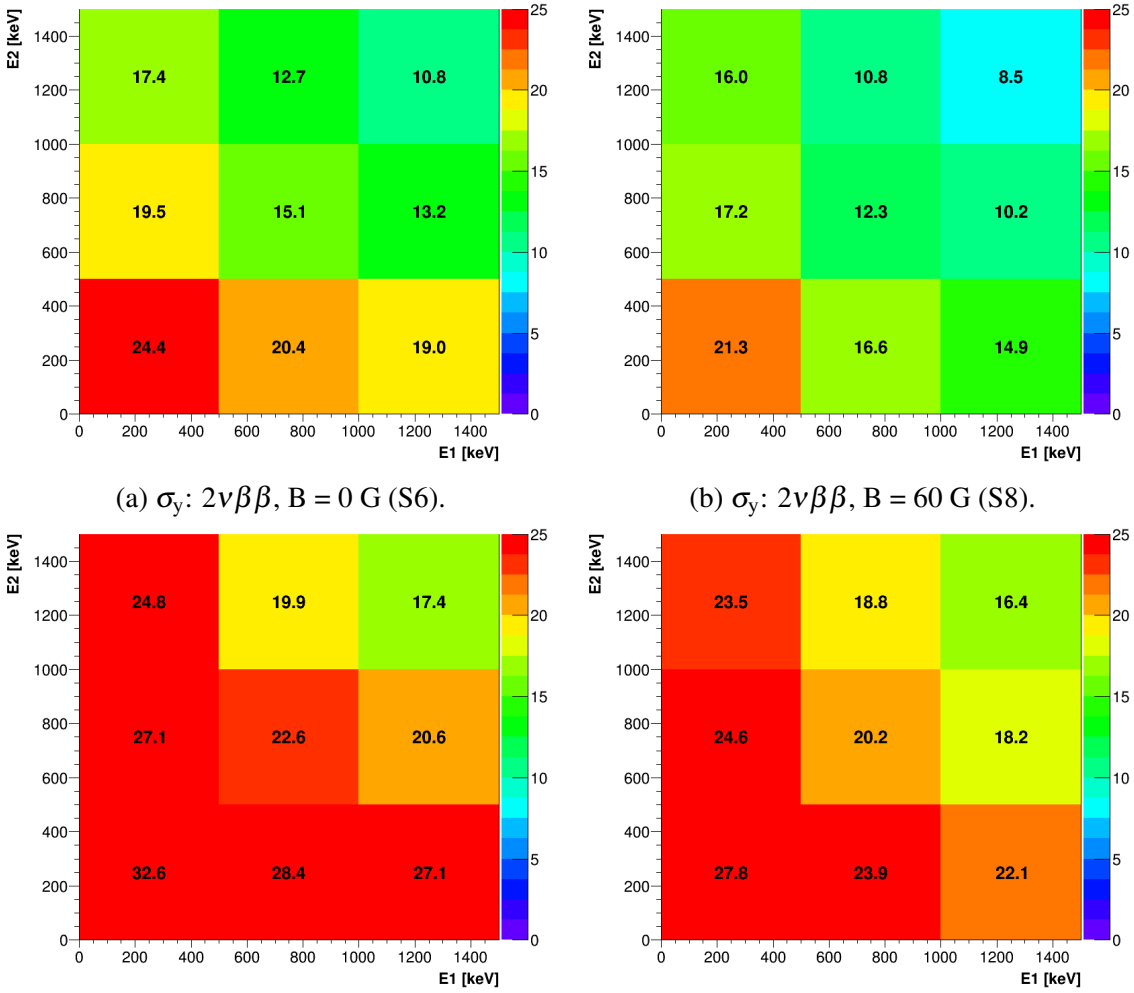

(a) σ_y: $2\nu\beta\beta$, B = 0 G (S6).

(b) σ_y: $2\nu\beta\beta$, B = 60 G (S8).

(c) σ_z: $2\nu\beta\beta$, B = 0 G (S6).

(d) σ_z: $2\nu\beta\beta$, B = 60 G (S8).

Figure 4.19: Comparison of sigma precisions (mm) in y-direction (top row) and z-direction (bottom row) in different energy regions for two magnetic field setups - without magnetic field (0 G) and with extreme magnetic field (60 G).

with higher magnetic field. However, the difference is so low that it is difficult to draw final conclusion as the difference might be partially caused by statistical fluctuations. In any case, the gain in vertex precision would not certainly be big enough to justify use of the magnetic field more than twice as big than planned (25 G).

4.3.4 Vertex Efficiencies

Vertex efficiency I define as a ratio of events from studied subsample, for which the projection of real vertex into yz plane is contained within the uncertainty rectangle given by vertex residuals $|\Delta y|$ and $|\Delta z|$, and all events in the subsample. In other words, it is a fraction of events in which vertex V_r is found inside of the uncertainty rectangle in the Figure 4.4. Efficiency gains values from interval $\langle 0,1 \rangle$. The vertex efficiency is, however, not possible to calculate for measured data for obvious reason - the position of real vertex is unknown. On the other side, such a variable give us information about how often the uncertainty rectangle given by reconstruction algorithm contains the real vertex.

Comparison of vertex efficiencies for $0\nu\beta\beta$ and $2\nu\beta\beta$ in Figure 4.20 show almost perfect homogeneity for all energy regions. Value of 0.25 with precision of ± 0.02 is obtained throughout all the energy configurations of two electrons. It implies that, regardless of the energies of two electrons, always 1 in 4 events contains real vertex V_r within the rectangular boundaries given by reconstructed vertices V_1 and V_2. Moreover, exactly the same pattern without any exception was observed in all following studies. It seems that the vertex efficiency is always 0.25 regardless of the situation. For this reason I am not going to discuss this topic in following sections.

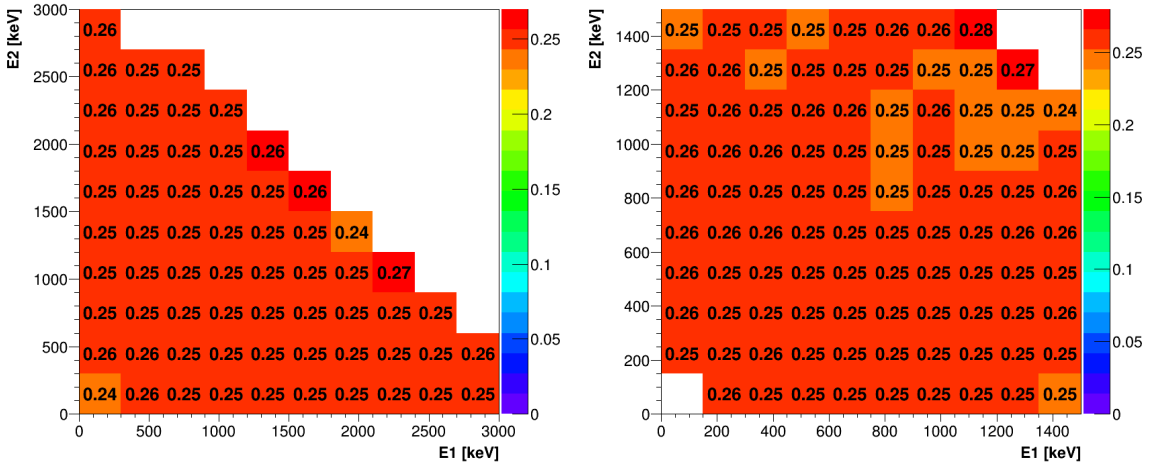

(a) Efficiency: $0\nu\beta\beta$ (S3).

(b) Efficiency: $2\nu\beta\beta$ (S7).

Figure 4.20: Comparison of vertex efficiencies as a function of energies of individual electrons. Note the difference in energy scales between both plots.

4.4 Vertex Precision as a Function of Electron Angles

Previous studies have shown a strong dependence of vertex precision on the energy of the electrons and, on the other side, not so strong dependence on magnetic field. Another quantity of interest in double beta decay experiments is an angular distribution of emitted electrons. Thanks to the tracker technology, SuperNEMO will be able to measure these distributions. Goal of this section is a quantification of vertex precision in dependence on the angle between the electrons. I will again take advantage of datasets listed in Table 4.2.

Electrons undergo several scattering events between the moment of decay and moment when they leave the source foil. In the example shown in Figure 4.21, electrons originally emitted into different sides of the source foil, exit it on the same side almost aligned with respect to each other. In the study, decay angle, i.e. angle between initial momenta of two electrons emitted in decay, I will label as Φ_{decay} (or just Φ_{dec})

This angle is not measurable in real experiment, only accessible by simulation. Therefore, I defined another angle Φ_{escape} (or just Φ_{esc}) defined as an angle between two electrons exactly in the moment when they exit the source foil[3]. Φ_{esc} I always extracted from SD bank (even though, it can be obtained from PTD bank - after particle track reconstruction), so it is not influenced by experimental uncertainties.

[3]Note that, the moment when electrons exit the source foil are not necessary simultaneous.

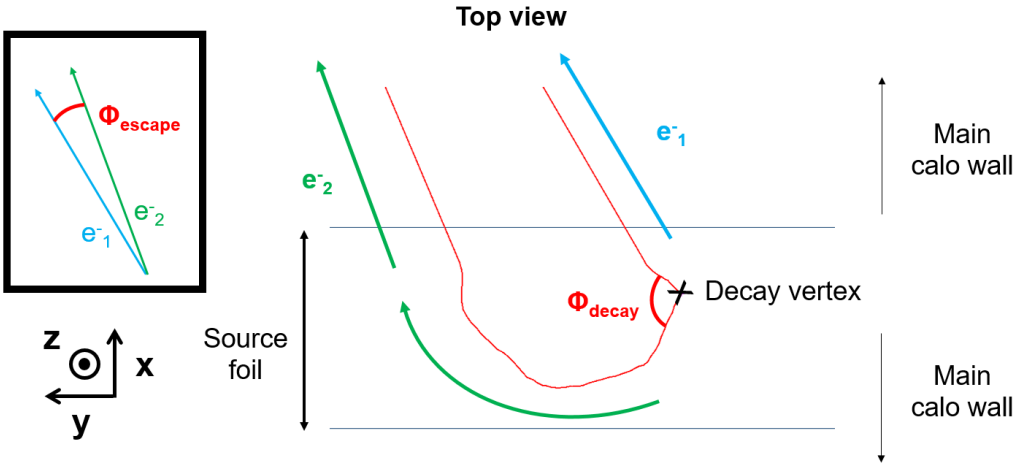

Figure 4.21: Scheme is representing electron tracks after emission from double beta decay of ^{82}Se inside of the source foil. Source foil is drawn in horizontal position and zoomed to reveal the scattering of the electrons inside of its 200 μm thick volume. Definitions of angles between electrons at the moment of decay (Φ_{decay}) and at the moment of exit from source foil (Φ_{escape}) are depicted in schematic form.

4.4.1 Decay Angle vs. Escape Angle

Figure 4.21 shows that the difference between Φ_{dec} and Φ_{esc} can be significant due to the scattering of the electrons inside of the source foil.

Figure 4.22 shows two-dimensional correlation plots between Φ_{dec} (horizontal axis) and Φ_{esc} (vertical axis) for four different double beta decay modes, namely $0\nu\beta\beta$, $0\nu\beta\beta\chi^0$, $0\nu\beta\beta\chi^0\chi^0$ and $2\nu\beta\beta$. In case of the standard $0\nu\beta\beta$, the spread of events away from the line $\Phi_{\text{esc}} = \Phi_{\text{dec}}$ is smaller than in the other three cases.

This tendency gets weaker with each following plot. Events distant from $\Phi_{\text{esc}} = \Phi_{\text{dec}}$ represent weak conservation of decay angle on the exit from the foil. Appearance of such events with each next plot signifies lowering level of the angle conservation. The difference in the plots here lies in the difference of the energy spectra for each of the processes. Presented processes are represented by energy spectra with gradually lower mean energy value. Therefore, in average, electrons are carrying less energy and thus they scatter more often. On the other side, electrons with higher energies tend to exit the foil more directly with fewer collisions so the probability to preserve their decay angle grows. This hypothesis is proven in Figure 4.23. The figure represents same correlation plots from first two datasets after low energy events were filtered out. Figure 4.23b represents correlation plot of those $0\nu\beta\beta$ events whose sum of electron energies was superior to 2.9 MeV. The spread with respect to $\Phi_{\text{esc}} = \Phi_{\text{dec}}$ line is smaller, indicating that electrons undergo a lower number of scatterings in the foil. Moreover, Figures 4.23c and 4.23d represent correlation plot for $0\nu\beta\beta\chi^0$ for all events whose energy was superior to 1.5 MeV and 2.0 MeV, respectively. With higher low energy threshold the plot starts to resemble the one belonging to $0\nu\beta\beta$ (Figure 4.22a). Even though, these plots represent different processes, they also represent similar mean electron energies. It is another proof of the hypothesis of energy of electron being the main factor when it comes to conservation of decay angle.

Based on the presented correlation plots it is possible to calculate probability of decay angle to be found in given interval for any observed escape angle. We can also conclude that, the subset of events when electrons are emitted roughly perpendicularly to each other (region

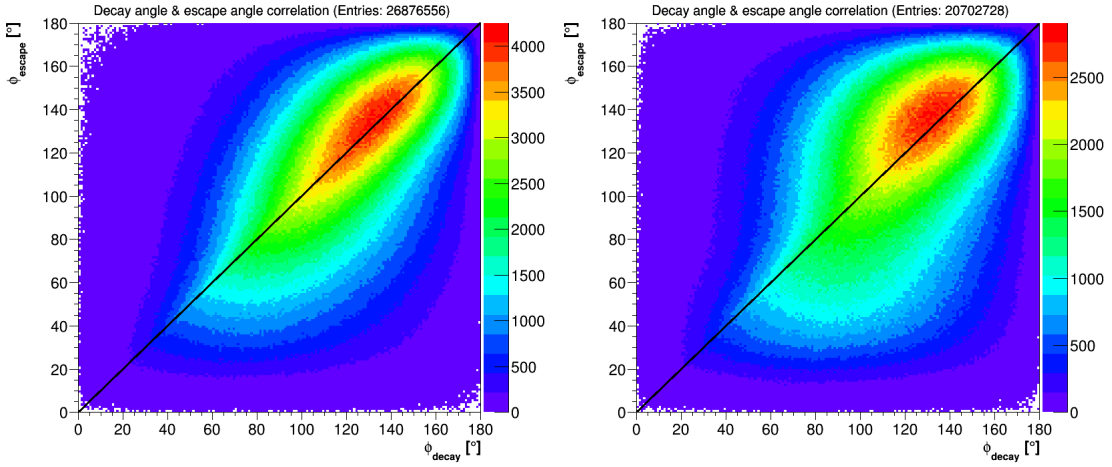

(a) $0\nu\beta\beta$ (S3).

(b) $0\nu\beta\beta\chi^0$ (S4).

(c) $0\nu\beta\beta\chi^0\chi^0$ (S5).

(d) $2\nu\beta\beta$ (S7).

Figure 4.22: Distributions of events in four double beta decay samples based on the decay and escape angles. Plots show correlation between decay (Φ_{dec}) and escape angle (Φ_{esc}). Black line represents events for which both angles were equal ($\Phi_{\text{esc}} = \Phi_{\text{dec}}$). No energy cuts were applied.

between roughly 80° and 100°) tend to have very spread-out spectrum of escape angles.

In following, let me compare the spectra of decay and escape angles. Figure 4.24 shows comparison of decay and escape angle spectra between chosen processes. While differences between the decay angle distributions are really small, the distributions of escape angles show much large difference. Same comparison in a $\cos(\Phi)$ scale can be found in Figure 4.25. Furthermore, Figure 4.26 demonstrates non-negligible effect of energy cut (E > 2.9 MeV) on the angular distribution of both decay and escape angle.

4.4.2 FWHM Precision

Previous study of vertex reconstruction precision showed strong dependence on the energy of the emitted electrons. In this study, we will have a look at the dependence on the escape angle.

Figure 4.27 compares FWHM precisions in both (y- and z-) directions for five different

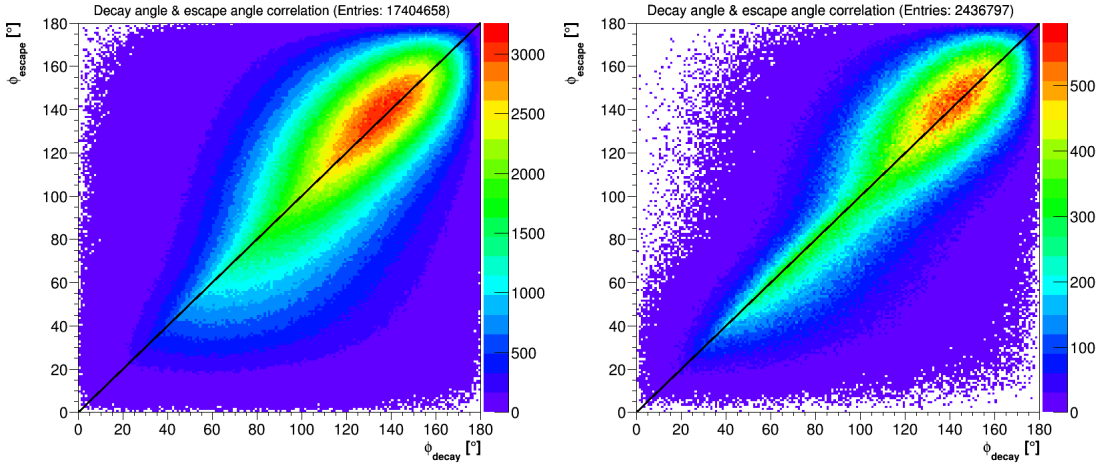

(a) $0\nu\beta\beta$ (S3), E_{th} = 2.7 MeV.

(b) $0\nu\beta\beta$ (S3), E_{th} = 2.9 MeV.

(c) $0\nu\beta\beta\chi^0$ (S4), E_{th} = 1.5 MeV.

(d) $0\nu\beta\beta\chi^0$ (S4), E_{th} = 2 MeV.

Figure 4.23: Distributions of events in two double beta decay samples based on the decay and escape angles. Plots show correlation between decay (Φ_{dec}) and escape angle (Φ_{esc}). Black line represents events for which both angles were equal ($\Phi_{esc} = \Phi_{dec}$). Plots were produced for same samples as in the Figures 4.22a and 4.22b after cuts on energy $E > E_{th}$ were applied. Minimum energy threshold E_{th} is marked in the caption of each individual figure.

processes. Interestingly, all plotted double-beta decay processes follow the same pattern. However, $0\nu\beta\beta$ represents the sample with the best overall precision while $2\nu\beta\beta$ the worst. This is once again an effect of energy spectra which was already discussed. If we perform energy cut (E > 2 MeV) on both modes with Majoron emission the precision improves and approaches the one of standard $0\nu\beta\beta$ without cut. Moreover, energy cuts (E > 2.7 MeV and E > 2.9 MeV) further improve the reconstruction precision of standard $0\nu\beta\beta$. All the effects are clearly visible in Figure 4.28.

Looking back to the Figure 4.27, it seems that decay of ^{214}Bi tend to follow different precision pattern and reach local maximum (worst precision) in lower angles than the double beta decay modes. For decisive comparison, however, study with significantly higher simulated sample of ^{214}Bi decay would be needed.

It is without a discussion that the vertex precision depends on the escape angle between

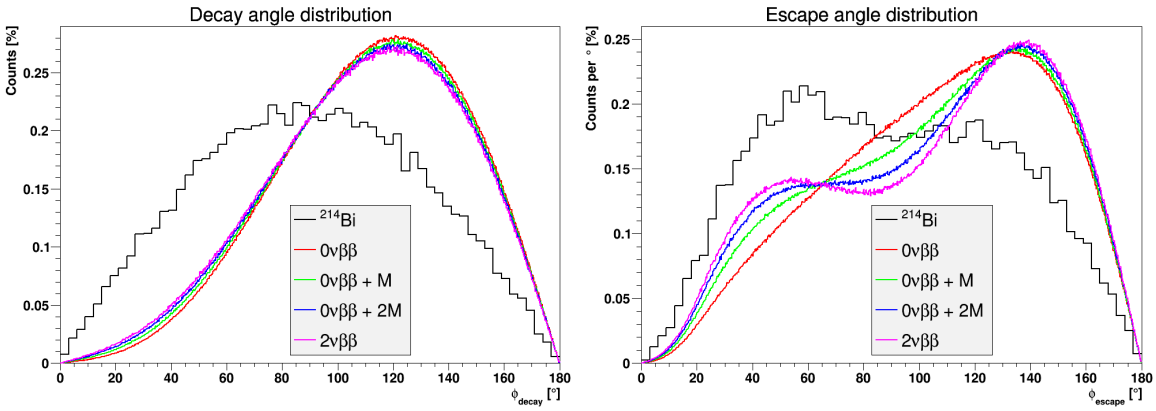

Figure 4.24: Distributions of decay angle (left) and escape angle (right) for five chosen data samples: decay of ^{214}Bi (S2), $0\nu\beta\beta$ (S3), $0\nu\beta\beta\chi^0$ (S4), $0\nu\beta\beta\chi^0\chi^0$ (S5) and $2\nu\beta\beta$ (S7). Distributions represent fraction of events (in %) per one degree. $0\nu\beta\beta + \mathrm{M}$ and $0\nu\beta\beta + 2\mathrm{M}$ in plots denote $0\nu\beta\beta\chi^0$ and $0\nu\beta\beta\chi^0\chi^0$, respectively.

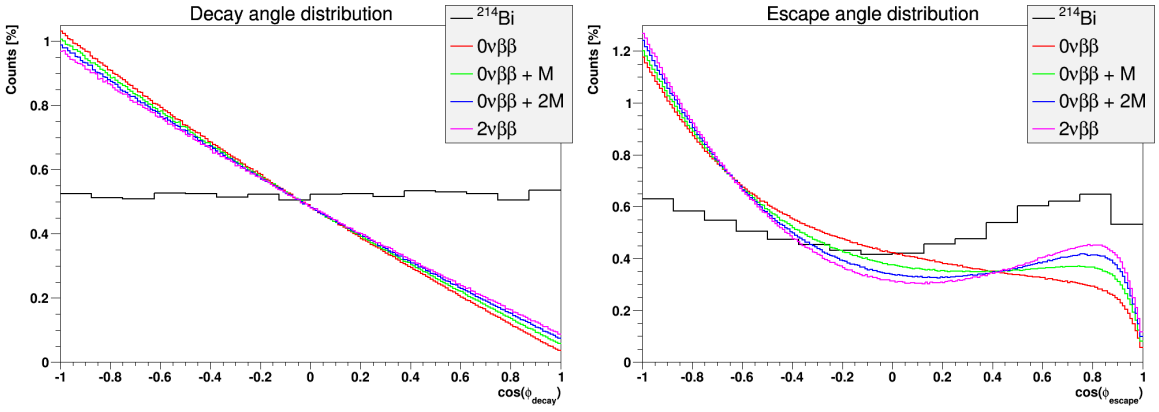

Figure 4.25: Distributions from Figure 4.24 represented in cos(Φ) scale. Distributions are normalized to equal area of 100%.

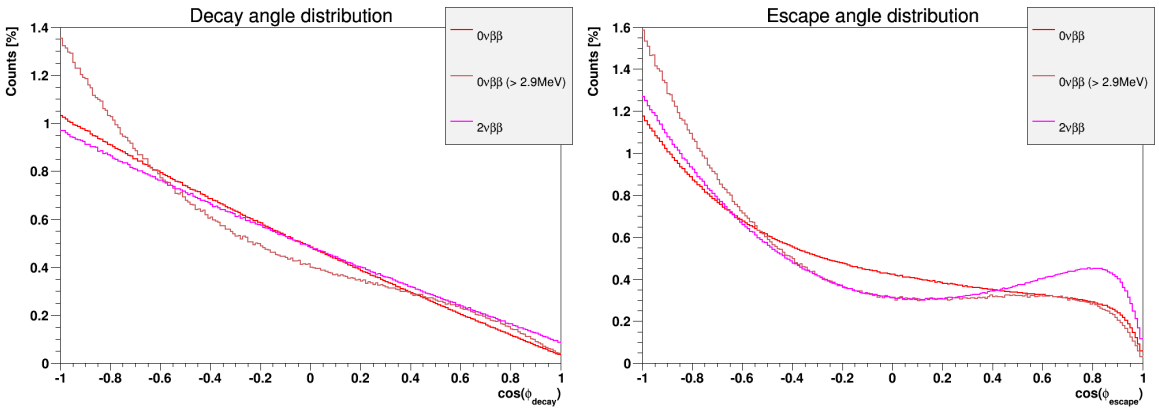

Figure 4.26: Distributions of decay angle (left) and escape angle (right) for $0\nu\beta\beta$ (S3) and $2\nu\beta\beta$ (S7). Red and pink lines are plotted for reference. Brown line represents distributions only of those $0\nu\beta\beta$ events which were measured by detector to reach sum of the electron energies at least 2.9 MeV. Plots show effects of the detection method and energy cuts. Distributions are normalized to equal area of 100%.

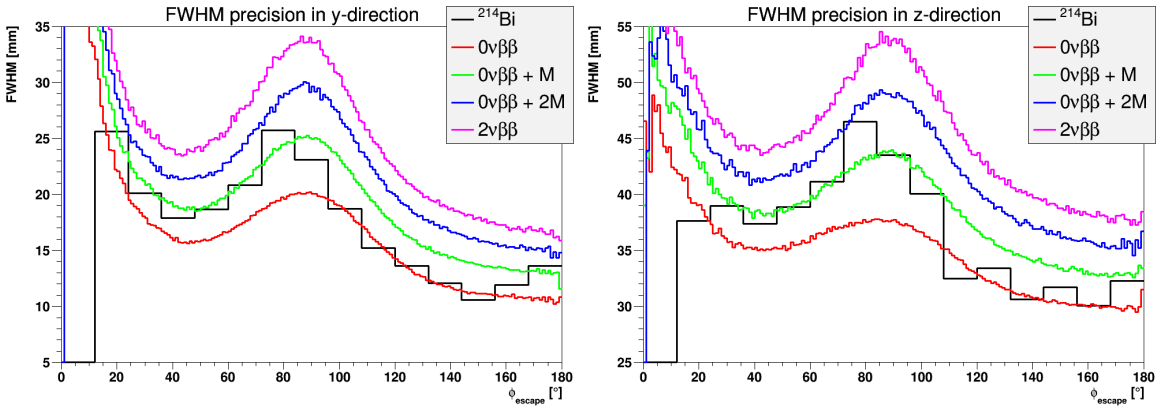

Figure 4.27: Dependence of FWHM vertex precision in both (y- and z-) directions as a function of Φ_{esc}. Comparison is performed for five chosen data samples: decay of ^{214}Bi (S2), $0\nu\beta\beta$ (S3), $0\nu\beta\beta\chi^0$ (S4), $0\nu\beta\beta\chi^0\chi^0$ (S5) and $2\nu\beta\beta$ (S7). Intervals $0° < \Phi_{esc} < 20°$ and $170° < \Phi_{esc} < 180°$ contain small number of data samples and, therefore, reliability of fit is questionable. No energy cuts were performed on any of the samples. $0\nu\beta\beta + \mathrm{M}$ and $0\nu\beta\beta + 2\mathrm{M}$ in plots denote $0\nu\beta\beta\chi^0$ and $0\nu\beta\beta\chi^0\chi^0$, respectively.

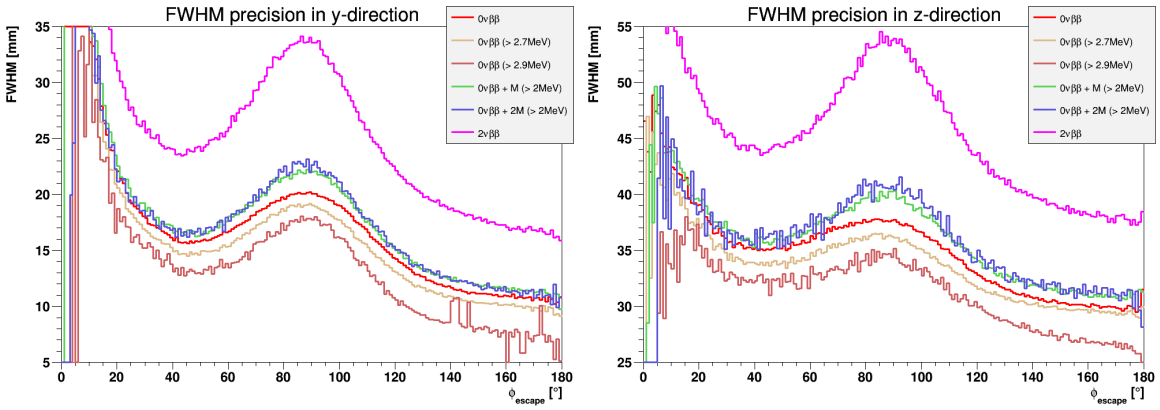

Figure 4.28: Dependence of FWHM vertex precision in both (y- and z-) directions as a function of Φ_{esc}. Plot includes $0\nu\beta\beta$ (red) and $2\nu\beta\beta$ (purple) samples from Figure 4.27 as reference. Comparison shows effect of energy cuts (listed in legend) on FWHM precision of $0\nu\beta\beta$ (S3), $0\nu\beta\beta\chi^0$ (S4) and $0\nu\beta\beta\chi^0\chi^0$ (S5) data samples. Intervals $0° < \Phi_{esc} < 20°$ and $170° < \Phi_{esc} < 180°$ contain small number of data samples and, therefore, reliability of fit is questionable. $0\nu\beta\beta + \mathrm{M}$ and $0\nu\beta\beta + 2\mathrm{M}$ in plots denote $0\nu\beta\beta\chi^0$ and $0\nu\beta\beta\chi^0\chi^0$, respectively.

the electrons as seen in Figures 4.27 and 4.28. If we exclude intervals (0°, 20°) and (170°, 180°), which do not contain sufficient statistics in order to perform reliable fit, we observe lightly improving precision from lowest angles to the highest with a significant worsening of the precision in the vicinity of 90°. The reasons behind the occurrence of the peak are clarified in Section 4.6.

4.4.3 Fit Function Justification

Typical distributions of vertex residuals depicted in Figure 4.5 might raise intuitive tendency to fit distribution of Δz by standard Gaussian fit. Δy seems to have pointier peak and slightly slower decreasing tails, which might make an impression, that Lorentz fit would be

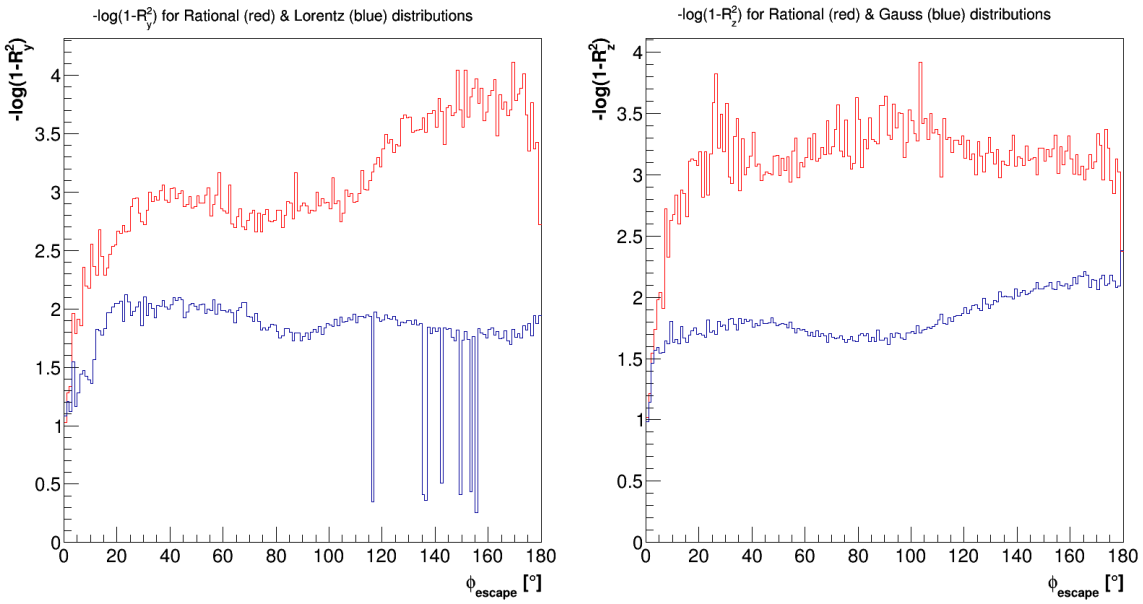

Figure 4.29: Plots comparing fit quality of distributions of vertex residuals. Red curve in both plots represent $-\log_{10}(1-R^2)$ coefficient of fit by rational function introduced in Equation 4.5. Blue curves represent alternative fit with Lorentz function (Δy residuals, figure on the left) or Gaussian function (Δz residuals, figure on the right). Coefficient is plotted as a function of escape angle between electrons. The comparison is presented for $2\nu\beta\beta$ sample (S7).

the best candidate. In Section 4.2.3, I extensively explained why such expectation is only a blind guess, with no deeper reason behind. Finally, in order to suit the needs for proper description of the functional shape I proposed very generic fitting function of four parameters given by Equation 4.5. I also commented that the validity of the fit was controlled by calculation of $-\log_{10}(1-R^2)$ where R^2 is coefficient given by Equation 4.12.

In order to prove that proposed fitting function performs better than Lorentz curve (for Δy) and Gaussian curve (for Δz), I performed both types of fit for each subsample and compared $-\log_{10}(1-R^2)$ coefficients.

Figure 4.29 compares $-\log_{10}(1-R^2)$ coefficient for fit with proposed rational function - blue fit - and Lorentz fit by Lorentz function (for Δy) and Gaussian fit (for Δz) - red curves. My proposed rational function is clearly performing well in all conditions. This serves as justification of my chosen fitting method, giving credibility to the presented data. The comparison was performed also for the other studies and my fitting function represented better choice.

4.5 Vertex Precision as a Function of Position on the Foil

One of the geometrical aspects which could potentially influence vertex precision is the position of the decayed nucleus on the source foil. Both emitted electrons travel different distances along different trajectories. These characteristics are dependent on the position where the event occurred. The electrons generated close to the edge of the source foil have higher chance to hit the X-calo and G-veto optical modules, having a much shorter tracks. In contrary, the electrons emitted in the center of the foil would travel, the most likely, longer

distances, producing more hits in tracker wire, therefore, potentially improving the vertex reconstruction. However, if we take magnetic field into account, such an events might curve enough to avoid the calorimeter and hit the foil resulting in failure to pass SDBDRC. These are some of the examples of effects influencing the vertex precision. The easiest way to investigate it is to set up a study similar to two in the previous sections.

In Figure 4.30 one can see distributions of event counts per bin passing SDBDRC. The presented plots represent four chosen double beta decay processes. Consistently with the projections depicted in Figure 4.8 the distributions are typically composed of two hot spots on each side of the foil along the horizontal y-axis. The edge bins, naturally, contain less events as the chance of tracking failure rises due to close proximity of the optical modules. The electrons can simply hit the optical module after really short track triggering minimal number of tracking wires, therefore, preventing the track reconstruction.

Let me now compare the vertex FWHM precisions for both Δy and Δz as a function of position on the foil (Figures 4.31 and 4.32). The overall precisions are gradually improving from $2\nu\beta\beta$ to $0\nu\beta\beta$. The reason behind is again the well-known increase of mean energy of the energy spectrum for each process. Furthermore, the $FWHM_y$ precision for each of four processes seems to be the best in the center of the foil while gaining the worst (highest) values in two symmetrical D-shaped spots on each side. In case of $FWHM_z$ the distribution looks very similar, however, two spots are O-shaped.

Understanding of the events contained within two spots might help us understand the factors influencing the precision. Therefore, I performed another analysis presented in following section.

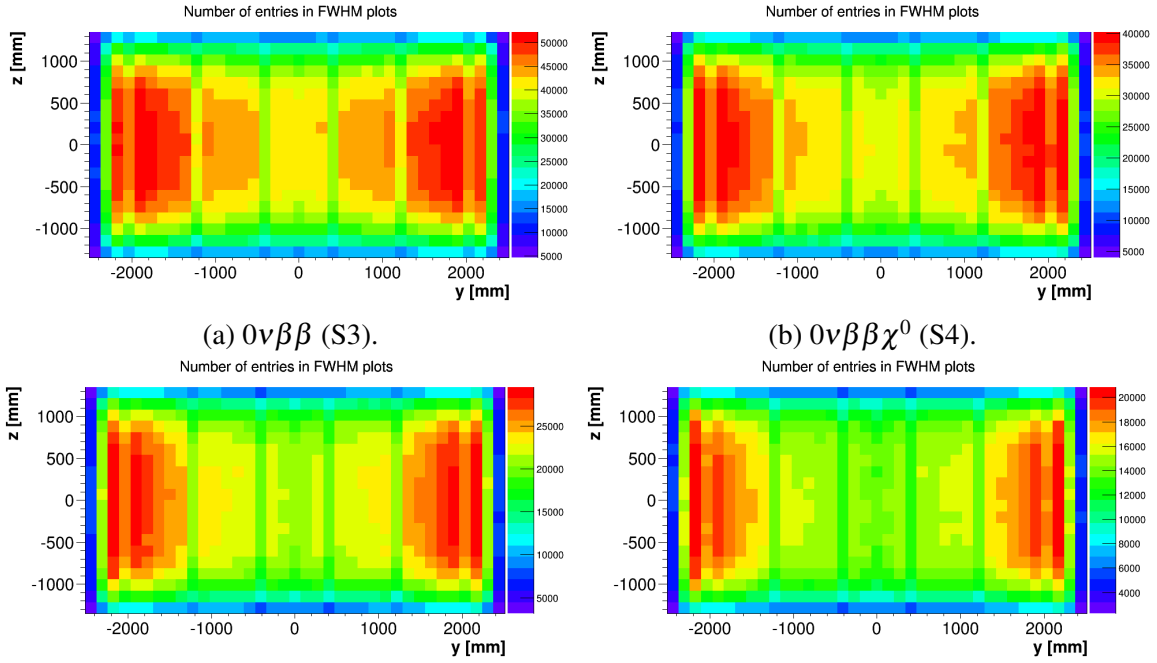

(a) $0\nu\beta\beta$ (S3).

(b) $0\nu\beta\beta\chi^0$ (S4).

(c) $0\nu\beta\beta\chi^0\chi^0$ (S5).

(d) $2\nu\beta\beta$ (S7).

Figure 4.30: Distribution of events passing SDBDRC as a function of position on the source foil. Source foil was divided into 37 horizontal (y-direction) and 20 vertical (z-direction) bins. Distribution represents four different double beta decay samples.

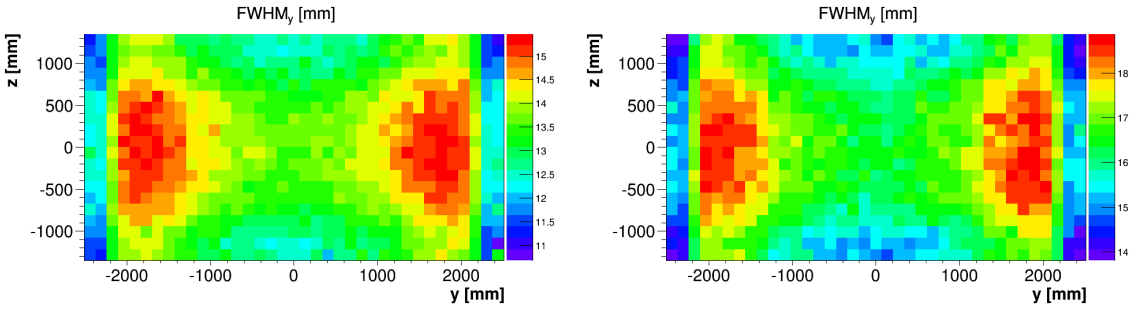

(a) FWHM$_y$: $0\nu\beta\beta$ (S3).

(b) FWHM$_y$: $0\nu\beta\beta\chi^0$ (S4).

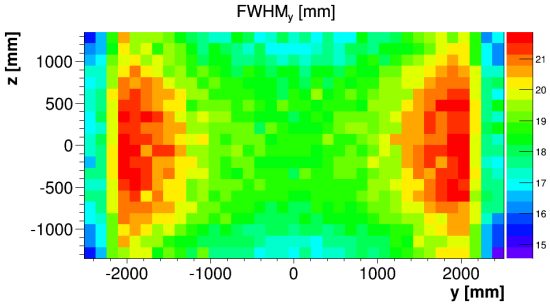

(c) FWHM$_y$: $0\nu\beta\beta\chi^0\chi^0$ (S5).

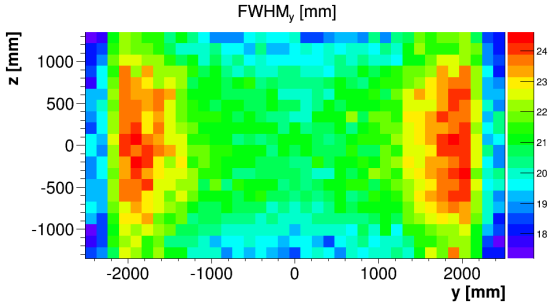

(d) FWHM$_y$: $2\nu\beta\beta$(S7).

Figure 4.31: FWHM vertex precision in y-direction as a function of position on the source foil. Source foil was divided into 37 horizontal (y-direction) and 20 vertical (z-direction) bins. Distribution represents four different double beta decay samples.

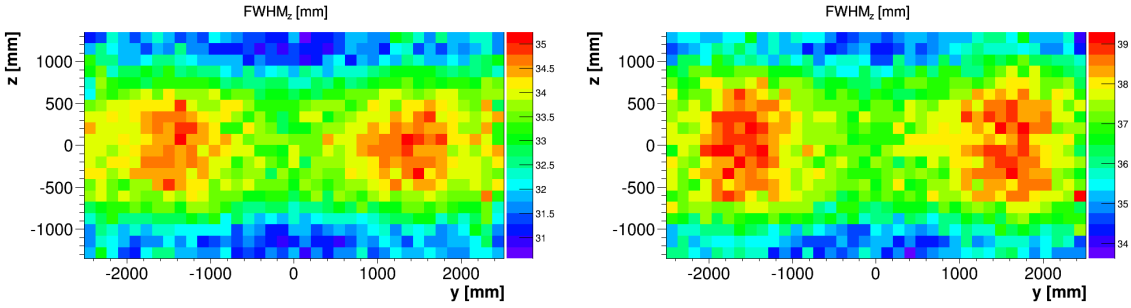

(a) FWHM$_z$: $0\nu\beta\beta$ (S3).

(b) FWHM$_z$: $0\nu\beta\beta\chi^0$ (S4).

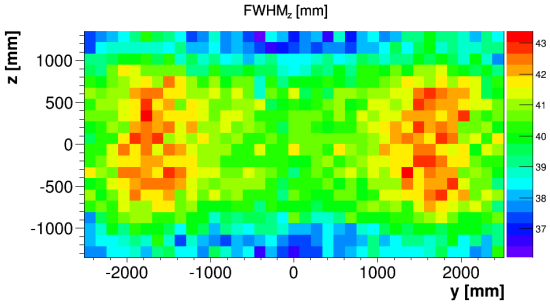

(c) FWHM$_z$: $0\nu\beta\beta\chi^0\chi^0$ (S5).

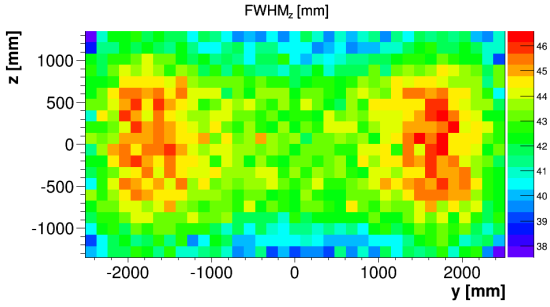

(d) FWHM$_z$: $2\nu\beta\beta$ (S7).

Figure 4.32: FWHM vertex precision in z-direction as a function of position on the source foil. Source foil was divided into 37 horizontal (y-direction) and 20 vertical (z-direction) bins. Distribution represents four different double beta decay samples.

4.6 Vertex Precision as a Function of Foil Angles

Vertex reconstruction precision seems to behave interestingly in dependence on escape angle between two electrons. Worsening of the precision in the region of escape angles around 90° might not be fully intuitive. The tracker is a stable part of demonstrator setup while two electrons with fixed escape angles between them might still account for many experimentally different situations. In order to gain more detailed information, I studied the precision as a function of "foil angles".

Foil angle is an angle between electron momentum (to be more precise its projection) in the moment of escape from source foil and a stable reference direction perpendicular to source foil. Note that, the angle is, therefore, defined for each individual electron. Figure 4.33 clarifies the definition of two source angles of interest called α and β.

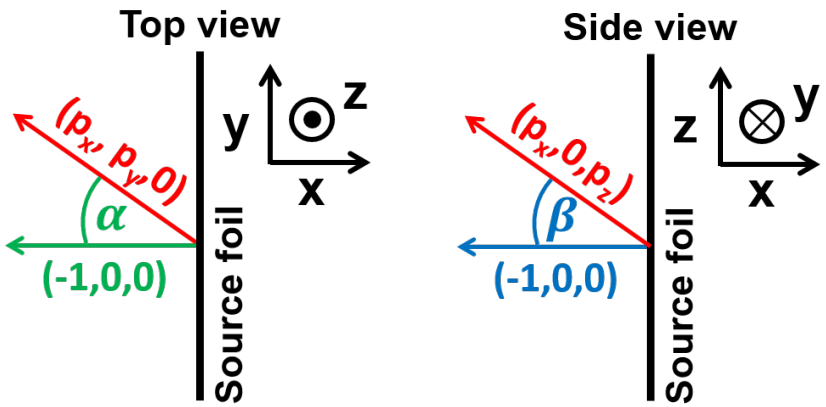

Figure 4.33: Definition of foil angles α and β. Note that, the figure on left represents top view while the figure on the right represents view from the side. The reference direction for both angles, is the same (-1,0,0) but the planes in which the angles lie are mutually perpendicular. Red arrow symbolizes projection of electron momentum into plane xy (left) or plane xz (right).

Electron momentum on the exit of the source foil $\vec{p} = (p_x, p_y, p_z)$ was projected into the xy plane $\vec{p_{xy}} = (p_x, p_y, 0)$ and xz plane $\vec{p_{xz}} = (p_x, 0, p_z)$. For both angles α and β vector $\vec{v} = (-1, 0, 0)$ served as reference - zero angle. Foil angles are therefore calculated following way:

$$\alpha = acos\left(\frac{\vec{p_{xy}} \cdot \vec{v}}{|\vec{p_{xy}}|}\right) = acos\left(\frac{-p_x}{\sqrt{p_x^2 + p_y^2}}\right), \tag{4.13}$$

$$\beta = acos\left(\frac{\vec{p_{xz}} \cdot \vec{v}}{|\vec{p_{xz}}|}\right) = acos\left(\frac{-p_x}{\sqrt{p_x^2 + p_z^2}}\right). \tag{4.14}$$

By definition, each angle takes values from range $\alpha, \beta \in \langle 0°, 180° \rangle$. Therefore, each value represents two scenarios differing only by sign of p_y for α and p_z for β. This symmetry is welcomed, as we do not expect different effect taking place between the two scenarios. On the other side, foil angle value distinguishes between the side of the source foil where

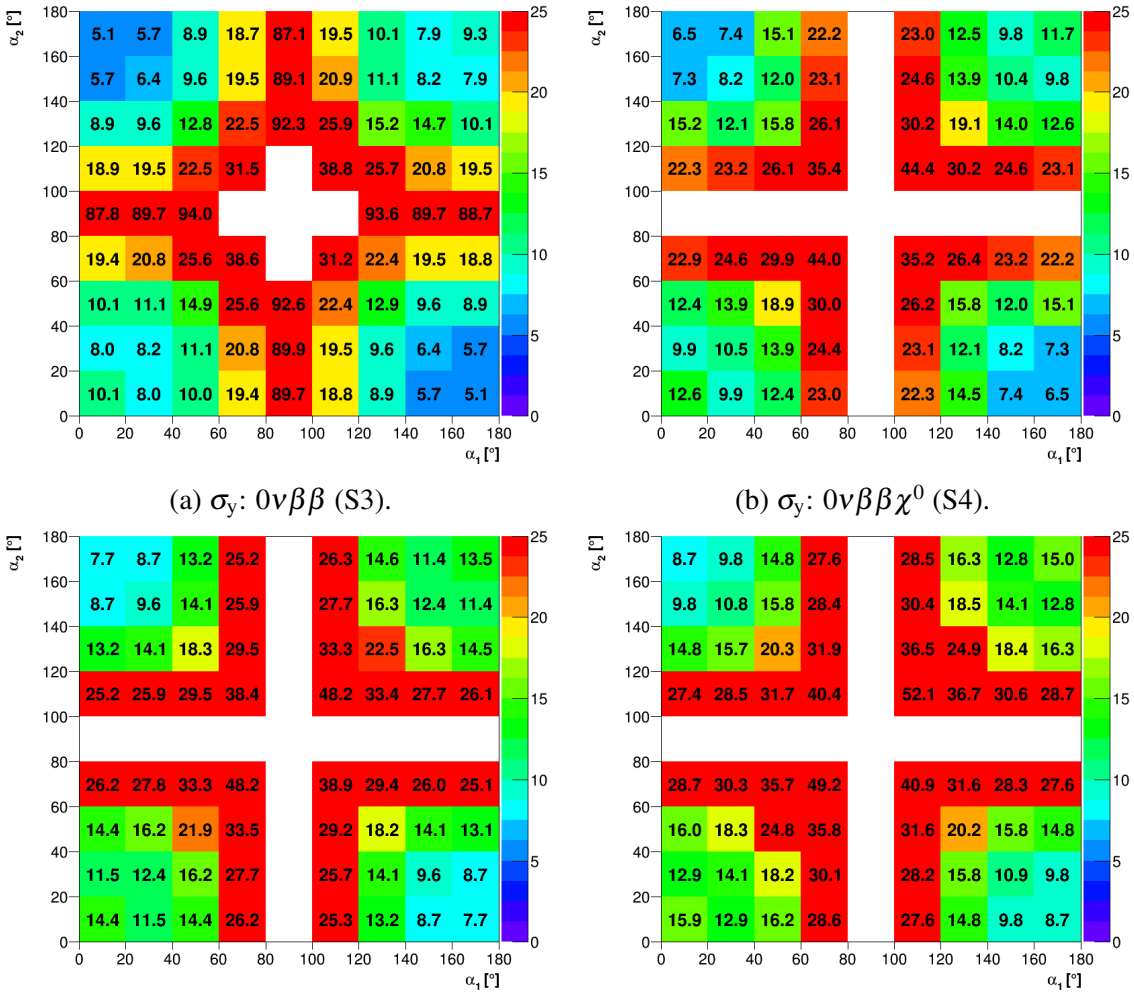

(a) σ_y: $0\nu\beta\beta$ (S3).

(b) σ_y: $0\nu\beta\beta\chi^0$ (S4).

(c) σ_y: $0\nu\beta\beta\chi^0\chi^0$ (S5).

(d) σ_y: $2\nu\beta\beta$ (S7).

Figure 4.34: Sigma precision of Δy residual as a function of foil angles α_1 (first electron) and α_2 (second electron). Four figures represent four different double beta processes.

electron exits it. $\alpha, \beta \in \langle 0°, 90° \rangle$ accounts for the left side[4] of the foil (i.e. negative x values) and $\alpha, \beta \in \langle 90°, 180° \rangle$ accounts for right side of the source foil (i.e. positive x values). Angle $\alpha, \beta = 90°$ represents electron emitted parallel to source foil. Such a definition gives us opportunity to study not only the effects of different angles, but also distinguish the scenarios when electrons are emitted to the same or opposite side of the foil.

4.6.1 Sigma Results

Figures 4.34, 4.35, 4.36 and 4.37 compare sigma precision results for both α and β foil angles in both directions y and z. Here, I compare four different modes of double beta decay, $0\nu\beta\beta$, $0\nu\beta\beta\chi^0$, $0\nu\beta\beta\chi^0\chi^0$ and $2\nu\beta\beta$. Before commenting the results, let me briefly discuss the meaning of the plots.

In each plot, horizontal axis represents foil angle of the first electron while vertical represents the foil angle of second electron. Assignment of the number to the electron is the same

[4] With respect to Figure 4.33

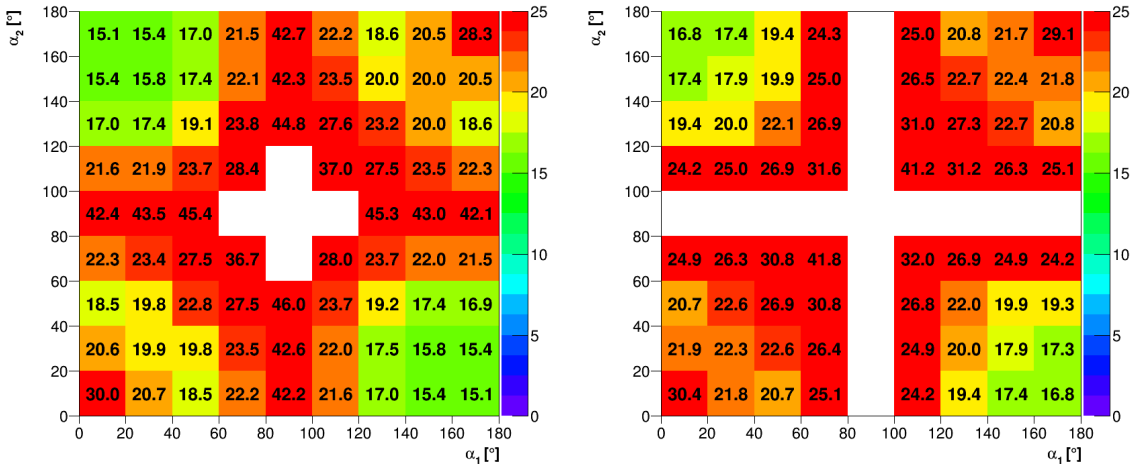

(a) σ_z: $0\nu\beta\beta$ (S3).

(b) σ_z: $0\nu\beta\beta\chi^0$ (S4).

(c) σ_z: $0\nu\beta\beta\chi^0\chi^0$ (S5).

(d) σ_z: $2\nu\beta\beta$ (S7).

Figure 4.35: Sigma precision of Δz residual as a function of foil angles α_1 (first electron) and α_2 (second electron). Four figures represent four different double beta processes.

as in the case of energy plots - first one is always the one which was detected first. All the plots share similarities which have to be discussed before we attempt to extract any information. In the center, there is a "central cross" representing the events when one of the electrons is emitted parallel (within the precision given by bin width) to the source foil. These bins are typically with no vertex precision assigned to them as the fit of distribution of vertex residuals is not precise enough. The situation in the central cross will be studied in following section. Central cross splits the plot into four quadrants. Top left and bottom right, those which are crossed by primary diagonal (when $\alpha_2 = 180° - \alpha_1$ or $\beta_2 = 180° - \beta_1$), represent all the events when electrons are emitted to the opposite sides of source foil. The other two quadrants, crossed by secondary diagonal (when $\alpha_2 = \alpha_1$ or $\beta_2 = \beta_1$) represent events when both electrons are emitted to the same side of the source foil. However, it is not possible to distinguish the sign of p_y for foil angle α (sign of p_z for foil angle β), therefore, each data point represents two different constellations of angle Φ_{esc} between two electrons. This has to be taken with precaution during the data analysis.

Firstly, I claim again that there is clear tendency of improved overall precision if we compare four presented double beta decay modes. $2\nu\beta\beta$ achieved the worst precision and

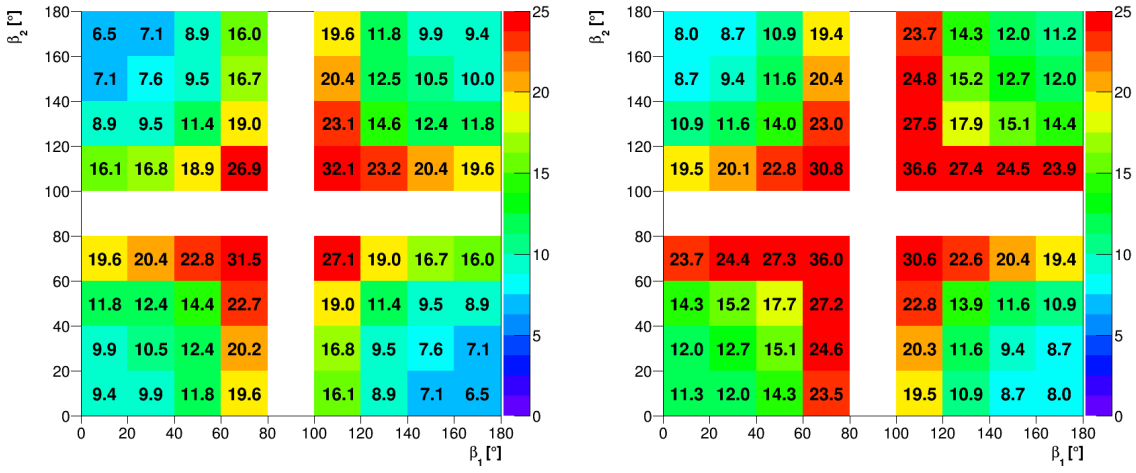

(a) σ_y: $0\nu\beta\beta$ (S3).

(b) σ_y: $0\nu\beta\beta\chi^0$ (S4).

(c) σ_y: $0\nu\beta\beta\chi^0\chi^0$ (S5).

(d) σ_y: $2\nu\beta\beta$ (S7).

Figure 4.36: Sigma precision of Δy residual as a function of foil angles β_1 (first electron) and β_2 (second electron). Four figures represent four different double beta processes.

$0\nu\beta\beta$, in contrary, the best precisions. This serves as another confirmation of the strong role of the energy of the emitted electrons for vertex precision. Furthermore, there is a clear symmetry between quadrants lying on the primary diagonal as well as between the two lying on the secondary diagonal. The symmetries represent the events when sides of the source foil are swapped. However, if we compare all four quadrants, the symmetry is not kept. Quadrants on the main diagonal tend to reach better precisions than two quadrants on the secondary diagonal. Let us have a closer look what this asymmetry implies. Let me compare four corner bins in Figure 4.34a. Each one represents electrons emitted perpendicularly to the source foil within the precision given by bin width (i.e. 20°). Two corner bins belonging to scenario of electron emission to the opposite side of the source foil (primary diagonal) represent precision in vertex reconstruction as good as 5.1 mm. In contrary, two corner bins representing the scenario of perpendicular emission to the same side (on the secondary diagonal) manifest almost two times worse vertex reconstruction precision of 9.3/10.1 mm. The difference is caused by the events with both electron trajectories being very similar. Several Geiger wires are triggered by both electrons which makes it more difficult for the reconstruction algorithm to distinguish which wire hit belongs to which electron. The effect

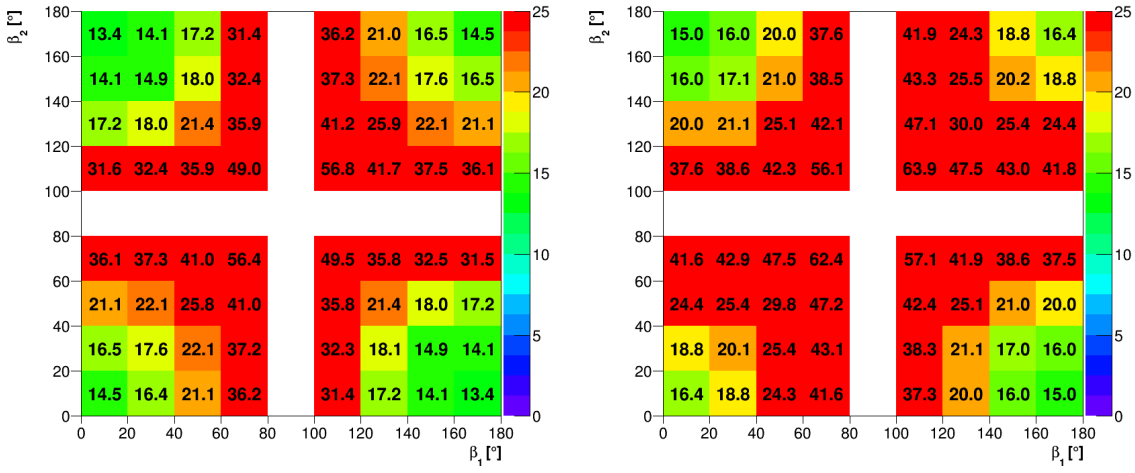

(a) σ_z: $0\nu\beta\beta$ (S3).

(b) σ_z: $0\nu\beta\beta\chi^0$ (S4).

(c) σ_z: $0\nu\beta\beta\chi^0\chi^0$ (S5).

(d) σ_z: $2\nu\beta\beta$ (S7).

Figure 4.37: Sigma precision of Δz residual as a function of foil angles β_1 (first electron) and β_2 (second electron). Four figures represent four different double beta processes.

is visible also in vicinity of top right and bottom left bin. Precision in all surrounding bins is better. In contrary, bins in the top left and bottom right of the plot are the bins with the best precisions in their quadrants. Corner bins, which are lying on the secondary diagonal belong to the events, in which electrons are escaping the foil perpendicularly, at the same side of the source foil. Their trajectories are very similar, therefore, they have high chance to share large number of Geiger cells. Electrons from events represented by corner bins on the main diagonal are detected on the different sides of the source foil and the chance to observe cell sharing is strictly zero. The credibility of this reasoning is underlined by the fact that the same effects are observed in all plots regardless of the process or direction (y or z).

Observation of the cell sharing effects is an interesting input into the discussion about the shape of FWHM precision as a function of Φ_{esc}. Let me take Figure 4.27 as a reference. If we ignore peak in the vicinity of 90°, the precision tends to be improved for the biggest angles towards 180°. In majority of such events, electrons are emitted into the opposite sides of the source foil, preventing the cell sharing. On the other side of the plot, in region of small angles, the cell sharing is highly probable and, therefore, vertex precision gets significantly lower, causing asymmetry between the lowest and the highest angles.

4.6.2 Events in Central Cross

Vertices belonging to events from bins adjacent to the central cross are reconstructed with much worse precision than the other events deeper into the quadrants. Moreover, the bins in the central cross have no value assigned to them in almost all the plots. This is not caused by lack of events in the cross. Figures 4.34a and 4.35a show that majority of the bins at all four ends of the central cross contain potentially enough events to be fitted. In fact, the real reason, why central cross tend to remain empty, lies in the fit quality criterion imposed in all my analyses. As I already discussed at the beginning of the chapter, only those bins are plotted, where quality of the bin fulfils condition $-\log_{10}(1-R^2) > 1$, i.e. $R^2 > 0.9$. Poor fit quality is not a result of lack of statistics, but it is signature of the dramatic change in the distribution of vertex residual Δy. The fit function fails to describe the distributions.

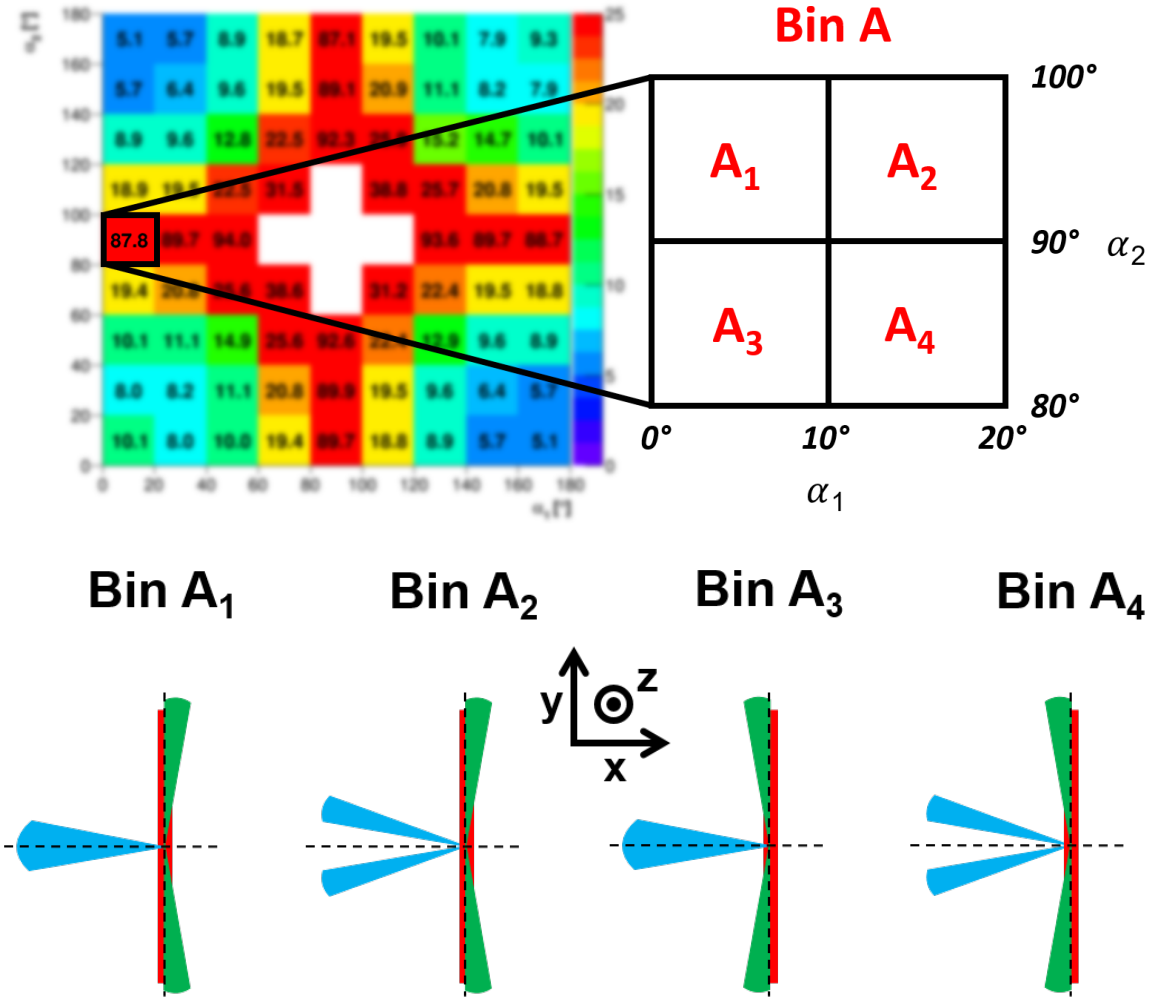

Figure 4.38: Top: Position of bin A within the diagram of foil angles α (sample in Figure 4.34a). Figure also shows the division of bin A into bins A_1 to A_4. Bottom: Schematic representation of electron configurations included in each of bins A_1 to A_4. Red rectangle symbolizes the source foil viewed from top. Black dashed lines depict the axes of symmetry of source foil. Blue (green) regions represent the span of foil angles α_1 (α_2), i.e. the relative possible directions of first (second) electron with respect to the source foil. Note that, the emission of the electrons can occur anywhere in the source foil, the placement in the center of foil is only symbolic. Bin A represents all the configurations at the same time.

The events in the central cross represent situation when one or another electron escapes foil parallel to the foil (within the precision given by bin width). Such trajectories are very difficult (if even possible) to reconstruct. Let us have a look at the situation in one of the bins. As a reference, I will study sample in Figure 4.34a ($0\nu\beta\beta$). It represents sigma precision in y-direction as a function of α foil angles. I will focus on the leftmost bin in the central cross. The bin is highlighted in top part of Figure 4.38. It includes all the events from following α ranges: $0° < \alpha_1 < 20°$, $80° < \alpha_2 < 100°$. I will call it bin A. The distribution of vertex residuals Δy in the bin is shown in the Figure 4.39. We can notice that the fit quality is much lower than standard. The shape of the distribution is very different to all the previous studied cases. Instead of the clear, well defined peak in the center, there is a plateau which changes the characteristic shape and prevents the fit function to adapt to the shape.

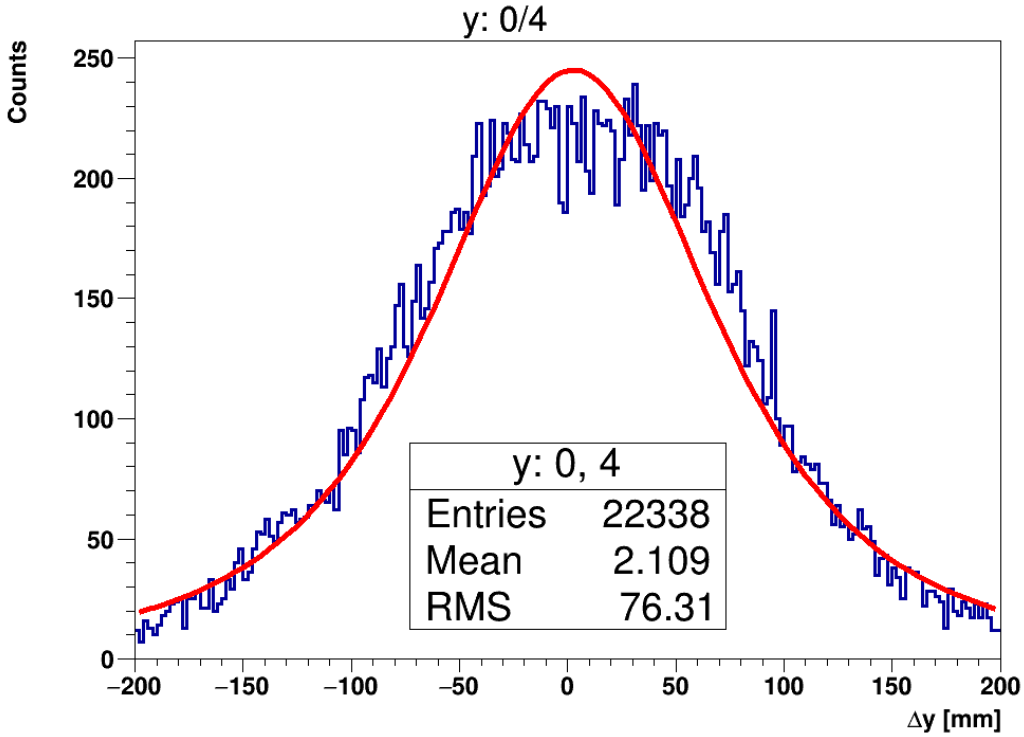

Figure 4.39: Distribution of vertex residuals Δy for events from bin A defined in Figure 4.38.

Due to odd number of divisions in both dimensions of the plot in Figure 4.34a, bin A includes both types of events, those, when electrons are emitted to the same side of the source foil as well as the other side. The previous analysis of foil angle data already showed that these two categories differ significantly due to effect of Geiger cell sharing. Therefore, I decoupled the events and split bin A into four smaller bins A_1, A_2, A_3 and A_4 as depicted in top part of Figure 4.38. Four bins represent four different configurations of the electrons. The configurations are symbolized in the bottom part of the same figure. Bins A_1 and A_2 represent two configurations when electrons are emitted to the opposite side of the source foil and bins A_3 and A_4 represent equivalent situations but with electron emission to the same side of the source foil.

Subsequently, I performed analysis of the vertex residuals in each of four bins. Figure 4.40 shows comparison of the distribution of vertex residuals Δy in bins A_1 to A_4. Interestingly, each one of the distributions is centered several tens of milimeters away from $\Delta y = 0$. For this purpose, I had to redefine my fitting function defined by Equation 4.5 and add pa-

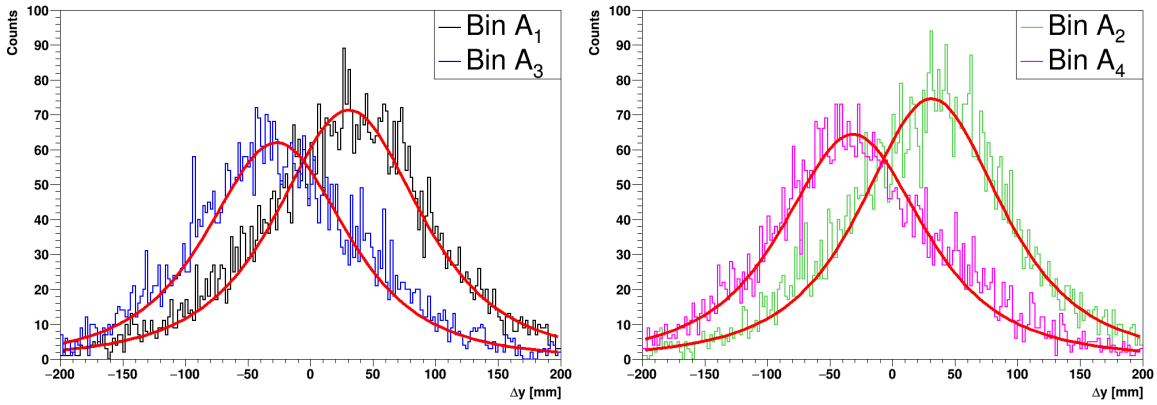

Figure 4.40: Distribution of vertex residuals Δy for events from bin A_1 to A_4 defined in Figure 4.38.

rameter x_0 which accounts for shift in peak position:

$$f(x) = \frac{N}{\left[(x-x_0)^2+\Gamma\right]^p}. \tag{4.15}$$

Such a function is, in fact, important only in case of events in the central cross due to their specific nature. Shift of the distribution has a crucial implications for the events in the central cross. In average, one of the vertices tends to be closer to the center of the foil (in horizontal, y-direction) more often than the other one, causing the shifts of Δy distributions. These shifts imply that the vertex reconstruction have tendency to misreconstruct the vertex by several milimeters more often than reconstruct it precisely ($\Delta y = 0$). Such set of events might degrade vertex precision when included in the dataset. Moreover, if we sum all four distributions in Figure 4.40 we obtain again distribution for bin A in Figure 4.39. The tendency of distributions for bins A_1 to A_4 to peak out of $\Delta y = 0$ explains atypical shape of the distribution for bin A, especially the increased width as well as the plateau in the center.

The analysis of central cross events gave us insight into the specific set of events which tend to be reconstructed very poorly. Due to the difficulties to reconstruct the vertices properly I suggest to completely ignore the events in the analysis in order to gain better vertex precision.

4.6.3 Events in Diagonals

Another interesting category of events lies on both diagonals inside of the quadrants. As an object of a study, I will use twelve bins extracted from results in Figure 4.34d ($2\nu\beta\beta$). Their choice and naming convention is clear from top part of Figure 4.41. In the bottom part of the same figure one can find all the configurations belonging to each bin.

Firstly, let me discuss the bins from secondary diagonal. They all represent configurations, when both electrons are emitted to the same side of the source foil. Their reconstruction precision is worse than the precision of their white counterparts. This is implied by effect of Geiger cell sharing which was already discussed. On top of this, we can observe remarkable effect. Figure 4.42 shows distributions of y-coordinates of first vertex (y_1) for all six configurations represented by black bins. Note that, the distributions of y-coordinates of second vertex (y_2) follow the same distribution, therefore it is sufficient to discuss only the first. As we approach the center of the plot $B_{00} \rightarrow B_{33}$ ($B_{88} \rightarrow B_{55}$), we can notice that the

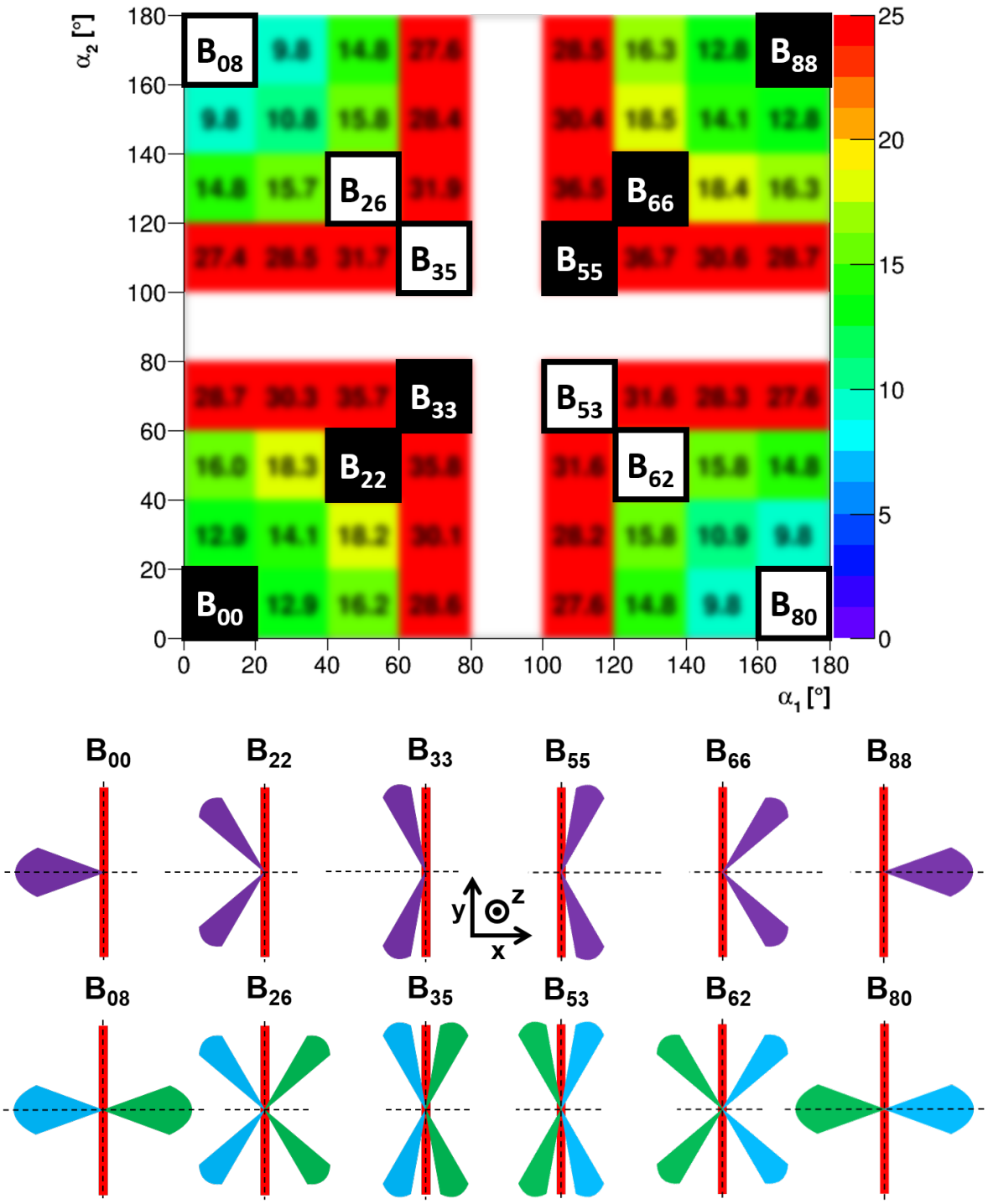

Figure 4.41: Top: Position of chosen diagonal bins within the diagram of foil angles α (sample in Figure 4.34d). The bins on the primary diagonal will be called "white" bins while bins on the secondary diagonal will be called "black" bins. Bottom: Schematic representation of electron configurations included in all chosen diagonal bins. Red rectangle symbolizes the source foil viewed from top. Black dashed lines depict the axes of symmetry of source foil. Blue (green) regions represent the span of foil angles α_1 (α_2), i.e. the relative possible directions of first (second) electron with respect to the source foil. Purple regions depict the situation when span of emission angles α_1 and α_2 are exactly the same. Note that, the emission of the electrons can occur anywhere in the source foil, the placement in the center of foil is only symbolic.

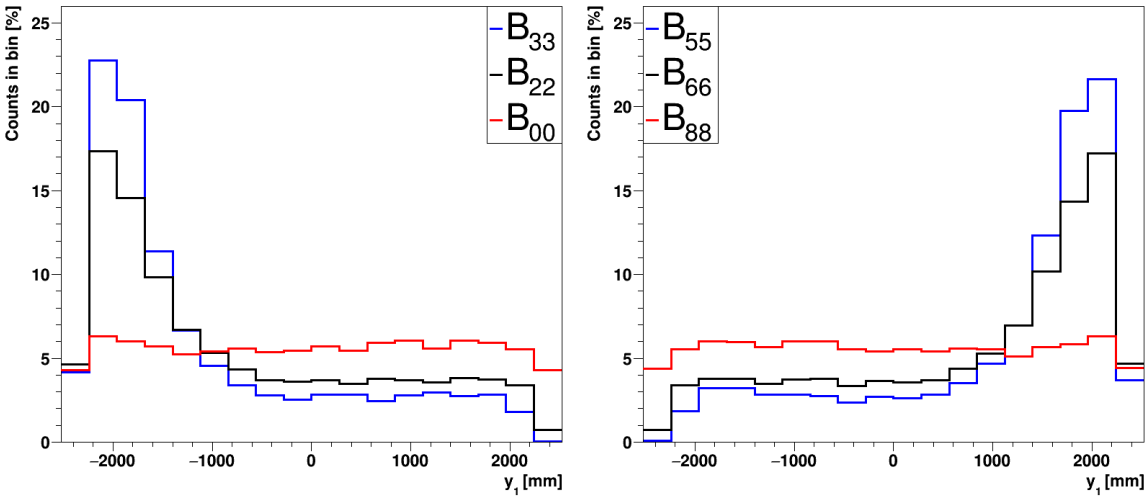

Figure 4.42: Distributions of y-coordinates of vertex V_1 in each of six black bins. Each distribution is normalized to total sum of 100%. The distributions of y-coordinates of vertex V_2 are not plotted, as they are represented by effectively the same functions.

vertices are preferentially reconstructed on the negative (positive) side of the y-axis. In case of the corner bins B_{00} and B_{88}, which represent emission perpendicular to the source foil, the distribution is very close to flat. The asymmetry is easily understandable if we take into account the presence of magnetic field. Homogeneous magnetic field of 25G in positive z-direction is applied in full volume of the demonstrator. The electrons are negatively charged particles, therefore, they are curved counterclockwise from the point of view opposite to the direction of the magnetic field. Figure 4.43 clarifies the situation in simple scheme. It represents the demonstrator from top view (see coordinate system).

The scheme represents four different electrons which exit the foil under the same angle relatively to the source foil[5]. All of the electrons in the figure represent same energy, i.e. curvature of their track is exactly the same. Two of the electrons marked by dashed lines are curved back to the source foil causing the elimination of such event. However, their symmetrical counterparts are registered in side calorimeters (X-calo) and the event stays valid from the point of view of SDBDRC. Events with both electrons emitted to the left side of the source foil (negative x) pass the SDBDRC more likely in the bottom side of the scheme (negative y). These events are represented by bins B_{22} and B_{33}. This asymmetry is exactly the effect seen in a left side of the Figure 4.42. In contrary, the electrons emitted to the right side of the source foil (positive x) pass the SDBDRC more likely in the top side of the scheme (positive y). They are represented by bins B_{55} and B_{66}. Once again, the effect is visible in the right side of the Figure 4.42.

Now, if we have a look at the configurations representing exactly the same situations, but with the electrons emitted to the other side of the source foil, we should recover the distribution symmetry along the y-axis. The electrons which are lost in the top part of the source foil by emission to the left side of the foil are compensated by the electrons emitted to the right side and vice versa. These configurations are represented by white bins (on the primary diagonal). Figure 4.44 is consistent with the assumption.

The distributions of vertices in z-direction do not show any of the aforementioned features and they do not change as we move along the diagonals. This fact is another proof that

[5]Note that this relative angle is measured with respect to the line parallel to source foil, therefore, they are not the same as our standard foil angles α.

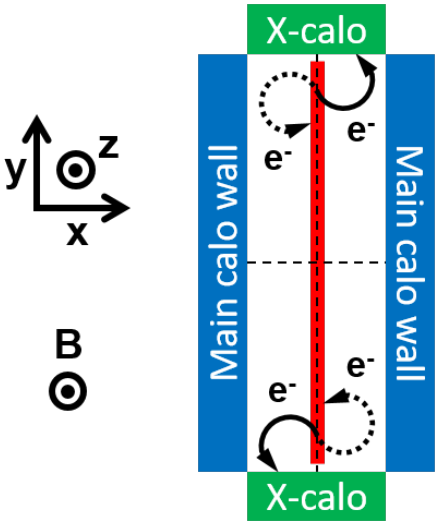

Figure 4.43: Scheme representing four symmetric configurations of electron emission from the foil. Each electron is emitted under exactly the same angle with respect to the y-axis. Magnetic field curves the electrons counterclockwise (view from top). Electrons represented by solid line are detected by X-calo calorimeter side wall (green) while electrons with dashed line trajectories are curved back to the source foil causing extra vertex on source foil. It leads to rejection of events belonging to these electrons by SDBDRC.

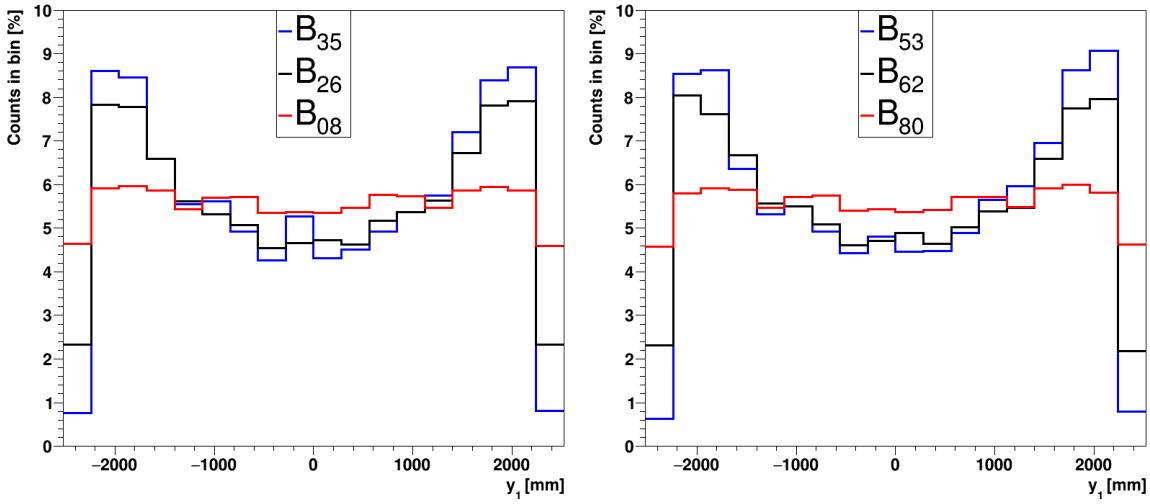

Figure 4.44: Distributions of y-coordinates of vertex V_1 in each of six white bins. Each distribution is normalized to total sum of 100%. The distributions of y-coordinates of vertex V_2 are not plotted, as they are represented by effectively the same functions.

the asymmetry in y-direction was caused by magnetic field. Finally, let us have a look how the distributions are really changed with a change of magnetic field. For a comparison, I took three samples of $2\nu\beta\beta$ decay events with three different magnetic fields (0 G, 25 G and 60 G), namely, S6, S7 and S8. In both I preserved events from off-diagonal quadrants. In scenario "A" I considered only the events from bottom left quadrant, i.e. $\alpha_1, \alpha_2 < 60°$, while in scenario "B" I analysed only events from top right quadrant, i.e. $\alpha_1, \alpha_2 > 120°$. Left side of the Figure 4.45 shows behaviour similar to the one in left side of the Figure 4.42. However, in case without magnetic field, the distribution tends to be flat. It is a final proof that the

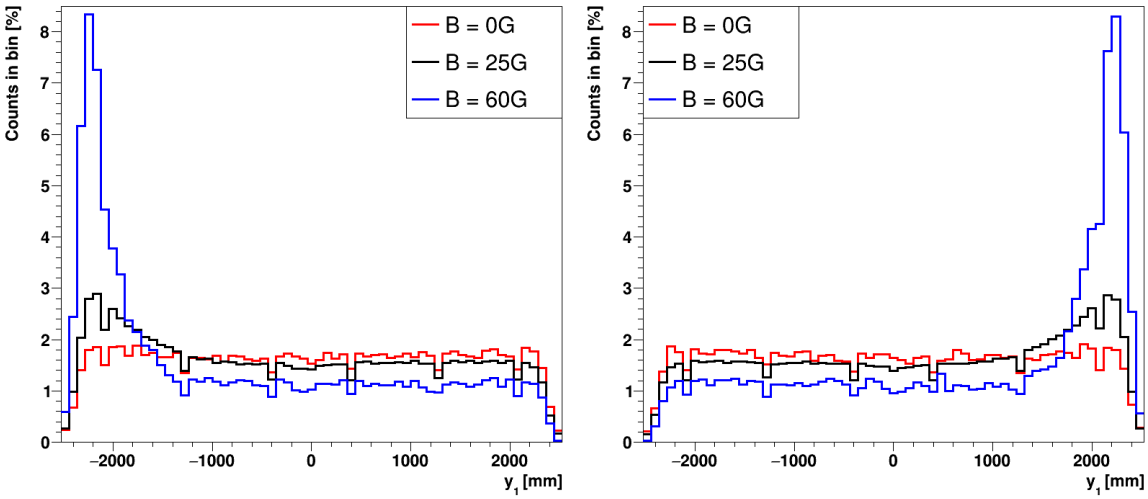

Figure 4.45: Distributions of y-coordinates of vertex V_1 for three different values of magnetic field ($2\nu\beta\beta$). Figure on the left represent all the events with $\alpha_1, \alpha_2 < 60°$ (both electrons emitted to the side of the foil with negative x). Figure on the right side represent all the events with $\alpha_1, \alpha_2 > 120°$ (both electrons emitted to the side of the foil with positive x). Each distribution is normalized to total sum of 100%. The distributions of y-coordinates of vertex V_2 are not plotted, as they are represented by effectively the same functions.

vertex asymmetry really comes from the presence of magnetic field. For the completeness, let me comment the scenario B. As seen in the right side of the Figure 4.45, the asymmetry shows the same behaviour, only the side was changed, as expected.

The presence of magnetic field combined with SDBDRC was proven to cause asymmetry in vertex distribution along the horizontal y-axis. This fact might come handy as a tool for background elimination. Let us change the charge of the particles in Figure 4.43 to a positive value. The particles in the magnetic field now spin on clockwise trajectories. We could follow the whole discussion for the positively charged particles from the very beginning and coming to the exactly the same conclusion - magnetic field causes the asymmetry of the vertex distribution in y-direction. However, there is one important detail. The asymmetry would be flipped, i.e. the events containing particles emitted to the left side of the source foil (negative x) would more likely pass SDBDRC if the original vertex was in the top part of the source foil (positive y), and vice versa. Therefore, the region close to the negative y-edge of the source foil would tend to keep negatively charged particle more often than those with positive charge if the event happens on the left side of the source foil (negative x). The inverted statement hold for the positive y edge. These two regions have potential to suppress the background events caused by positively charged particles in favour of signal events which always contain negatively charged particles. It is questionable how big the suppression effect would be, and whether it would perform better than simple suppression based on the clockwiseness of the track, however, such question is beyond the scope of the thesis.

As I already commented, curvature of particles cause asymmetry presented in scheme in Figure 4.43. The curvature is naturally influenced by magnetic field as it was shown. In order to finally demonstrate that the effect really comes from the effect from Figure 4.43, I performed simulation where except for application of SDBDRC I also eliminated all the events which were detected in X-calo wall. The result is shown in Figure 4.46. The figure was produced under exactly the same conditions as the ones showed in Figure 4.30 except

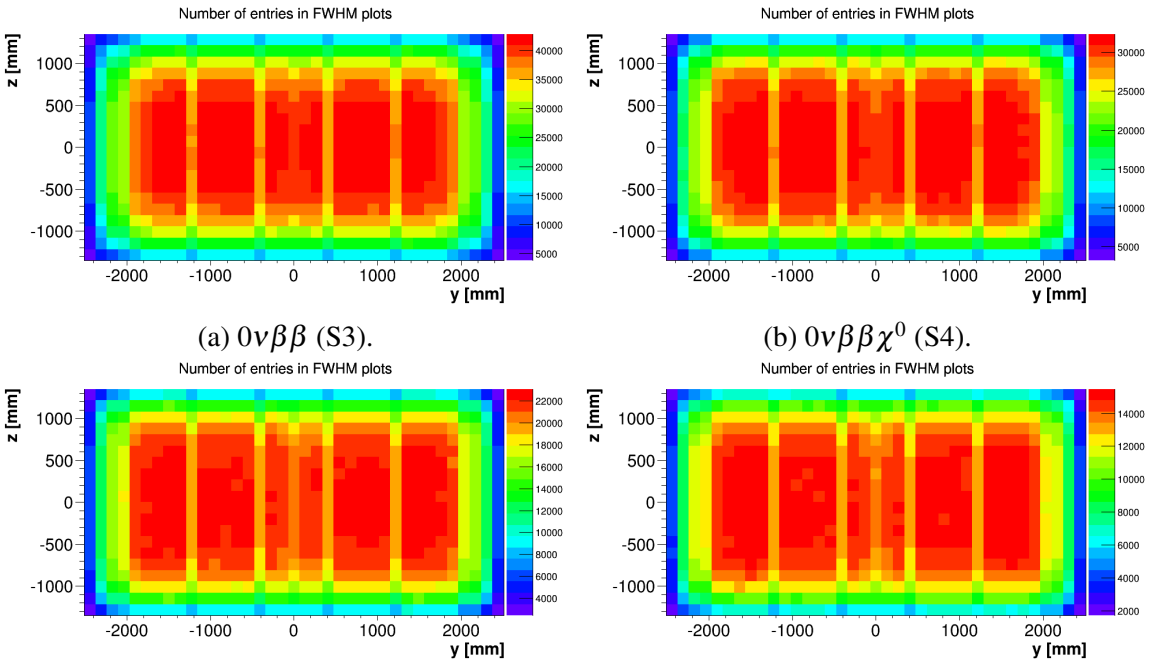

(a) $0\nu\beta\beta$ (S3).

(b) $0\nu\beta\beta\chi^0$ (S4).

(c) $0\nu\beta\beta\chi^0\chi^0$ (S5).

(d) $2\nu\beta\beta$ (S7).

Figure 4.46: Distribution of events passing SDBDRC as a function of position on the source foil. Distributions are the same as those presented in the Figure 4.30, however, in these, all the events detected in X-calo were eliminated. Source foil was divided into 37 horizontal (y-direction) and 20 vertical (z-direction) bins. Distribution represents four different double beta decay samples.

for the fact that in Figure 4.30 were accepted events which were detected in X-calo. We can clearly see disappearance of two spots, even though, both figures were produced under magnetic field of 25G. If one needs to avoid the effect of asymmetrical curvature at the end of source foils, it is simply sufficient to ignore all the events detected by X-calo walls.

4.7 Conclusions

The study of the vertex precision provided wide palette of observations which might serve as useful guidelines in order to choose events with a tracking information of the highest quality. Let me sum up the most important results of the chapter:

1. **Energy dependence** - All four studies have shown that the vertex precision is mainly given by the kinetic energies of the electron. Within the same studied sample regardless of the type of study (escape angle, foil position, foil angles) the precision was improved by observation of electrons of higher average energies. The choice of electrons with higher energies was done either by direct cut on the energy (for example study of the escape angle distributions) or by simply comparing the precisions for four different double beta decay processes with different mean electron energy. The energy dependence is mainly caused by scattering of the electrons which occurs in the source foil. The lower energy electrons tend to scatter much more, preserving the information about the decay angle worse than the electrons of higher energies. For the highest

electron energies the correlation between Φ_{dec} and Φ_{esc} tends to approach $\Phi_{dec} = \Phi_{esc}$ as shown in Figure 4.23.

2. **Vertex efficiency** - Study of the vertex efficiency performed for all the previous studies and shown in Section 4.3 revealed total independence of the efficiency on any of the studied parameters. Results have shown, that regardless of the situation, always roughly one event in four is reconstructed in a way that, the real vertex V_r lies in the rectangular area delimited by two reconstructed vertices V_1 and V_2 in the yz plane.

3. **The dependence on side of the foil** - The analysis of foil angles revealed, that the events when electrons are emitted to the same side of the foil, are reconstructed less precisely than equivalent events (in terms of relative angle to source foil) emitted to the opposite sides. This effect is due to the fact that the electrons emitted to the same side have high possibility to trigger same Geiger wires. In the emission to the opposite side this effect does not exist.

4. **Assymetry of precision between small and large Φ_{esc}** - Events with the smallest escape angles (i.e. $\Phi_{esc} \lesssim 50^\circ$) tend to have worse vertex precision then the equivalent events for the highest angles (i.e. $\Phi_{esc} \gtrsim 120^\circ$) as depicted in Figures 4.27 and 4.28. The asymmetry is caused by the effect of cell sharing explained in previous point. Lower escape angles include events when both electrons are emitted to the same side of the source foil much more often than the highest angles where the effect, in contrary, occurs less and less likely as we approach $\Phi_{esc} = 180^\circ$. Therefore, the cell sharing is the key to understanding of the characteristic shape of the vertex precision as a function of escape angle.

5. **Worsened precision for $\Phi_{esc} \approx 90^\circ$** - Except for improvement of the vertex precision as we approach $\Phi_{esc} = 180^\circ$, the vertex precision manifest local worsening in region of $\Phi_{esc} \approx 90^\circ$ as seen in Figures 4.27 and 4.28. Here, another effect has to be considered. If we take into account all possible situations when electrons leave source foil under $\Phi_{esc} = 90^\circ$, in terms of foil angles, we find out that the more an electron is perpendicular to the source foil, the more another one is parallel to the foil and vice versa. As it was shown in study of foil angles, events with electrons which escape parallel to foil, belong to the central cross or close to it, where the vertex precision is the worst. The contribution of these scenarios spoil the vertex precision for $\Phi_{esc} \approx 90^\circ$. For all the scenarios with higher and lower escape angles, such an effect is getting smaller while the aforementioned effect of Geiger cell sharing (point 3.) gradually takes over and determine the shape of the lowest and highest angles.

6. **Two spots in the foil distribution** - In analysis of the vertex precision in dependence on the position on the source foil, two spots of lower precision (and abundance of events which passed SDBDRC) was observed. Two spots were symmetrically distributed on the ends of the source foil, along the horizontal y-axis. It was shown to be effect of the presence of magnetic field. Figure 4.43 represents the events with the electrons emitted to the same relative angle with respect to the source foil, but in different positions and sides of the source foil. Side calorimeter walls (in green) cause some events to pass the SDBDRC while equivalent ones on the other side of the source foil are rejected because the magnetic field curves them back into the foil. It causes the two spots on the ends on the foil. However, these events tend to be also reconstructed less precisely than the events closer to the center of the source foil. As the magnetic

field is oriented in the positive direction of dimension z, the two spots are observed only in y-direction and not z-direction. If necessary, one can possibly eliminate this class of the events by ignoring events when at least one electron was detected in the calorimeter wall on the side.

7. **Potential for data cuts** - The analyses showed small or questionable potential for data cuts which could enhance the signal to background ratio. Case of the energy distributions of the vertex precisions showed high dependence of the precision on the energy of both electrons. This suggests, that the cut imposed on the distance of two vertices would be equivalent to cut in energy and, therefore not enhancing signal to background ratio further. However, in order to study difference in vertex precision after application of the same energy cut, one would need much larger data samples than those which were used in my studies. The energy cuts to E > 2.7 MeV or stricter, significantly diminish statistics of all double beta decay modes except for $0\nu\beta\beta$ which makes it significantly difficult to collect sufficient statistics. Potential to enhance signal to background ratio might, however, come from the asymmetry mentioned in point 6. where the events in two spots at both ends of source foil are able to discriminate between the charge of the particle. However, this speculation would need further investigation, beyond the scope of the thesis.

The studies presented in the chapter represent the first step towards the precise investigation of vertex reconstruction, which might in future yield better precision in the measurements of angular distributions. Different features of effects which impact the vertex precision were discussed and quantified. Except for that, these studies represent test of applicability of different methodologies which can be possibly used to evaluate and compare the vertex precision.

Chapter 5

Simulations of SuperNEMO Neutron Shielding

Among all the other sources of background, neutrons can also cause indirectly a fake double beta event in the detector. It is, therefore, inevitable for experiments of high sensitivity such as SuperNEMO to take them into account. According to their different character we can divide background neutrons into external and internal.

External neutrons are produced in materials outside the detector. Their typical source in LSM is a rock surrounding the lab. Analyses have shown a presence of Uranium and Thorium in the rock. These elements produce alpha particles which are capable to produce neutrons via (α, n) reactions. They also undergo spontaneous fission also capable to produce neutrons. LSM is the deepest European laboratory with overburden on the level of 4800 m.w.e. Only roughly one in a million cosmic muons reach the lab which is 1.7 km deep underground. However, these remaining high energy muons interact with the rock and can possible produce neutrons. It is necessary to develop a shielding which is able to effectively capture neutrons and lower the chance for observation of fake double beta decay event caused by neutron.

Internal neutrons, as the name suggests, are produced inside of the detector materials. Each material for SuperNEMO demonstrator is carefully chosen and tested for radiopurity in order to eliminate any source of internal background to maximal possible level. Naturally, it is not possible to eliminate internal neutrons completely and, therefore, their sources have to be well known and described. In SuperNEMO, there are two main sources of internal neutrons. First of all, it is roughly 286 kg of glass used in the PMTs. The glass contains ^{238}U which fissions spontaneously by production of roughly 2 neutrons per fission. The activity of the glass was measured to be on the level of 1 Bq/kg. The glass is expected to account for roughly 10^4 neutrons produced every year. Second main source of internal neutrons can be found in a small metallic component of feedthroughs on top and bottom of the demonstrator used for gas ventilation. These feedthroughs contain Beryllium as well as Uranium. Uranium produces neutrons via spontaneous fission, while Beryllium is capable to effectively capture alpha particles and produce neutrons via (α, n) reactions. Total mass of these tiny metallic parts in demonstrator will account for roughly 12 kg but is still expected to contribute to roughly 5×10^3 internal background neutrons every year. Even though, radiopure detector materials produce orders of magnitude less neutrons every year than the ones coming from external sources, they are almost impossible to be shielded which makes them in general potentially more dangerous.

The background neutrons can be thermalized in the shielding and/or detector materials.

Subsequently, they can be captured while gammas of few MeV are produced. For these high energy gammas, positron-electron pair production is dominating process. Due to uncertainties in track reconstruction positron might be reconstructed as an electron. Such an event represent fake (background) double beta decay event.

The tasks presented in the current chapter were performed during early works on the design of SuperNEMO demonstrator shielding. It represents first rough estimations of external neutron backgrounds which contributed to the discussion of the neutron shielding design. The goal of the chapter is to perform a first comparison between scenarios with different shielding materials. The fluxes passing through shielding are estimated based on the realistic background measured in LSM. Materials capturing the most of the neutrons in the detectors were identified.

5.1 Simulations of the Shielding

Following study is dedicated uniquely to the external neutron background. The main goal is to compare a shielding performance of three different materials (polyethylene, water and wood) of three different thicknesses (10 cm, 20 cm and 30 cm). Combination of these materials and their thicknesses represent nine "wall scenarios" ("shielding scenarios"). The simulation was performed in two phases. In the first phase, background neutrons from spectrum measured in LSM was propagated through a simple wall for each one of the nine wall scenarios. In second phase, the neutron spectrum which passed the wall was used as an input spectrum for Falaise simulation in order to identify the materials and regions of the demonstrator which captured the majority of the neutrons.

External neutrons are induced in the rock surrounding LSM by cosmic muons which have to pass 4800 m.w.e. overburden. They are also produced by Uranium and Thorium isotopes in the rock. They produce neutrons directly in spontaneous fission or alpha particles able to induce neutrons via (α, n) reactions.

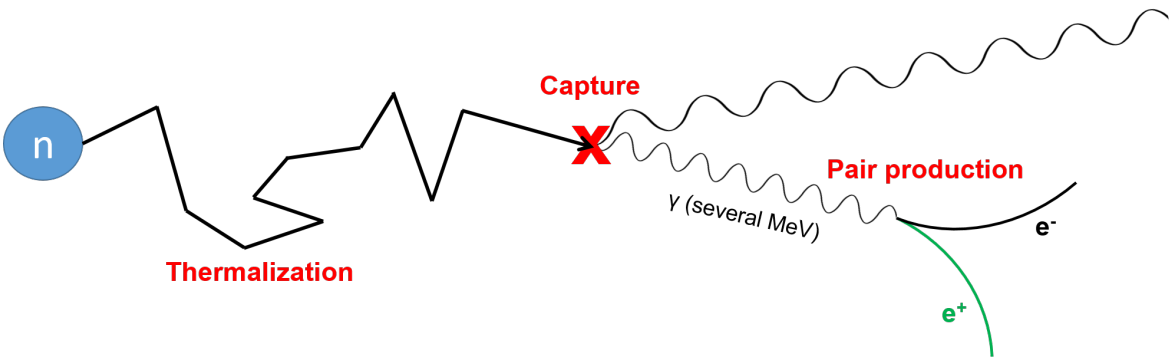

Figure 5.1: Scheme describing the process which leads to the production of fake double-beta events induced by neutrons. The process is described in more detail in the text.

Figure 5.1 depicts simplified scheme of production of fake double-beta signal in the demonstrator caused by neutron. Neutron originating in the rock surrounding the lab looses kinetic energy in a sequence of collisions. These collisions occur either in the shielding or in the demonstrator construction material. In each collision the neutron undergoes, there is a chance that the neutron would be captured by nucleus it collides with. Majority of the neutrons are slowed all the way down to thermal energy (0.3 eV) before they are captured. At

the thermal energy neutron's cross section for capture increases drastically. However, neutrons with higher energies can also be captured before thermalization is finished. Nucleus which captured neutron has changed its structure and now it has excess excitation energy which has to be released. It does so, typically, in a form of one or few gamma rays of several MeV. Each gamma with energy superior to 1.022 MeV (two electron or positron masses) is capable to produce electron-positron pair. The probability of the process is increasing with the gamma energy. The magnetic field present in the demonstrator ensures opposite clockwiseness of trajectories belonging to the particles with opposite charge. However, if trajectories are straight enough, positron trajectory can be misreconstructed as an electron. The sequence of events composed of a neutron thermalization, followed by neutron capture, pair production and misreconstruction of positron as electron might seem very unlikely. Nevertheless, neutrons are particles without charge which are very difficult to stop. There are millions of neutrons emitted from rock every year into the lab and each can potentially produce fake signal. It is important to estimate not only their numbers but also how often they are captured in the detector.

5.1.1 Phase One: Neutrons Passing Through Shielding

As a first step towards the estimation of effects of external neutron background, it is important to know the neutron energy spectrum produced by rock in LSM. In my simulations I used spectrum estimated by [104]. The resulting spectrum is depicted in Figure 5.2.

Note that, the spectrum provided by the article was estimated for all neutrons with energy higher than 1 MeV. Therefore, the spectrum in the lowest, roughly 1 MeV section (before first red data point), was obtained by simple linear extrapolation. Total integral flux of neutrons

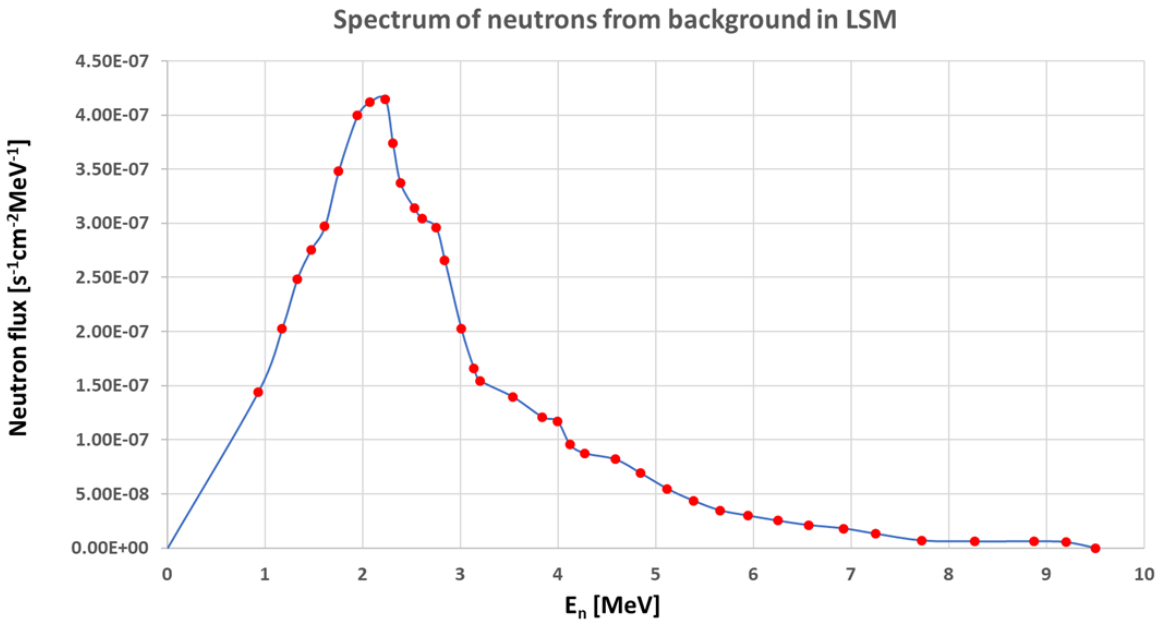

Figure 5.2: Spectrum of external neutrons $B_{LSM}(E_n)$ as measured in [104]. Red dots represent data points obtained from the article. Blue lines represent simple linear interpolations of the function in order to obtain continuous spectrum. Note that, the region for the lowest energy region $\langle 0$ MeV, 1 MeV) is not covered in the article and was extrapolated towards $B_{LSM}(0) = 0$.

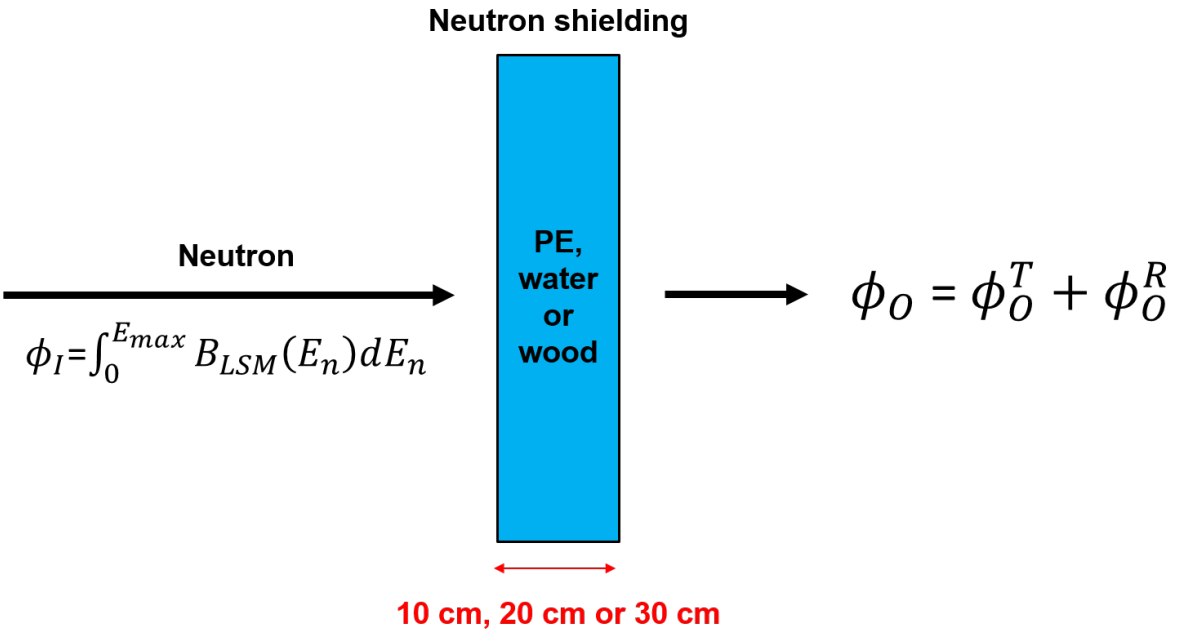

Figure 5.3: Schematic representation of first phase simulation geometry. Neutron was shot perpendicularly (in vacuum) towards a wall composed of one of three materials named in the figure. Each simulated neutron sample represented proportion of total flux Φ_I with given weight. Its calculation is explained in text. Thickness of the wall was set either to 10 cm, 20 cm or 30 cm in dependence on the wall scenario. Total outgoing flux Φ_O was accumulated as a total sum of all neutron sample weights which passed the wall. Those samples which passed to the other side with remaining energy of E < 0.3 eV were scored also to thermal flux Φ_O^T, the rest was scored into flux Φ_O^R. The size of wall in both directions perpendicular to impacting neutron was 1 m which was sufficient to prevent neutrons leaking to the side.

measured in LSM is 10^{-6} $s^{-1}cm^{-2}$, therefore, the spectrum in Figure 5.2 is normalized to this value.

Interest of the first phase of the neutron simulation is in the test of different shielding materials. Three materials were chosen: polyethylene, water and wood. Simulation was performed using Geant software package, version 4.10.02.b01. Geometry of the simulation is depicted and briefly explained in Figure 5.3.

Inside of the wall, neutrons were slowed down or, possibly, stopped. Only neutrons which passed through were scored in a spectrum. This spectrum represents spectrum of neutrons which could be seen behind shielding made of chosen material. Nine different simulations were performed each containing 8×10^6 samples. Water in simulation was composed of Hydrogen and Oxygen atoms in ratio 2:1. Water is standard material already defined in the Geant package as well as polyethylene. Polyethylene in Geant is composition of Carbon and Hydrogen in ratio 1:2. The only material which I had to define by hand was wood. In my simulation, wood was composed of Hydrogen, Carbon and Oxygen in following respective ratio 4:2:1.

Energy spectrum was sampled by neutrons from flat energy distribution between 0 MeV and E_{max} = 9.5 MeV. Flat distribution of samples is useful to obtain homogeneous sample coverage (and also statistical uncertainty) all over the neutron spectrum. In order to take into account the shape of the background distribution (Figure 5.2), different simulated neutron samples did not represent same proportion of flux. Proportion of neutron flux carried by

Mat.	d [cm]	$\Phi_O^T \times 10^9$ [$s^{-1}cm^{-2}$]	$\Phi_O^R \times 10^9$ [$s^{-1}cm^{-2}$]	Φ_O^T / Φ_O^R [1]	$\Phi_O \times 10^9$ [$s^{-1}cm^{-2}$]	$\Phi_I \times 10^9$ [$s^{-1}cm^{-2}$]
PE	10	114	285	0.401	399	1000.1
water	10	114	391	0.292	505	1000.1
wood	10	96	479	0.201	575	999.9
PE	20	37	48	0.778	85	1000.2
water	20	64	95	0.673	159	999.8
wood	20	91	150	0.605	241	999.7
PE	30	7	9	0.805	16	999.6
water	30	19	23	0.813	42	1000.3
wood	30	38	44	0.863	83	999.8

Table 5.1: Results of the first phase of shielding simulation. For each of the nine wall scenarios flux which passed through the shielding is displayed. Fluxes marked with index "O" represent the flux behind the wall. Index Φ_O^T represents flux of all neutrons which passed wall with remaining energy of E < 0.3 eV (thermal). In contrary, Φ_O^R represents the rest of the spectrum behind the wall, i.e. E > 0.3 eV. Φ_I displays flux impacting the wall. The value is within statistical precision equal to 10^{-6} $s^{-1}cm^{-2}$ in each wall scenario.

neutron sample was expressed by weight w. Sample with random energy E_n represented a flux given by value $B_{LSM}(E_n)$ given by function in Figure 5.2. The weight w is, however, not yet complete. The numerical value $B_{LSM}(E_n)$ of LSM neutron background spectrum represents number of neutrons per unit energy (and unit area and unit time). Therefore, it is crucial to know which fraction of energy spectrum each generated sample is representing. As it was already mentioned, in each (out of nine) wall scenarios $N_S = 8 \times 10^6$ neutron samples were simulated. They homogeneously covered energy interval $\langle 0$ MeV, 9.5 MeV$\rangle$. Therefore, each simulated sample represented a $\Delta E/N_S$ of energy interval. Here, $\Delta E = E_{max} - E_{min}$ is an energy range covered by generator's interval (i.e. $E_{min} = 0$ MeV and $E_{max} = 9.5$ MeV). Finally, the weight of each sample was given by

$$w = \frac{B_{LSM}(E_n)\Delta E}{N_S}. \tag{5.1}$$

Weight w represents a fraction of integral flux per unit area and unit time ($\Phi_I = 10^{-6}$ $s^{-1}cm^{-2}$) contributed by sample with energy E_n. Therefore, the sum of all weights over all samples should (within a negligible statistical error for large samples) give total integral flux. It is a confirmation mechanism that everything goes well in the simulation. Obtained values of total initial flux Φ_I are shown in last column of Table 5.1.

After the weight of sample was calculated, the neutron sample was propagated through the wall of given material and thickness. Let me remind at this point, once again, that while the thickness of the wall was finite, the other two dimensions were effectively infinite, meaning that the other two dimensions were large enough to prevent neutrons exiting on a side of the wall. Fraction of the neutron flux was captured inside of the wall or deflected back, however, many of the neutrons were only slowed down and propagated to the other side of the wall. These neutrons were scored, according to their remaining energy after moderation, into resulting output spectrum. Integral flux of the neutrons which passed the wall in each of the nine wall setups is shown in the Table 5.1.

Table contains values of total flux of thermal neutrons ($E_n < 0.3$ eV) Φ_O^T which passed the

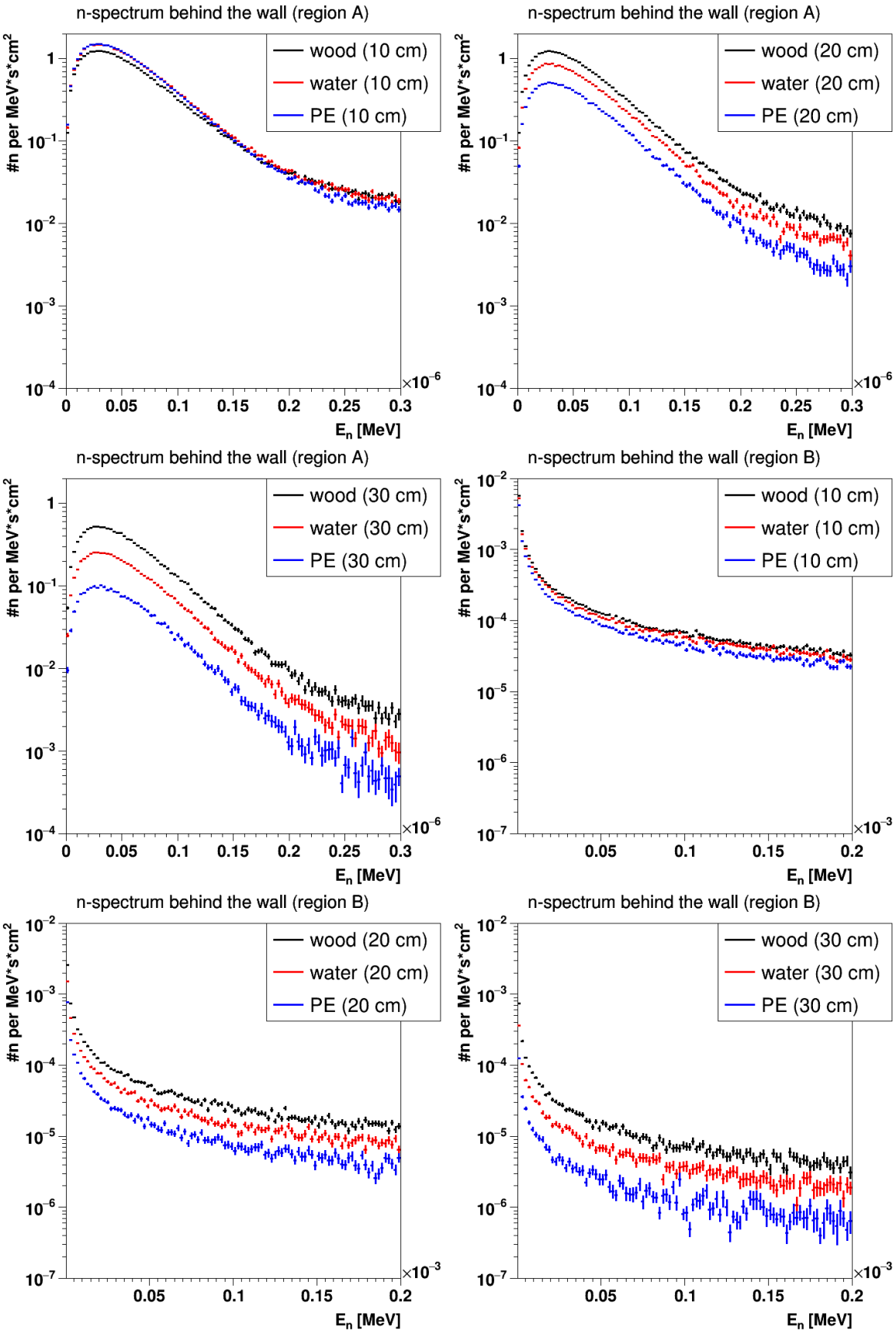

Figure 5.4: Spectrum of neutrons which passed the shielding in nine different wall scenarios. Figures represent first two energy regions: A - ⟨0 eV, 0.3 eV⟩ and B - ⟨0.3 eV, 200 eV⟩. Every single figure depicts three wall scenarios with the same thickness in order to compare performance of the materials.

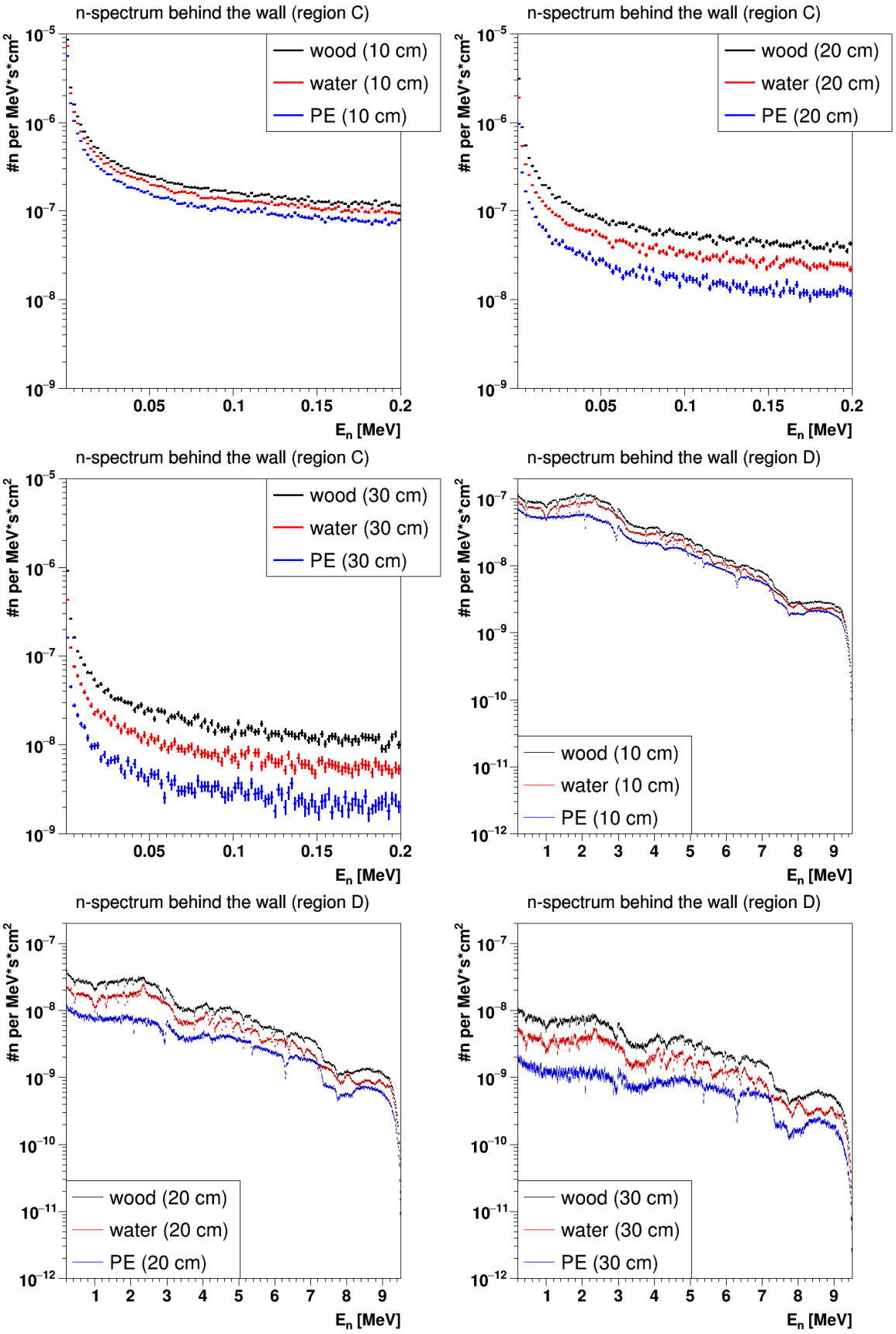

Figure 5.5: Spectrum of neutrons which passed the shielding in nine different wall scenarios. Figures represent first two energy regions: C - ⟨0.2 keV, 200 keV⟩ and D - ⟨0.2 MeV, 9.5 MeV⟩. Every single figure depicts three wall scenarios with the same thickness in order to compare performance of the materials.

wall, Φ_O^R - flux of all the rest of neutrons ($E_n > 0.3$ eV) passing the wall, total outgoing flux on the other side of the wall $\Phi_O = \Phi_O^T + \Phi_O^R$ and total incoming flux Φ_I given by spectrum of background neutrons in LSM. Incoming spectrum is obtained as a sum of weights of all the generated particle samples and can serve as estimation of precision of the simulation.

For a given thickness, polyethylene is the best shielding material. With only 10 cm thickness, polyethylene is capable to stop roughly 60% neutrons, while water and wood of the same thickness only less than 50%. In scenarios with wall of 10 cm thickness polyethylene seems to produce the largest contribution of thermal neutron flux. Polyethylene does not only stop the neutrons of any energy more effectively than water or wood, it is also very effective in thermalization of neutrons passing the wall. In scenarios with 30 cm thick wall, almost half of the remaining neutron flux is thermalized. This is similar for all the three materials. Nevertheless, polyethylene stops neutrons more than twice as effectively than water and more than four times as effectively as wood. For any given thickness, polyethylene performs the best while wood shows the worst results. It is also important to note at this point, that the results of wood shielding in my simulation are dependent on the definition of wood as a material. Definition of such an amorphous material like wood, can be, in principle, chosen in many different ways. Wet wood contains more water (more Hydrogen) than dry wood and composition of other elements might differ as well. It has to be taken into account when comparisons are discussed.

The neutron which passed the wall have access to the detector and can potentially cause fake double beta-signal. Not only fluxes but also spectra of neutrons behind the wall were saved in the simulations. They are plotted in Figures 5.4 and 5.5. The neutron spectrum, typically, covers several orders of magnitudes in energy. Therefore, I decided to split it into four different energy regions called A, B, C and D which I have plotted separately. Their limits are following: A - ⟨0 eV, 0.3 eV), B - ⟨0.3 eV, 200 eV), C - ⟨0.2 keV, 200 keV), D - ⟨0.2 MeV, 9.5 MeV). Weight of each generated neutron sample was scored into one of these four regions in dependence on the remaining neutron's kinetic energy after passing the wall. Sample of weight w represents a fraction of integral flux (in $s^{-1}cm^{-2}$) not normalized to energy. Energy regions A, B, C and D cover different proportions of full spectrum and, therefore they contain, in principle, different number of samples. In order to be capable to compare fluxes between the regions it was necessary to normalize flux again back to the unit of energy. The width of bin b_w was different in each region. The energy normalization is performed simply by dividing the weight of neutron sample by bin width into which it was scored, i.e. (w/b_w). Outcoming energy spectra behind wall for all wall scenarios in regions A, B, C and D, respectively, are shown in Figures 5.4 and 5.5.

5.1.2 Phase Two: Mapping of Demonstrator

Phase one of the neutron simulation provided very useful information about spectra of remaining neutrons behind the shielding (Figures 5.4 and 5.5). These neutrons have access to detector and have possibility to produce fake double-beta events. They were used as an input spectra in the second phase of the simulation. The question of interest in this phase is to determine number of neutrons per year which are captured in demonstrator. It is important to evaluate the number of neutrons captured every year in the different demonstrator construction materials and compare their contribution.

The simulation was performed by Falaise version 2.0.0. As it was mentioned in the introduction to the chapter, this work was performed when the early discussions of the shielding design for demonstrator took place. Therefore, shielding was not yet included in the soft-

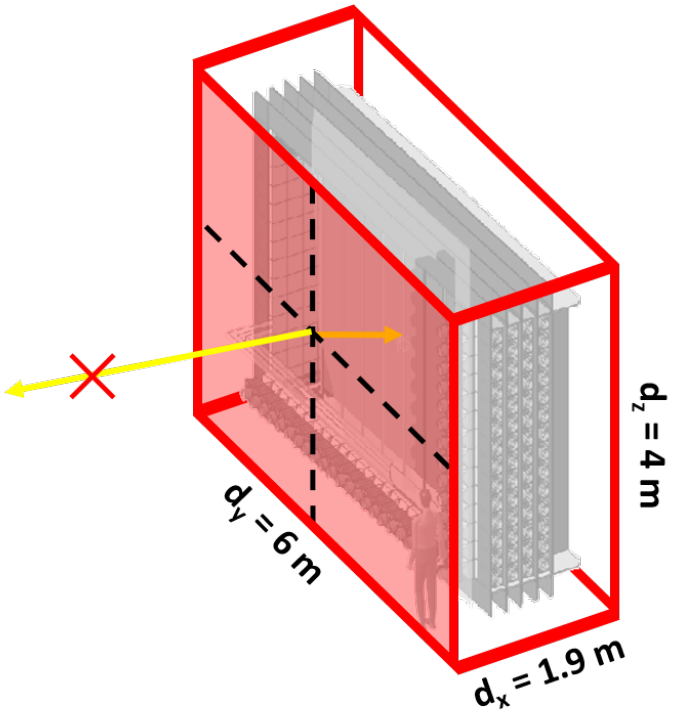

Figure 5.6: Schematic representation of simulation's setup in phase two. Figure shows wire model of box surrounding the demonstrator. From each of six surfaces neutrons were shot homogeneously to 4π solid angle. Yellow arrows represent example of two neutrons originating in same point in the box. Neutron which was heading inside was followed in the simulation while neutron exiting out of the box was immediately rejected (symbolized by red cross). The box was for the purposes of display negligibly expanded. Real box was touching the demonstrator from each side.

ware. It is a reason why the passage of neutrons through wall was simulated separately in phase one using Geant package. Neutron spectrum which passed the wall in one of nine wall scenarios was a starting point for phase two. Similarly to first phase, neutrons were generated in a flat spectrum to ensure homogeneous exposure of the spectrum. Neutrons were generated in box tightly surrounding the demonstrator. The box's center matched the center of demonstrator. The size of the box was $187\times600\times406\text{cm}^3$. Neutrons were shot from random positions distributed on the surface of the box into 4π angle directions. Those with initial momentum heading out of the box were not taken into account.

Figure 5.6 represents simple scheme of setup in simulation in phase two. Rejection of neutrons emitted outside caused loss of 50% of the simulated samples, however, the version of Falaise in use lacked possibility to generate particles into predefined solid angles.

In phase one simulation, I concluded that spectra of neutrons passing the shielding span over many orders of magnitude in energy. Thermal neutrons have a much larger probability to be captured due to their cross sections. They represent, however, crucial but extremely narrow stripe of the spectrum. This give rise to a difficulty to properly sample all the energies. In the second phase, I sampled energy range of 0 MeV to 8 MeV. Version of Falaise in use (2.0.0) allowed to generate only flat energy spectrum for generated particles. Such an generator generates samples homogeneously. Therefore, if we generate N samples homogeneously in energy interval (0 MeV, 8 MeV), only a fraction of them would fall into interval (0 eV, 0.3 eV) which is seven orders of magnitude smaller. The chance, that sample would

be generated as thermal neutron is equal to proportion between the widths of two intervals which is equal to 0.3 eV / 8×10^6 eV = 3.75 $\times10^{-8}$. Probability to generate thermal neutron in flat distribution is then only 3.75 $\times10^{-6}$ %. In order to generate one single thermal neutron one would need to generate in average more than 26 million samples. It was necessary to modify approach to properly sample the thermal neutrons which are probably the most crucial contribution of neutron captures. I decided to divide phase two into two smaller similar simulations. In first one, simulation S^T, only thermal neutrons from energy region of A (defined previously) were simulated. In second one, simulation S^R, the rest of the spectrum was simulated, i.e. energy regions B, C and D together. Neutrons in both of them, as pre-announced, were simulated as a flat spectrum. In S^T neutrons were simulated from energy range of ⟨0.001 eV, 0.3 eV), in S^R from energy range of ⟨0.3 eV, 8 MeV).

Weight of each data sample was calculated exactly the same way as I have shown in phase one simulation. In this case, however, the flux was entering through the surface of roughly S = 90 m^2 of the box around the demonstrator and the simulation represented the background collected during period t = 3.15×10^7 s (one year). The weight from Equation 5.1, expressed flux in $s^{-1}cm^{-2}$ had to be multiplied by period t and surface S to give number of neutrons passing through box surface S captured in demonstrator during one year. Therefore, the weight in phase two was calculated as

$$w = \frac{B^i_{WALL}(E_n)\Delta E S t}{N_S}. \tag{5.2}$$

$B^i_{WALL}(E_n)$ represents spectrum passed through the wall in wall scenario of interest (Figures 5.4 and 5.5). ΔE is a width of the energy range from which neutrons were randomly generated. In the simulation (S^T), simulated range covered interval ⟨0.001 eV, 0.3 eV), therefore, its ΔE = 0.299 eV. Furthermore, simulation S^R covered neutron from range of ⟨0.3 eV, 8 MeV), which gives ΔE = 7.9999997 MeV. N_S represents number of samples in the simulation. This number was also different for both S^T and S^R. In simulation S^T, sample number of N_S = 1.9997×10^7 was left after outward going neutrons were eliminated. The real simulated number of generated events was exactly 4×10^7. In case of simulation S^R, 3.2×10^7 samples were generated out of which N_S = 1.59979×10^7 were heading inside of the box. The final weight assigned to the neutron sample represents a number of neutrons per year. It is important to remind, that the same neutron sample was used for each of nine scenarios, the difference between the results comes only from the difference in the shape of the spectra given by $B^i_{WALL}(E_n)$ represented by plots in Figures 5.4 and 5.5.

In both simulations, I was interested in the locations of neutron captures inside of the demonstrator. If generated neutron sample was captured, name of the material, in which capture happened, was saved. Weights of neutrons were scored into separate data containers, each representing one of the materials. Finally, the sum inside of each container represent number of captures expected in the material during one year of operation of detector.

Tables 5.2 and 5.3 represent simulated neutron captures inside of four materials with the most neutron captures. Both tables are expressed in thousands of neutron counts per year. Table 5.2 represents all the captures of neutrons initiated by neutrons from thermal part of the spectrum (E < 0.3 eV, region A) in simulation S^T. On the other side, Table 5.3 represents all the captures of neutrons initiated by neutrons from rest of the spectrum (E > 0.3 eV, regions B, C and D) from simulation S^R.

The results clearly show that the vast majority of neutrons from both parts of spectrum are captured in Iron. Iron captures roughly 93% of all neutrons from thermal part of the spectrum and roughly 88% of all neutrons from the rest of the spectrum. Iron is a very widely used

$E_n \leq 0.3$ eV (S^T)		Wall scenario								
		30 cm			20 cm			10 cm		
		PE	water	wood	PE	water	wood	PE	water	wood
All		168	437	896	874	1494	2121	2666	2667	2250
Detector material	Iron	157	409	837	817	1396	1982	2492	2493	2103
	Plexiglass	4.8	12	25	25	42	60	76	76	64
	SN-metal	4.5	12	24	23	40	57	71	71	60
	Copper	0.8	2.2	4.5	4.4	7.5	11	13	13	11

Table 5.2: Table displays number of expected captured neutrons inside of the demonstrator per year caused by thermal neutrons behind the wall (flux Φ_O^T, energy region A). Columns represent nine different shielding wall scenarios. First row displays number of all captures in detector followed by four lines representing detector materials with most captures. Values are represented in thousands of neutrons per year.

$E_n > 0.3$ eV (S^R)		Wall scenario								
		30 cm			20 cm			10 cm		
		PE	water	wood	PE	water	wood	PE	water	wood
All		103	274	539	579	1150	1843	3450	4658	5626
Detector material	Iron	91	242	478	513	1019	1635	3063	4132	4992
	Plexiglass	3.8	10	19	20	40	62	118	165	205
	SN-metal	5.3	14	28	30	60	97	176	234	275
	Copper	1.8	4.6	9.1	10	20	32	60	81	97

Table 5.3: Table displays number of expected captured neutrons inside of the demonstrator per year caused by neutrons with energy superior to 0.3 eV after they passed the wall (flux Φ_O^R, energy regions B, C and D). Columns represent nine different shielding wall scenarios. First row displays number of all captures in detector followed by four lines representing detector materials with most captures. Values are represented in thousands of neutrons per year.

material in the demonstrator. It is used in all supporting constructions which hold the module together. Plexiglass is used in calorimeter - for instance, in side calorimeter (xcalo) it serves as a light guide and it has a form of cubic blocks. Furthermore, material denoted as SN-metal is composed of Nickel (77 %), Iron (16 %), Cobalt (0.05 %) and Molybdenum (0.02 %). The material is used for shielding of PMTs against magnetic field (to ensure their proper performance). Copper is used in all parts where good electrical conductivity is needed, for example in Geiger cell endcaps shown in Figure 5.13.

After a sample was captured, coordinates x,y and z of position of the capture was also saved. Such an information is useful to build a 3D map of all neutron captures in demonstrator. The demonstrator volume (and part of its vicinity) was divided into cubic bins of $4\times4\times4$ cm^3. When neutron was captured, its weight was scored into the bin in which neutron capture occurred. With addition of information about the material where capture occurred, I was able to produce such 3D maps for each material separately.

Maps in Figure 5.7 show 2D projections of 3D distribution of all captures in the demonstrator. Projections are always projected into xy plane (top view), xz plane (xcalo side view) and yz plane (main calorimeter view from side). The projections represent sum of all neutron captures in direction perpendicular to the plane of projection. This give rise to apparent

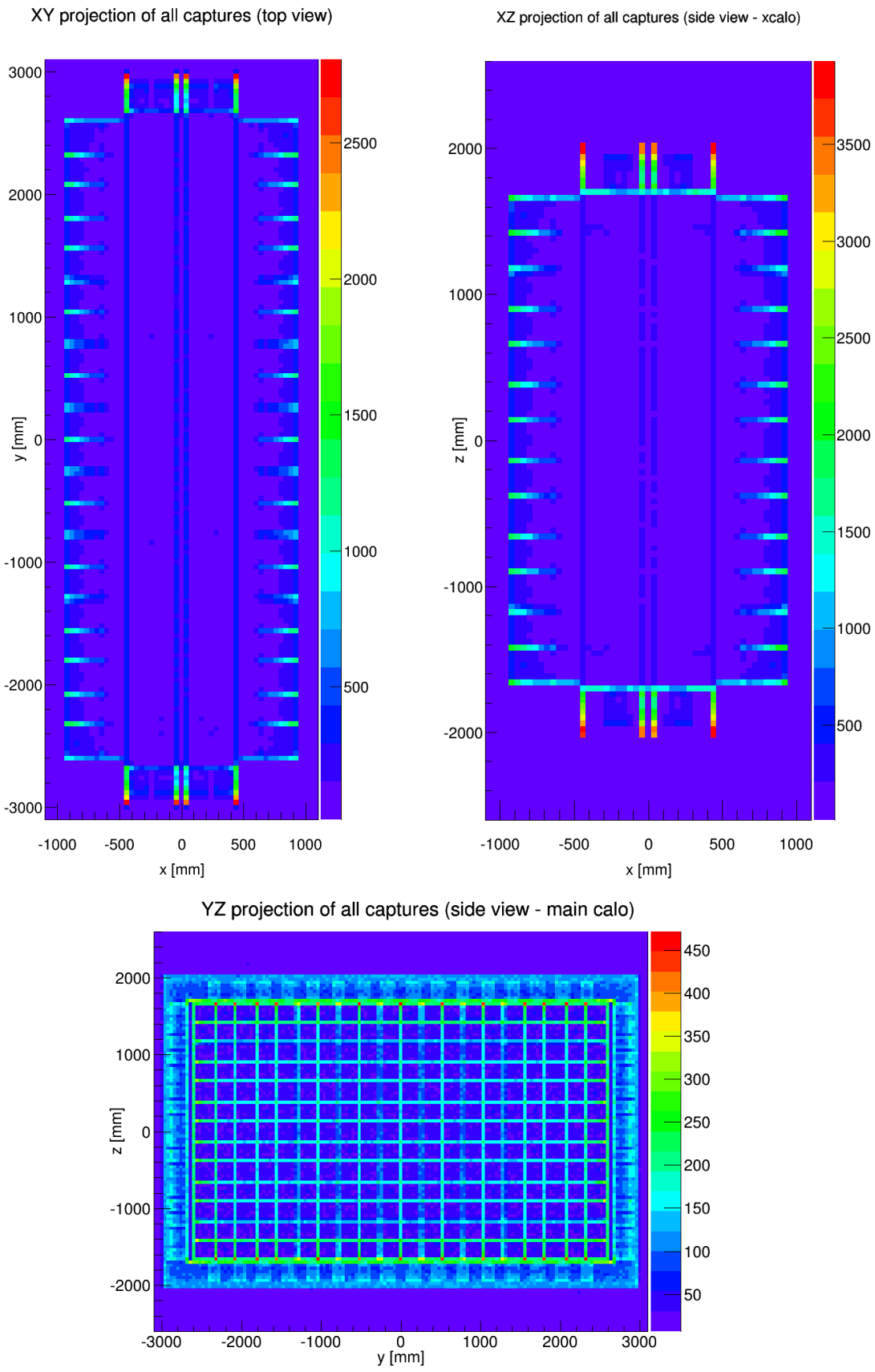

Figure 5.7: Projections of 3D maps of neutron captures in the demonstrator. All captures (regardless of material) caused by thermal neutron flux behind shielding Φ_O^T are included. Numerical value represents number of captures per year in 16 cm^2 (surface of bin). Results represent wall scenario with PE shielding of 10 cm thickness.

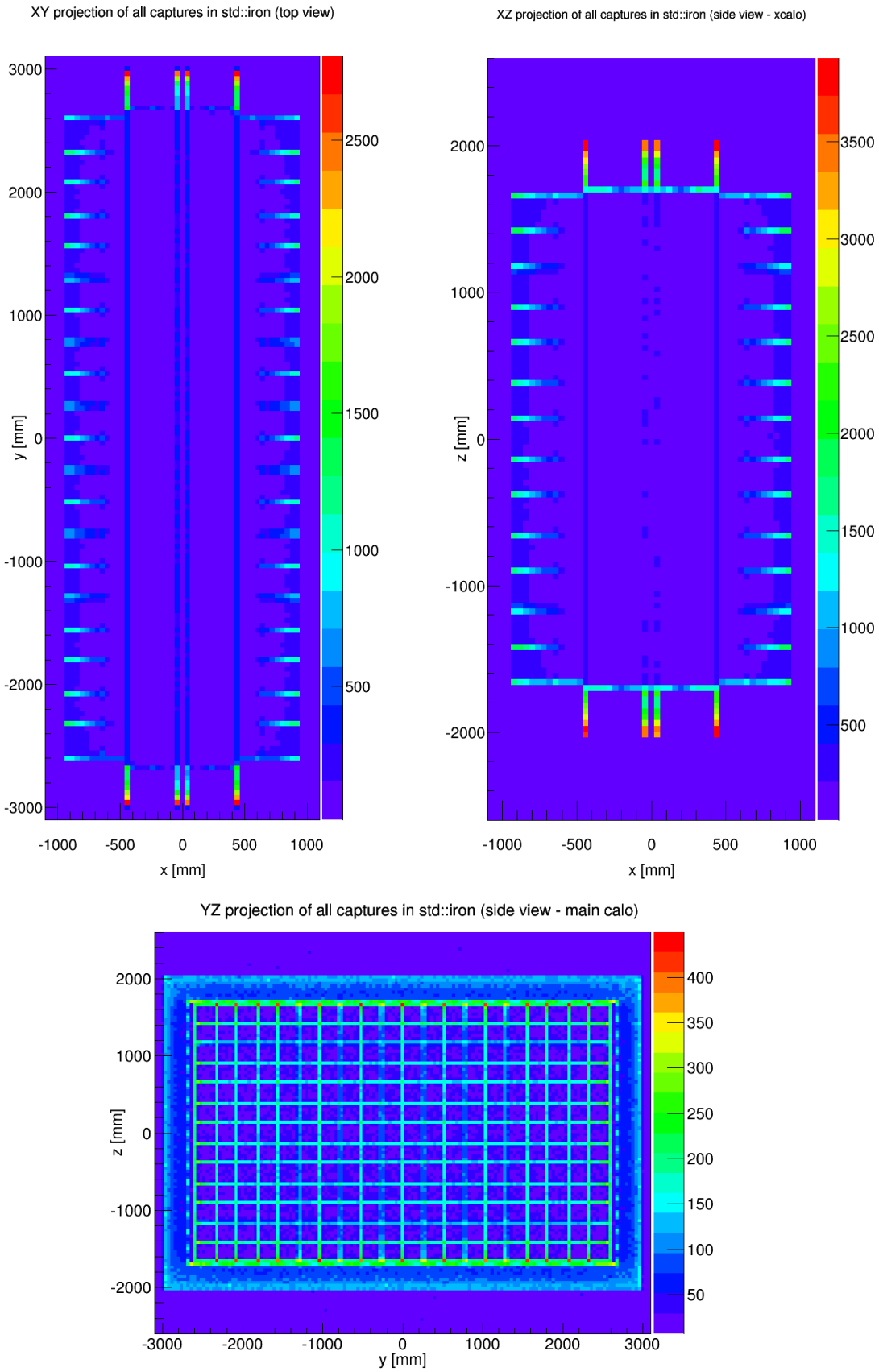

Figure 5.8: Projections of 3D maps of neutron captures in the demonstrator. Only captures in Iron caused by thermal neutron flux behind shielding Φ_O^T are included. Numerical value represents number of captures per year in 16 cm^2 (surface of bin). Results represent wall scenario with PE shielding of 10 cm thickness.

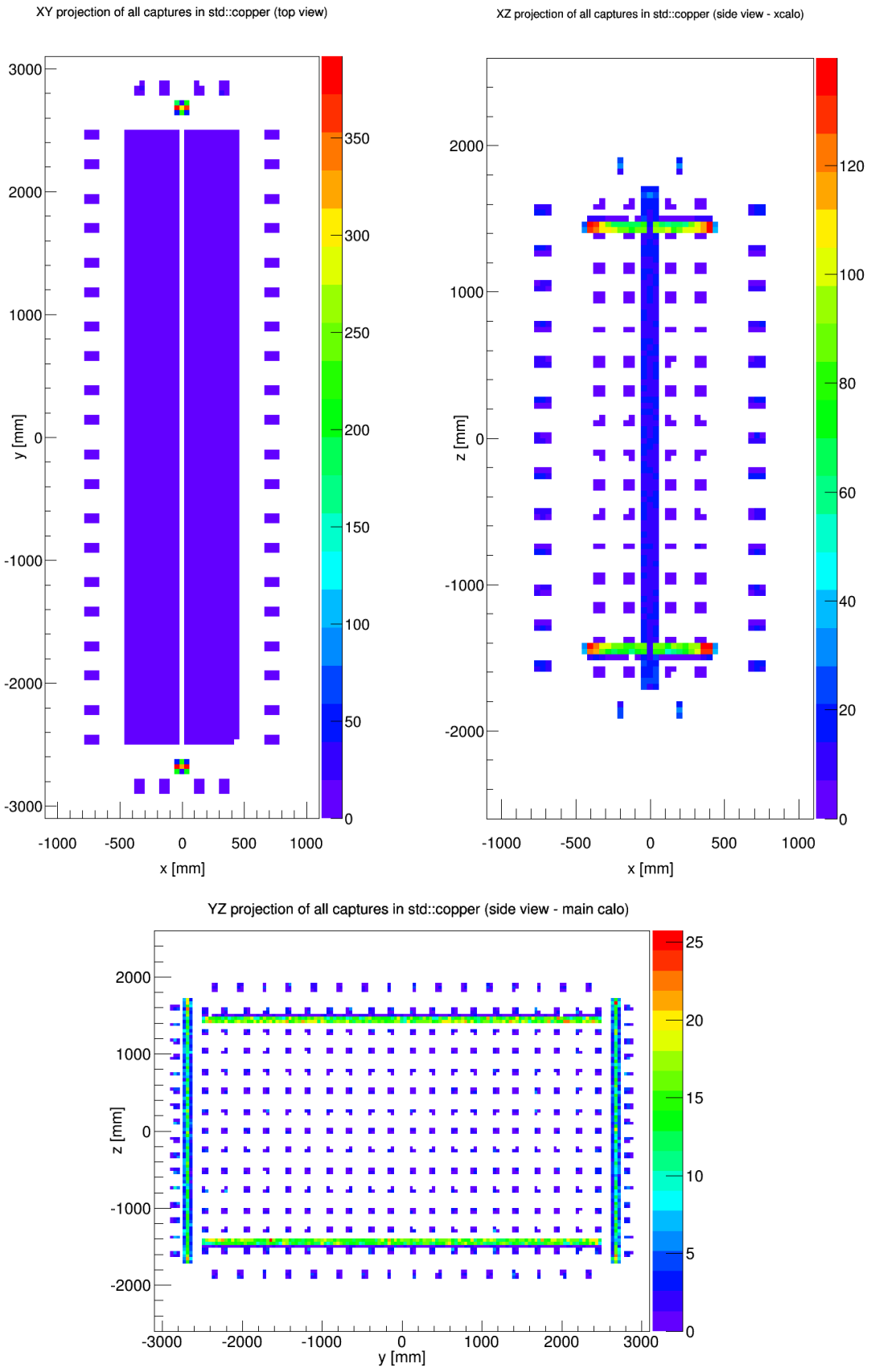

Figure 5.9: Projections of 3D maps of neutron captures in the demonstrator. Only captures in Copper caused by thermal neutron flux behind shielding Φ_O^T are included. Numerical value represents number of captures per year in 16 cm^2 (surface of bin). Results represent wall scenario with PE shielding of 10 cm thickness.

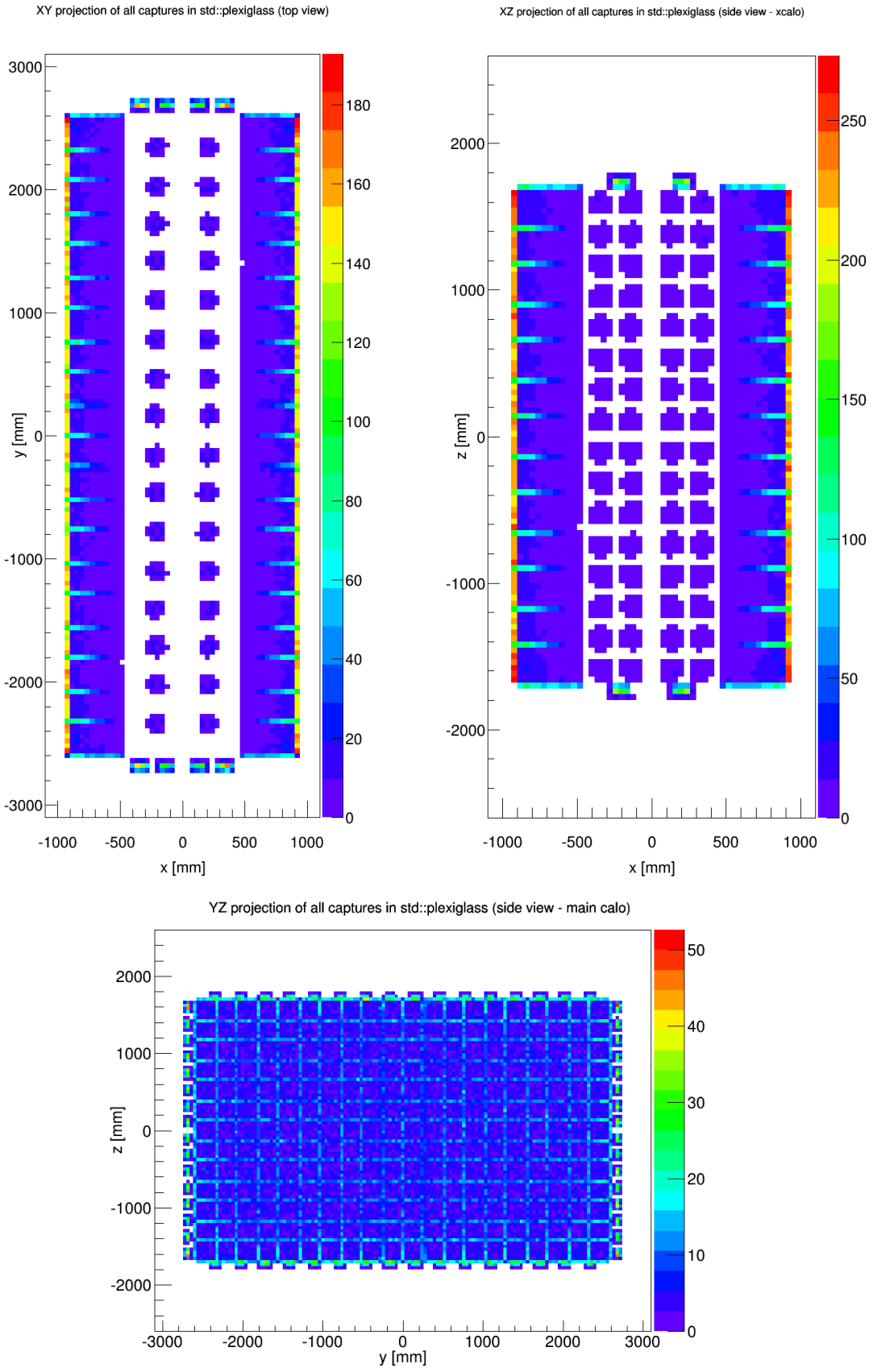

Figure 5.10: Projections of 3D maps of neutron captures in the demonstrator. Only captures in Plexiglass caused by thermal neutron flux behind shielding Φ_O^T are included. Numerical value represents number of captures per year in 16 cm^2 (surface of bin). Results represent wall scenario with PE shielding of 10 cm thickness.

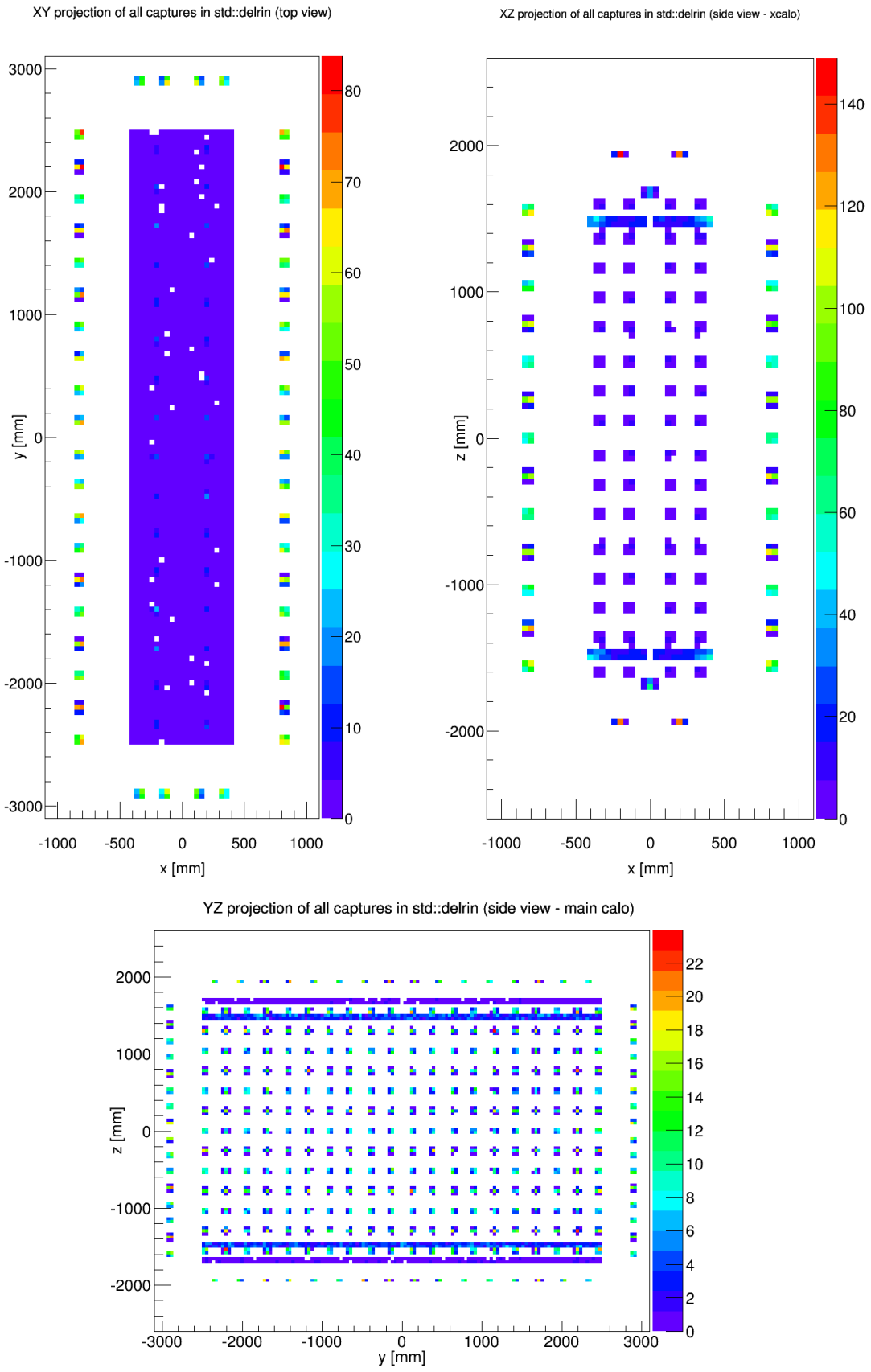

Figure 5.11: Projections of 3D maps of neutron captures in the demonstrator. Only captures in Delrin caused by thermal neutron flux behind shielding Φ_O^T are included. Numerical value represents number of captures per year in 16 cm^2 (surface of bin). Results represent wall scenario with PE shielding of 10 cm thickness.

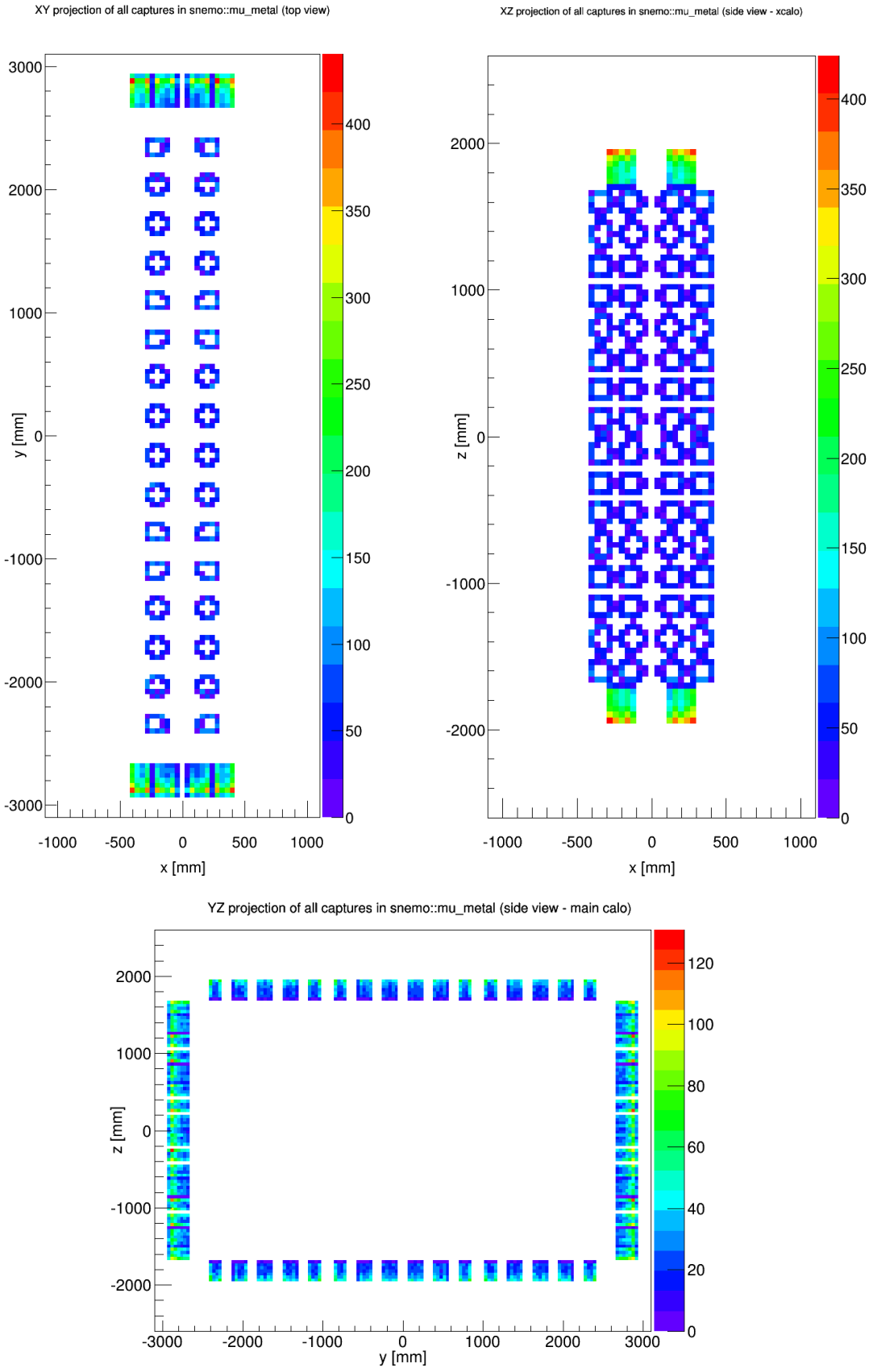

Figure 5.12: Projections of 3D maps of neutron captures in the demonstrator. Only captures in SN-metal caused by thermal neutron flux behind shielding Φ_O^T are included. Numerical value represents number of captures per year in 16 cm^2 (surface of bin). Results represent wall scenario with PE shielding of 10 cm thickness.

red hot spots in some projections. These hot spots are caused by the integration of bins over the third dimension. The frequency of the captures have to be considered by comparison of all three projections in order to avoid wrong conclusions. Each 2D bin is represented in number of neutrons captured during one year per 16 cm^2. Figures 5.8, 5.9, 5.10, 5.11 and 5.12 represent same type of projections, this time for captures in Iron, Copper, Plexiglass, Delrin and SN-metal, respectively. In case of Iron it is possible to recognize the supporting structures of the detector. Delrin is a material not included in the Tables 5.2 and 5.3. Delrin is used as radiopure insulator which can be found for example in the endcap of each Geiger cell. Its photo can be found in Figure 5.13. SN-metal structures, as already discussed, serve as a magnetic field shielding in order to protect PMTs (for xcalo and gveto). They can be clearly recognized in Figure 5.12. Figures 5.7 to 5.12 provide great demonstration of the distribution of materials in the detector.

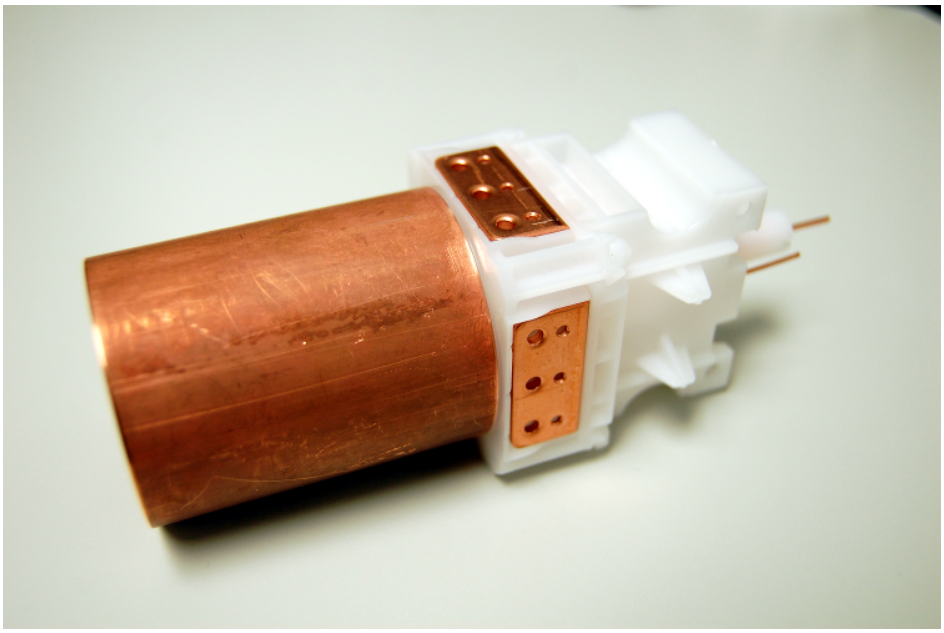

Figure 5.13: Photo of Geiger cell endcap. White part, made of Delrin, serves as an insulator.

Neutron simulations represent first estimation of neutron fluxes which could be expected with use of different types of shielding. The information was used to form first design proposals for the neutron shielding. Simulation in second phase was performed without physical presence of the shielding in the simulation's setup. This approximation, however, cannot reproduce effects of neutrons which are scattered back into the wall after they have already passed it. They can be subsequently thermalized and re-emitted back into the volume of demonstrator. The phase two of the simulation accounts only for neutrons directly traversing shielding and interacting in the module or leaving. Full realistic simulations will be performed after the shielding will be implemented into the Falaise. For the moment the result proposed in this section are sufficient approximation demonstrating the behaviour of neutrons in the detector and giving a reference point for future work.

5.2 Problem of Neutron Capture Generators

Neutron simulations performed in previous sections studied the effects of neutron propagation and capture in the detector. It gives an information about the potential of the captures

to generate fake double-beta signal. In order to obtain real estimation of background from neutrons one would need to follow the gammas produced in the capture. Even though, the process of gamma deexcitation is fully implemented in Geant package, the performance of used model is not sufficient. In following section, I will briefly explain the pitfalls of generators of gammas originating from thermal neutron capture.

Neutron interactions are probably the most difficult processes to be reliably simulated. Used interaction models are frequently only phenomenological. Data describing the nuclear levels and the transitions are frequently not precise enough to give results of the highest precision. All these factors contribute to complexity of computational tasks involving neutrons.

It is, therefore, important to be familiar with the performance of the simulation code in conditions of the problem in question. For majority of the applications (especially problems including high energy neutrons) available codes for simulation work precisely enough to give reliable final results. However, the central, and most important process of this chapter is the neutron capture of thermal neutrons. Due to their large cross sections for neutron capture, thermal neutrons are potentially the biggest contributor to the detector's background out of all the neutron spectrum.

5.2.1 Thermal Neutrons in Geant4

Simulation of all the physics in Falaise (simulation code for SuperNEMO demonstrator) is delegated to Geant4 [100, 101, 102]. Therefore, in order to test the performance of neutron simulation, I decided to test it directly in Geant4.

I set up very simple simulation. Thermal neutrons (i.e. E_n = 0.3 eV) were produced in the center of $1\times1\times1$ m^3 cube made of ^{54}Fe. Their initial momentum was isotropic. The neutrons were scattered in the cube until they were captured. The dimensions of cube were large enough to ensure that all the neutrons are captured inside of it. I generated 5×10^5 neutrons. Example of ten events from the simulation are shown in Figure 5.14. After each

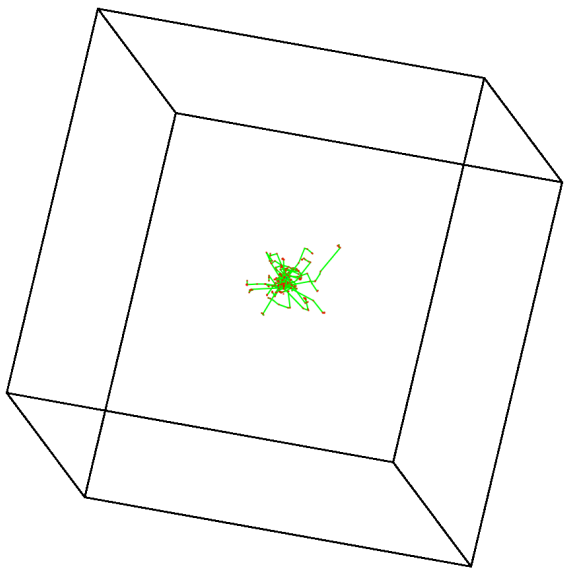

Figure 5.14: Example of 10 thermal neutron events. Neutrons (green tracks) at thermal energy (E = 0.3 eV) were shot from the center of the cube ($1\times1\times1$ m^3) into full (4π) solid angle. Cube was sufficiently large to capture all the generated neutrons.

E_γ [MeV]	I_{G4} $[\frac{\gamma}{100ev.}]$	I_{NDS} $[\frac{\gamma}{100ev.}]$	I_{G4}/I_{NDS} [1]
0.412	15.23	19	**0.80**
0.931	1.73	2.1	**0.83**
1.24	0.79	1	**0.79**
1.638	1.38	1.7	**0.81**
1.918	1.69	2.1	**0.81**
2.052	1.60	2	**0.80**
2.47	3.15	3.9	**0.81**
2.618	1.89	2.4	**0.79**
2.67	1.22	1.5	**0.81**
2.873	0.89	1.1	**0.81**
3.005	0.81	1	**0.81**
3.028	2.12	2.6	**0.82**
3.38	1.21	1.5	**0.81**
3.508	0.81	1	**0.81**
3.552	1.15	1.4	**0.82**
3.792	1.47	1.8	**0.82**
4.455	1.27	1.6	**0.79**
4.495	2.70	3.4	**0.79**
4.589	2.12	2.6	**0.82**
4.707	0.98	1.8	**0.54**
4.802	2.30	2.9	**0.79**
5.391	0.97	1.2	**0.81**
5.507	1.89	2.4	**0.79**
5.745	1.86	2.3	**0.81**
6.268	2.59	3.2	**0.81**
6.826	1.50	1.9	**0.79**
7.246	1.61	2	**0.81**
8.886	9.95	12.3	**0.81**
9.297	111.61	66	**1.69**

Table 5.4: Results from thermal neutron simulation represented in Figure 5.14. Each line represents one of the gamma lines emitted after thermal neutron capture on ^{54}Fe. Table compares intensities of the line obtained from Geant4 simulation (I_{G4}) to intensities in Nuclear Data Sheets (I_{NDS}) obtained from [105]. Intensities are represented in number of observed gammas per 100 events.

neutron was captured, it produced one or several gammas. I scored each gamma energy into single gamma spectrum. Energies of all gammas produced in one capture were summed up, and the result was scored in another spectrum.

Table 5.4 shows a summary of the obtained intensities for all gammas of intensity superior or equal to one gamma per 100 events. The results are compared to the expected intensities based on nuclear data. In last column, ratio of intensity obtained by simulation and expected intensity is shown. The comparison shows that gamma of highest energy is overestimated by almost 70% while all the other gammas are underestimated by roughly 20%. Moreover, energy of the highest gamma line (E_γ = 9.297 MeV) represents situation when nucleus is deexcited by one gamma all the way to the ground state. The intensity of this gamma obtained from simulation is I_{G4} = 111.61 gammas per 100 events. The value of intensity implies, that this gamma occurs in average more than once per event. Therefore, simulation produces events when this gamma is emitted at least twice. The energy released by this highest gamma line is equal to the difference between highest possible state and ground state. It represents the Q-value of the neutron capture. Emission of two 9.297 MeV gammas, therefore represent non-conservation of the energy in the event.

Problem of non-conservation of energy is clearly visible in Figure 5.15. Figure shows spectrum of energies released per one event.

The region of the energy spectrum marked by blue rectangle represents all the events in which more energy was emitted than it should have been. It is possible to find examples when energy twice as higher than Q-value was released. Naturally, this is unwanted feature. The study was repeated for ^{56}Fe, ^{63}Cu and ^{65}Cu and compared with [106], [107] and [108]. The results showed violation of energy conservation in all of these cases.

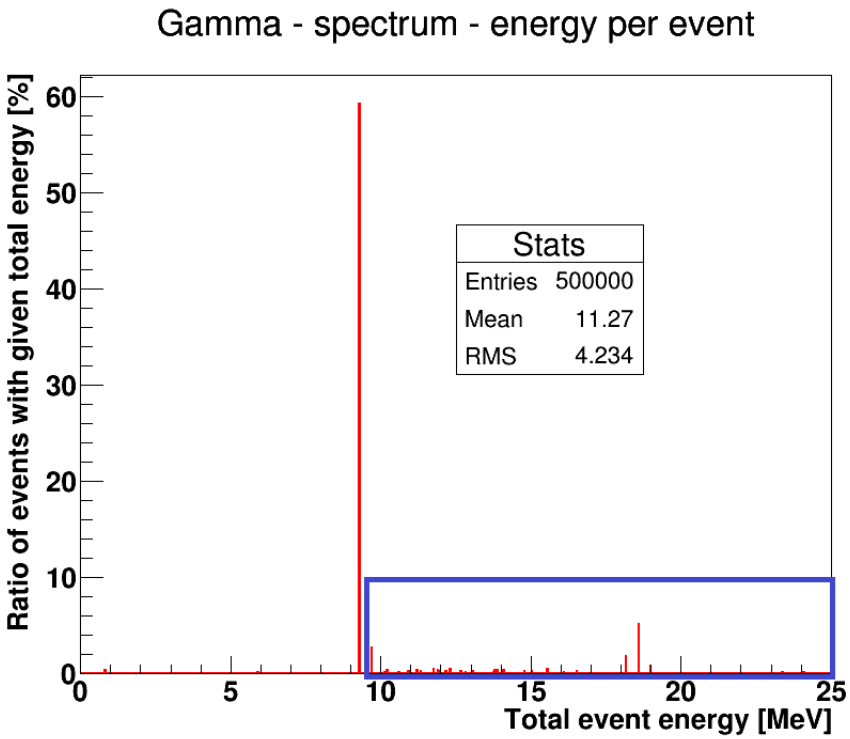

Figure 5.15: Spectrum of energies per event obtained from thermal neutron simulation represented in Figure 5.14. Region of spectrum marked by blue rectangle represents all the events in which energy emitted by gammas is higher than Q-value of neutron capture. These events violate conservation of energy.

5.2.2 Stair Generator

The non-conservation of the energy in the thermal neutron capture is caused by neglecting the correlations between the gammas. The excess excitation energy can be released by one gamma or several gammas in a cascade.

Figure 5.16 - Left shows the simplest non-trivial deexcitation scheme with one intermediate level. Energy difference between the highest energy state E_H and ground state E_0 can be released in two possible ways. Either via one gamma (γ_{00}) or two gammas in coincidence (γ_{10} + γ_{11}). Regardless of the fact, whether the excitation energy $E_H - E_0$ was released by one or several gammas, the energy released by deecitation must be always the same. The generator in Geant4, however, did not fulfil this condition. If we look at the right side of the Figure 5.16, we can see an illustration of the scheme from left for a randomly chosen cascade probabilities x_{101} and x_{111} in a form of single gamma energy spectrum. γ_{10} and γ_{11} originate in the same cascade, therefore, their intensities will always be equal. The proportions of intensities γ_{10}/γ_{00} and γ_{11}/γ_{00} depend only on the proportion of cascade probabilities x_{101}/x_{111}.

Let us assume now, that both cascades x_{101} and x_{111} happen exactly 50% of the time. It means that the intensity of each of two gammas γ_{10} and γ_{11} are the same as the intensity of γ_{00}. Moreover, we know that average number of gammas per capture would be 1.5 because 50% of time nucleus is deexcited by one gamma and rest of the time by two gammas.

Now, let me propose a simple neutron capture generator. First of all, the generator chooses randomly (based on the gamma per event distributions) a number of emitted gammas. In our example we have 50% chance to generate two gammas. Say, the generator

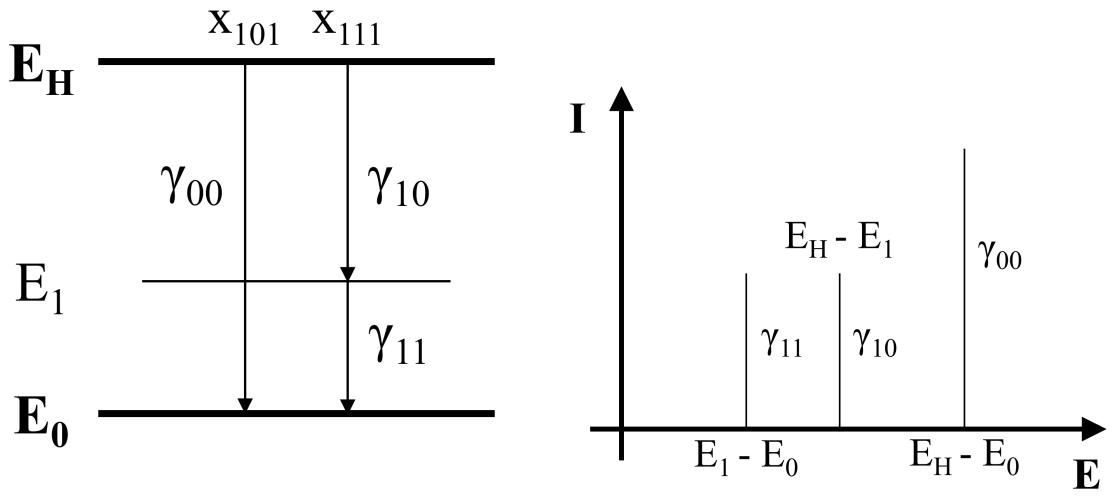

Figure 5.16: Left: Example of simple system with three nuclear states. E_0 denotes energy of ground state, E_1 energy of first excited state and by E_H we understand the energy of the highest excited state. E_H is always a state of nucleus immediately after the thermal neutron is captured. Right: Representation of decay scheme from left as it would be seen in the energy spectrum (for specific choice of cascade probabilities x_{101} and x_{111}). Naming convention of cascades and gammas is explained in the text.

have chosen two gammas in first event. In next step, the generator has to choose (randomly) the gammas which are emitted. If we pick them only based on the intensities in the energy spectrum in the right side of Figure 5.16, we could pick, for example, emission of γ_{00} along with γ_{11}. Both gammas emit together energy larger than difference $E_H - E_0$, therefore, energy is not conserved. However, in our example, the mean number of emitted gammas, as well as single gamma energy spectrum, is preserved. Such an approximation causes energy non-conservation in Geant4 generator. Moreover, it is possible to obtain γ_{00} repetitively in the same event, which causes events with emission of several Q-values of energy. While such an statistical, average approach is acceptable as a good approximation for some high energy applications, it is not suitable for the study of neutron background in SuperNEMO demonstrator. Energy of gamma emitted after neutron capture influences cross section of the pair production, in other words, how likely is it to obtain potential fake double-beta event. If several gammas are emitted in a cascade, there is a chance that both would produce pair and violate proper signature of fake double-beta decay event. Creation of several gammas in a cascade increase chance of rejection of fake-double beta signal. Therefore, it is important to have generator with proper simulation of both, the gamma multiplicities in cascade (gamma correlations) as well as energy conservation. This is however, very difficult task to fulfil.

In order to preserve energy, the gammas have to be generated in correlation, i.e. as a whole cascade. Such an approach could be achieved by generator which I call "Stair Generator". The principle is simple. The generator takes a database of single gammas and their intensities (data obtained from measurement) as an input. Each gamma has a designated level of origin. In example from Figure 5.16 γ_{00} and γ_{10} would have origin state E_H while γ_{11}'s origin state would be E_1. The generator starts generating always at the highest level E_H. Among all the gammas which originate in E_H, first gamma in cascade would be chosen randomly. The probability is proportional to the intensity of the gamma. Gamma subsequently leads to lower energy level, where another gamma is randomly chosen among all those which

E_γ [MeV]	I_{SG} $[\frac{\gamma}{100ev.}]$	I_{NDS} $[\frac{\gamma}{100ev.}]$	I_{SG}/I_{NDS} [1]
0.412	19.9599	19	**1.05**
0.931	0	2.1	**0.00**
1.24	0	1	**0.00**
1.638	1.661	1.7	**0.98**
1.918	0	2.1	**0.00**
2.052	2.02	2	**1.01**
2.47	0.6708	3.9	**0.17**
2.618	1.12	2.4	**0.47**
2.67	0	1.5	**0.00**
2.873	0	1.1	**0.00**
3.005	0	1	**0.00**
3.028	1.62	2.6	**0.62**
3.38	0.8999	1.5	**0.60**
3.508	0	1	**0.00**
3.552	2.06	1.4	**1.47**
3.792	0.4857	1.8	**0.27**
4.455	0	1.6	**0.00**
4.495	2.16	3.4	**0.64**
4.589	2.99	2.6	**1.15**
4.707	0.7729	1.8	**0.43**
4.802	2.16	2.9	**0.74**
5.391	1.99	1.2	**1.66**
5.507	2.32	2.4	**0.97**
5.745	2.06	2.3	**0.90**
6.268	3.74	3.2	**1.17**
6.826	1.51	1.9	**0.79**
7.246	2.0693	2	**1.03**
8.886	12.65	12.3	**1.03**
9.297	67.6032	66	**1.02**

Table 5.5: Results obtained by Stair Generator. Each line represents one of the gamma lines emitted after thermal neutron capture on ^{54}Fe. Table compares intensities of the lines obtained from Stair Generator (I_{SG}) to intensity in Nuclear Data Sheets (I_{NDS}) obtained from [105]. Intensities are represented in number of observed gammas per 100 events.

originate in the level. The process is repeated until the ground state is reached. Such an approach preserves energy in the event by generation of full cascades, the correlations between gammas are taken into account.

Table 5.5 shows gamma intensities I_{SG} obtained by simulation of 10^6 events with Stair Generator. The results are compared with values I_{NDS} obtained from nuclear data sheets [105]. The correspondence for many gammas is very precise. However, many gammas are underestimated or overestimated by several tens of %. Note that, by the nature of generator, it is ensured, that energy is preserved exactly in each event. However, except for gammas, whose intensities are overestimated or underestimated, we can find examples of gammas which are not generated at all. These gammas originate in states lower than E_H. Problem of the generator is that, it relies strongly on the consistency of data. However, the data contains several gammas unassociated with any of the states. Therefore, many of the gammas are not accessible by generator because their origin states are never reached. Let me show an example based on Figure 5.16 - Left. γ_{11} is produced only if generator reaches excited level E_1. Only possibility to reach the state is by emission of γ_{10}. If this gamma is missing from the experimental dataset, the state E_1 is never reached and γ_{11} never produced. In principle, the generator should work reliably with perfectly consistent dataset (all gammas are associated and properly connected). It is, however, rarely true.

5.2.3 Possible Solution

As we learned in the previous section, it is important to have a generator which accounts not only for correlations of gammas, but also for imprecisions in the input datasets. For this purpose, I propose a possible solution. It represents interesting proposal to solve the

problems with gammas from thermal neutron capture and might help in the future to pave a road for precise estimation of fake double-beta decay rates originating from neutrons.

5.2.3.1 Naming Convention

In order to describe proposed generator, let me first clarify naming conventions used in the problem. Figure 5.17 represents cascade scheme similar to the one in Figure 5.16 - Left, but this time with two intermediate states E_1 and E_2.

First of all, let us discuss the convention used to designate full gamma cascades. In the example, there are four different cascades: x_{1001}, x_{1011}, x_{1101} and x_{1111}. The index holds a full information about the structure of cascade. Let me take cascade x_{1011} as an example. The cascade starts with transition $E_H \rightarrow E_1$ followed by transition $E_1 \rightarrow E_0$. The cascade involves states E_H, E_1 and E_0. If we list all four states involved in our system in order of descending energy (E_H, E_2, E_1, E_0) and then represent each state by 0 or 1, we obtain the naming convention. 1 is assigned, if state is involved in the cascade, 0 is assigned otherwise. Therefore, cascade involving chain of transitions: $E_H \rightarrow E_2 \rightarrow E_0$ is designated by x_{1101}. The number of indices always corresponds to number of all states in the system. Note that, all the cascades start and end by ones simply because the highest state E_H and ground state E_0 has to be always involved. These two indices might be omitted. If we do so, we can define one-to-one correspondence between binary numbers and cascades. We just need to rewrite binary number (after omission of leading and final one in the index) in decimal system. Such an alternative notation is shown in bracket under the original (binary) notation in Figure 5.17. In decimal notation the structure of the cascade is not obviously visible just by looking at the index, however, it is much more practical when it comes to calculations. For systems with many intermediate states, binary notation becomes lengthy and cumbersome. In following, I will always follow decimal notation for simplicity.

With decimal notation in mind, it is trivial task to calculate how many possible cascades can be expected in the system given the number of intermediate levels. In my example, there are two intermediate levels E_1 and E_2. In each cascade, none of the levels might be involved (x_{1001} / x_0), one level might be involved (x_{1011} / x_1 and x_{1101} / x_2), or both of them might be involved (x_{1111} / x_3). There is no other possibility unless we add another intermediate level.

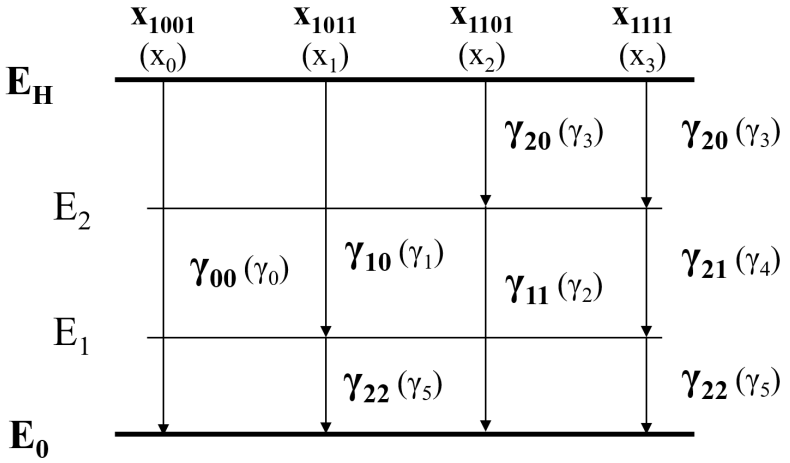

Figure 5.17: Scheme of gamma deexcitation cascades after thermal neutron capture. The scheme represents situation with two intermediate excited states E_1 and E_2.

If we omit the ones at the beginning and the end of cascade each one can be represented by any two digit combination of 0 and 1. Therefore, there is 2^2 cascades in the example. Accordingly, with n intermediate states one could draw 2^n different cascades.

In case of single gammas, the convention is bit more complicated. Different gammas are shared between the cascades, so their naming convention cannot be derived from the name of the cascade they belong to. As a first step, I divided the gammas into classes. Zero class gamma is the one which connects the highest state E_H with the ground state E_0 (γ_{00}). In each system, regardless of the number of intermediate states, there is only one zero class gamma. It is always the one which skips all the intermediate states. First class gamma, I call the gamma which skips one level less than zero class gamma (γ_{10} and γ_{11}). Zero class gamma was skipping two states, therefore, first class gamma (in system with two intermediate states) skips one level. Every higher class skips one less state. In our system with two intermediate states the last class is second class when gammas do not skip any intermediate level (γ_{20}, γ_{21} and γ_{22}). In other words, such gamma connects neighbouring levels. Number of classes depends on number of intermediate states. Each gamma has two indices. First index denotes class to which gamma belongs. Second index serves to differ between the gammas in same class. The lowest index is always 0 and it denotes gamma of highest energy of level from which it originates. For instance, γ_{10} and γ_{11} both belong to first class, but γ_{10} originates in level E_H which is higher level of origin than in case of γ_{11} (level E_2). In this sense, the gammas belonging to the same class are denoted by increasing second index as their state of origin is lower. Index of last gamma in the class always equals the number of class. If we keep that in mind, we can easily calculate number of single gammas for given number of intermediate states. There is always one zero-class gamma. First class includes always two gammas and class i contains i+1 gammas. The highest class is always n-th class (where n is number of intermediate states in the system) with n+1 gammas. To obtain total number of single gammas in the system we have to sum up all the gammas from all classes, i.e. numbers from 1 up to n+1 (including). The total sum is (n+1)(n+2)/2. Two index convention is very useful in order to easily cover all possible gammas for given system, however, one index is more practical to be used. Example of such convention can be found in brackets next to each gamma in Figure 5.17. In following examples, I will keep on using the simpler one-index notation.

Table 5.6 summarizes number of cascades (N_C) and unique single gamma transitions (N_γ) as a function of number of intermediate states in the system (n).

n	**0**	**1**	**2**	**3**	**4**	**5**	**6**	**7**	**8**	**9**	**10**	**11**	**12**	**13**
N_C	1	2	4	8	16	32	64	128	256	512	1024	2048	4096	8192
N_γ	1	3	6	10	15	21	28	36	45	55	66	78	91	105

Table 5.6: Table displays number of all possible cascades N_C and single gamma transitions N_γ in a system with n intermediate states.

5.2.3.2 Description of Generator

Cascade variables x_i can be used to store probabilities of cascade occurrence. If we would have the proper values, we would be able to generate thermal neutron capture gammas properly in the coincidence and with energy conserved in the event. On the other side, standard nuclear tables provide intensities of single gammas in form of γ_j variables. As

an additional information, usually, the level of origin for each gamma is provided. The intensities are represented in number of gammas per 100 events (i.e. in %).

The task is, therefore, to find a relationship between cascade variables x_i and single gamma intensities γ_j. As it was discussed already, this is possible only to a certain precision, as the data might miss some gamma transitions causing the exact generators to fail.

Imagine, we know the probabilities x_i for each single cascade to occur (with infinite precision). In such case, we would be able to easily calculate how often gamma occurs. For instance, probability of γ_3 to occur in random event is given by probability $p_3 = x_2 + x_3$. It can be created by any of these two cascades. Such an relation can be written for each of the gammas:

$$\begin{aligned} p_0 &= x_0 \\ p_1 &= x_1 \\ p_2 &= x_2 \\ p_3 &= x_2 + x_3 \\ p_4 &= x_3 \\ p_5 &= x_1 + x_3. \end{aligned} \tag{5.3}$$

Here, p_j represents probability (ideal intensity) of γ_j to occur. Composition of the equations is clear from Figure 5.17. These are the equation for case with two intermediate states. Note that, cascade probabilities are normalized to one:

$$x_0 + x_1 + x_2 + x_3 = 1, \tag{5.4}$$

because in each event any cascade should always occur. Cascades are also mutually exclusive. However, this does not hold for single gammas:

$$p_0 + p_1 + p_2 + p_3 + p_4 + p_5 > 1. \tag{5.5}$$

Sum of their probabilities is always higher than one (except for the trivial case with no intermediate state) and represents the average number of gammas per 100 events. However, all we have available are the gamma intensities γ_j which might not be perfectly consistent due to experimental uncertainties. Nevertheless, if they were, the measured intensities γ_j should be exactly same as gamma probabilities (p_j) obtained by ideal measurement:

$$\gamma_j = p_j. \tag{5.6}$$

Equations 5.6 form a set of "Structure Equations" (SE). Six SE encode all the necessary relations for the case of two intermediate states. Such equations could be written for case with any number of intermediate states.

As the name suggest, cascade probabilities are probability variables, therefore their values should be always in the interval $\langle 0, 1 \rangle$. At this point, I would like to point out specific property of SE. Let us have a look back to Equation 5.3. Based on the previous remark, non-observation of γ_3 in experimental data (i.e. $p_3 = 0$) would imply $x_2 = 0$ and $x_3 = 0$. As neither of the cascade variables can be negative, this is the only possibility. However, $x_3 = 0$ would imply $p_2 = p_4 = 0$. It is a (welcomed) consequence of the correlations between the gammas in the cascades.

Experimental datasets usually originate from sets of different experiment with different experimental uncertainties or sensitivities of measurement setups. Therefore, it is no surprise

that situation when $\gamma_3 = 0$ and $\gamma_2 \neq 0$ can occur even though it should not (see Figure 5.17). Strictly speaking, for such a combination of single gamma probabilities, no solution in form of (non-negative) cascade probabilities x_i would exist. The Stair Generator worked on bit different principle, however, this was exactly the reason why it did not work properly.

In order to account for experimental uncertainties in the input datasets, we have to take an approximative approach. It is important to have an approach which would allow us to reproduce measured intensities as precise as possible while preserving the cascades and, the most importantly, the energy.

Let me start with Equation 5.6. It represents (in case of two intermediate states) exact relations between the cascade probabilities and single gamma intensities in ideal case. Let me define a function $\delta_j(x_i)$:

$$\delta_j(x_i) = \gamma_j - p_j. \tag{5.7}$$

In case of ideal data, obviously, $\delta_j = 0$. Based on the experimental uncertainties discussed above, it is impossible to reach such a solution. In such case $\delta_j^2(x_i)$ expresses the imprecision of the solution. p_j is a linear function of cascade probabilities x_i. Therefore, $\delta_j^2(x_i)$ is also a function of cascade probabilities. It is always non-negative, which is ensured by raising δ_j to a second power. Single gamma intensities γ_j serve as functional parameters given by data. Finally, variation of all the cascade probabilities x_i, within the allowed interval $\langle 0, 1 \rangle$, influences a variation of $\delta_j^2(x_i)$ values. The values of interest are those as close to zero as possible. Nevertheless, each $\delta_j^2(x_i)$ function reaches the minimal value for different set of cascade coefficients. To ensure, that we have found the minimal global value, it is necessary to minimize sum of all the contributions:

$$\Delta(x_i) = \sum_{allgammas}^{N_\gamma} \Delta_j^2(x_i). \tag{5.8}$$

In case of two intermediate states $\Delta(x_i)$ function has a following form:

$$\Delta(x_0,\, x_1,\, x_2,\, x_3) = \delta_0^2 + \delta_1^2 + \delta_2^2 + \delta_3^2 + \delta_4^2 + \delta_5^2, \tag{5.9}$$

where

$$\begin{aligned}
\delta_0(x_0) &= \gamma_0 - x_0, \\
\delta_1(x_1) &= \gamma_1 - x_1, \\
\delta_2(x_2) &= \gamma_2 - x_2, \\
\delta_3(x_2,x_3) &= \gamma_3 - x_2 - x_3, \\
\delta_4(x_3) &= \gamma_4 - x_3, \\
\delta_5(x_1,x_3) &= \gamma_5 - x_1 - x_3.
\end{aligned} \tag{5.10}$$

γ_j are gamma intensities given by experimental measurements. Finally, solution to the problem is a quadruplet of cascade probabilities $x_0^s,\, x_1^s,\, x_2^s,\, x_3^s$ fulfilling all the following conditions:

$$\begin{aligned}
0 \leq x_0^s,\, x_1^s,\, x_2^s,\, x_3^s &\leq 1, \\
x_0^s + x_1^s + x_2^s + x_3^s &= 1, \\
\Delta(x_0^s,\, x_1^s,\, x_2^s,\, x_3^s) &= min\big[\Delta(x_i)\big].
\end{aligned} \tag{5.11}$$

This is a well known problem of finding constrained functional extremes. It can be approached by method of Lagrange multiplier. The whole presented approach can be applied

to systems with arbitrary number of intermediate levels, limited only by amount of computing power. Each extra intermediate level adds to the complexity of the problem factor of two (number of cascades). Nevertheless, vast majority of the cascades could be considered as zero for each γ_j which is equal to zero (as already discussed). Once, all the cascade probabilities are obtained, random number generator can choose between the cascades randomly. The conservation of energy is guaranteed. One has to be careful about appearance of non-existing gamma lines in the spectrum, however, this effect is a price to be paid for incompleteness of data.

The generator proposed in this section has ability to improve with improved data precision, which I consider as the most important feature.

5.2.3.3 Solution for a System with Two Intermediate States

In the current section, I will show an explicit solution for a problem defined in Equation 5.11. It will be solved for a particular example of system with two intermediate states (depicted in Figure 5.17). In the process, I will develop a matrix formalism which will, finally, make it applicable to a problem with arbitrary number of intermediate states.

During the whole derivation to follow, I will work in the space of column vectors, e.g. v represents column vector while v^T stands for a row vector. Before I will start the main derivation, let me define "cascade vector" x, "probability vector" p, "gamma intensity vector" γ and "delta difference vector" δ in following way:

$$x = \begin{pmatrix} x_0 \\ x_1 \\ x_2 \\ x_3 \end{pmatrix}, \quad p = \begin{pmatrix} p_0 \\ p_1 \\ p_2 \\ p_3 \\ p_4 \\ p_5 \end{pmatrix}, \quad \gamma = \begin{pmatrix} \gamma_0 \\ \gamma_1 \\ \gamma_2 \\ \gamma_3 \\ \gamma_4 \\ \gamma_5 \end{pmatrix}, \quad \delta = \begin{pmatrix} \delta_0 \\ \delta_1 \\ \delta_2 \\ \delta_3 \\ \delta_4 \\ \delta_5 \end{pmatrix}. \tag{5.12}$$

Note the dimensions of each vector. Cascade vector x has 4 components (number of cascades) while the other two contain 6 components (number of gammas). Such definitions will be useful later in the derivation. Equation 5.3 can be rewritten in vector form $p_j = s_j^T x$. Here, s_j is one of six vectors which keep information about the structure of the cascades. For our system their specific form is as follows:

$$s_0 = \begin{pmatrix} 1 \\ 0 \\ 0 \\ 0 \end{pmatrix}, s_1 = \begin{pmatrix} 0 \\ 1 \\ 0 \\ 0 \end{pmatrix}, s_2 = \begin{pmatrix} 0 \\ 0 \\ 1 \\ 0 \end{pmatrix}, s_3 = \begin{pmatrix} 0 \\ 0 \\ 1 \\ 1 \end{pmatrix}, s_4 = \begin{pmatrix} 0 \\ 0 \\ 0 \\ 1 \end{pmatrix}, s_5 = \begin{pmatrix} 0 \\ 1 \\ 0 \\ 1 \end{pmatrix} \tag{5.13}$$

Furthermore, if we define matrix S:

$$S = (s_0, s_1, s_2, s_3, s_4, s_5) = \begin{pmatrix} 1 & 0 & 0 & 0 & 0 & 0 \\ 0 & 1 & 0 & 0 & 0 & 1 \\ 0 & 0 & 1 & 1 & 0 & 0 \\ 0 & 0 & 0 & 1 & 1 & 1 \end{pmatrix}, \tag{5.14}$$

we can express Equations 5.3 in simple and compact matrix form:

$$p = S^T x. \tag{5.15}$$

Following the definitions of vector p, γ and δ we can also rewrite delta differences δ_i given by Equation 5.10 into matrix form:

$$\delta = \gamma - p = \gamma - S^T x. \tag{5.16}$$

Finally, the global difference function Δ given by Equation 5.9 takes form of dot product[1] of δ vector with itself:

$$\Delta = \delta^T \delta = (\gamma^T - p^T)(\gamma - p) = \gamma^T \gamma - 2p^T \gamma + p^T p. \tag{5.17}$$

In the equation, I took advantage of Equation 5.16. In last step, I used the symmetry of dot product, $\gamma^T p = p^T \gamma$. Matrix formalism introduced in text above is applicable for any system regardless of the number of intermediate states. Even though, I am focusing on the particular case, the final result will be applicable for any problem of this type.

With the formalism at the place, it is possible to discuss the problem given in Equation 5.11. One needs to find a minimum of function Δ for values of vector x whose components add up to one. It is an optimization problem when extremes of the function of multiple variables have to be found given a constraint. It can be solved by method of Lagrange multiplier.

First of all, let me remind the method of Lagrange multiplier. If we want to find extreme(s) of (for instance) two-dimensional function f(x,y) in region given by equation g(x,y) = 0, one should define so-called Lagrange function first:

$$\mathscr{L}(x,y,\lambda) = f(x,y) + \lambda g(x,y). \tag{5.18}$$

Here, λ is so-called Lagrange multiplier. Extreme(s) of function f in the region g = 0 are all lying in points obtained as a solution to a system of equations:

$$\frac{\partial \mathscr{L}}{\partial x} = 0, \quad \frac{\partial \mathscr{L}}{\partial y} = 0, \quad \frac{\partial \mathscr{L}}{\partial \lambda} = 0. \tag{5.19}$$

For each λ obtained as a solution, vector (x, y) represents sought constrained extreme. The method is applicable to functions f of arbitrary number of variables.

Let me now apply the method to our problem. The function f which we need to minimize is function Δ, depending on all the components (variables) of vector x. The constraint g = 0 in our problem is given by the sum of all components of vector x which should always add to one (full probability), i.e.

$$g(x_0,x_1,x_2,x_3) = 1 - x_0 - x_1 - x_2 - x_3 = 0. \tag{5.20}$$

Therefore, the Lagrange function defining the problem is following:

$$\mathscr{L}(x_0,x_1,x_2,x_3,\lambda) = \Delta(x_0,x_1,x_2,x_3) + \lambda g(x_0,x_1,x_2,x_3). \tag{5.21}$$

By putting all the partial derivations of Lagrange function equal to zero (according to recipe from Equation 5.19) we get a set of equations:

$$\frac{\partial \mathscr{L}}{\partial x_0} = 0, \quad \frac{\partial \mathscr{L}}{\partial x_1} = 0, \quad \frac{\partial \mathscr{L}}{\partial x_2} = 0, \quad \frac{\partial \mathscr{L}}{\partial x_3} = 0, \quad \frac{\partial \mathscr{L}}{\partial \lambda} = 0. \tag{5.22}$$

[1] Note that, whenever dot product of two vector appears throughout the derivation, it stands for the standard vector dot product known from classical geometry, i.e. $v_1^T v_2 = v_1^T \mathbb{I}_N v_2$. N is a number of components of vectors v_1 and v_2 and $\mathbb{I}_N$ stands for square unity matrix of dimension N.

Now, if we realize that

$$\frac{\partial g}{\partial x_a} = \frac{\partial(1 - x_0 - x_1 - x_2 - x_3)}{\partial x_a} = -1, \quad a = 0,1,2,3, \tag{5.23}$$

we can rewrite Equations 5.22 into form

$$\frac{\partial \Delta}{\partial x_0} = \lambda, \quad \frac{\partial \Delta}{\partial x_1} = \lambda, \quad \frac{\partial \Delta}{\partial x_2} = \lambda, \quad \frac{\partial \Delta}{\partial x_3} = \lambda, \quad g = 0. \tag{5.24}$$

It is possible to eliminate (in our case) unwanted λ multiplier by subtraction of second, third and fourth equation from the first one and obtaining set of four equations (of four variables):

$$\frac{\partial \Delta}{\partial x_0} - \frac{\partial \Delta}{\partial x_1} = 0, \quad \frac{\partial \Delta}{\partial x_0} - \frac{\partial \Delta}{\partial x_2} = 0, \quad \frac{\partial \Delta}{\partial x_0} - \frac{\partial \Delta}{\partial x_3} = 0, \quad g = 0. \tag{5.25}$$

As it will turn out soon, this is a set of linear equations which can be solved by application of basic linear algebra. Note that, all the process presented until this point was not dependent on the number of cascades, neither the number of gammas involved in the problem. The specific case of two intermediate states (4 cascades, 6 gammas) is chosen as an example clarifying the general matrix notation and the calculation process.

In steps to follow, it is necessary to evaluate all the partial derivations of Δ function with respect to cascade probability x_a. Before I do that, it is important to express some intermediate relations. Let me, firstly, define four-component base vectors e_0 - e_3:

$$e_0 = \begin{pmatrix} 1 \\ 0 \\ 0 \\ 0 \end{pmatrix}, \quad e_1 = \begin{pmatrix} 0 \\ 1 \\ 0 \\ 0 \end{pmatrix}, \quad e_2 = \begin{pmatrix} 0 \\ 0 \\ 1 \\ 0 \end{pmatrix}, \quad e_3 = \begin{pmatrix} 0 \\ 0 \\ 0 \\ 1 \end{pmatrix}. \tag{5.26}$$

Number of these vectors is given by number of cascades (cascade probabilities) assumed in the problem. It is also useful to underline that for any vector v (or matrix M) and its transpose v^T (M^T), following relations hold:

$$\left(\frac{\partial v}{\partial \alpha}\right)^T = \frac{\partial v^T}{\partial \alpha}, \quad \left(\frac{\partial M}{\partial \alpha}\right)^T = \frac{\partial M^T}{\partial \alpha} \tag{5.27}$$

for any variable α. It is easily to see, that by performing partial derivation with respect to any of the cascade probabilities x_a, on vector x we obtain one of the base vectors e_a:

$$\frac{\partial x}{\partial x_a} = e_a. \tag{5.28}$$

Furthermore, vector γ and matrix S are constant and they yield zero when derived with respect to x_a:

$$\frac{\partial \gamma}{\partial x_a} = 0, \quad \frac{\partial S}{\partial x_a} = 0. \tag{5.29}$$

Given the Equations 5.15, 5.28 and 5.29, following holds:

$$\frac{\partial p}{\partial x_a} = S^T e_a. \tag{5.30}$$

Finally, we have all the ingredients in order to compute derivations of global difference function Δ. By putting Equations 5.17, 5.27, 5.29, 5.30 and symmetry of dot product together, we can write:

$$\frac{\partial \Delta}{\partial x_a} = 2e_a^T SS^T x - 2e_a^T S\gamma. \tag{5.31}$$

First three in Equations 5.25 have a form of difference of derivations of Δ. Using Equation 5.31 we can write:

$$\frac{\partial \Delta}{\partial x_a} - \frac{\partial \Delta}{\partial x_b} = 2(e_a^T - e_b^T)SS^T x - 2(e_a^T - e_b^T)S\gamma, \tag{5.32}$$

and Equations 5.25 gain form:

$$\begin{aligned}
(e_0^T - e_1^T)SS^T x &= (e_0^T - e_1^T)S\gamma, \\
(e_0^T - e_2^T)SS^T x &= (e_0^T - e_2^T)S\gamma, \\
(e_0^T - e_3^T)SS^T x &= (e_0^T - e_3^T)S\gamma, \\
(e_0^T + e_1^T + e_2^T + e_3^T)x &= 1.
\end{aligned} \tag{5.33}$$

In last equation g = 0, I took advantage of the fact that $(e_0^T+e_1^T+e_2^T+e_3^T)x = x_0 + x_1 + x_2 + x_3$. Having a closer look at the system in Equation 5.33 it is possible to spot hidden matrix equation of form Ax = b where

$$A = \begin{pmatrix} (e_0^T - e_1^T)SS^T \\ (e_0^T - e_2^T)SS^T \\ (e_0^T - e_3^T)SS^T \\ e_0^T + e_1^T + e_2^T + e_3^T \end{pmatrix}, \quad b = \begin{pmatrix} (e_0^T - e_1^T)S\gamma \\ (e_0^T - e_2^T)S\gamma \\ (e_0^T - e_3^T)S\gamma \\ 1 \end{pmatrix}. \tag{5.34}$$

Finally, the sought vector x is, therefore, calculated as:

$$x = A^{-1}b \tag{5.35}$$

where A^{-1} is inverse of matrix A. Matrix A is a square matrix of dimension equal to number of cascades involved in the system in question. It is relatively straightforward to extend matrix A and vector b into systems with higher number of intermediate states, namely, systems with N_C cascades and N_γ gammas:

$$A = \begin{pmatrix} (e_0^T - e_1^T)SS^T \\ (e_0^T - e_2^T)SS^T \\ \vdots \\ (e_0^T - e_{N_C}^T)SS^T \\ \sum_{i=0}^{N_C} e_i^T \end{pmatrix}, \quad b = \begin{pmatrix} (e_0^T - e_1^T)S\gamma \\ (e_0^T - e_2^T)S\gamma \\ \vdots \\ (e_0^T - e_{N_C}^T)S\gamma \\ 1 \end{pmatrix}. \tag{5.36}$$

Structure matrix S and vector γ are expanded accordingly, following the definition at the beginning of the section.

5.2.3.4 Proof of the Concept by Analytical Solution

In order to prove the concept I will present solution of two (intermediate) state system which was used as an example throughout the whole discussion about the generator. The task is simple. We need to compose the matrix A and vector b from Equation 5.34, find

the inverse matrix A^{-1} and subsequently calculate $A^{-1}b$. Let me start with matrix A. As a first step, it is helpful to compose row vectors of form e_a^T - e_b^T. Following the definition in Equations 5.26 we can write:

$$\begin{aligned} e_0^T - e_1^T &= \begin{pmatrix} 1 & -1 & 0 & 0 \end{pmatrix}, \\ e_0^T - e_2^T &= \begin{pmatrix} 1 & 0 & -1 & 0 \end{pmatrix}, \\ e_0^T - e_3^T &= \begin{pmatrix} 1 & 0 & 0 & -1 \end{pmatrix}. \end{aligned} \tag{5.37}$$

Taking advantage of definition of matrix S in Equation 5.14 we can write:

$$SS^T = \begin{pmatrix} 1 & 0 & 0 & 0 & 0 & 0 \\ 0 & 1 & 0 & 0 & 0 & 1 \\ 0 & 0 & 1 & 1 & 0 & 0 \\ 0 & 0 & 0 & 1 & 1 & 1 \end{pmatrix} \begin{pmatrix} 1 & 0 & 0 & 0 \\ 0 & 1 & 0 & 0 \\ 0 & 0 & 1 & 0 \\ 0 & 0 & 1 & 1 \\ 0 & 0 & 0 & 1 \\ 0 & 1 & 0 & 1 \end{pmatrix} = \begin{pmatrix} 1 & 0 & 0 & 0 \\ 0 & 2 & 0 & 1 \\ 0 & 0 & 2 & 1 \\ 0 & 1 & 1 & 3 \end{pmatrix}. \tag{5.38}$$

Following the recipe in Equation 5.34, with help of Equations 5.37 and 5.38 we can evaluate matrix A and vector b:

$$A = \begin{pmatrix} 1 & -2 & 0 & -1 \\ 1 & 0 & -2 & -1 \\ 1 & -1 & -1 & -3 \\ 1 & 1 & 1 & 1 \end{pmatrix}, \quad b = \begin{pmatrix} \gamma_0 - \gamma_1 - \gamma_5 \\ \gamma_0 - \gamma_2 - \gamma_3 \\ \gamma_0 - \gamma_3 - \gamma_4 - \gamma_5 \\ 1 \end{pmatrix}. \tag{5.39}$$

It is now simple task to calculate matrix inverse A^{-1}:

$$A = \begin{pmatrix} 1/4 & 1/4 & 0 & 1/2 \\ -1/2 & 0 & 1/4 & 1/4 \\ 0 & -1/2 & 1/4 & 1/4 \\ 1/4 & 1/4 & -1/2 & 0 \end{pmatrix}. \tag{5.40}$$

Finally, the solution $x = A^{-1}b$ has a following form:

$$\begin{aligned} x_0 = \frac{1}{2} &+\frac{1}{2}\gamma_0 &-\frac{1}{4}\gamma_1 &-\frac{1}{4}\gamma_2 &-\frac{1}{4}\gamma_3 & &-\frac{1}{4}\gamma_5, \\ x_1 = \frac{1}{4} &-\frac{1}{4}\gamma_0 &+\frac{1}{2}\gamma_1 & & -\frac{1}{4}\gamma_3 &-\frac{1}{4}\gamma_4 &+\frac{1}{4}\gamma_5, \\ x_2 = \frac{1}{4} &-\frac{1}{4}\gamma_0 & &+\frac{1}{2}\gamma_2 &+\frac{1}{4}\gamma_3 &-\frac{1}{4}\gamma_4 &-\frac{1}{4}\gamma_5, \\ x_3 = & &-\frac{1}{4}\gamma_1 &-\frac{1}{4}\gamma_2 &+\frac{1}{4}\gamma_3 &+\frac{1}{2}\gamma_4 &+\frac{1}{4}\gamma_5. \end{aligned} \tag{5.41}$$

As it could be expected, solution has form $x = c + M\gamma$ where c is a constant vector with dimension of x vector and M is matrix which is mixing all the gammas together to form cascade probabilities x_i. Note that, each column (therefore all the elements) of matrix M add up to zero while all the components of the vector c add up to one exactly. It is a consequence of constraint $x_0 + x_1 + x_2 + x_3 = 1$ which ensures that at least one of the cascades happens regardless of the experimental values which are stored in γ vector.

Let me now demonstrate the performance of obtained result. The whole discussion was motivated by the imprecisions in experimental data. As it was discussed, inconsistent input

in form of γ_j intensities (missing transitions) made some of the transitions unreachable by previously presented stair generator. Solution proposed in this section should not only conserve energy and γ correlations but the limit of its performance is given only by consistency of the γ transition values plugged into it. This also implies that, for perfectly consistent data set, the generator should give exact solution. Let me check this property. Let us have a following input dataset:

$$\gamma^T = \begin{pmatrix} \gamma_0 & \gamma_1 & \gamma_2 & \gamma_3 & \gamma_4 & \gamma_5 \end{pmatrix} = \begin{pmatrix} 0.5 & 0.05 & 0.4 & 0.45 & 0.05 & 0.1 \end{pmatrix}. \quad (5.42)$$

I will call this dataset ideal and denotes it by letter I because it represents perfectly consistent data as if they were measured by ideal experiment. If we now plug these γ (I) values into solution in Equation 5.41 we obtain following cascade probability vector:

$$x^T = \begin{pmatrix} x_0 & x_1 & x_2 & x_3 \end{pmatrix} = \begin{pmatrix} 0.5 & 0.05 & 0.4 & 0.05 \end{pmatrix}, \quad (5.43)$$

Taking advantage of structural equations given in Equation 5.3 we can calculate all the gamma probabilities p_i which would be produced by the generator.

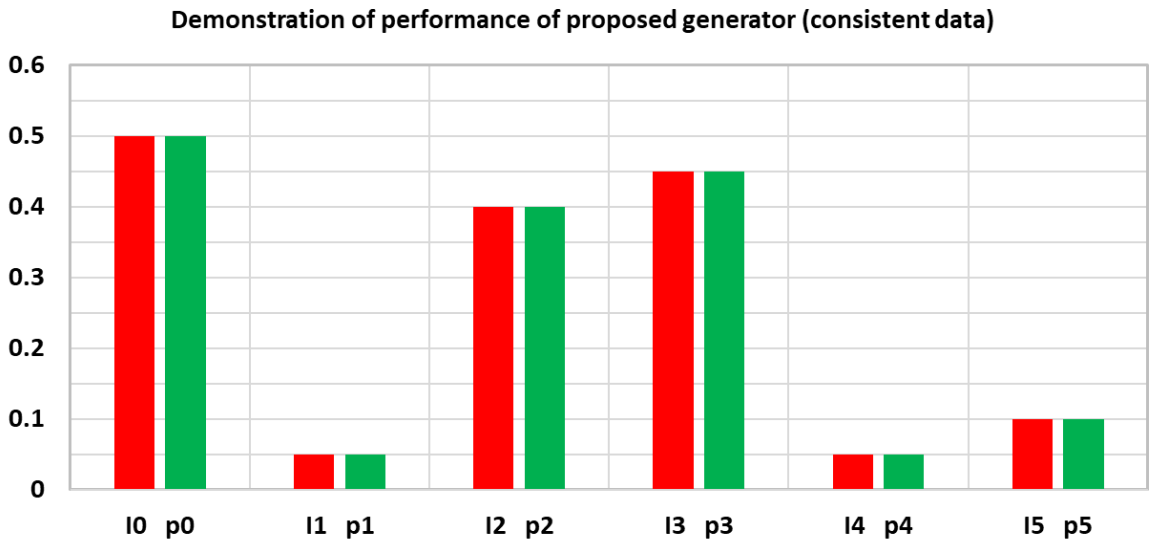

Figure 5.18: Comparison of ideal gamma intensities (red) with intensities generated by my generator (green).

Figure 5.18 contains comparison of ideal gamma intensities (red) from Equation 5.42 compared to intensities computed by the generator (green) based on Equations 5.41 and structure equations. Generator is exactly matching the intensities provided by dataset. Even though, this example is necessary check of basic performance, it does not yet reveal the real power of the generator. If ideal data were plugged into stair generator, the result would be also exact.

However, the main advantage of my generator is the possibility to work with imprecise data. Imagine that (ideal) intensities in Equation 5.42 would be measured with realistic detector giving rise to experimental uncertainties. Imagine that detector would measure slightly biased values:

$$\gamma^T = \begin{pmatrix} \gamma_0 & \gamma_1 & \gamma_2 & \gamma_3 & \gamma_4 & \gamma_5 \end{pmatrix} = \begin{pmatrix} 0.53 & 0.05 & 0.43 & 0.48 & 0 & 0.1 \end{pmatrix}. \quad (5.44)$$

These values are strictly speaking inconsistent, as it is not possible to find cascade probabilities x_0, x_1, x_2 and x_3 such that, the resulting gamma probabilities p_i obtained from Equations

5.3 would be matching these measured values. Intensities of γ_0, γ_2 and γ_3 are off by 0.03 while γ_4 is missing completely. After we plug the γ values into the generator (Equation 5.41) we obtain following cascade probabilities:

$$x^T = \begin{pmatrix} x_0 & x_1 & x_2 & x_3 \end{pmatrix} = \begin{pmatrix} 0.5 & 0.0475 & 0.4275 & 0.025 \end{pmatrix}. \tag{5.45}$$

As usual, these probabilities can be turned into gamma probabilities (intensities) as produced by generator by using structure equations. Figure 5.19 is comparing the ideal data (I, red), with imprecise experimental data used as a generator input (γ, blue) and gamma intensities obtained by generator given the input (p, green). In case of γ_0, γ_2 and γ_3 the generator

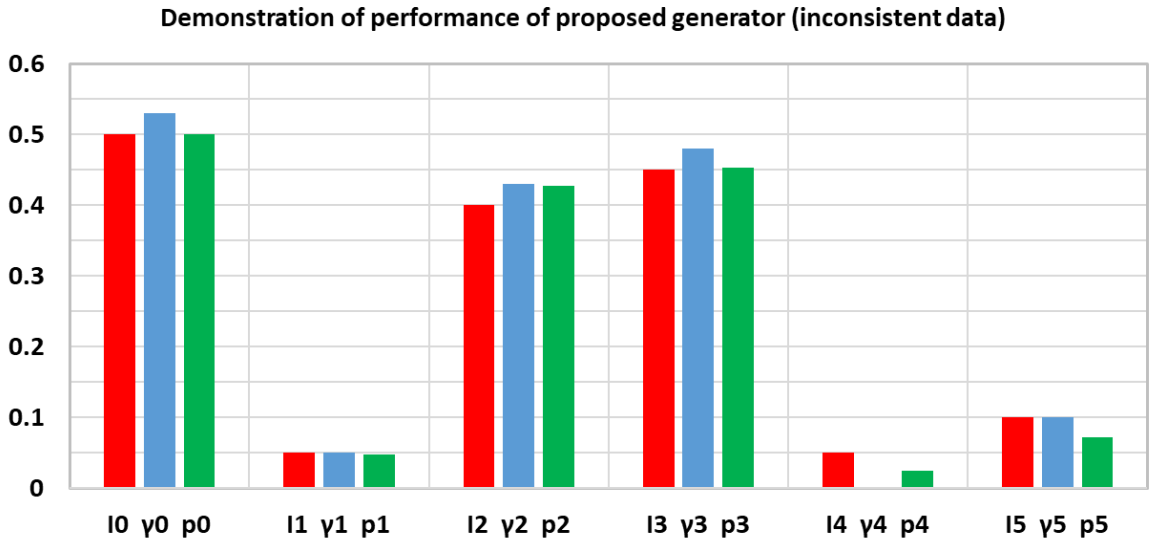

Figure 5.19: Comparison of ideal gamma intensities (red) with intensities biased by measurement uncertainties (blue) and resulting gamma intensities generated by my generator (green).

(green) was capable to totally or partially compensate the mismatch of measurement (blue) and ideal data (red). In case of γ_0, the errors cancelled out perfectly resulting in generator being more precise that the input dataset. In other two cases, results from generator are closer to reality than measurement. This is thanks to the structure of the cascades encoded in the generator's equations. Furthermore, γ_4 is not present in experimental dataset. However, the generator reproduces this transition at least partially. It is for a price of underestimation of γ_5, nevertheless, it is inevitable effect which we pay for imprecise data. Appearance of γ_4 in my example is a triumph of my generator. If we remind the structure of the cascades from Figure 5.17 we see that γ_4 is intermediate link between γ_3 and γ_5 in cascade x_3. Stair generator would be capable of generating γ_3 but after it would fall to the E_2 excited state it would not be capable of reaching ground state E_0, causing not only γ_4 to be left out but γ_5 being suppressed.

It is possible to conclude, that my proposed generator represents a possibility to reconstruct gamma correlations as precisely as the input dataset allows. The presented example for two intermediate states was chosen for simplicity and clarity, however, Equation 5.36 offers recipe for solution of any system. One only needs to compose the matrix of structure S specific for the system. After matrix A is composed, it needs to be inverted. The dimension of the matrix is $N_C \times N_C$ where N_C is a number of possible cascades in the system. Based on the Table 5.6 we can see that, the number of cascades grows exponentially with

the number of intermediate states in the system. However, even for complex systems, the diagonalization of large matrices is achievable with computers nowadays. Furthermore, the structure equations can be simplified significantly based on the selection rules which might prohibit some particular gamma transitions to occur. The calculation needs to be performed only once. After the vector of cascade probabilities x is obtained for given dataset, it does not have to be recalculated, unless more precise experimental data are obtained as an input. Proposed generator is conceptually general and it can be also applied for any systems where decay cascades occur (regardless of particles produced in the transitions). It is also possible to generalize the generator in order to work with transitions originating from lower than the highest excited state E_H.

5.3 Conclusions

The estimation of neutron background is generally difficult task to perform. In the chapter, I compared neutron fluxes which could be expected to pass through shielding for nine specific cases. Subsequently, estimation of neutron capture counts inside of the demonstrator was performed. Materials with most of the captures were identified and mapped in form of three dimensional capture maps.

The neutrons were followed all the way to the capture. Physics implemented in Geant software package is sufficient and well implemented for such task. However, in second part of the chapter it was shown, that the model of production of gammas produced in thermal neutron capture is not sufficient for the task of estimation of background caused by neutrons. Energy conservation and gamma coincidences are not preserved. New potential approach which could take these two features into account was proposed. The performance of the generator was demonstrated on a simple example. In future, I plan to apply the approach on the real data for chosen isotopes and use it to estimate fake double-beta events caused by neutron capture.

Chapter 6

Estimation of Sensitivity of SuperNEMO to $0\nu\beta\beta$ with Majoron Emission

Main interests of double beta decay experiments are usually focused towards yet unobserved $0\nu\beta\beta$ or $2\nu\beta\beta$ which was already proven to exist experimentally for various different nuclei. However, there exist another more exotic double beta decay theories predicting existence of $0\nu\beta\beta$ with emission of so-called Majoron(s):

$$0\nu\beta\beta\chi^0 \quad : \quad (A,Z) \rightarrow (A,Z+2) + 2e^- + \chi^0, \tag{6.1}$$

$$0\nu\beta\beta\chi^0\chi^0 \quad : \quad (A,Z) \rightarrow (A,Z+2) + 2e^- + 2\chi^0. \tag{6.2}$$

Here, χ^0 stands for a Majoron. Majoron is a massless Goldstone boson which arise due to a violation of global B-L symmetry assumed in certain models. Its existence might have important implications in Cosmology [109, 110, 111] or Astrophysics [112, 113, 114, 115].

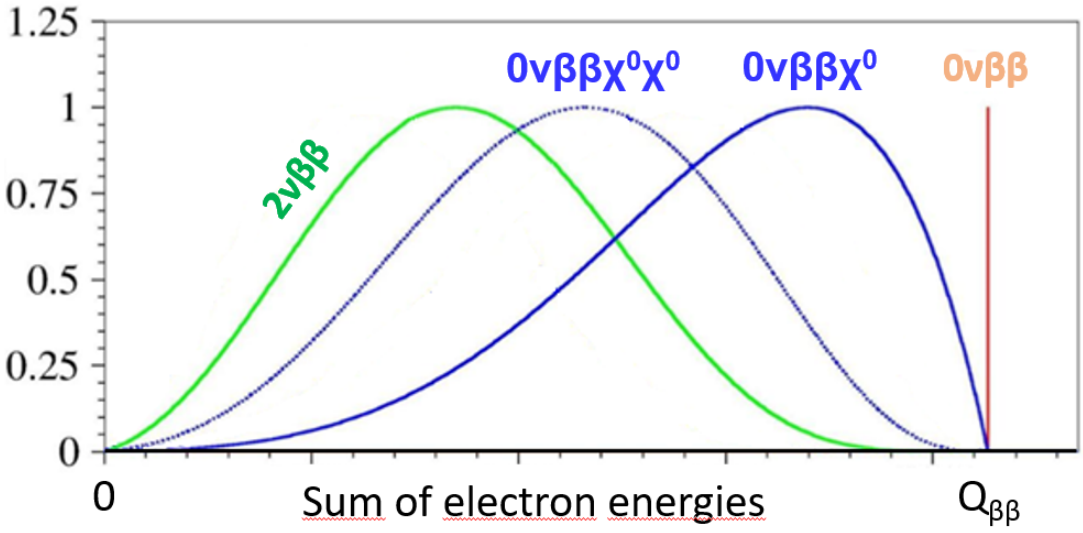

Figure 6.1: Theoretical electron energy spectra of various types of double beta decay. In green and orange one can see the spectra of $2\nu\beta\beta$ and $0\nu\beta\beta$, respectively. In blue, spectra of $0\nu\beta\beta$ with emission of one or two Majorons is depicted. The energy spectrum of two electrons is a signature to distinguish processes represented in the plot.

Different Majoron models result in different electron energy spectra. Examples of some of them are shown in Figure 6.1. Each double beta decay spectrum has its own so-called "spectral index". This is the possibility to distinguish them in the scientific literature. In the whole thesis, under symbol $0\nu\beta\beta\chi^0$ we understand process with spectral index n = 1 and symbol $0\nu\beta\beta\chi^0\chi^0$ stands for process with spectrum of index n = 3.

NEMO-3, set the limit for half life of $0\nu\beta\beta\chi^0$ to 1.5×10^{22} yr (90% CL) and limit for $0\nu\beta\beta\chi^0\chi^0$ at 3.1×10^{21} yr (90% CL) [116]. The goal of the chapter is to evaluate how much can SuperNEMO improve these values.

6.1 Calculation of Half-Life Limits

As shown in Figure 6.1, different double-beta decay processes can be distinguished based on the shape of two electron energy spectrum. Therefore, it is important to study energy spectrum of processes of interest ($0\nu\beta\beta\chi^0$ and $0\nu\beta\beta\chi^0\chi^0$) along with their backgrounds, in order to find regions of interest (ROI) where one would have the best chance to observe the decay. Subsequently, I will apply the recipe of Feldman and Cousins (presented in Appendix B) to estimate the sensitivity of SuperNEMO experiments to $0\nu\beta\beta\chi^0$ and $0\nu\beta\beta\chi^0\chi^0$. The sensitivity will be studied for two different CL as a function of background activities of ^{208}Tl and ^{214}Bi.

6.1.1 Calculation of Detection Efficiencies ε

Among other parameters, Equation B.15 (used for calculation of sensitivity) includes detection efficiency ε. Parameter ε expresses a fraction of all events of a particular process which were successfully detected and reconstructed and which passed all the eventual data cuts. The parameter can naturally be obtained only from a simulation. Simulation is performed for N events of every single process (for example $2\nu\beta\beta$) with application of all the detection imperfection (e.g. energy resolution, track reconstruction, etc.) and data cuts of interest. Only N_p events pass the requirements of data cuts. Detection efficiency is then simply the ratio of events which passed over all the events which were simulated:

$$\varepsilon = \frac{N_p}{N}. \tag{6.3}$$

Example of calculated ε parameters can be found in Table 4.1 in Section 4.1.2.1. Table compares detection efficiencies of four different processes after Standard Double Beta Decay Reconstruction Criteria (SDBDRC - defined in the same section) were applied. Furthermore, second column of the table is demonstration, that the different choice of data cuts alter the efficiencies. Cut on energy E > 2 MeV resulted in slightly less $0\nu\beta\beta$ being accepted, however, significantly less $2\nu\beta\beta$ pass through such cut. It is a mechanism, which evaluates how well chosen cut can discriminate between true signal and background.

Before I will discuss the sensitivities of SuperNEMO, it is important to extract detection efficiencies. In order to eliminate events of arguable quality, I will always apply SDBDRC to accept or reject event. The list of five conditions which event has to meet is exhaustively discussed in Section 4.1.2.1.

In this study, I consider $0\nu\beta\beta\chi^0$ and $0\nu\beta\beta\chi^0\chi^0$ as a signal events. On the other side, $0\nu\beta\beta$, $2\nu\beta\beta$ or decay of ^{208}Tl or ^{214}Bi can mimic the decay and will be considered as major contributors to background. It is important to find a cut (on energy) which favours the signal and suppress the background the most.

Samp.	Process	Nucleus	Magnetic field [G]	Number of simulated events
S3	$0\nu\beta^-\beta^-$	^{82}Se	25	1.04×10^8
S4	$0\nu\beta^-\beta^-\chi^0$	^{82}Se	25	1.04×10^8
S5	$0\nu\beta^-\beta^-\chi^0\chi^0$	^{82}Se	25	1.038×10^8
S7	$2\nu\beta^-\beta^-$	^{82}Se	25	1.04×10^8
S9	β^-	^{208}Tl	25	1.04×10^8
S10	β^-	^{214}Bi	25	1.04×10^8

Table 6.1: List of simulated samples produced by Falaise 2.0.0 used in the study.

Each of these six processes have different shape of energy spectrum. Therefore, by variation of energy cut $E_{min} \leq E < E_{max}$ one can observe the change in ratio of detection efficiencies between signal and background processes.

I established such study by using Falaise 2.0.0. Each of the six samples from Table 6.1 were passed through SDBDRC with extra energy cut accepting only events with energy in interval (E_{min}, E_{max}). I was varying values of E_{min} and E_{max} from 0 keV to 3500 keV by a step of 100 keV. I combined all the possible values while keeping $E_{min} < E_{max}$. For each cut detection efficiency coefficient ε was calculated.

Results are presented in Figure 6.2. Energy distributions with peak at the end of the spectrum tend to produce ε plots with highest values on top while the ones with peak towards the low energies produce ε plots with maximums on the left side. Six presented arrays of ε values serve as an input for calculation of signal-to-background ratios in following section.

6.1.2 Calculation of Signal-to-Background Ratios

Detection efficiencies ε give us very important information about capabilities of energy cut to suppress background and favour signal. Nevertheless, in order to find out what will be the real ratio between signal counts and background counts this is not yet full information. For a given process, number of observed counts with exposure am_st depends not only on ε but also on a half life $T_{1/2}$ of the process. This becomes clear if we invert Equation B.8:

$$n = ln(2)\frac{N_A}{W}\varepsilon\frac{am_st}{T_{1/2}}. \tag{6.4}$$

This formula I used for estimation of expected background counts originating from $0\nu\beta\beta$ and $2\nu\beta\beta$ of ^{82}Se. Half life of $2\nu\beta\beta$ is already observed process and its half life is known. The one I used was $T^{2\nu}_{1/2} = 0.92\times10^{20}$ yr [117]. In case of $0\nu\beta\beta$, only lower limit is available, so I used value of $T^{0\nu}_{1/2} = 2.4\times10^{24}$ yr published in [118]. Furthermore, isotopical mass of ^{82}Se is W = 81.92 g/mol. Exposure am_st was variable and is discussed later.

In case of ^{208}Tl and ^{214}Bi decays, the approach is bit different. These two processes are standard backgrounds for observation of $0\nu\beta\beta$. These isotopes can be found directly in source foil and, therefore, it is important to suppress their presence. The radiopurity of material is expressed typically in terms of activity (A) per kilogram of source foil. The total observed counts from such decay (assuming that the activity does not change with time) can be calculated following way:

$$n = \varepsilon A a m_s t. \tag{6.5}$$

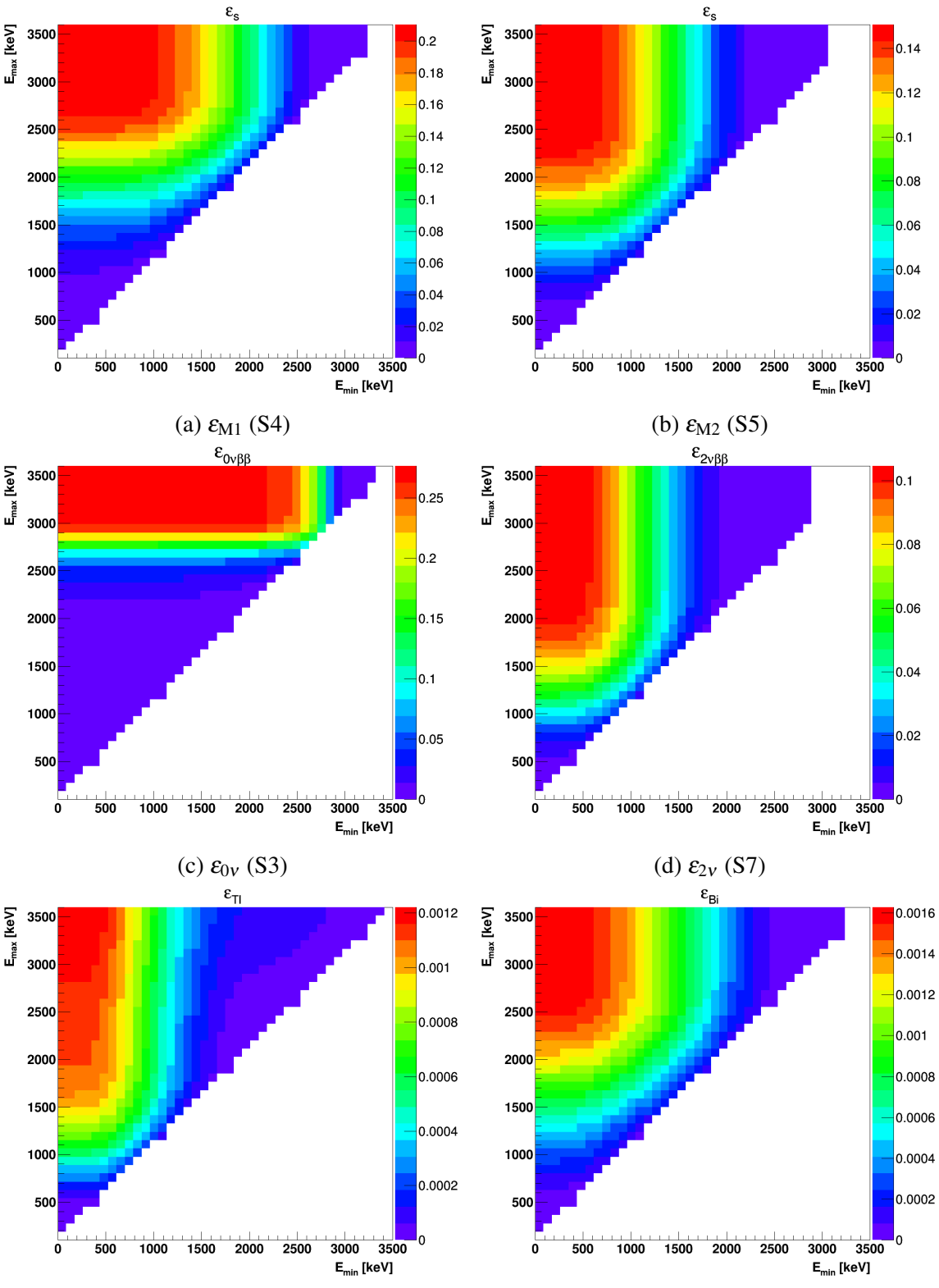

(a) ε_{M1} (S4)

(b) ε_{M2} (S5)

(c) $\varepsilon_{0\nu}$ (S3)

(d) $\varepsilon_{2\nu}$ (S7)

(e) ε_{Tl} (S9)

(f) ε_{Bi} (S10)

Figure 6.2: Detection efficiencies of six processes for different energy intervals obtained by simulation.

Goal of SuperNEMO is to keep the activities of ^{208}Tl and ^{214}Bi below 2 μBq/kg and 10 μBq/kg, respectively. In order to discuss the contribution of ^{208}Tl and ^{214}Bi on choice of ROI with the best signal-to-background ratio I performed studies of 4 (extreme) scenarios when activities A_{Tl} and A_{Bi} had all possible combinations of values 0 and 300 μBq/kg.

Calculation of background counts is simple summation through all the sources, i.e. $2\nu\beta\beta$, $0\nu\beta\beta$ and decays of ^{208}Tl and ^{214}Bi. If we want to evaluate ratio of signal and background counts we need to provide also number of counts produced by $0\nu\beta\beta\chi^0$ ($0\nu\beta\beta\chi^0\chi^0$). One of the possibilities would be to take advantage of half life limit given for both processes. However, this is not necessary. In the analysis, we need to find the most suitable energy ROI which would maximize the signal to background ratio r. We need to compare r for different scenarios, however, we are not interested in its value in absolute terms. The half life of the signal process does not make a difference in the study. Therefore, I decided to express the number of counts in terms of Equation 6.5. The frequency of occurence of both decay channels $0\nu\beta\beta\chi^0$ and $0\nu\beta\beta\chi^0\chi^0$ I express via activities $A_1 = A_2 = 1000$ μBq/kg. Such a choice was made for esthetical reasons, in order to obtain signal-to-background ratios in units, tens or larger orders of magnitude.

Finally, if we combine all the signal and background counts expressed via Equations 6.4 and 6.5 into signal-to-background ratio r, we obtain:

$$r = \frac{\varepsilon_i A_i}{ln(2)\frac{N_A}{W}\left(\frac{\varepsilon_{2\nu}}{T^{2\nu}_{1/2}} + \frac{\varepsilon_{0\nu}}{T^{0\nu}_{1/2}}\right) + \varepsilon_{Tl}A_{Tl} + \varepsilon_{Bi}A_{Bi}}. \tag{6.6}$$

Numerator stands for number of counts of $0\nu\beta\beta\chi^0$ (i = 1) or $0\nu\beta\beta\chi^0\chi^0$ (i = 2) depending on which of the two we are studying currently. Denominator combines all four sources of background. All the detection efficiencies ε depend on chosen energy cut and is provided by results in Figure 6.2.

Similarly to detection efficiencies, the signal-to-background ratio is changing as a function of chosen ROI and can be represented in form of plots similar to Figure 6.2. Figures 6.3a - 6.3d represent distributions of signal-to-background ratios for $0\nu\beta\beta\chi^0$ process for four different constellations of activities A_{Tl} and A_{Bi}. Constellation, without Bi an Tl backgrounds ($A_{Tl} = A_{Bi} = 0$ μBq/kg) in Figure 6.3a shows how $2\nu\beta\beta$ and $0\nu\beta\beta$ contribute to the distribution of signal-to-ratio plots for different ROI. Other three plots are scenarios when at least Tl or Bi background is present. The change in shape is negligible, which implies that either $2\nu\beta\beta$ or $0\nu\beta\beta$ is a major contribution for background for $0\nu\beta\beta\chi^0$. The situation is clarified in Figure 6.3e. It contains spectra of $0\nu\beta\beta\chi^0$ in comparison to all relevant backgrounds in SuperNEMO after experiment would run for half a year observing 7 kg of ^{82}Se. The spectrum assumes scenario of $A_{Tl} = A_{Bi} = 300$ μBq/kg. Red dashed line represent sum of all backgrounds while blue dashed line the spectrum of $0\nu\beta\beta\chi^0$. It is obvious, that in energies below 2500 keV $2\nu\beta\beta$ is hugely dominating. Above this value, in region of signal's peak, $2\nu\beta\beta$ spectrum dramatically drops and we can observe contributions of roughly the same order of magnitude from $0\nu\beta\beta$, Bi and Tl. Nevertheless, activity values of Bi and Tl are very extreme, exceeding the SuperNEMO design values tens up to hundred of times. In standard situation, therefore, the most important background contribution around peak of $0\nu\beta\beta\chi^0$ comes from $0\nu\beta\beta$. Regardless of the activities of Tl or Bi the ROI in all scenarios is interval (2600 keV, 2700 keV). This is the interval with the highest chance to observe the decay if it exists.

Analogical signal-to-background ratio plots but for $0\nu\beta\beta\chi^0\chi^0$ can be found in Figures 6.4a - 6.4d. Background scenarios remained exactly the same. It is possible to notice roughly

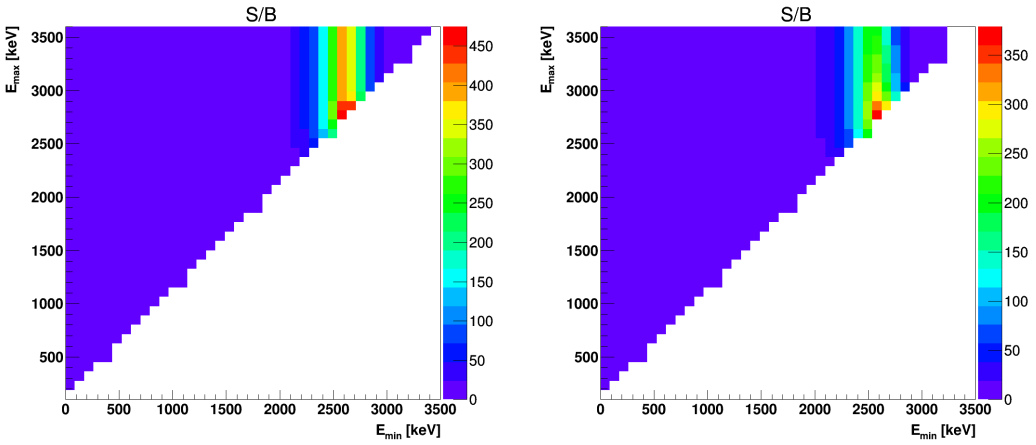

(a) $A_{Bi} = 0$, $A_{Tl} = 0$

(b) $A_{Bi} = 0$, $A_{Tl} = 300$

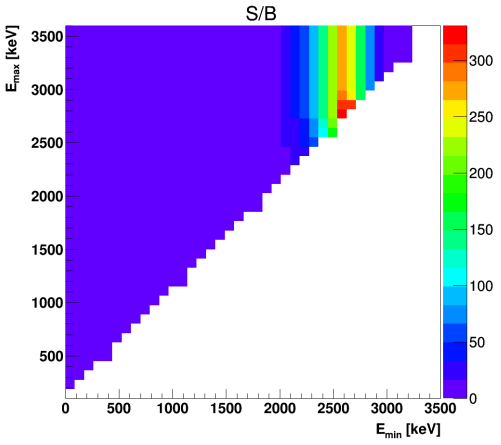

(c) $A_{Bi} = 300$, $A_{Tl} = 0$

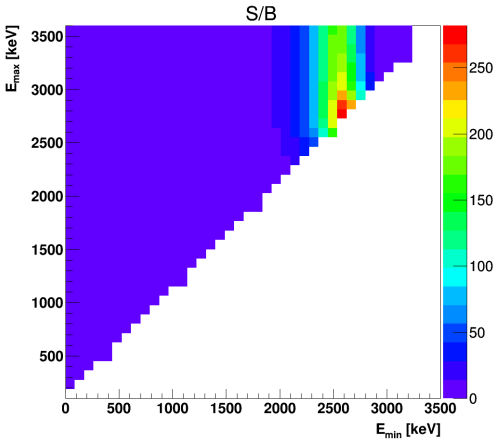

(d) $A_{Bi} = 300$, $A_{Tl} = 300$

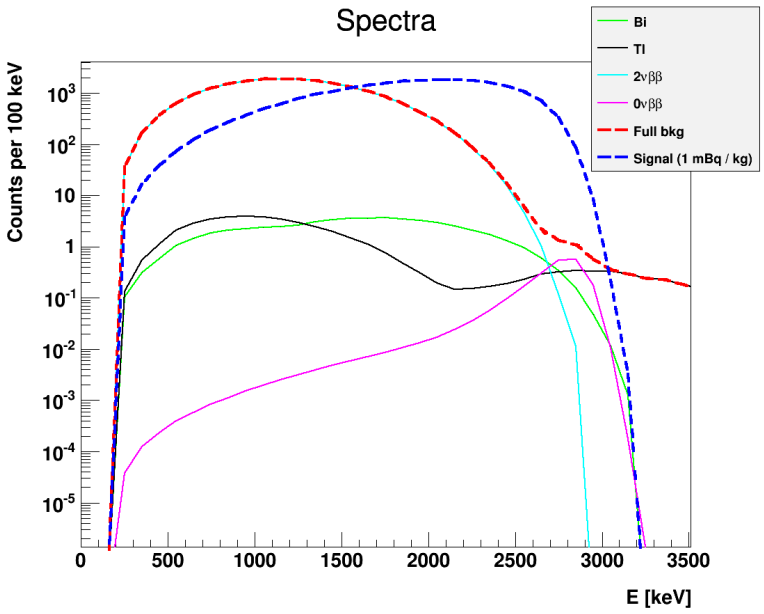

(e) Spectrum of $0\nu\beta\beta\chi^0$ vs. backgrounds.

Figure 6.3: Expected signal ($0\nu\beta\beta\chi^0$) to background ratio (a-d) as a function of chosen energy interval. Figure e) represents a energy spectra of $0\nu\beta\beta\chi^0$ and all the background processes. Red dashed line represents sum of all background contributions while blue dashed line represents spectrum of $0\nu\beta\beta\chi^0$. Spectrum generated for exposure of 3.5 kg·yr. A_{Tl} and A_{Bi} in captions are expressed in μBq/kg.

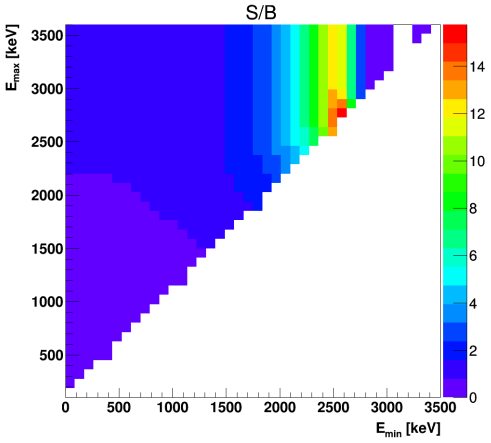

(a) $A_{Bi} = 0$, $A_{Tl} = 0$

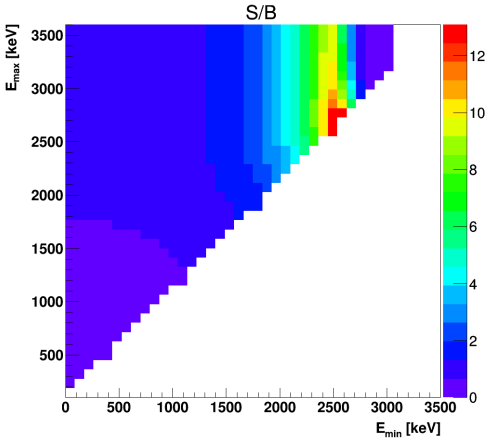

(b) $A_{Bi} = 0$, $A_{Tl} = 300$

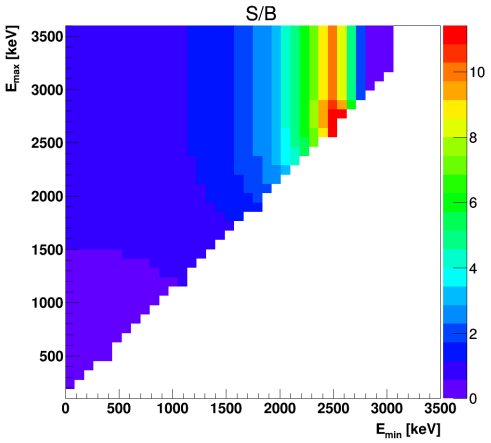

(c) $A_{Bi} = 300$, $A_{Tl} = 0$

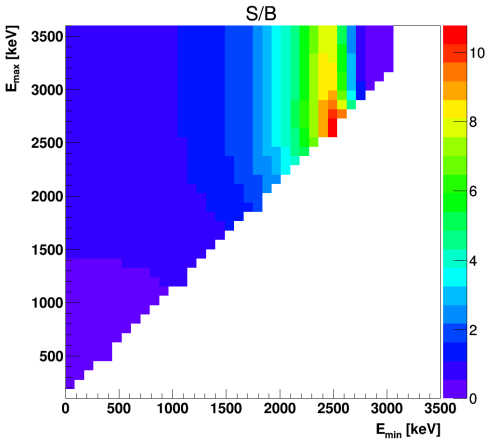

(d) $A_{Bi} = 300$, $A_{Tl} = 300$

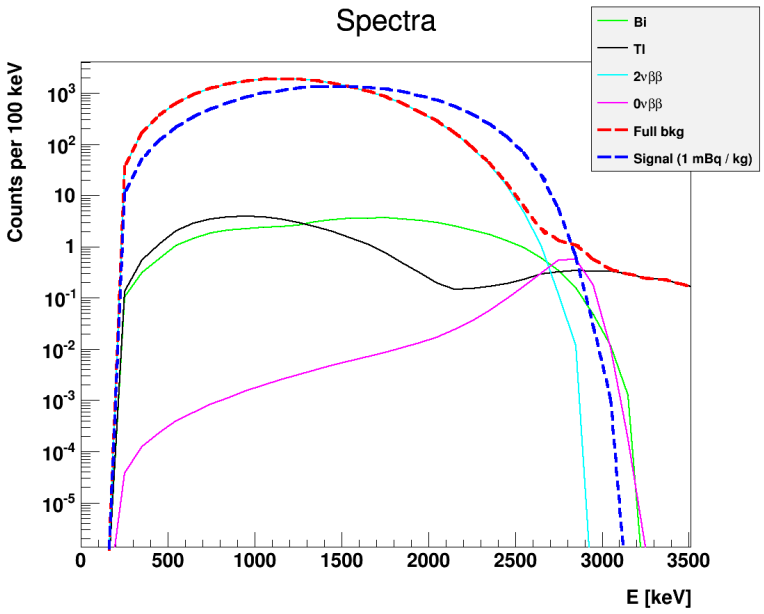

(e) Spectrum of $0\nu\beta\beta\chi^0\chi^0$ vs. backgrounds.

Figure 6.4: Expected signal ($0\nu\beta\beta\chi^0\chi^0$) to background ratio (a-d) as a function of chosen energy interval. Figure e) represents a energy spectra of $0\nu\beta\beta\chi^0\chi^0$ and all the background processes. Red dashed line represents sum of all background contributions while blue dashed line represents spectrum of $0\nu\beta\beta\chi^0\chi^0$. Spectrum generated for exposure of 3.5 kg·yr. A_{Tl} and A_{Bi} in captions are expressed in μBq/kg.

forty-fold drop in r in the hot spots (peak value) in comparison to scenarios with $0\nu\beta\beta\chi^0$. The reason is clear if we compare Figure 6.3e with 6.4e. Background spectra in both plots are generated under exactly the same conditions ($A_{Tl} = A_{Bi} = 300$ μBq/kg, t = 0.5 yr, exposure 7 kg), however, the shape of the signal (blue dashed line) changed. Peak of spectrum of $0\nu\beta\beta\chi^0\chi^0$ is shifted to the lower energies relatively to $0\nu\beta\beta\chi^0$. This region is strongly dominated by spectrum $2\nu\beta\beta$ causing dramatic drop in signal-to-background ratio. It is much more difficult to distinguish $0\nu\beta\beta\chi^0\chi^0$ from $2\nu\beta\beta$ than it was in case of $0\nu\beta\beta\chi^0$. We should, therefore, expect much lower sensitivity values for $0\nu\beta\beta\chi^0\chi^0$ than for $0\nu\beta\beta\chi^0$. ROI with the best signal-to-background ratio and, therefore, the best region to search for the decay was similarly to $0\nu\beta\beta\chi^0$ computed as (2600 keV, 2700 keV).

6.1.3 Sensitivity Results

Signal-to-background ratio plots presented in previous section are crucial inputs in order to find the energy cut with the best chance for observation of $0\nu\beta\beta\chi^0$ or $0\nu\beta\beta\chi^0\chi^0$. The ROIs extracted in previous section are useful if we obtain significant signal over the background. Such ROI would give the observation of highest significance. In case when discovery could not be claimed, it is important to set lower limit on the decay's half-life. The best possible limit experiment can provide, however, does not necessarily have to be extracted from ROI with best signal-to-background ratio.

In what follows I will, finally, employ previously discussed Feldman-Cousins recipe in order to compute half-life limits of SuperNEMO with respect to these two processes.

The recipe takes number of expected background counts b as an input. Four contributions to $0\nu\beta\beta\chi^0$ and $0\nu\beta\beta\chi^0\chi^0$ backgrounds discussed previously produce total counts which can be calculated by following equation:

$$b = am_s t \left[ln(2)\frac{N_A}{W}\left(\frac{\varepsilon_{2\nu}}{T^{2\nu}_{1/2}} + \frac{\varepsilon_{0\nu}}{T^{0\nu}_{1/2}}\right) + \varepsilon_{Tl}A_{Tl} + \varepsilon_{Bi}A_{Bi} \right]. \tag{6.7}$$

Here, set of four ε values (detection efficiencies) are again taken from result in Figure 6.2. Half-lives of $2\nu\beta\beta$ and $0\nu\beta\beta$ were set to values of $T^{2\nu}_{1/2} = 0.92\times10^{20}$ yr [117] and $T^{0\nu}_{1/2} = 2.4\times10^{24}$ yr [118], as discussed in previous section. In all the performed calculations, the mass of the pure ^{82}Se in Selenium foils was set to m = 7 kg.

Number of background counts is the only input for Feldman-Cousins recipe. For each value of expected background one obtains upper values of expected signal counts μ_U. Relationship of expected background counts and limit given by the recipe can be found in Figure 6.5.

Green and purple dots represent the values which I obtained after I implemented the recipe for 90% and 95 % CL, respectively. I performed calculations for range of (non-equidistant) values up to b = 276.6. Under 276.6, each upper limit was extracted by interpolation between two closest calculated values. For higher values than b = 276.6 I extrapolated the function by using:

$$\mu_U = \alpha\sqrt{b}. \tag{6.8}$$

For 90% CL, I used function where $\alpha = 1.81$ and for 95% CL, I used function where $\alpha = 2.13$. The two extrapolation functions are also shown in Figure 6.5 as red and yellow dashed lines. We can observe that in the region b = (120, 276.6) these extrapolation functions overlap very precisely with the values obtained by Feldman-Cousins calculation. Furthermore, the choice of extrapolation was not based only on the similarity with performed calculated green and

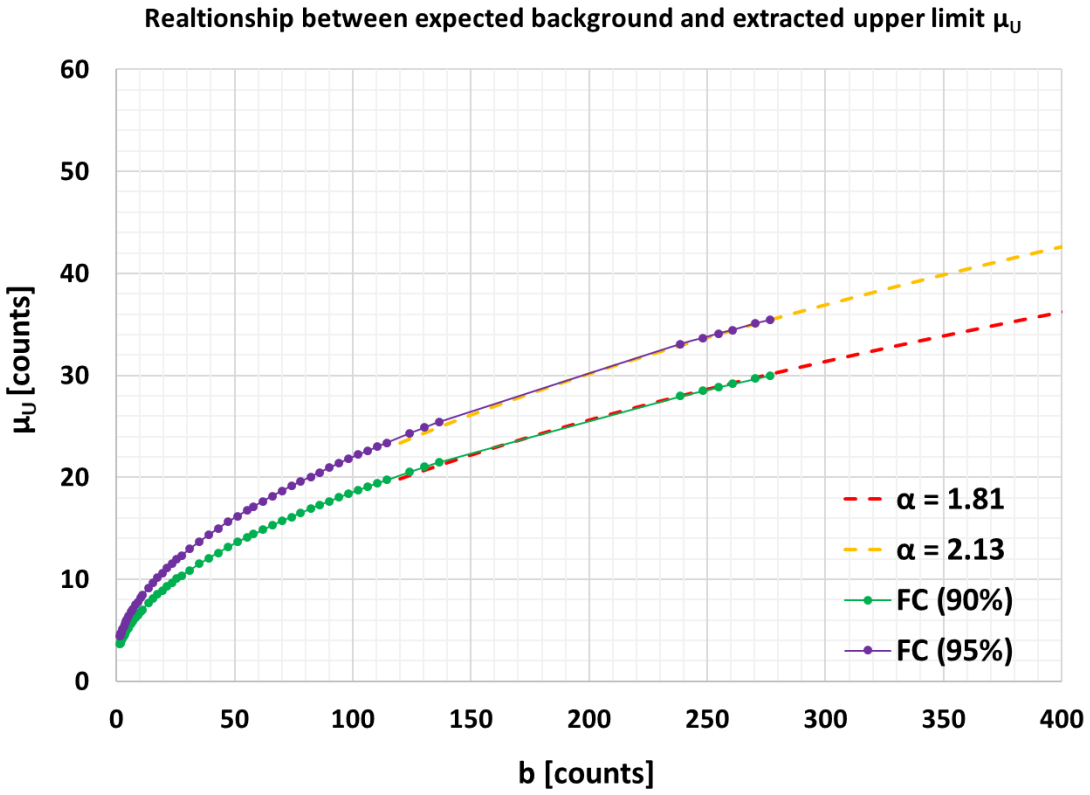

Figure 6.5: Plot showing relationship between expected number of background counts and upper limit on signal counts resulting from two different approaches. The details are commented in the text.

purple functions. For given number of background counts, the statistical fluctuations can be described by Poisson distribution. However, as we reach higher values, the distribution starts to resemble Gaussian bell. Expected fluctuations of background on a level of one standard deviation is simply given by $\sqrt{b}$ in such case. This represents notoriously known CL of 68.27%. For 90% CL we need 1.64 standard deviations (i.e. $1.64\sqrt{b}$) and for 95% CL we need 1.96 standard deviations ($1.96\sqrt{b}$). Such and approach to calculation of half-life limit was already presented in Equation 1.24 without further discussion.

I can conclude, that my extrapolation curves follow this trend. Instead of obtaining $\alpha = 1.64$ for 90% CL and $\alpha = 1.96$ for 95% CL, I received little higher factors of $\alpha = 1.81$ and $\alpha = 2.13$, respectively. This is not a fault, it is acceptable result coming from conservatism introduced in several steps of the Feldman-Cousins recipe. Obtained limit is slightly overestimated which result into little lower half-life limits. It is an acceptable effect.

After the number of background counts was calculated, functions from Figure 6.5 were used to extract the limit. Last necessary input for the calculation was the Tl and Bi activities. Studies were performed for various scenarios of different Tl and Bi activities and lengths of measurement. These values are explicitly noted in each plot. Background spectrum for both studied processes with Majoron(s) is mainly dominated by $2\nu\beta\beta$. In order to observe effect of presence of Tl and Bi, several scenarios were studied. The most extreme cases assumed up to 20 times higher Bi activity and 50 times higher Tl activity in comparison to design goal of SuperNEMO ($A_{Tl} < 2\ \mu$Bq/kg, $A_{Bi} < 10\ \mu$Bq/kg).

Half-life limit was always computed based on μ_U extracted from plot in Figure 6.5. Afterwards, μ_U was plugged into Equation B.15. The limit was obtained for same set of

ROI[1] as it was previously performed with detection efficiencies ε. In each case, the result from ROI with the highest limit was chosen and plotted. Results were produced for both 90% and 95% CL using my own code fully implementing every detail of the calculation.

Figures 6.6 represent half-life limits achievable for $0\nu\beta\beta\chi^0$ after 0.5, 1, 2, 5, 10 or 15 years. Plots are showing the decrease of achievable limit with raising activity of Bi. Red scenario always represent situation with no background from Tl and green one with A_{Tl} = 100 μBq/kg (50 times larger than expected in SuperNEMO).

Sensitivity to $0\nu\beta\beta\chi^0$ starts at a level of 5.67×10^{22} yr (90% CL) for an extreme case scenario A_{Tl} = 100 μBq/kg A_{Bi} = 200 μBq/kg only after a half year of measurement (exposure of 3.5 kg·yr). This value is already almost four times larger than value 1.5×10^{22} yr (90% CL) published by previous NEMO-3 result in [116]. In some of the plots it is possible to observe non-linear behaviour of the limit as a function of Bi background. This is usually due to change of ROI between two points. ROI containing the highest half-life limit is represented by cell colour in Tables C.1 and C.2 in Appendix C. The tables contain all the values plotted in Figures 6.6.

Figure 6.7a shows potential of improvement of the half-life limit as a function of measurement time for both CL and the most extreme scenarios (background-less and scenario with the most extreme Bi and Tl background). We can observe that the limit can overpass value of 10^{23} yr (90% CL) in less than 1.5 years which represents almost one order of magnitude improvement in comparison to NEMO-3 result.

While for $0\nu\beta\beta\chi^0$ six different ROI were offering the best half-life limit in dependence on time of measure, CL and activities of Bi and Tl in case of $0\nu\beta\beta\chi^0\chi^0$ situation was very different. ROI yielding the best half-life limit for this process was always (1000 keV, 2900 keV) due to different spectral shape, shifted to low energies relatively to $0\nu\beta\beta\chi^0$. In this ROI, Bi and Tl contamination contributed negligibly (compared to largely dominating $2\nu\beta\beta$) to the background and the resulting limits remained almost unchanged even for extreme values[2] of Bi and Tl contamination. Therefore, the calculation was performed only for one scenario - the scenario assuming the SuperNEMO design contamination limits of $A_{Bi} = 10\mu$Bq/kg and $A_{Tl} = 2\mu$Bq/kg.

The results for CL = 90% and CL = 95% are plotted in Figure 6.7b. We can observe that the limit 3.1×10^{21} yr (90% CL) on $0\nu\beta\beta\chi^0\chi^0$ from [116] obtained by NEMO-3 should be improved even faster than the one for $0\nu\beta\beta\chi^0$. In Table C.4 in Appendix C we can find that this limit should be improved after less than 0.1 yr and improved by one order of magnitude after less than 4.5 yr!

Note that, the ideal scenario (no Tl or Bi background), is much closer to expected Tl and Bi activities than any of the other scenarios, as the expected SuperNEMO design activities of Tl and Bi are on the level of $A_{Tl} < 2$ μBq/kg, $A_{Bi} < 10$ μBq/kg. The ideal scenario can be, therefore, considered with a good approximation as a reliable estimation. However, in both cases also the realistic scenarios are computed as well.

6.2 Conclusions

The goal of chapter was to discuss the methodology of half-life limit calculations for rare processes and to apply them in order to estimate expected sensitivities which could be

[1] It was combination of all different possible lower and upper boundaries on interval 0 keV - 3600 keV with step of 100 keV.

[2] Hundreds of times higher than SuperNEMO design values.

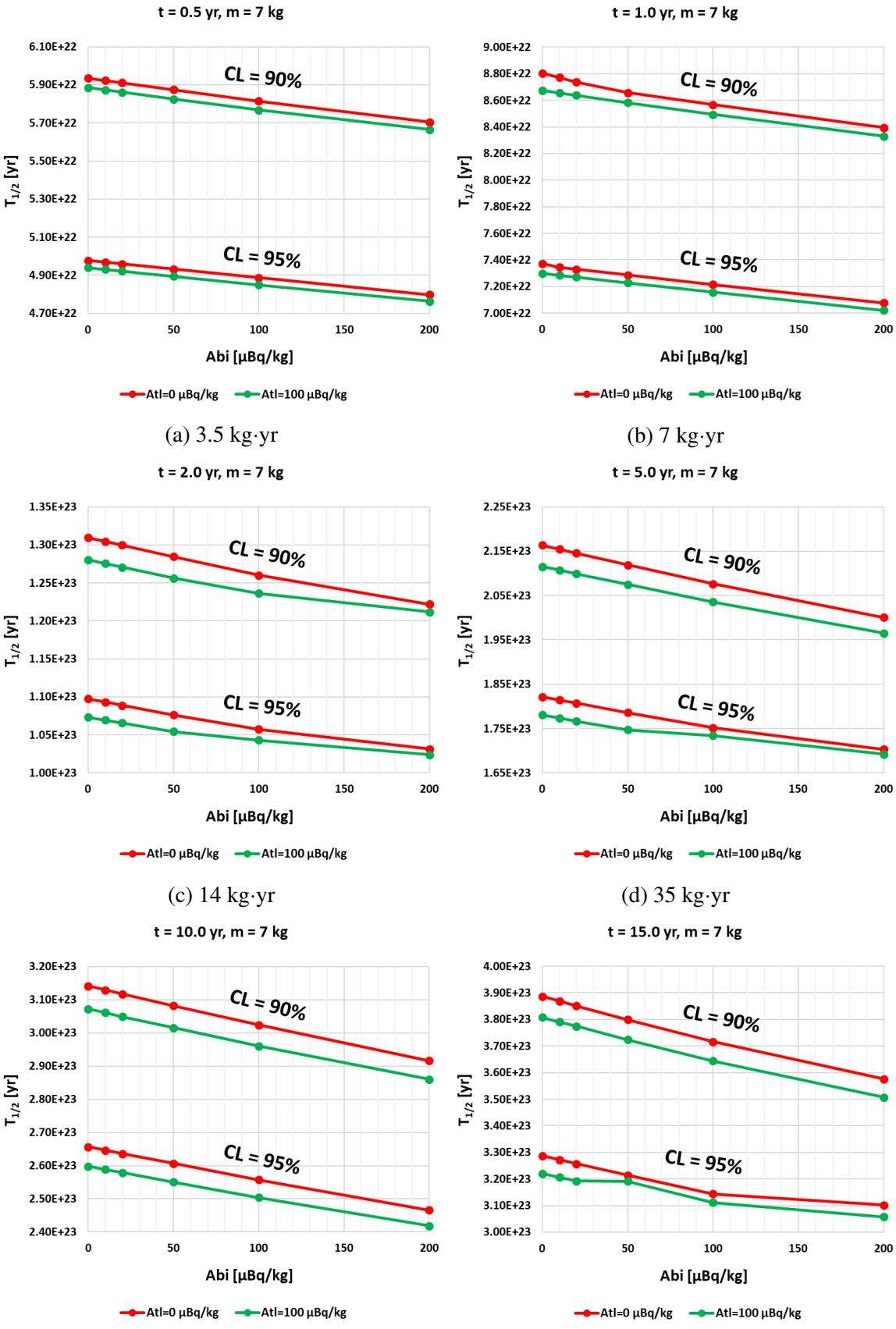

(a) 3.5 kg·yr

(b) 7 kg·yr

(c) 14 kg·yr

(d) 35 kg·yr

(e) 70 kg·yr

(f) 105 kg·yr

Figure 6.6: Plots of half life limits calculated for different exposures confidence levels and Bi and Tl background activities. Half life limits calculated for $0\nu\beta\beta\chi^0$.

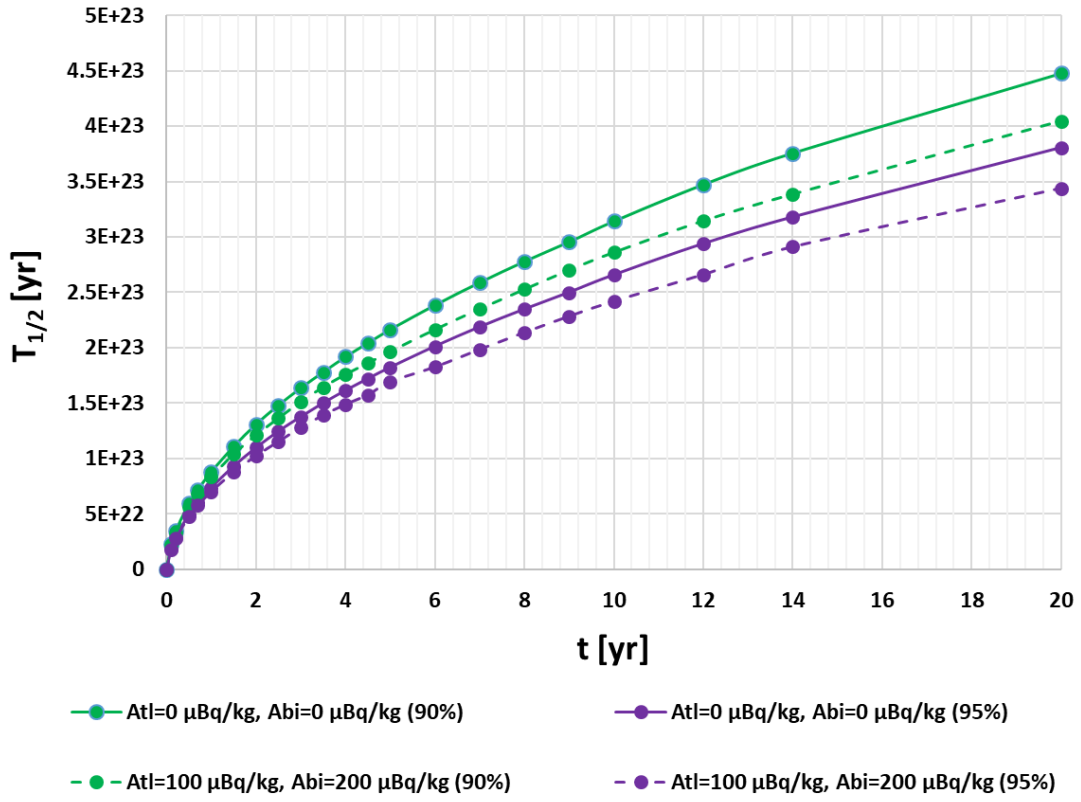

(a) $0\nu\beta\beta\chi^0$

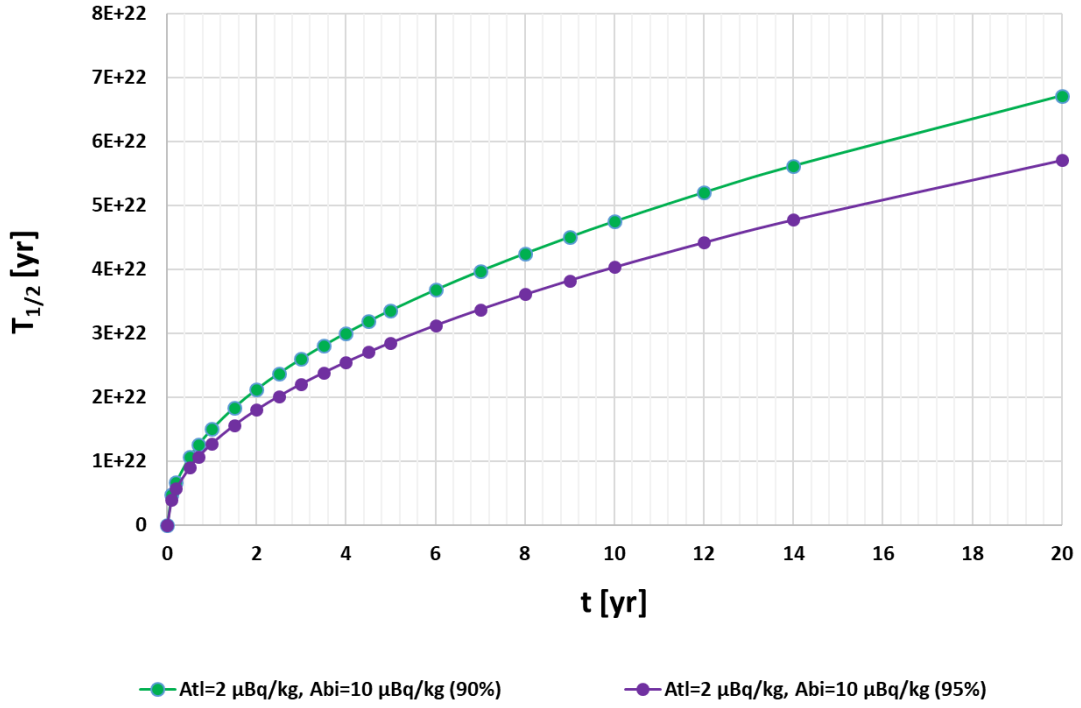

(b) $0\nu\beta\beta\chi^0\chi^0$

Figure 6.7: Plots of half life limit as a function of SuperNEMO measurement time for the worst case scenario and ideal case scenario on two different confidence levels.

reached by SuperNEMO for $0\nu\beta\beta\chi^0$ and $0\nu\beta\beta\chi^0\chi^0$.

I have shown a methodology to calculate sensitivities of rare decays using Feldman-Cousins. I profited from estimation of detection efficiencies and signal-to-background ratios using simulation in Falaise (software package for simulations of SuperNEMO module). The results led to choice of energy interval (2600 keV, 2700 keV) as a ROI with the best signal-to-background ratio for both $0\nu\beta\beta\chi^0$ and $0\nu\beta\beta\chi^0\chi^0$. Expected sensitivities were calculated for both processes for different exposures, background activities of Tl and Bi and different CL. Results presented in Figures 6.6 and 6.7 have shown that the major improvement of half life limit for both the processes can be expected already after few months even in the worst case scenario.

Summary

Proof of existence of $0\nu\beta\beta$ decay would without doubt represent very important sought step beyond the physics of Standard Model. Such a discovery would also represent a large development in nuclear theory, especially in calculation of nuclear matrix elements. Period of 2020-2030 will be a decade of astonishing ton scale experiments in the field of $0\nu\beta\beta$. It gives a possibility to probe its half-life up to 10^{28} years and effective neutrino mass down to few meV in dependence on the nuclear matrix elements calculations.

Presented thesis contributed to these efforts by variety of different results. At the end of 2016, it was possible to finish construction of main calorimeters in LSM with my contribution to the assembly process and quality testing of optical modules.

Mapping measurements of ^{207}Bi calibration sources helped to reject the possibility of the accidental deposition of ^{207}Bi outside of the mylar foil, in the Copper source frame. The Copper frame in such case would be an obstacle for the electrons on their flight to the calorimeter in calibration. Frame would reduce their energy which would lead to imprecisions in energy calibration. All controlled sources were from this point of view without problems. Thanks to the study, it was also possible to choose sources with the ^{207}Bi droplet deposited very close (within one millimeter) from the center of the frame. Furthermore, the precise knowledge of exact source positions (along with the introduction of positioning conventions) serves as an input for precise simulations of calibration system. On the other side, the relative activity measurements helped to rank the sources and subsequently distribute them in the demonstrator in order to optimize homogeneity of exposure of the calorimetric walls during calibration. Absolute activity measurements provide information helpful for decision on duration of calibration. What is the most important, in NEMO-3 the activities of calibration sources were known with a 5% precision. This uncertainty is the main contributor to the final uncertainty on the half-life of $2\nu\beta\beta$. After the refinement of uncertainties presented in the chapter about activity measurements, the uncertainty of half-life of $2\nu\beta\beta$ could be reduced not only for future SuperNEMO results but after recalculation also for results given by NEMO-3, because the sources were used for its calibration.

Vertex reconstruction precision study has shown a strong dependence of precision on single energies of emitted electrons. On the other side, the effect of magnetic field seems to be rather negligible. It was also shown that the vertex precision gets significantly worse if one of the electron escapes the source foil in parallel. The effect of cell sharing was identified in the results. This effect degrades the vertex precision of events with electrons emitted to the same side of the source foil. Finally, it was shown that if we accept events detected by side (xcalo) calorimeter, it might cause inhomogeneity in the distribution of the reconstructed vertices on the source foil. Such and effect would not be observed without presence of mag-

netic field. These valuable guidelines will be used for the choice of proper data cuts after SuperNEMO will begin its data taking period. It will result in the reduction of systematic uncertainties of electron tracking. In final result it will help to clarify whether discrepancies between expected results in electron angular distributions are sign of new physics or systematic effect.

Studies of neutron shielding represent twofold contribution. Firstly, it is a first estimation of the quality of shielding in design phase. It was possible to conclude that the polyethylene is a material of preference. Furthermore, it was shown that the parts of detector made of Iron will represent the major contribution to all the gamma radiation produced by neutron capture inside of the shielding. Software for all these tasks was developed and is routinely used. Secondly, the presented neutron simulations contributed to more general question of neutron generators. Problem of the proper generation of gammas from thermal neutron capture was addressed and demonstrated. Theoretical basis for new approach to generation of neutron captures was presented and demonstrated on illustrative example.

In the last chapter discussion of half-life limits of $0\nu\beta\beta$ mode with Majoron emission took place. The best ROI for observation of both types of $0\nu\beta\beta$ with Majoron emission (with one and also two Majorons) was shown to be (2600 keV, 2700 keV) in the case when the decay would be observed. In case if SuperNEMO demonstrator would not observe the decay, it was shown, that limits on both the decay channels obtained by NEMO-3 could be improved within few months or less. Within up to 5 years of measurement one can expect the improvement of both results by at least one order of magnitude.

After several years of preparation, next year, 2019, SuperNEMO demonstrator enters the well deserved phase of data taking. No one can predict whether the $0\nu\beta\beta$ will be observed or not, but finally, it is clear that SuperNEMO detector will once again push the limits of our knowledge closer to new discoveries. After all, who knows what will be the next big discovery in neutrino physics?

Bibliography

[1] Becquerel, H., Comptes-rendus de l'Académie des sciences, séance du 24 février 1896 (in French) (1896) 420.

[2] Becquerel, H., Comptes-rendus de l'Académie des sciences, séance du séance du 1er mars 1896 (in French) (1896) 501.

[3] Chadwick, J., Verhandlungen der Deutschen Physikalischen Gesellschaft (in German) (1914) 383.

[4] and, Proceedings of the Royal Society of London A: Mathematical, Physical and Engineering Sciences **141** (1933) 502.

[5] Pauli, W., letter to the nuclear conference in tuebingen on the 4-th of december, in *Pauli Archive at CERN.*, 1930.

[6] Cowan, C. L., Reines, F., Harrison, F. B., Kruse, H. W., and McGuire, A. D., Science **124** (1956) 103.

[7] Wang, K. C., Phys. Rev. **61** (1942) 97.

[8] Glashow, S. L., Nuclear Physics **22** (1961) 579 .

[9] Englert, F. and Brout, R., Phys. Rev. Lett. **13** (1964) 321.

[10] Higgs, P. W., Phys. Rev. Lett. **13** (1964) 508.

[11] Guralnik, G. S., Hagen, C. R., and Kibble, T. W. B., Phys. Rev. Lett. **13** (1964) 585.

[12] Weinberg, S., Phys. Rev. Lett. **19** (1967) 1264.

[13] Salam, A. and Svartholm, N., *Elementary particle theory: Relativistic groups and analyticity. Proccedings of the Eighth Nobel Symposium held May 19-25, 1968 at Aspenäsgarden, Lerum, in the county of Älvsborg, Sweden*, Nobel symposium, Almqvist & Wiksell, 1968.

[14] Abe, F. et al., Phys. Rev. Lett. **74** (1995) 2626.

[15] Abachi, S. et al., Phys. Rev. Lett. **74** (1995) 2422.

[16] Kodama, K. et al., Physics Letters B **504** (2001) 218 .

[17] Aad, G. et al., Physics Letters B **716** (2012) 1 .

[18] Chatrchyan, S. et al., Physics Letters B **716** (2012) 30 .

[19] Ahmad, Q. R. et al., Phys. Rev. Lett. **87** (2001) 071301.

[20] Danby, G. et al., Phys. Rev. Lett. **9** (1962) 36.

[21] Anicin, I. V., ArXiv Physics e-prints (2005).

[22] Perl, M. L. et al., Phys. Rev. Lett. **35** (1975) 1489.

[23] Aartsen, M. G. et al., Phys. Rev. Lett. **117** (2016) 071801.

[24] Katz, U. and Spiering, C., Progress in Particle and Nuclear Physics **67** (2012) 651 .

[25] Salaris, M. and Cassisi, S., *Evolution of Stars and Stellar Populations*, Wiley, 2005.

[26] Cleveland, B. T. et al., The Astrophysical Journal **496** (1998) 505.

[27] Inoue, K., Nuclear Physics B - Proceedings Supplements **59** (1997) 267 , Proceedings of the Fourth KEK Topical Confernce on Flavor Physics.

[28] Abdurashitov, J. N. et al., Phys. Rev. C **80** (2009) 015807.

[29] Cribier, M. et al., Nuclear Physics B - Proceedings Supplements **70** (1999) 284 , Proceedings of the Fifth International Workshop on topics in Astroparticle and Underground Physics.

[30] Gribov, V. and Pontecorvo, B., Physics Letters B **28** (1969) 493 .

[31] Pontecorvo, B., Sov. Phys. JETP **7** (1958) 172, [Zh. Eksp. Teor. Fiz.34,247(1957)].

[32] Maki, Z., Nakagawa, M., and Sakata, S., Progress of Theoretical Physics **28** (1962) 870.

[33] Fukuda, Y. et al., Phys. Rev. Lett. **81** (1998) 1562.

[34] Mikheyev, S. P. and Smirnov, A. Y., Yadernaya Fizika **42** (1985) 1441.

[35] West, R. M., Lauberts, A., Jorgensen, H. E., and Schuster, H. E., Astronomy and Astrophysics **177** (1987) L1.

[36] Podsiadlowski, P., Publications of the Astronomical Society of the Pacific **104** (1992) 717.

[37] Hirata, K. et al., Phys. Rev. Lett. **58** (1987) 1490.

[38] Haines, T. et al., Nuclear Instruments and Methods in Physics Research Section A: Accelerators, Spectrometers, Detectors and Associated Equipment **264** (1988) 28 .

[39] Alexeyev, E., Alexeyeva, L., Krivosheina, I., and Volchenko, V., Physics Letters B **205** (1988) 209 .

[40] Arnett, W. D., Bahcall, J. N., Kirshner, R. P., and Woosley, S. E., Annual Review of Astronomy and Astrophysics **27** (1989) 629.

[41] Bilenky, S. M., Giunti, C., and Grimus, W., The European Physical Journal C **1** (1998) 247.

[42] Goeppert-Mayer, M., Phys. Rev. **48** (1935) 512.

[43] Barabash, A., Physics Procedia **74** (2015) 416 , Fundamental Research in Particle Physics and Cosmophysics.

[44] National nuclear data center database, https://www.nndc.bnl.gov/chart/, 2017.

[45] Furry, W. H., Phys. Rev. **56** (1939) 1184.

[46] Caurier, E., Zuker, A. P., Poves, A., and Martínez-Pinedo, G., Phys. Rev. C **50** (1994) 225.

[47] Macko, M., QRPA with Nonlinear Phonon Operator: Can It Work?, Master's thesis, Comenius University in Bratislava, 2015.

[48] Yao, J. M., Song, L. S., Hagino, K., Ring, P., and Meng, J., Phys. Rev. C **91** (2015) 024316.

[49] Umehara, S. et al., Phys. Rev. C **78** (2008) 058501.

[50] Agostini, M., First results from gerda phase ii, Presentation at conference Neutrino 2016, 2016.

[51] Barabash, A. S., Brudanin, V. B., and NEMO Collaboration, Physics of Atomic Nuclei **74** (2011) 312.

[52] Argyriades, J. et al., Nuclear Physics A **847** (2010) 168 .

[53] Arnold, R. et al., Phys. Rev. D **92** (2015) 072011.

[54] Danevich, F. A. et al., Search for double beta decay of ^{116}Cd with enriched $^{116}CdWO_4$ crystal scintillators (Aurora experiment), in *Journal of Physics Conference Series*, volume 718 of *Journal of Physics Conference Series*, page 062009, 2016.

[55] Barabash, A., Nuclear Physics A **935** (2015) 52 .

[56] Alduino, C. et al., Phys. Rev. C **93** (2016) 045503.

[57] Gando, A. et al., Phys. Rev. Lett. **117** (2016) 082503.

[58] Arnold, R. et al., Phys. Rev. D **94** (2016) 072003.

[59] Barabash, A. S., arXiv e-prints (2017) arXiv:1702.06340.

[60] Klapdor-Kleingrothaus, H. et al., The European Physical Journal A - Hadrons and Nuclei **12** (2001) 147.

[61] Aalseth, C. E. et al., Phys. Rev. D **65** (2002) 092007.

[62] Klapdor-Kleingrothaus, H., Krivosheina, I., Dietz, A., and Chkvorets, O., Physics Letters B **586** (2004) 198 .

[63] Agostini, M. et al., Phys. Rev. Lett. **111** (2013) 122503.

[64] Agostini, M. et al., Physics Procedia **61** (2015) 828 , 13th International Conference on Topics in Astroparticle and Underground Physics, TAUP 2013.

[65] Andreotti, E. et al., Astroparticle Physics **34** (2011) 822 .

[66] Sisti, M. et al., Nuclear and Particle Physics Proceedings **273–275** (2016) 1719 , 37th International Conference on High Energy Physics (ICHEP).

[67] Beeman, J. W. et al., Adv. High Energy Phys. **2013** (2013) 237973.

[68] Albert, J. B. et al., Nature **510** (2014) 229.

[69] Gando, A. et al., Phys. Rev. Lett. **110** (2013) 062502.

[70] Mott, J., *Search for double beta decay of* ^{82}*Se with the NEMO-3 detector and development of apparatus for low-level radon measurements for the SuperNEMO experiment*, PhD thesis, University College London, 2013.

[71] Dassie, D. et al., Nuclear Instruments and Methods in Physics Research Section A: Accelerators, Spectrometers, Detectors and Associated Equipment **309** (1991) 465 .

[72] Arnold, R. et al., Nuclear Instruments and Methods in Physics Research Section A: Accelerators, Spectrometers, Detectors and Associated Equipment **354** (1995) 338 .

[73] LAL preprints **94–29** (1994).

[74] Arnold, R. et al., Nuclear Instruments and Methods in Physics Research Section A: Accelerators, Spectrometers, Detectors and Associated Equipment **536** (2005) 79 .

[75] Arnold, R. et al., Phys. Rev. D **93** (2016) 112008.

[76] Argyriades, J. et al., Nuclear Physics A **847** (2010) 168 .

[77] Simard, L. and the Nemo-3 collaboration, Journal of Physics: Conference Series **375** (2012) 042011.

[78] Arnold, R. et al., Nuclear Physics A **781** (2007) 209 .

[79] Arnold, R. et al., Phys. Rev. D **95** (2017) 012007.

[80] Arnold, R. et al., Phys. Rev. Lett. **107** (2011) 062504.

[81] Argyriades, J. et al., Phys. Rev. C **80** (2009) 032501.

[82] Arnold, R. et al., The European Physical Journal C **70** (2010) 927.

[83] Blondel, S. et al., Conseil Scientifique de l'IN2P3 (2011).

[84] Hodák, R. et al., Improvement of the energy resolution of the scintillating detectors for the low background measurement, in *American Institute of Physics Conference Series*, volume 1672 of *American Institute of Physics Conference Series*, page 130003, 2015.

[85] Marquet, C. et al., Journal of Instrumentation **10** (2015) P09008.

[86] Salazar, R. and Bryant, J., PoS **ICHEP2016** (2016) 808.

[87] Jakůbek, J., Journal of Instrumentation **4** (2009) P03013.

[88] Platkevic, M. et al., Nuclear Instruments and Methods in Physics Research Section A: Accelerators, Spectrometers, Detectors and Associated Equipment **591** (2008) 245 , Radiation Imaging Detectors 2007.

[89] Llopart, X., Ballabriga, R., Campbell, M., Tlustos, L., and Wong, W., Nuclear Instruments and Methods in Physics Research Section A: Accelerators, Spectrometers, Detectors and Associated Equipment **581** (2007) 485 , VCI 2007.

[90] Ballabriga, R., Campbell, M., and Llopart, X., Nuclear Instruments and Methods in Physics Research Section A: Accelerators, Spectrometers, Detectors and Associated Equipment **878** (2018) 10 , Radiation Imaging Techniques and Applications.

[91] Turecek, D., Jakubek, J., Kroupa, M., and Soukup, P., Energy calibration of pixel detector working in time-over-threshold mode using test pulses, in *2011 IEEE Nuclear Science Symposium Conference Record*, pages 1722–1725, 2011.

[92] Jakubek, J., Nuclear Instruments and Methods in Physics Research Section A: Accelerators, Spectrometers, Detectors and Associated Equipment **607** (2009) 192 , Radiation Imaging Detectors 2008.

[93] Jakubek, J., Nuclear Instruments and Methods in Physics Research Section A: Accelerators, Spectrometers, Detectors and Associated Equipment **633** (2011) S262 , 11th International Workshop on Radiation Imaging Detectors (IWORID).

[94] Turecek, D., Holy, T., Jakubek, J., Pospisil, S., and Vykydal, Z., Journal of Instrumentation **6** (2011) C01046.

[95] Holy, T. et al., Nuclear Instruments and Methods in Physics Research Section A: Accelerators, Spectrometers, Detectors and Associated Equipment **591** (2008) 287 , Radiation Imaging Detectors 2007.

[96] IAEA, Live chart of nuclides, https://www-nds.iaea.org/relnsd/vcharthtml/VChartHTML.html.

[97] Macko, M., Method for Evaluation of Bi-207 Radioactive Source Deposition Distribution (Article in preparation) .

[98] Blank, B. et al., Nuclear Instruments and Methods in Physics Research Section A: Accelerators, Spectrometers, Detectors and Associated Equipment **776** (2015) 34 .

[99] INTERNATIONAL ATOMIC ENERGY AGENCY, *Update of X Ray and Gamma Ray Decay Data Standards for Detector Calibration and Other Applications*, INTERNATIONAL ATOMIC ENERGY AGENCY, Vienna, 2007.

[100] Agostinelli, S. et al., Nuclear Instruments and Methods in Physics Research Section A: Accelerators, Spectrometers, Detectors and Associated Equipment **506** (2003) 250 .

[101] Allison, J. et al., IEEE Transactions on Nuclear Science **53** (2006) 270.

[102] Allison, J. et al., Nuclear Instruments and Methods in Physics Research Section A: Accelerators, Spectrometers, Detectors and Associated Equipment **835** (2016) 186 .

[103] Brun, R. and Rademakers, F., Nuclear Instruments and Methods in Physics Research Section A: Accelerators, Spectrometers, Detectors and Associated Equipment **389** (1997) 81 , New Computing Techniques in Physics Research V.

[104] Chazal, V. et al., Astroparticle Physics **9** (1998) 163 .

[105] Junde, H., Nuclear Data Sheets **109** (2008) 787 .

[106] Bhat, M., Nuclear Data Sheets **85** (1998) 415 .

[107] Singh, B., Nuclear Data Sheets **108** (2007) 197 .

[108] Browne, E. and Tuli, J., Nuclear Data Sheets **111** (2010) 1093 .

[109] Berezinsky, V. and Valle, J. W. F., Physics Letters B **318** (1993) 360.

[110] Dolgov, A. D. and Takahashi, F., ArXiv High Energy Physics - Phenomenology e-prints (2004).

[111] Kazanas, D., Mohapatra, R. N., Nasri, S., and Teplitz, V. L., Phys. Rev. D **70** (2004) 033015.

[112] Kachelriess, M., Tomàs, R., and Valle, J. W. F., Phys. Rev. D **62** (2000) 023004.

[113] Tomàs, R., Päs, H., and Valle, J. W. F., Phys. Rev. D **64** (2001) 095005.

[114] Hannestad, S., Keränen, P., and Sannino, F., Phys. Rev. D **66** (2002) 045002.

[115] Farzan, Y., Phys. Rev. D **67** (2003) 073015.

[116] Arnold, R. et al., Nuclear Physics A **765** (2006) 483.

[117] Barabash, A. S., ArXiv e-prints (2017).

[118] Azzolini, O. et al., Phys. Rev. Lett. **120** (2018) 232502.

[119] Macko, M., Acta Phys. Polon. Supp. **9** (2016) 797.

[120] Gómez-Cadenas, J. et al., Journal of Cosmology and Astroparticle Physics **2011** (2011) 007.

[121] Philosophical Transactions of the Royal Society of London A: Mathematical, Physical and Engineering Sciences **236** (1937) 333.

[122] Feldman, G. J. and Cousins, R. D., Phys. Rev. D **57** (1998) 3873.

Appendix A

Complete Results of Measurements of ^{207}Bi Calibration Sources

This appendix contains full database of all the results obtained in measurements of ^{207}Bi calibration sources in Chapter 3.

A.1 Mapping Results

In this section, I present statistics (Tables A.1 and A.2) and the final measured quantities (Tables A.3 and A.4) obtained by source mapping by pixel detectors. All the necessary information concerning the measurements and analysis can be found in Section 3.2.

M.	Detector	t_{live} [s]	N_{ROI} [cnts]	N_{TOT} [cnts]	$\frac{N_{ROI}}{N_{TOT}}$ [%]	$\frac{N_{ROI}}{t_{live}}$ [Hz]	$\frac{E_{ROI}}{t_{live}}$ [keV / s]
73	H04-W0163	5 994	49 656	114 585	43.34	8.28	92.88
74	H11-W0163	6 384	53 527	123 395	43.38	8.38	101.28
75	L05-W0163	6 392	81 876	161 538	50.69	12.81	143.86
76	H04-W0163	5 894	46 150	104 733	44.06	7.83	87.35
77	H11-W0163	5 852	51 400	118 735	43.29	8.78	106.09
78	L05-W0163	5 837	68 141	134 683	50.59	11.67	130.98
79	H04-W0163	6 074	50 034	115 418	43.35	8.24	91.72
80	H11-W0163	6 047	53 649	124 042	43.25	8.87	108.39
81	L05-W0163	6 045	76 828	151 907	50.58	12.71	142.19
82	H04-W0163	13 848	118 802	276 970	42.89	8.58	97.38
83	H11-W0163	5 836	48 506	113 138	42.87	8.31	102.19
84	L05-W0163	5 835	75 618	150 765	50.16	12.96	145.45
85	H04-W0163	6 531	55 041	126 510	43.51	8.43	95.21
86	H11-W0163	6 430	53 571	125 558	42.67	8.33	101.54
87	L05-W0163	6 427	78 772	154 925	50.85	12.26	138.21
88	H04-W0163	6 912	60 879	139 663	43.59	8.81	99.39
89	H11-W0163	6 745	59 920	141 226	42.43	8.88	109.31

Table A.1: See caption of Table A.2.

M.	Detector	t_{live} [s]	N_{ROI} [cnts]	N_{TOT} [cnts]	$\frac{N_{ROI}}{N_{TOT}}$ [%]	$\frac{N_{ROI}}{t_{live}}$ [Hz]	$\frac{E_{ROI}}{t_{live}}$ [keV / s]
90	L05-W0163	6 774	80 838	158 929	50.86	11.93	134.37
91	H04-W0163	5 540	48 098	111 111	43.29	8.68	98.68
92	H11-W0163	5 425	48 289	113 016	42.73	8.90	109.29
93	L05-W0163	5 410	65 486	129 454	50.59	12.10	135.48
94	H04-W0163	2 874	26 003	59 589	43.64	9.05	101.37
95	H11-W0163	2 809	24 183	55 942	43.23	8.61	104.32
96	L05-W0163	2 822	34 871	68 967	50.56	12.36	139.01
111	H11-W0163	13 813	125 124	288 873	43.31	9.06	110.18
112	H11-W0163	5 602	46 438	106 760	43.50	8.29	100.79
113	L05-W0163	5 605	68 085	135 183	50.37	12.15	135.97
114	H04-W0163	7 622	68 413	158 181	43.25	8.98	100.87
115	H11-W0163	7 525	71 050	163 248	43.52	9.44	113.96
116	L05-W0163	7 539	92 141	185 290	49.73	12.22	136.50
118	H04-W0163	45 816	414 630	957 375	43.31	9.05	101.76
119	H11-W0163	45 671	396 247	929 737	42.62	8.68	103.72
120	L05-W0163	45 669	552 206	1 095 402	50.41	12.09	134.99
121	H04-W0163	45 375	367 970	853 014	43.14	8.11	90.69
122	H11-W0163	44 766	404 234	941 025	42.96	9.03	111.26
123	L05-W0163	44 762	542 330	1 070 742	50.65	12.12	135.26
124	H04-W0163	43 554	390 466	904 988	43.15	8.97	101.72
125	H11-W0163	41 787	343 470	784 633	43.77	8.22	99.51
126	H04-W0163	199 776	1 474 716	3 428 264	43.02	7.38	82.38
126*	H04-W0163	166 317	1 290 921	3 038 524	42.49	7.76	86.55
127	L05-W0163	41 480	500 823	982 522	50.97	12.07	135.98
128	H04-W0163	15 920	133 303	310 626	42.91	8.37	95.11
130	H11-W0163	15 546	128 427	294 117	43.67	8.26	100.12
131	L05-W0163	15 564	183 819	365 429	50.30	11.81	133.09
132	H11-W0163	197 260	1 719 104	3 955 332	43.46	8.71	104.58
132*	H11-W0163	165 699	1 440 205	3 324 424	43.32	8.69	104.86
133	H04-W0163	34 414	310 293	724 374	42.84	9.02	101.63
135	H11-W0163	37 880	333 898	763 859	43.71	8.81	105.33
137	L05-W0163	37 579	425 656	839 072	50.73	11.33	127.27
138	L05-W0163	13 224	159 769	318 364	50.18	12.08	137.11
139	L05-W0163	197 151	2 342 662	4 723 626	49.59	11.88	133.00
139*	L05-W0163	165 604	1 965 319	3 973 773	49.46	11.87	133.82

Table A.2: Statistics of all performed ^{207}Bi deposition distribution measurements. M. in the first column stands for number of measured source. N_{ROI} stands for number of counts in ROI during measurement, N_{TOT} number of all measured counts and E_{ROI} represents energy integrated in ROI during the measurement. Rows with asterisk denote repeated measurement under same experimental conditions. Type of the source (with or without plastic envelope) can be extracted from second column of Tables A.3 and A.4.

M.	Position	x_0 [mm]	y_0 [mm]	HWHM [mm]	$x_0 - C_X$ [mm]	$y_0 - C_Y$ [mm]	p_x [1]	p_y [1]	r [mm]
73	US	5.31	4.56	2.06	0.12	0.41	0.03	0.06	0.42
74	US	5.79	4.09	2.18	0.60	-0.10	0.15	-0.02	0.61
75	US	5.19	4.85	1.83	-0.26	0.44	-0.06	0.07	0.51
76	US	5.35	4.31	2.51	0.16	0.15	0.04	0.02	0.22
77	US	5.03	4.74	2.01	-0.16	0.55	-0.04	0.08	0.57
78	US	5.66	4.71	2.11	0.21	0.29	0.05	0.05	0.36
79	US	5.03	5.39	2.14	-0.16	1.23	-0.04	0.19	1.24
80	US	5.42	4.27	2.21	0.22	0.08	0.06	0.01	0.24
81	US	5.49	4.19	1.90	0.04	-0.23	0.01	-0.03	0.23
82	US	4.75	4.72	2.26	-0.44	0.57	-0.11	0.09	0.72
83	US	5.47	4.23	2.48	0.27	0.04	0.07	0.01	0.28
84	US	5.79	5.00	1.85	0.34	0.58	0.09	0.09	0.67
85	US	5.49	4.41	2.23	0.30	0.25	0.08	0.04	0.39
86	US	5.04	4.72	2.15	-0.16	0.53	-0.04	0.08	0.56
87	US	5.54	4.79	1.92	0.09	0.37	0.02	0.06	0.38
88	US	5.78	4.38	2.19	0.59	0.23	0.15	0.03	0.63
89	US	5.36	5.00	2.11	0.17	0.81	0.04	0.12	0.82
90	US	4.95	4.57	1.88	-0.50	0.15	-0.13	0.02	0.53
91	US	5.28	4.42	2.13	0.09	0.26	0.02	0.04	0.28
92	US	5.36	4.88	2.14	0.16	0.69	0.04	0.11	0.71
93	US	4.94	4.99	1.97	-0.51	0.57	-0.13	0.09	0.76
94	US	4.84	4.78	2.15	-0.35	0.62	-0.09	0.10	0.71
95	US	5.14	4.31	2.09	-0.05	0.12	-0.01	0.02	0.13
96	US	5.28	4.29	1.89	-0.17	-0.13	-0.04	-0.02	0.21
111	WO-DU	4.61	6.97	2.09	0.37	0.25	0.09	0.04	0.44
112	WO-DU	4.67	6.74	2.09	0.43	0.03	0.11	0.00	0.43
113	WO-DU	4.80	6.95	1.79	0.28	0.00	0.07	0.00	0.28
114	WO-DU	4.73	6.97	2.03	0.49	0.29	0.12	0.04	0.57
115	WO-DU	4.73	6.84	2.21	0.49	0.12	0.12	0.02	0.51
116	WO-DU	4.59	7.14	1.62	0.07	0.19	0.02	0.03	0.20
118	WO-DU	5.05	6.84	2.05	0.81	0.15	0.20	0.02	0.82
119	WO-DU	3.45	7.22	1.71	-0.79	0.51	-0.20	0.08	0.93
120	WO-DU	4.52	7.36	1.79	0.00	0.41	0.00	0.06	0.41
121	WO-DU	4.84	7.54	2.07	0.60	0.85	0.15	0.13	1.04
122	WO-DU	4.37	7.55	2.09	0.13	0.83	0.03	0.13	0.84
123	WO-DU	4.72	7.42	1.80	0.20	0.47	0.05	0.07	0.51
124	WO-DU	5.14	7.48	2.06	0.90	0.79	0.22	0.12	1.20
125	WO-DU	4.48	7.57	2.06	0.24	0.85	0.06	0.13	0.89
126	WO-DU	3.02	6.79	2.44	-1.22	0.11	-0.31	0.02	1.23
126*	WO-DU	3.00	7.01	2.14	-1.24	0.33	-0.31	0.05	1.28
127	WO-DU	3.91	6.91	1.94	-0.61	-0.03	-0.15	-0.01	0.61
128	WO-DU	3.86	7.42	2.08	-0.39	0.73	-0.10	0.11	0.83
130	WO-DU	3.32	10.17	2.63	-0.91	3.45	-0.23	0.53	3.57

Table A.3: See caption of Table A.4.

M.	Position	x_0 [mm]	y_0 [mm]	HWHM [mm]	$x_0 - C_X$ [mm]	$y_0 - C_Y$ [mm]	p_x [1]	p_y [1]	r [mm]
131	WO-DU	4.08	6.81	1.85	-0.44	-0.14	-0.11	-0.02	0.46
132	WO-DU	3.99	7.29	1.96	-0.25	0.57	-0.06	0.09	0.62
132*	WO-DU	3.94	7.46	1.95	-0.29	0.74	-0.07	0.11	0.79
133	WO-DU	4.10	6.20	2.03	-0.14	-0.49	-0.04	-0.08	0.51
135	WO-DU	4.40	7.18	2.03	0.16	0.46	0.04	0.07	0.48
137	WO-DU	4.25	7.29	1.81	-0.27	0.35	-0.07	0.05	0.44
138	WO-DU	4.52	7.16	1.79	0.00	0.22	0.00	0.03	0.22
139	WO-DU	4.50	6.88	1.61	-0.02	-0.07	0.00	-0.01	0.07
139*	WO-DU	4.47	7.03	1.62	-0.05	0.08	-0.01	0.01	0.10

Table A.4: Results of all performed ^{207}Bi deposition distribution measurements. M. in the first column stands for number of measured source. Next column represents the position of measurement defined in Figures 3.19 and 3.20. Based on the position it is possible to know of which type the source was (with or without plastic envelope). Following two columns show positions of source in the pixel detector coordinates. Column number five represents the characteristic droplet size. Finally, in rows six and seven one can find coordinates of dislocation vector followed by two dislocation parameters p_x and p_y. Last column shows the length of the dislocation vector. Its colour coding symbolizes source quality category (A, B or C) defined in Section 3.2.5. Rows with asterisk denote repeated measurement under same experimental conditions.

A.2 Results of Activity Measurements

A.2.1 Results of Relative Activity Measurements

Section contains all the results of relative activity measurements of ^{207}Bi sources. Tables A.5 and A.6 represent relative activities of all sources which were measured with white plastic envelope while Tables A.7 and A.8 represent same results for the sources without the envelope. The tables use two different reference sources (84 for type w/ and 138 for type w/o). The comparison of absolute activities of sources 84 and 138 can be obtained from absolute activity measurements.

Type	No.	t_{live} [s]	N_{570} [cnts]	$\frac{\Delta N_{570}}{N_{570}}$ [%]	N_{TOT} [cnts]	$\frac{N_{570}}{t_{live}}$ [s^{-1}]	$\frac{N_{TOT}}{t_{live}}$ [s^{-1}]	A_{rel} [S84 = 1]
w/	**84**	**7390**	**34053**	**0.154**	**338162**	**4.61**	**45.8**	**1.000**
w/	81	7394	33621	0.110	333834	4.55	45.1	**0.987**
w/	75	7619	34533	0.081	341826	4.53	44.9	**0.984**
w/	96	7218	32405	0.104	319655	4.49	44.3	**0.974**
w/	94	7314	32603	0.116	324974	4.46	44.4	**0.967**
w/	88	7410	32533	0.136	324199	4.39	43.8	**0.953**
w/	82	7267	31586	0.120	314609	4.35	43.3	**0.943**
w/	80	7448	32294	0.120	322290	4.34	43.3	**0.941**

Table A.5: See caption of Table A.6.

Type	No.	t_{live} [s]	N_{570} [cnts]	$\frac{\Delta N_{570}}{N_{570}}$ [%]	N_{TOT} [cnts]	$\frac{N_{570}}{t_{live}}$ [s^{-1}]	$\frac{N_{TOT}}{t_{live}}$ [s^{-1}]	A_{rel} [S84 = 1]
w/	93	8196	35342	0.118	350392	4.31	42.8	**0.936**
w/	87	7428	31889	0.148	318155	4.29	42.8	**0.932**
w/	91	56102	240690	0.063	2404055	4.29	42.9	**0.931**
w/	92	7258	31101	0.116	309094	4.29	42.6	**0.930**
w/	95	7428	31526	0.108	315701	4.24	42.5	**0.921**
w/	89	7517	32112	0.112	319652	4.27	42.5	**0.927**
w/	83	7602	31889	0.084	318915	4.19	42.0	**0.910**
w/	85	7454	31254	0.119	310831	4.19	41.7	**0.910**
w/	90	7498	31355	0.096	314275	4.18	41.9	**0.908**
w/	77	8205	34297	0.088	339887	4.18	41.4	**0.907**
w/	79	7493	31115	0.092	308023	4.15	41.1	**0.901**
w/	86	7593	31213	0.092	309770	4.11	40.8	**0.892**
w/	74	7669	31449	0.098	312844	4.10	40.8	**0.890**
w/	78	7420	30316	0.094	301933	4.09	40.7	**0.887**
w/	134	7328	29909	0.103	298950	4.08	40.8	**0.886**
w/	76	7859	32030	0.124	319952	4.08	40.7	**0.884**
w/	136	7684	31052	0.105	310044	4.04	40.3	**0.877**
w/	73	7452	29897	0.090	298045	4.01	40.0	**0.871**

Table A.6: Results of relative activity measurements of all sources with plastic envelope. First two columns represent source type, t_{live} is a live measurement time, N_{570} stands for number of counts extracted from 570 keV peak and $\Delta N_{570}/N_{570}$ is its relative uncertainty. N_{TOT} represents total number of counts in full spectrum. Finally, A_{rel} is relative activity of the source, where source number 84 (red letters) is reference for all the sources with plastic envelope. Yellow cell colour (source number) represents category of "golden" source, and gray represents "silver" source. Definition of "golden" and "silver" source is introduced in Section 3.3.1.1.

Type	No.	t_{live} [s]	N_{570} [cnts]	$\frac{\Delta N_{570}}{N_{570}}$ [%]	N_{TOT} [cnts]	$\frac{N_{570}}{t_{live}}$ [s^{-1}]	$\frac{N_{TOT}}{t_{live}}$ [s^{-1}]	A_{rel} [S138 = 1]
w/o	133	7586	33795	0.123	340533	4.45	44.9	**1.028**
w/o	114	7522	33219	0.094	330179	4.42	43.9	**1.019**
w/o	116	7372	32240	0.131	317808	4.37	43.1	**1.009**
w/o	115	7571	33050	0.107	330979	4.37	43.7	**1.007**
w/o	111	7726	33655	0.112	332957	4.36	43.1	**1.005**
w/o	**138**	**7627**	**33068**	**0.089**	**327634**	**4.34**	**43.0**	**1.000**
w/o	**138***	**3746**	**30289**	**0.575**	**-**	**8.09**	**-**	**1.000**
w/o	120	7410	32046	0.095	318219	4.32	42.9	**0.997**
w/o	113	7348	31749	0.096	313164	4.32	42.6	**0.997**
w/o	135	7712	33105	0.101	327312	4.29	42.4	**0.990**
w/o	131	7817	33531	0.083	333485	4.29	42.7	**0.989**

Table A.7: See caption of Table A.8.

Type	No.	t_{live} [s]	N_{570} [cnts]	$\frac{\Delta N_{570}}{N_{570}}$ [%]	N_{TOT} [cnts]	$\frac{N_{570}}{t_{live}}$ [s^{-1}]	$\frac{N_{TOT}}{t_{live}}$ [s^{-1}]	A_{rel} [S138 = 1]
w/o	132*	3702	29501	0.582	-	7.97	-	**0.986**
w/o	123*	3644	28812	0.589	-	7.91	-	**0.978**
w/o	119	7414	31165	0.100	310274	4.20	41.8	**0.970**
w/o	139	81670	341677	0.064	3399944	4.18	41.6	**0.965**
w/o	137	7574	30538	0.085	301950	4.03	39.9	**0.930**
w/o	112	7386	29199	0.099	291560	3.95	39.5	**0.912**

Table A.8: Results of relative activity measurements of all sources without plastic envelope. All the measurements were done in CENBG except for three marked by asterisk. Meaning of all the columns and cell colours (yellow, gray) remains the same as in Table A.6. For all the sources without plastic envelope, source number 138 (red letters) is a reference. Measurement of source number 138 without asterisk serves as reference for all measurements performed in CENBG and the one with asterisk is reference for measurements done in LSM.

A.2.2 Results of Absolute Activity Measurements

Tables A.9 and A.10 contain data of absolute activity measurements obtained in my analysis while Tables A.11 and A.12 contain results obtained in independent analysis by my colleague Frédéric Perrot. Graphical comparison of both results are presented in Section 3.3.2.

My results									
		570 keV				1064 keV			
No.	t_{live} [s]	**S** [cnts]	**ΔS** [cnts]	**A** [Bq]	**ΔA** [Bq]	**S** [cnts]	**ΔS** [cnts]	**A** [Bq]	**ΔA** [Bq]
75	82855	116491	551	**141.0**	**0.68**	57019	335	**136.9**	**1.52**
76	166203	218103	1051	**131.6**	**0.65**	104795	566	**125.5**	**1.36**
80	82911	113954	539	**137.8**	**0.67**	54700	367	**131.3**	**1.52**
81	83144	118993	534	**143.5**	**0.66**	57223	321	**136.9**	**1.50**
82	82765	114450	580	**138.7**	**0.72**	55765	367	**134.1**	**1.54**
84	83130	117165	544	**141.3**	**0.67**	55572	328	**133.0**	**1.48**
87	83145	112393	522	**135.6**	**0.65**	54247	343	**129.8**	**1.47**
88	83147	114116	517	**137.6**	**0.64**	54440	286	**130.3**	**1.40**
89	83137	111141	506	**134.1**	**0.63**	53767	307	**128.7**	**1.42**
91	83139	110327	502	**133.1**	**0.62**	52990	310	**126.8**	**1.40**
92	83142	110803	516	**133.6**	**0.64**	53104	292	**127.1**	**1.38**
93	83134	113476	549	**136.9**	**0.68**	54164	320	**129.6**	**1.44**
94	83105	117105	546	**141.3**	**0.68**	55823	339	**133.7**	**1.50**
95	83105	110106	550	**132.9**	**0.68**	52758	334	**126.3**	**1.43**
96	83108	115202	567	**139.0**	**0.70**	55635	340	**133.2**	**1.49**
111	83106	109979	553	**132.7**	**0.68**	52740	311	**126.3**	**1.40**
113	83080	107195	527	**129.4**	**0.65**	51030	293	**122.2**	**1.35**
114	83036	110262	585	**133.2**	**0.72**	52661	275	**126.2**	**1.36**

Table A.9: See caption of Table A.10.

My results									
		570 keV				1064 keV			
No.	t_{live} [s]	S [cnts]	ΔS [cnts]	A [Bq]	ΔA [Bq]	S [cnts]	ΔS [cnts]	A [Bq]	ΔA [Bq]
115	83025	110519	528	**133.5**	**0.65**	52438	285	**125.7**	**1.36**
116	83137	109065	526	**131.6**	**0.65**	52441	302	**125.5**	**1.38**
120	83120	108656	516	**131.1**	**0.64**	52456	304	**125.6**	**1.39**
131	83078	108195	543	**130.6**	**0.67**	51958	319	**124.4**	**1.40**
133	83118	114013	587	**137.6**	**0.72**	54398	302	**130.2**	**1.42**
135	83143	107808	570	**130.0**	**0.70**	52135	294	**124.8**	**1.37**
138	83110	110446	527	**133.3**	**0.65**	52788	323	**126.4**	**1.42**

Table A.10: Absolute activities of 25 measured calibration sources obtained in my own analysis. The table contains the source number, live time of the measurement, number of counts in peak (S) and activity (A) with their absolute uncertainties. Analysis was done for two gamma peaks (570 keV and 1064 keV) as explained in Section 3.3.2.

Frédéric's results									
		570 keV				1064 keV			
No.	t_{live} [s]	S [cnts]	ΔS [cnts]	A [Bq]	ΔA [Bq]	S [cnts]	ΔS [cnts]	A [Bq]	ΔA [Bq]
75	82855	116973	392	**141.6**	**0.50**	56912	273	**136.7**	**1.44**
76	166203	217984	595	**131.5**	**0.39**	104958	385	**125.7**	**1.27**
80	82911	114237	389	**138.2**	**0.49**	54665	268	**131.2**	**1.39**
81	83144	118869	400	**143.4**	**0.51**	57396	275	**137.4**	**1.45**
82	82765	115025	390	**139.4**	**0.50**	55674	270	**133.9**	**1.42**
84	83130	117036	400	**141.2**	**0.51**	55797	272	**133.6**	**1.41**
87	83145	112259	392	**135.4**	**0.50**	54403	270	**130.2**	**1.38**
88	83147	114001	393	**137.5**	**0.50**	54516	269	**130.5**	**1.38**
89	83137	110980	388	**133.9**	**0.49**	53735	268	**128.6**	**1.37**
91	83139	110137	387	**132.8**	**0.49**	53161	267	**127.2**	**1.36**
92	83142	110664	389	**133.5**	**0.49**	53168	266	**127.2**	**1.35**
93	83134	113311	393	**136.7**	**0.50**	54374	269	**130.1**	**1.38**
94	83105	116793	399	**140.9**	**0.51**	55933	273	**133.9**	**1.42**
95	83105	110280	391	**133.1**	**0.49**	53005	268	**126.9**	**1.35**
96	83108	115313	397	**139.1**	**0.50**	55812	273	**133.6**	**1.42**
111	83106	110147	389	**132.9**	**0.49**	52900	267	**126.7**	**1.35**
113	83080	107304	418	**129.5**	**0.52**	51134	270	**122.5**	**1.32**
114	83036	110350	425	**133.3**	**0.53**	52596	272	**126.0**	**1.35**
115	83025	110288	426	**133.2**	**0.53**	52442	272	**125.7**	**1.35**
116	83137	108912	416	**131.4**	**0.52**	52422	271	**125.5**	**1.35**
120	83120	108812	419	**131.3**	**0.53**	52320	272	**125.2**	**1.35**
131	83078	107957	417	**130.3**	**0.52**	51962	271	**124.5**	**1.34**

Table A.11: See caption of Table A.12.

Frédéric's results									
		570 keV				1064 keV			
No.	t_{live} **[s]**	**S [cnts]**	**Δ*S*** **[cnts]**	**A [Bq]**	**Δ*A*** **[Bq]**	**S [cnts]**	**Δ*S*** **[cnts]**	**A [Bq]**	**Δ*A*** **[Bq]**
133	83118	113458	426	**136.9**	**0.54**	54269	276	**129.9**	**1.39**
135	83143	108053	420	**130.3**	**0.53**	52212	271	**125.0**	**1.34**
138	83110	110478	421	**133.3**	**0.53**	52832	273	**126.5**	**1.36**

Table A.12: Absolute activities of 25 measured calibration sources obtained in analysis of Frédéric Perrot. The table contains the source number, live time of the measurement, number of counts in peak (S) and activity (A) with their absolute uncertainties. Analysis was done for two gamma peaks (570 keV and 1064 keV) as explained in Section 3.3.2.

Appendix B

Detailed Description of Feldman-Cousins Method

B.1 Calculation of Half-Life of Rare Processes

Double-beta decay processes are very rare and difficult to observe. Their half lives are extremely long, measured in millions of ages of universe. In case when the decay is observed, it is possible to calculate its half life based on the number of detected decays. Any type of nuclear decay follows universal law of radioactive decay:

$$N(t) = N_0 e^{-\lambda t}. \tag{B.1}$$

Number of remaining nuclei which have not yet decayed, N(t), fall exponentially with time. N_0 represents number of initial nuclei at the beginning of the observation. The rate at which system of nuclei decay is influenced by decay constant λ. Decay constant is related to half life ($T_{1/2}$) via very well known relation:

$$\lambda = \frac{ln(2)}{T_{1/2}}. \tag{B.2}$$

Large values of λ describe fast decays with short half lives. In contrary, low values, describe decays which are very slow with large half lives. The latter is exactly a case for any type of double-beta process. By multiplication of both sides of Equation B.2 by measurement period t, we can conclude, that exponent λt in Equation B.1 is proportional to ratio of measurement period and decay's half life: $t/T_{1/2}$. Shortest half lives of double-beta decay processes are on the level of 10^{15} years while standard duration of double beta decay experiment is measured in years, rarely in decades. The ratio between measurement period and half life of double beta decay process is at maximum at the level of $t/T_{1/2} \approx 10^{-14}$. Exponent λt is, therefore, always extremely tiny as well and we can write:

$$1 \gg \lambda t \gg (\lambda t)^2 \gg ... \gg (\lambda t)^i, \quad i = 3,4,5,... \tag{B.3}$$

Number of decayed nuclei n_D during a period t can be calculated as a difference in numbers of nuclei at the beginning of measurement N_0 and remaining nuclei N(t) given by Equation B.1:

$$n_D = N_0 - N_0 e^{-\lambda t} = N_0 \left(\lambda t - \frac{(\lambda t)^2}{2!} + \frac{(\lambda t)^3}{3!} - ... \right) \approx N_0 \lambda t. \tag{B.4}$$

Exponential decay formula was expanded into Taylor polynomial. Thanks to Equation B.3 it was possible to neglect all the terms except for the first one and obtain very simple relation (for very rare decays). Number of initial nuclei at the beginning of the measurement N_0 can be estimated if we know amount - mass (m) of the observed isotope in the source. For given isotope, molar mass W expresses mass of one mole of the isotope. Therefore, ratio m/W expresses number of moles of the isotope in given source sample. Furthermore, Avogadro's constant N_A defines number of objects (in our case nuclei) needed to compose one mole. Therefore, m/W moles of observed isotope contains

$$N_0 = \frac{mN_A}{\mathrm{W}} \tag{B.5}$$

nuclei. If we know mass of the observed source we can estimate number of nuclei at the beginning of observation. It is important to keep in mind, that the mass of the isotope of interest is not the same as mass of the source which contains the isotope. Typically, sources are composed of many different isotopes and only fraction of their mass, given by their abundance (a), is composed of the isotope of interest. It is important to keep in mind, therefore, that m in my equations represents the fraction of mass belonging to pure isotope in the source of mass. One can also express m in terms of full source mass m_s as a product of source mass and abundance of isotope in the source, i.e.

$$m = am_s. \tag{B.6}$$

If we now combine Equations B.2, B.4, B.5 and B.6 we obtain:

$$n_D = ln(2)\frac{N_A}{\mathrm{W}}\frac{am_s t}{T_{1/2}}. \tag{B.7}$$

The equation expresses number of decays n_D for rare process with half life $T_{1/2}$ if m_s kilograms of isotope with molar mass of W and abundance a is observed during period of time t. Equation gives us the direct recipe to improve chances to observe sought decay. Number of decays is proportional to abundance of the isotope in the source a, mass of the source m_s and length of the measurement t. Number of decays can be enhanced by observation of larger source masses during longer period of times. On top of that, the chances are improved if source is enriched, i.e. abundance of observed isotope a in source is higher. Quantity am_st (mt) is called exposure and it serves for comparison of different double beta decay experiments.

In Equation B.7, n_D stands for real number of decays given the experimental parameters explained above. However, number of observed decays n_{OS} is lower. Some of the decays are not detected due to imprecisions in reconstruction or simply by imposing various different data cuts. The relation between number of real decays n_D and number of observed decays n_{OS} can be expressed via detection efficiency ε. It is a ratio of observed signal events to all decays: $\varepsilon = n_{OS} / n_D$. ε can be obtained from simulations. Finally, let me express half life from Equation B.7:

$$T_{1/2} = ln(2)\frac{N_A}{\mathrm{W}}\varepsilon\frac{am_s t}{n_{OS}}. \tag{B.8}$$

Here, n_D was substituted by number of observed signal events n_{OS} by experiment. Due to the presence of background in experiments, it is not possible to tell with 100% certainty how many real decays n_{OS} were observed (and how many detected events have origin in background). However, having precise background model, it can be estimated to a certain

confidence level as a value denoted μ[1]. Strictly speaking, n_{OS} cannot be measured, therefore, Equation B.8 is used for calculation of half life in double beta decay experiments where μ is plugged instead of n_{OS}.

B.2 Statistical Nature of Observed Counts

Equation B.8 gives a recipe for calculation of half life of rare decay if number of observed counts is given. Radioactive decay is, however, statistical process. Two perfectly identical copies of the same experiment might, therefore, provide different observed counts, due to the statistical fluctuations. It is important to take this fact into account in order to avoid mistakes in analysis and avoid dependence of the result on random factor. Discussion to follow is based on the one presented in [120].

B.2.1 Experiments Without Background

In order to avoid random factor in calculation of half life, one needs to consider ensemble of identical experiments instead of single measurement done by one particular example. In average, such experiment detects n_O total counts (signal + background). In case of background-less experiments, therefore, each count represents true signal. Estimation of true detected signals μ is, therefore, identical to number of all observed counts, i.e. $n_O = \mu$. As it was already discussed, identical experiments yield different number of counts due to the statistical fluctuations. Probability to observe n counts in specific experiment (if average of μ true signals are expected) is given by Poisson distribution:

$$P(n,\mu) = \frac{\mu^n}{n!} e^{-\mu}. \tag{B.9}$$

For example, with μ = 3 expected true signals, 42.3% of identical experiments would observe less counts and roughly 5% unfortunate experiments would not observe a single count! What conclusion can a single experiment draw about average value of true expected signals given from observation of n events? Common method to report a result is given in terms of so-called confidence intervals proposed by Neyman in [121]. The idea is to propose interval $\mu \in (\mu_L, \mu_U)$ instead of single value. Here, μ_U represents number of expected true events such that, only α fraction of identical experiments would report lower or equal observed number of counts. Similarly, μ_L is value of true expected signals such that only β fraction of identical experiments would observe higher or equal number of counts. Fractions α and β represent scenarios of experiments not covered by the interval. In contrary, 1 - α - β represent all the scenarios covered in the interval. It expresses the level of belief that the interval covers the true value. That is where term confidence level comes from.

Let me demonstrate with an example, how confidence intervals are calculated. I will assume background-less experiment, which observed n = 3 counts, as an example. Let me choose $\alpha = \beta = 0.05$ (5%). Upper limit, μ_U in such case is a value for which cumulative probability to observe number of counts less or equal to three is 5%. Limit can be obtained, therefore, if we solve following equation:

$$\alpha = 0.05 = \sum_{i=0}^{3} P(i,\mu_U). \tag{B.10}$$

[1]Methodology to calculate μ if number of background counts b is given will be discussed in following sections

Equation can be solved numerically with result $\mu_U = 7.754$. Subsequently, we can calculate lower limit μ_L in similar fashion. We search for a mean value of true signals μ_L for which 5% of experiments would report three or more counts. The value is a solution to the equation:

$$\beta = 0.05 = \sum_{i=3}^{\infty} P(i, \mu_L). \tag{B.11}$$

Numerical solution provides value $\mu_L = 0.818$. Finally, we say that confidence interval (0.818, 7.754) covers value of true expected signals μ at the confidence level (CL) of 90% (1 - α - β). Note that, choice $\alpha = 0.03$ and $\beta = 0.07$ would yield different confidence interval but with a same confidence level. Such an interval is also valid, however, it is common choice to set symmetric intervals. In case when $\alpha \neq 0$ and $\beta \neq 0$ we talk about central interval. There are situations when only one-sided interval is preferable. If we repeat the same procedure, this time with $\alpha = 0$ and $\beta = 0.05$, we obtain interval (0, 7.554). Such interval offers uniquely upper limit at the confidence level of 95%. Furthermore, choice $\alpha = 0.05$ and $\beta = 0$ yields interval (0.818, ∞) again on 95% confidence level. However, in this case only lower limit is reported. It is always important to precise what kind of interval (one-sided or central) is presented along with confidence level, when reporting result of such experiment.

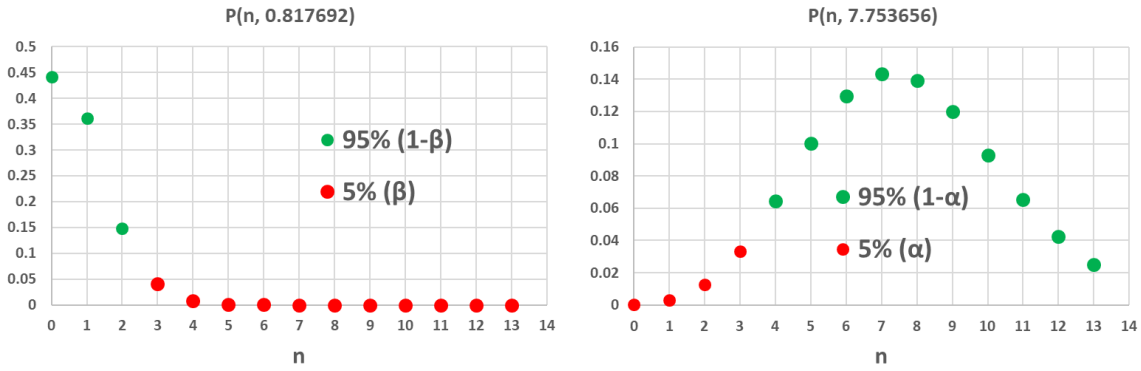

Figure B.1: Left: Poisson distribution for $\mu = 0.817692$. Value μ represents lower limit of confidence interval μ_L. It was chosen in a way, that all the scenarios $n \geq n_O = 3$ (red dots) give a cumulative probability of β: 5%. Right: Poisson distribution for $\mu = 7.753656$. Value μ represents upper limit of confidence interval μ_U. It was chosen in a way, that all the scenarios $n \leq n_O = 3$ (red dots) give a cumulative probability of α: 5%.

Let me briefly summarize the method for calculation of confidence intervals. Backgroundless experiment with n_O observed counts should report mean expected number of true signals μ from interval (μ_L, μ_U). Here, the limits of the interval are calculated in following way:

$$\begin{aligned} \alpha &= \sum_{i=0}^{n_O} P(i, \mu_U), \\ \beta &= \sum_{i=n_O}^{\infty} P(i, \mu_L). \end{aligned} \tag{B.12}$$

Here, α and β are chosen constants which decide between scenarios when only lower, upper or both limits are given. The confidence level of the presented interval is given in % and is calculated as 1 - α - β.

B.2.2 Experiments with Background - Collapse of Classical Method

In following, I will assume more realistic situation of experiments with non-zero background. Mean expected number of counts is in such case composed of two components, the mean expected signal μ (same as in case of background-less experiments) and mean expected number of background counts b. If we average over ensemble of identical experiments, in average we expect to observe $n_O = \mu + b$ counts. Following the same logic as in previous section, the probability to observe n counts in one of the experiments is again given by Poisson distribution:

$$P(n, \mu + b) = \frac{(\mu + b)^n}{n!} e^{-(\mu+b)}. \tag{B.13}$$

Compared to Equation B.9, number of mean expected counts n_O is higher by number of expected background counts b. After addition of expected background counts, Equations B.12 get following form:

$$\begin{aligned} \alpha &= \sum_{i=0}^{n_O} P(i, \mu_U + b), \\ \beta &= \sum_{i=n_O}^{\infty} P(i, \mu_L + b). \end{aligned} \tag{B.14}$$

By setting $\alpha = 0.05$, $\beta = 0$, one can calculate one-sided confidence intervals $(0, \mu_U)$ in similar fashion as in background-less case. Let me assume experiment with four expected background counts, b = 4. I will compare experiments which observed number of counts lower than background, i.e four different experiment scenarios n = 3,2,1,0. For each of four scenarios, plot similar to Figure B.1 - Right was produced and shown in Figure B.2.

Value of mean total expected counts μ + b differs in dependence of scenario. Experiment with three measured counts calculates μ + b = 7.754 counts as a solution to first equation in Equation B.14. If we subtract background (four counts), we obtain upper limit of confidence interval μ_U = 3.754. It is no surprise that, the lower the number of measured counts is the lower μ_U is. However, for experiment scenarios n = 2,1,0 we obtain μ_U = 2.296, 0.744, -1.004, respectively. Case, when no count is measured, gives a non-physical negative value of upper limit. Moreover, if we try to correct such value and report $\mu_U = 0$, the confidence interval would be an empty set. Due to the presence of background, value μ_U is "pushed" out of the physical region. Classical method provides absurd results for measurements observing much less counts n than expected background b.

B.3 Feldman-Cousins Method

Previously presented problem with construction of reasonable confidence intervals is not the only pitfall of classical method.

Experiments which observe number of counts lower than background, are, quite naturally, able to report only upper limit on the expected mean signal μ_U. Such an upper boundary can be plugged into Equation B.8 in order to calculate respective half-life. Half-life and number of signal counts μ are inversely proportional. Therefore, plugging upper limit on expected mean signal μ_U into Figure B.8 yields lower boundary on half life as follows:

$$T_{1/2} \geq ln(2) \frac{N_A}{W} \varepsilon \frac{a m_s t}{\mu_U}. \tag{B.15}$$

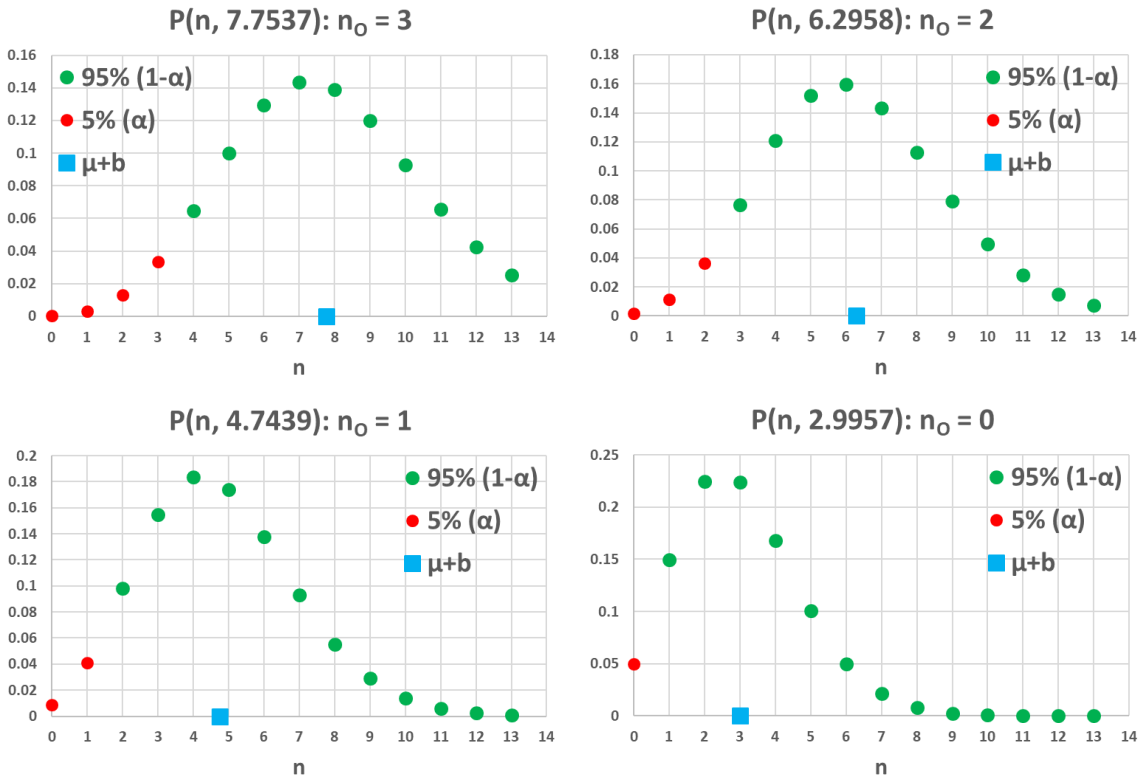

Figure B.2: Poisson distributions of four different values of mean expected counts μ + b. Value μ + b was chosen in a way that cumulative probability of n $\leq$ n_O (red dots) is equal exactly to chosen α (5%). Blue dot marks position of μ + b on x-axis (numerical value is given in each title). Each plot represents different measured number of counts n_O of identical experiments with expected background b = 4.

Using a classical method, two experiments which observe same number of total counts but expect different backgrounds, would report different upper limits of true mean signal (μ_U). This is not surprising, however, if both experiments observed less counts than background (no discovery), the one with higher expected background would report lower value of μ_U, i.e. higher low limit on half life. This is an anomaly of the method, because experiment with larger expected background should not get better results than one with lower background.

All of the previous fundamental problems with classical method were solved by Feldman and Cousin in their famous article from 1997 [122]. Their method takes advantage of construction of so-called confidence belts. Construction of confidence belts in some sense resembles the process of construction of confidence intervals from classical method.

Let me describe the process in detail. As previously, let us have an experiment with expected background b. The experiment detects n counts. Probability, that an experiment with b background counts observes n total counts is governed by Poisson probability P(n, μ + b) given by Equation B.13. μ, the mean true signal count, is unknown and has to be extracted. In classical method, the approach was rather direct. We attempted to adapt limits of confidence interval (μ_L, μ_U) in a way that cumulative probability of P(i, μ_U + b) (P(i, μ_L + b)) for all i $\leq$ n (i $\geq$ n) covered α (β) portion of probability. Feldman-Cousins method is not as straightforward. In this method, intervals (n_j^{min}, n_j^{max}) are constructed for equidistantly distributed succession of values μ_j. Calculation is performed for variety of chosen values μ_j.

Such intervals are called confidence belts.

Calculation of confidence belts proceeds in following steps:

1. Value of μ_j is chosen.
2. Values of integer quantities n_j^{min} and n_j^{max} are calculated. They should satisfy following relations:

$$1-\alpha \leq \sum_{i=n_j^{min}}^{\infty} P(i,\mu_j+b), \tag{B.16}$$

$$1-\beta \leq \sum_{i=0}^{n_j^{max}} P(i,\mu_j+b). \tag{B.17}$$

   Coefficients α and β are chosen based on the type of interval and confidence level which we would like to reach (central or one-sided). For given α and β, solution is a couple of n_j^{min} and n_j^{max} where n_j^{min} is minimal value satisfying the Equation B.16 while, simultaneously n_j^{max} is maximal value satisfying the Equation B.17.
3. Values n_j^{min} and n_j^{max} are kept.
4. μ_j is incremented by a small chosen amount $\Delta\mu$, $\mu_{j+1} = \mu_j + \Delta\mu$ is obtained. Algorithm continues with μ_{j+1} at point 2.
5. When sufficient interval of values of μ_j is calculated, the algorithm stops.

Figure B.3 contains clarification of Equations B.16 and B.17 for $\mu_j + b = 8.56$. Note that, similarly to confidence intervals from classical method, confidence level CL = 1 - α - β. In the classical method, we adapted value of variables μ_L and μ_U in order to solve Equations B.14. μ_L and μ_U are real numbers so the equations are solvable exactly (within numerical

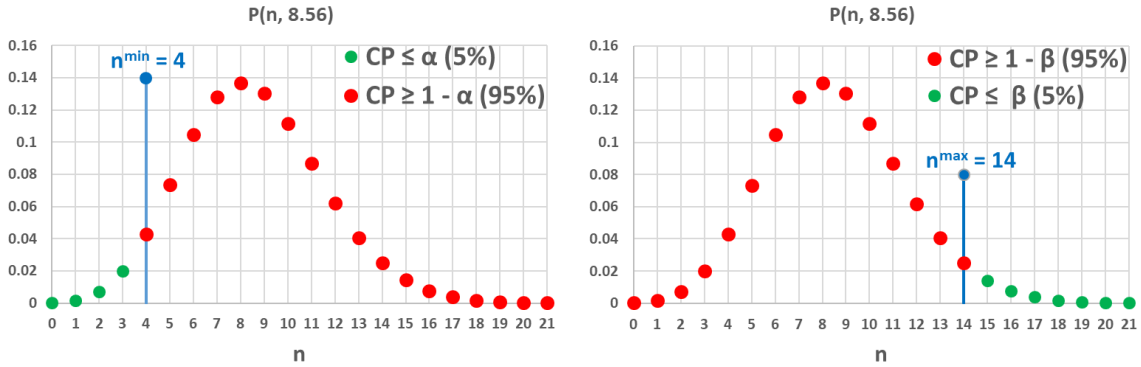

Figure B.3: Example of calculation of (central) confidence belt for μ_j = 8.56 - b. Left: According to Equation B.16, n_j^{min} = 4 because cumulative probability (CP) of red dots is superior to 1 - α = 95%. At the same time, value n = 5 would cause CP of red dots drop below 95%. Right: According to Equation B.17, n_j^{max} = 14 because cumulative probability (CP) of red dots is superior to 1 - β = 95%. At the same time, value n = 13 would cause CP of red dots drop below 95%.

imprecision). However, in problem of confidence belts, values n_j^{min} and n_j^{max} are integers. The cumulative probability of P(n, μ_j + b) for all $n_j^{min} \leq n \leq n_j^{max}$ will practically always exceed CL = 1 - α - β. Such conservativeness is unavoidable effect.

Result of the whole algorithm is a set of μ_0, μ_1, ..., μ_N values with respective confidence belts (n_0^{min}, n_0^{max}), (n_1^{min}, n_1^{max}), ..., (n_N^{min}, n_N^{max}). The confidence belts can be represented in two-dimensional plots which can be found in Figure B.4.

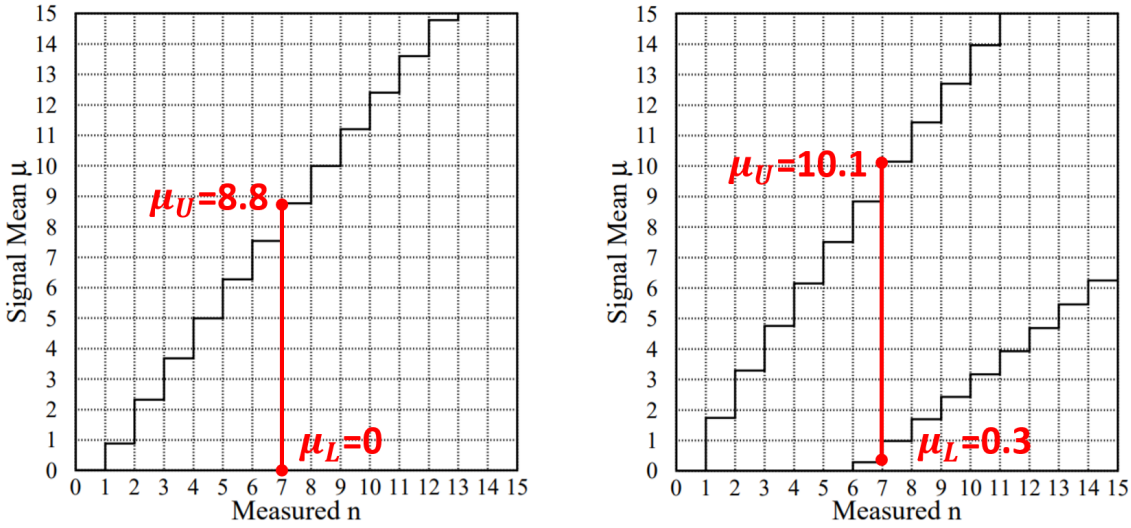

Figure B.4: Representation of confidence belts as a function of μ_j (y-axis). X-axis represents number of total counts n observed by experiment. Source: [122]. Both plots are generated for case with b = 3. They are described in more detail in the text. Left: Plot showing confidence level low limits n_j^{min} in dependence on μ_j for one-sided intervals with β = 0. Right: Plot showing confidence level limits n_j^{min} and n_j^{max} in dependence on μ_j for central interval.

The plots represent two different type of belt intervals. Left one, with α = 0.1 (10%) and β = 0 represents one-sided belts where only n_j^{min} is finite and $n_j^{max} = \infty$. They are generated for case with three expected background counts (b = 3). If experiment observes, for instance, n = 7, it reports confidence interval given by vertical section in value n = 7, as depicted in Figure B.4. Experimentalist in the scenario on the left side would report confidence interval of μ = (0, 8.8) while the same experiment with the same expected background would report interval (0.3, 10.1). Both cases offer interval on a confidence level CL = 1 - α - β of 90%. The difference lies in the choice whether experimentalist prefer to publish only upper limit or central interval. Such a degree of freedom creates ambiguity in reported results. What is even worse, the plots offer empty confidence interval in case if experiment observed zero counts (n = 0). The solution which is a triumph of Feldman-Cousins method is in the ordering principle presented in following section.

B.3.1 Ordering Principle

Confidence belts in Figure B.4 represent two possible analyses methods for the same experiment with three background counts. Moreover, if we keep confidence level at the same value of 90% we can shift the belts to the left or right in dependence on α and β. This becomes clear if we have a look at the Figure B.3. Imagine that we keep the sum of α + β

= 0.1 constant. If we gradually decrease α, value n^{min} would decrease as well. β, however, would be increased, pushing n^{max} to lower values.

Choice of α and β is distinguishing between scenario when central interval or one-sided interval is reported. Nevertheless, it makes sense to expect only upper limit μ_U when measured number of counts is less or equal to expected background and central interval otherwise. Such an option is not possible with the method proposed in the latest section. Method which would change α and β dynamically for different μ_j is needed.

Solution how n_j^{min} and n_j^{max} in Figure B.3 was found, can be reformulated bit differently. In order to find value n^{max} = 14 we can say that we had to gradually sum the probabilities P(0, 8.56) + P(1, 8.56) + ..., until cumulative sum exceeded value of 1 - β. This happened when P(14, 8.56) was added so we concluded that n^{max} = 14. We added values P(i, 8.56) in well defined order (i = 0,1,2, etc.). It is example of type of ordering based on which, we accept or reject individual values. Another type of ordering can be observed in the same figure, on the left side, in case when n^{min} = 4 was calculated. All the probabilities P(i, 8.56) were added in descending order $\infty \rightarrow 4$. Term P(4, 8.56) caused the sum to exceed 95% (1 - α) and, therefore, n^{min} = 4.

B.3.1.1 Likelihood Ratio Ordering Principle

The ordering principles of ascending / descending order are not the only possibilities. More sophisticated principles can be proposed. Feldman and Cousins proposed likelihood ratio ordering principle as a core of their universal method presented in this section.

The principle is tailored to build the interval from the center by adding terms P(i, μ_j + b) to the left and right based on their likelihood ratios R given by:

$$R = \frac{P(i, \mu_j + b)}{P(i, \mu_j^{best} + b)}. \tag{B.18}$$

Here, μ_j^{best} is a value which maximize P(i, μ_j + b) for given i and b. Method of likelihood ratio ordering, adds the terms P(i, μ_j + b) with highest likelihood ratio into cumulative sum. The method gives priority to values of P(i, μ_j + b) as close as possible to the most probable value μ_j^{best}.

It is easy to demonstrate the principle with an example. In order to obtain a direct comparison with Figure B.3, I will assume construction of interval given by μ_j + b = 8.56. While the calculation of case (descending / ascending order) presented in the figure did not rely on the value of b (only on μ_j + b), we did not have to precise it. However, in case of likelihood ratio ordering the result depends on both μ_j and b. In the following, I will assume expected background of three counts, b = 3. I will present example of case μ_5 = 0.5 (I skipped μ_0 = 0, μ_1 = 0.1, ..., μ_4 = 0.4).

Detailed clarification of such calculation is displayed in Table B.1. Each row represents one value of total counts observed by experiment. Second column displays Poisson probability of obtaining n counts if μ_5 + b are expected. Following column shows μ_5^{best} which is a value of μ which maximizes P(n, μ + b) for given n and b. This value cannot be negative. In following column P(n, μ_5^{best} + b) is calculated. Fifth column holds value of likelihood ratio R given in Equation B.18. Finally, last column displays order of descending value of R. The order in which values P(n, μ_5 + b) are added to cumulative sum is great demonstration of the method of likelihood ratios. First term added to the sum is n = 4 followed by n = 3,2,5,1,0 and 6. Their cumulative sum is equal to 0.935 and it just enough terms to exceed value of 0.9 which is 90% CL. On this confidence level, therefore, we calculated that for μ_5 = 0.5 (b

μ_5 = 0.5, b = 3					
n	**P(n, μ_5+b)**	**μ_5^{best}**	**P(n, μ_5^{best}+b)**	**R**	**Order**
0	0.030	0	0.050	0.607	6
1	0.106	0	0.149	0.708	5
2	0.185	0	0.224	0.826	3
3	0.216	0	0.224	0.963	2
4	0.189	1	0.195	0.966	1
5	0.132	2	0.175	0.753	4
6	0.077	3	0.161	0.480	7
7	0.039	4	0.149	0.259	8
8	0.017	5	0.140	0.121	9
9	0.007	6	0.132	0.050	
10	0.002	7	0.125	0.018	
11	0.001	8	0.119	0.006	

Table B.1: Example of calculation of confidence belt for experiment which expects 3 background counts. The calculation is performed for μ_5 = 0.5. More information about the calculation and content of the table is provided in text.

= 3), n_5^{min} = 0 and n_5^{min} = 6. If we added following term in order (n = 7) cumulative sum would reach 0.973, exceeding also 0.95 (95%), in such scenario, n_5^{min} = 0 and n_5^{min} = 7. By addition of yet another term (n = 8) sum reaches 0.99 which results into n_5^{min} = 0 and n_5^{min} = 8 at 99% confidence level.

Method of likelihood ratio ordering builds confidence belts from center and expands it to the left and right simultaneously. Note that, the algorithm might lead into intervals when some value in the middle is not included in the cumulative sum while reaching wanted CL. In such case conservative approach should be chosen and the missing value should be included also to achieve continuous interval.

I performed calculation such as the one presented in Table B.1 for many different values of $0 \leq \mu_j \leq 15$ with step $\Delta\mu = \mu_{j+1} - \mu_j = 0.01$. The resulting intervals (n_j^{min}, n_j^{max}) I represented in form of confidence belts similar to Figure B.4. The result for 90% and 95% can be found in Figure B.5.

As the value of μ is rising, we can notice that interval (n_j^{min}, n_j^{max}) changes from one-sided regime ($n_j^{min} = 0$) into central interval regime ($n_j^{min} \neq 0$). Vertical cross section in given value n, bounded from the bottom by blue curve (μ_L) and from top by red curve (μ_U), represent confidence intervals reported by experiment. Confidence intervals (μ_L, μ_U) for experiment which observed n = 0 were empty in Figure B.4. This was due to the ordering method used to produce confidence belts. Such a behaviour is not present in case of likelihood ratio ordering as can be seen in Figure B.5. This is a triumph of likelihood ratio method. Moreover, the method also automatically generates one sided confidence interval (0, μ_U) or central interval (μ_L, μ_U), depending on how significant the number of observed counts is relatively to the background.

B.3.1.2 Numerical Artefacts

Confidence belts, like those presented in Figure B.5 can be produced for any value of background b. For given number of observed events n, we can extract confidence interval (μ_L, μ_U) as a function of expected background b.

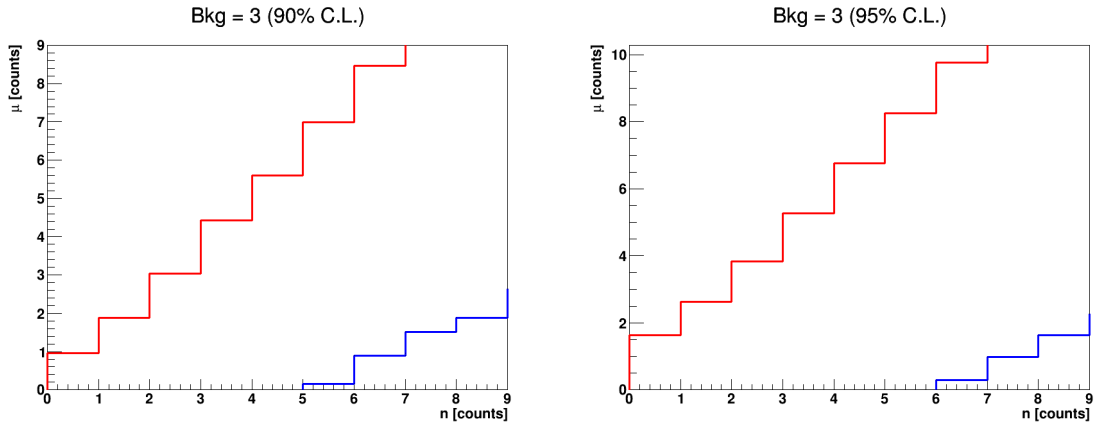

Figure B.5: Results from my own implementation of Feldman-Cousins recipe. Plots represent example of confidence belts generated for 90% CL (left) and 95% CL (right) for experiment which expects 3 background counts. Likelihood ratio ordering method was implemented. In comparison to Figure B.4 likelihood ratio method provides non-empty confidence interval for experiment observing zero counts.

Figure B.6 shows how upper limit μ_U of confidence interval (90% CL) changes with increasing expected background b for n = 0, 2, 4. Black dashed line represents calculation based on the previously presented method of likelihood ratio ordering. Limit tends to be improved (lower) with higher expected background. However, the functions in the plot are not perfectly smooth. They contain sharp local peaks where functional value grows a little and then continue decreasing again. These are effects caused by discreteness of Poisson distribution. In order to obtain nicely smooth, never increasing function, we need to apply a correction. The values in the regions between two peaks are set to a value of next peak in order to flatten the curve. The curves after the application of correction are presented as solid red lines. Proposed correction is something what we can afford to do, as it overestimates the upper limit of confidence interval, setting it to more conservative value.

B.3.2 Experiments with no Discovery

Method of likelihood ratio ordering proved itself to be effective, preventing the appearance of empty confidence intervals. The method relaxes the requirement to choose α and β thresholds from method with ascending / descending ordering. One only needs to choose CL and perform the calculation.

In this section, I am interested in experiments which did not observe the process of interest and cannot claim the discovery. Such an experiment observes less or equal number of counts than the expected background, n $\leq$ b. With a method of likelihood ratio ordering, such experiment is always capable to report upper limit μ_U. Thanks to the Equation B.15 the limit can be transformed into low limit on a half-life. Figure B.5 implies that, the lower the number of counts n observed by experiment is under the expected background, the better upper limit μ_U experiment is able to report. Experiment with higher expected background would report better limit than experiment with lower background if both experiments measured same number of counts. This is an unwanted anomaly already discussed to arise in classical method.

Experiment expecting 4 background counts during given period of time has a 19.5% chance to observe four counts assuming no other source of counts, P(4,4) = 0.195. It also

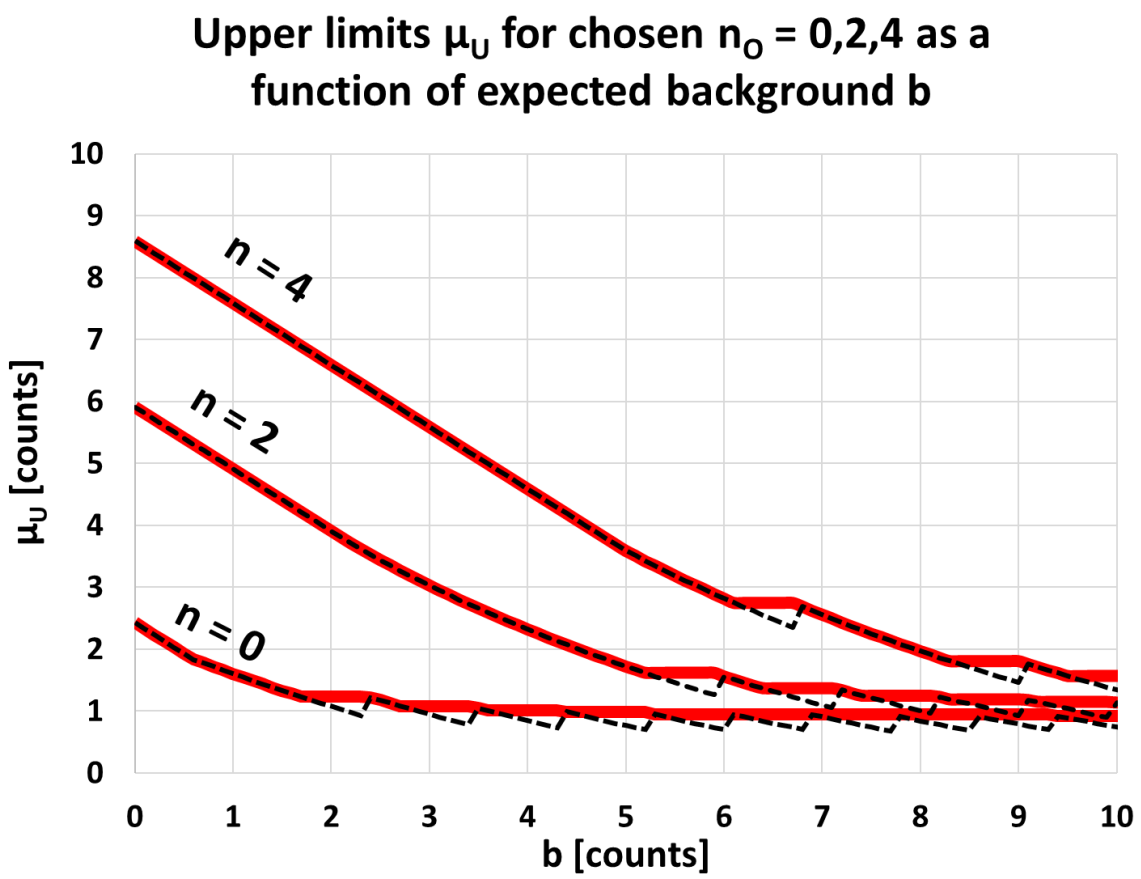

Figure B.6: Plots of upper limits μ_U as a function of background expected by experiment. Plot is constructed for experiments observing n = 0,2 or 4 total counts. Calculation represents 90% CL. Dashed black lines show calculation with no correction obtained by application of likelihood ratio ordering method to Feldman-Cousins recipe. Red solid lines are same results after correction was applied in order to prevent intervals where function increases.

has a probability of 19.5% to observe 3 counts, P(3,4) = 0.195, 14.7% to observe 2 counts, P(2,4) = 0.147, etc.. To some extent, number of events which experiment detects, is partially random, only governed by Poisson distribution. We need a method which assigns unique value of upper limit μ_U to experiments with no discovery only based on the expected background b, regardless of number of counts it has detected. Solution is, to report a mean value of all upper limits over all experiments with the same expected background and different detected counts. The value is calculated as follows:

$$\mu_U = \sum_{n=0}^{\infty} P(n,b)U(n,b). \tag{B.19}$$

Here, U(n,b) is an upper limit which experiment would report based on the likelihood ratio ordering method if it observed n events and expected background b (for given CL). Such a limit is weighted by probability P(n,b), that the experiment measures n counts if only background is present.

Such a calculation method ensures that the experiments with better background suppression but no discovery, would be able to publish better limit than the one with more background.

Feldman-Cousins method presented above is standard frequentist method used to evalu-

ate exclusion regions for half-life of undiscovered processes. The upper value μ_U calculated by method presented in this chapter and represented by Equation B.19 can be plugged into Equation B.15 and provide a lower limit on half life of the undiscovered process. If real half-life of the sought (existing) process is lower than this limit, the experiment should be able to observe it. Application of this method in simulation is presented in Chapter 6 dedicated to to estimation of expected limit achievable by SuperNEMO experiment to $0\nu\beta\beta$ with Majoron emission.

Appendix C

Numerical Values of Half-Life Limits for $0\nu\beta\beta\chi^0$ and $0\nu\beta\beta\chi^0\chi^0$

The appendix is dedicated to all the half-life limit values calculated in Chapter 6. Values are plotted in Figures 6.6 and 6.7 in aforementioned chapter. Tables C.1 and C.2 contain all the half-life limits obtained for $0\nu\beta\beta\chi^0$. Colour of each cell represents the ROI for which the limit was obtained. The definition of colour coding is introduced in Table C.3.

t = 0.5 yr			A_{Bi} [μBq/kg]					
			0	10	20	50	100	200
CL = 90%	A_{Tl} [μBq/kg]	0	0.594	0.592	0.591	0.587	0.582	0.570
		100	0.589	0.587	0.586	0.583	0.577	0.567
CL = 95%		0	0.498	0.497	0.496	0.493	0.489	0.480
		100	0.494	0.493	0.492	0.489	0.485	0.476
t = 1 yr			A_{Bi} [μBq/kg]					
			0	10	20	50	100	200
CL = 90%	A_{Tl} [μBq/kg]	0	0.880	0.877	0.874	0.866	0.857	0.839
		100	0.867	0.866	0.864	0.858	0.849	0.833
CL = 95%		0	0.737	0.735	0.733	0.729	0.722	0.708
		100	0.730	0.729	0.727	0.723	0.716	0.702
t = 2 yr			A_{Bi} [μBq/kg]					
			0	10	20	50	100	200
CL = 90%	A_{Tl} [μBq/kg]	0	1.310	1.305	1.300	1.285	1.260	1.222
		100	1.281	1.276	1.271	1.256	1.236	1.212
CL = 95%		0	1.098	1.093	1.089	1.077	1.057	1.031
		100	1.073	1.070	1.066	1.054	1.043	1.024
t = 5 yr			A_{Bi} [μBq/kg]					
			0	10	20	50	100	200
CL = 90%	A_{Tl} [μBq/kg]	0	2.164	2.154	2.145	2.119	2.076	2.001
		100	2.115	2.107	2.099	2.075	2.036	1.965
CL = 95%		0	1.822	1.814	1.807	1.786	1.752	1.703
		100	1.781	1.774	1.767	1.747	1.734	1.692

Table C.1: See caption of Table C.2.

t = 10 yr			A_{Bi} [μBq/kg]					
			0	10	20	50	100	200
CL = 90%	A_{Tl} [μBq/kg]	0	3.141	3.129	3.117	3.082	3.024	2.916
		100	3.072	3.061	3.049	3.015	2.960	2.860
CL = 95%		0	2.656	2.646	2.636	2.606	2.558	2.466
		100	2.598	2.588	2.579	2.550	2.504	2.419
t = 15 yr			A_{Bi} [μBq/kg]					
			0	10	20	50	100	200
CL = 90%	A_{Tl} [μBq/kg]	0	3.887	3.869	3.851	3.799	3.716	3.576
		100	3.808	3.791	3.774	3.724	3.644	3.507
CL = 95%		0	3.287	3.272	3.257	3.214	3.144	3.102
		100	3.221	3.206	3.192	3.192	3.112	3.057

Table C.2: Half-life limits of $0\nu\beta\beta\chi^0$ achievable by SuperNEMO as a function of Bi (A_{Bi}) and Tl (A_{Tl}) contamination, time of measurement (t) and confidence level (CL). The ROI with the best half-life limit were varying, therefore, colour of the cell represents the ROI for given value. Colours are defined in Table C.3. Half-life limit values in table are expressed in 10^{23} yr.

Color codes of the best ROI intervals		
(2500 keV, 2800 keV)	(2500 keV, 2900 keV)	(2400 keV, 2900 keV)
(2500 keV, 3000 keV)	(2400 keV, 3000 keV)	(2400 keV, 3100 keV)

Table C.3: Colour coding definition for intervals with the best obtained half-life limit. Each cell colour in Tables C.1 and C.2 represents different ROI for which the half-life limit was obtained.

ROI yielding the best half-life limit for $0\nu\beta\beta\chi^0\chi^0$ was always (1000 keV, 2900 keV) due to different spectral shape, shifted to low energies relatively to $0\nu\beta\beta\chi^0$. In this ROI, Bi and Tl contamination contributed negligibly (compared to dominating $2\nu\beta\beta$) to the background and the resulting limits remained almost unchanged even for extreme values[1] of Bi and Tl contamination. Therefore, the calculation was performed only for scenario with the SuperNEMO design contamination limits of $A_{Bi} = 10\mu$Bq/kg and $A_{Tl} = 2\mu$Bq/kg. Resulting half-life limits are represented in Tables C.4, C.5 and C.6.

t [yr]	0.1	0.2	0.5	0.7	1	1.5	2
CL = 90%	0.475	0.671	1.061	1.256	1.501	1.838	2.123
CL = 95%	0.403	0.570	0.902	1.067	1.275	1.562	1.804

Table C.4: See caption of Table C.6.

t [yr]	2.5	3	3.5	4	4.5	5	6
CL = 90%	2.373	2.600	2.808	3.002	3.184	3.356	3.676
CL = 95%	2.017	2.209	2.386	2.551	2.706	2.852	3.124

Table C.5: See caption of Table C.6.

[1] Hundreds of times higher than SuperNEMO design values.

t [yr]	7	8	9	10	12	14	20
CL = 90%	3.971	4.245	4.503	4.746	5.199	5.616	6.712
CL = 95%	3.374	3.607	3.826	4.033	4.418	4.772	5.704

Table C.6: Half-life limits of $0\nu\beta\beta\chi^0\chi^0$ achievable by SuperNEMO as a function of time of measurement (t) and confidence level (CL). The ROI with the best half-life limit was in each case (1000 keV, 2900 keV). Bi and Tl contaminations were set to $A_{Bi} = 10\mu$Bq/kg and $A_{Tl} = 2\mu$Bq/kg in the calculation. Half-life limit values in table are expressed in 10^{22} yr.